UNIVERSITA' DEGLI STUDI DI PARMA

Dottorato di ricerca in Scienze Chimiche
Ph.D. in Chemical Science

Ciclo XXVIII (2013-2015)

# *Supramolecular coordination complexes as building blocks for porous and magnetic materials*

Coordinator:
Prof. Roberto Cammi

Tutor:
Prof. Matteo Tegoni

Co-tutor:
Prof. Luciano Marchiò

Ph.D. candidate: Corrado Atzeri

2016

*To my parents,*

*Anna Maria and Renato,*

*Gratefully*

# Contents

# Abstract

In this work, new coordination polymers based on two different classes of synthons are presented. In addition, manganese-based metallacrowns of magnetic interest are studied, both in the solid state and in solution.

Firstly, functionalized bispyrazolylmethane derivatives are employed as bridging ligands for the establishment of silver-based coordination polymers; the influence of the substituent groups and of the counterions on the supramolecular packing is also investigated.

Secondly, the use of metallacrown (MC) complexes as building blocks for porous coordination polymers is discussed. The design of a new metallacrown species is presented, which shows the tendency of aggregating in the solid state to form coordination polymers. Two new coordination polymers are indeed reported, of which one is the first MC-based permanently porous coordination network ever presented. The solid resists solvent evacuation and exhibits gas uptake ability.

Furthermore, the isolation and characterization of a new metallacryptate species based on manganese ions is described. The metal-rich structure comprises nine Mn(II)/Mn(III) ions and presents an *inverse* metallacrown core subunit that binds a $\mu_3$-$O^{2-}$ ion. The metallacryptate is isolated in high yields and stable in solution.

Lastly, a family of *3d-4f* heterometallic metallacrowns is characterized in solution by means of UV-Vis spectrophotometry and of paramagnetically shifted $^1$H-NMR. The lanthanide-induced shifts observed in the spectra are employed to describe the molecules behaviour in solution and are qualitatively related to the magnetic properties of the compounds.

# Chapter I

## *Introduction on porous coordination polymers*

## 1.1 - Metal-Organic Frameworks and Porous Coordination Polymers

Over the last three decades, the science of porous solid materials has become one of the most intensely studied areas of research for chemists, physicists, and materials scientists (Fig. 1.1). These materials have found a large number of applications in many fields, such as adsorption, separation and purification[1-3], as well as catalysis[1,4-6]. Porous solids acting as adsorbents or membrane fillers are playing key roles in separations and purifications of various chemicals that we encounter in our daily activities. Such applications require systems able of optimizing two different properties: high adsorbent capacity and selectivity. In order to ensure a relevant amount of stocked gas, we need systems that can adsorb discrete quantity of molecules on the surface; hence, systems with high values of superficial area ($cm^3$ of adsorbed gas per grams of substance), result particularly efficient.

On the other hand, in order to be suitable for gaseous mixtures purifications, porous systems require high adsorption selectivity. This selectivity can be gained in different ways, *i.e*. tailoring the pores size or functionalizing the cavity to establish preferential interactions.[7]

Historically, the concept of porous solid was introduced in 1756 by the swedish mineralogist Fredrik Cronstedt, who found that the stilbite, heated at high temperature, produced high amounts of steam from the water that had been adsorbed by the material[8]. Based on this, he called the material zeolite, from the Greek zéo-lithos, meaning boiling stone. Later, other minerals were found with the same characteristics and, in 1862, the chemist Sainte Claire Devill[9] synthesized the first zeolite in a laboratory.

Nowadays, porous systems are classified according to the average diameter of the cavities, the structure of the pores and the chemical properties of the material. The different classifications focus on a particular aspect and are independent each other. Nano-porous materials, which have pores size between 1 nm and 100 nm, according to the IUPAC[10] nomenclature, are divided in: i) microporous systems (pores diameter < 2 nm) , ii) mesoporous systems (pores diameter 2-50 nm) and iii) macroporous systems (pores diameter > 50 nm).

In the past years, a new class of synthetic porous materials, namely **M**etal-

**O**rganic **F**rameworks (MOFs), also known as **P**orous **C**oordination **P**olymers (PCPs) or **P**orous **C**oordination **N**etworks (PCNs)[11], has proved to be one of the most prolific areas of chemistry and material science research.

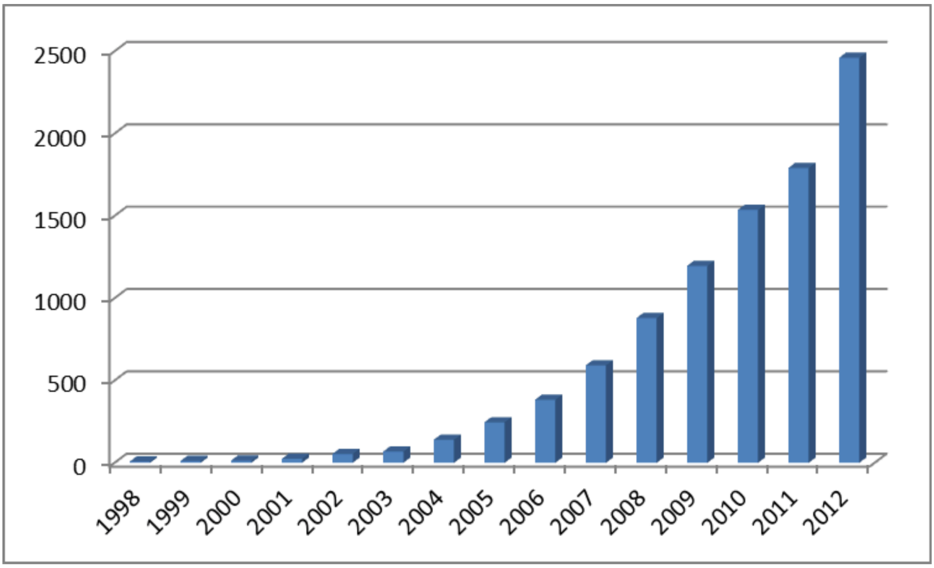

**Fig. 1.1**: Number of publications per year for metal-organic frameworks (source: SciFinder, until January 2013).

MOFs and PCPs are infinitely extended metal-ligand networks made by the ordinate and periodic repetition of metal nodes and bridging organic ligands[12-13]. Both classes of materials have shown to be porous and can be endowed with large surface areas and tunable pores; different pore topology and size can lead to versatile architectures and various applications.[7] The term metal-organic framework was popularized by Yaghi *et al.* around 1999, in connection to three-dimensional (3D) porous coordination networks (PCNs).[11] The distinction between MOFs and PCPs is not well defined and it is subject of discussion. The main feature, on which the classification is made, is that for PCPs the supramolecular structures are based on weak interactions (VdW, C-H···π, stacking π). Instead, MOFs possess a rigid 3D framework, built on stronger coordination bonds. MOFs can exhibit exceptionally high porosity and are typically synthesized by a simple self-assembly reaction between various metal ion and organic linkers (Fig. 1.2) under mild hydro- or solvothermal procedures.[14] Consequently, MOFs are ideal candidate for gas separation and purification as well as adsorbents.[15]

Transition metals, driven by their preferred coordination geometry, can act as acceptor units that can self-assemble with the donor ligands into predictable structures. The metals, in fact, can act as nodes of the overall scaffold and favour the formation of the supramolecular assembly.

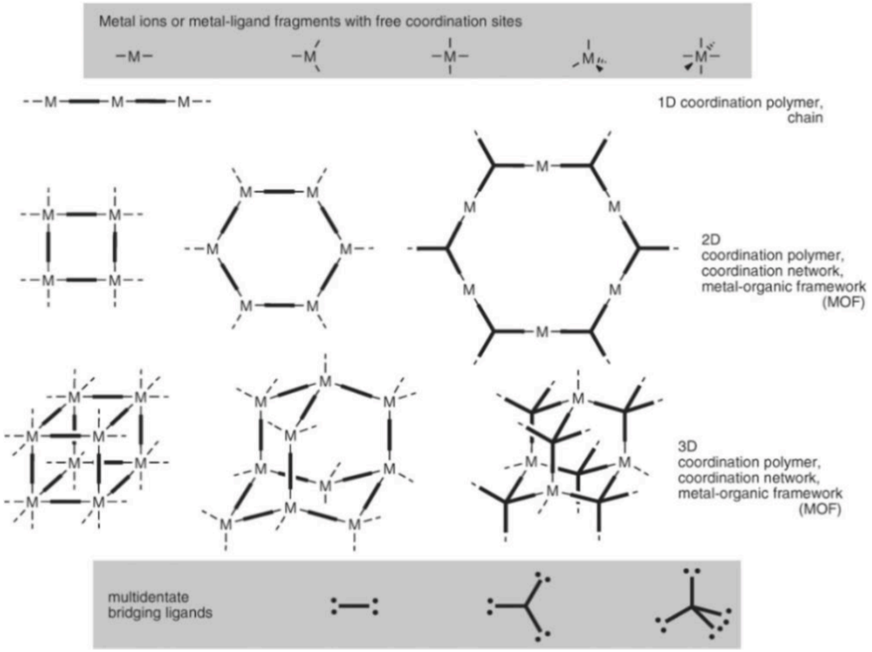

**Fig.1.2**: Schematic representation of the structural variability that can be presented by coordination polymers/MOFs.[16]

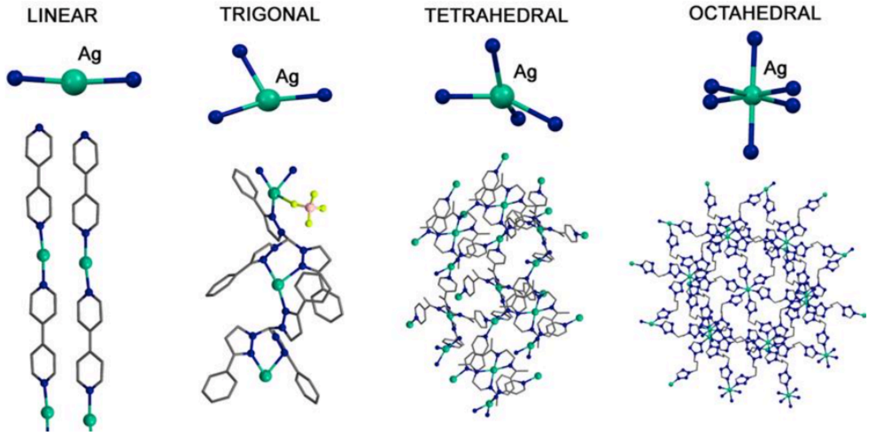

**Fig. 1.3**: Silver metal ions geometry and a few examples of corresponding coordination polymers[17].

The ligand plays a key role in the control of the architectures. In fact, the ligand has to bridge between different metals in order to build network structure[18-19]. The ligands can be defined as multitopic depending on the number of donor atoms. Also, the mutual orientation of these donor atoms defines the ligand geometry and the coordinative directionality.

For example, polycarboxylate ligands are largely used to design coordination polymers[20-22]. A few examples of common polycarboxilate anions used in the chemistry of MOFs are:

- benzene-1,4-dicarboxylate (*bdc*$^{2-}$, terephthalate, with a 180º angle between the two carboxylic groups,
- benzene-1,3-dicarboxylate (*ip*$^{2-}$, isophthalate), in which the two carboxylate moieties are rigidly predisposed at 120º,
- benzene-1,3,5-tricarboxylate (*btc*$^{3-}$, trimesate), with 120º between the three carboxylic groups.

Another very commonly employed class of neutral ligands is represented by polypyridines, which include pyrazine and 4,4'-bipyridine. Differently from the former class of polycarboxylates, this latter class of ligands does not bear negative charges and can therefore be used as a supplementary building unit without altering the charge balance of a system.

The angle originated by the organic bridge, plus the angles established by the metal ion preferred coordination, can provide a certain level of predictability in the design of coordination polymers, which favours the obtainment of materials exhibiting the target properties.

pyrazine

oxalate

4,4'-bipyridine

benzene-1,4-dicarboxylate

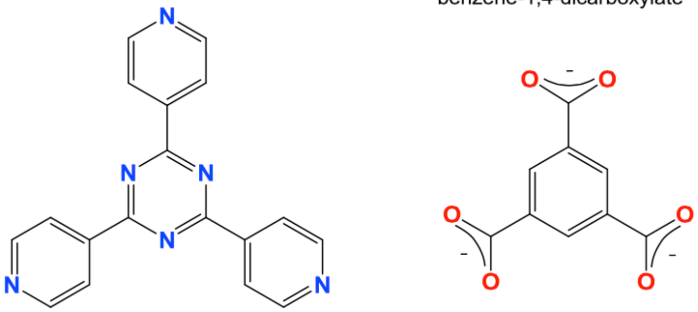

2,4,6-tris(4-pyridil)-1,3,5-triazine

benzene-1,3,5-tricarboxylate

**Fig. 1.4**: Examples of nitrogen and oxygen donor ligands useful for the construction of coordination polymers[17].

## 1.2 - A few examples reported in literature

Although the pore size and shape of an adsorbent are the major factors in determining the adsorptions selectivity of guest molecules, the nature of the guest-surface interaction is also important. A remarkable selective adsorption of $C_2H_2$ over $CO_2$ was achieved by $Cu_2(pzdc)_2(pyz)$[23] (Fig. 1.5); this complex has a porous structure containing 1D open channels of 4 x 6 Å in cross-section size. The surface of the channels contains O atoms, which can act as basic adsorptions sites for guest molecules.

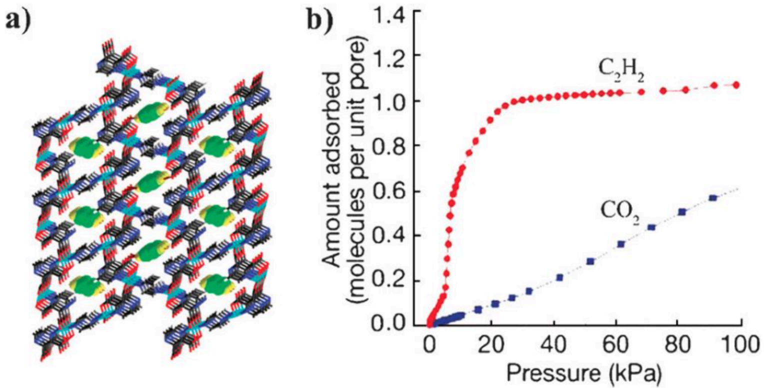

**Fig. 1.5**: a) Structure of $Cu_2(pzdc)_2(pyz)$ with $C_2H_2$ (green and yellow, space- filling model) at 170 K. b) Adsorption isotherms on $Cu_2(pzdc)_2(pyz)$ at 300 K[23].

Shimizu and co-workers directly observed the $CO_2$ bonding within an amine-functionalized MOF, $[Zn_2(Atz)(ox)]$ (Atz = aminotriazolato, ox = oxalate)[24] at low pressure from the X-ray crystallographic resolution of the adsorbed $CO_2$ (Fig. 1.6). From the structural refinement, two independent $CO_2$ binding sites were located in the pores of this MOF: one is near the free amine group and the other is close to the oxalates. The $O(CO_2) \cdots H\text{-}N(NH_2)$ hydrogen bond and interactions between the N lone pair of the amine group and C atom of $CO_2$ and between the O atom of oxalate group and O atom of $CO_2$ have been confirmed. Furthermore, the $CO_2 \cdots CO_2$

cooperative interaction (between C and O atoms) was also observed. Accompanied with molecular simulation studies, the authors concluded that the combination of appropriate pore size, strong interaction between $CO_2$ and functional groups on the pore surface, and cooperative binding of $CO_2$ molecules is responsible for the low-pressure binding of $CO_2$ in this MOF.[24]

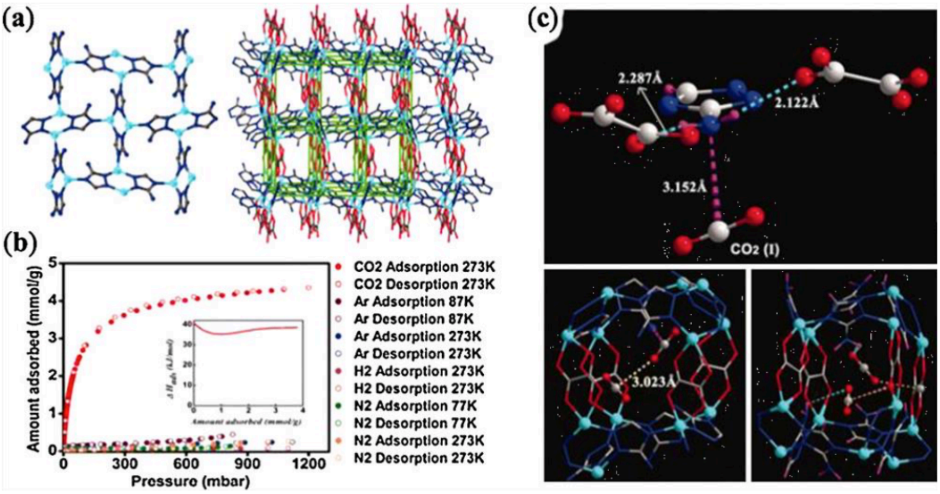

**Fig. 1.6**. Structure (a) and gas adsorption properties (b) of $[Zn_2(Atz)(ox)]$ (Zn, cyan; C, black; N, blue); the $CO_2$ binding (directly determined by X-ray structure refinement at 173 K within the pores of $[Zn_2(Atz)(ox)]$ (c)[24].

As a last example, Fig. 1.7 depicts the framework constructed with Cu(II) and the ligand 5,5'– ((pyridine–3,5–dicarbonyl)bis(azanediyl))diisophthalate (PDAI). This ligand presents two isophthalate and one pyridine group connected through amide bonds, and was designed to build a copper paddlewheel-based MOF PCN-124[25]. The open metal sites and amide groups were expected to increase the interaction between adsorbed $CO_2$ and the pore surface and could serve as Lewis acids, Lewis Bases, or hydrogen bond donors for tandem catalysis. PCN-124 possesses a self-interpenetrated 3D structure and crystallizes in the space group *Im3-m*. Similar to other MOFs consisting of isophthalate moieties, 24 isophthalate moieties and 12 Cu(II) paddlewheel motifs assemble into cuboctahedral building unit (Fig. 1.7c).

These cuboctahedral cages are further linked by the ligand to generate a 3D cubic framework (Fig. 1.7d). One axial site of the Cu(II) paddlewheel motif in the molecular cage coordinates to the pyridine group of the ligand from another identical framework to form a self-interpenetrated structure (Fig. 1.7b and 1.7e). Thus each cuboctahedral structural building unit becomes a 36-connected node, leading to a highly connected framework with excellent chemical and thermal stability.[25]

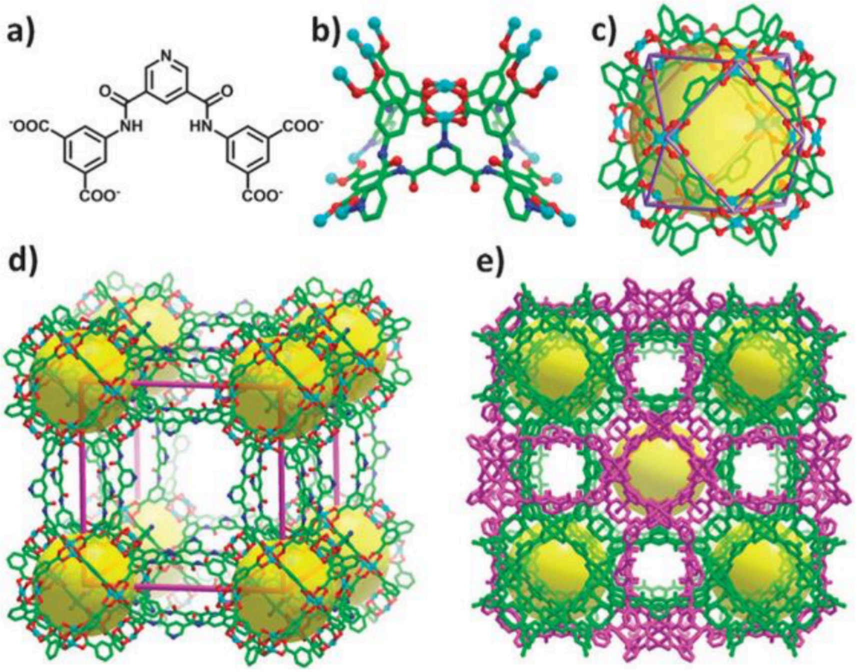

**Fig. 1.7**: (a) 5, 5'–((pyridine–3,5–dicarbonyl)bis(azanediyl))diisophthalate, PDAI. (b) Coordination environment of the dinuclear Cu (represented in cyan) paddlewheel motifs and ligands in PCN-124. (c) A cuboctahedral cage in PCN-124. (d) A single cubic framework of PCN-124 constructed by ligand skeletons bridging cage molecular building blocks (Cu, cyan; O, red; N, blue; C, green). (e) The self-interpenetrated structure of PCN-124[25].

The permanent porosity of PCN-124 was confirmed by various gas adsorption measurements (Fig. 1.8).[25] The $N_2$ adsorption isotherm exhibited reversible type I behaviour revealing the microporous nature. The calculated Langmuir and BET surface areas are 2002 $m^2g^{-1}$ and 1372 $m^2g^{-1}$, respectively; two different kind of micropores with diameters of 7.6 Å and 9.5 Å were calculated based on the $N_2$ isotherm.[25] The linearly arranged open metal sites and amide groups in the framework of PCN-124 provided a favourable environment for $CO_2$ adsorption.

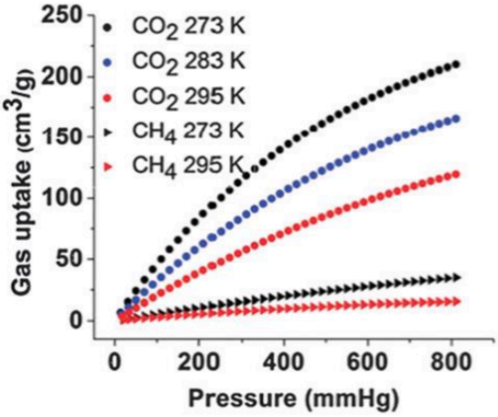

**Fig. 1.8**: $CO_2$ and $CH_4$ adsorption isotherms of PCN-124[25].

## 1.3 - References

1 - C. Janiak, *Dalton Trans.*, 2003, 2781–2804.

2 - J.-R. Li, R. J. Kuppler and H.-C. Zhou, *Chem. Soc. Rev.*, 2009, **38**, 1477–1504.

3 - J. L. C. Rowsell and O. M. Yaghi, *Angew. Chem., Int. Ed.*, 2005, **44**, 4670–4679.

4 - J.-Y. Lee, O. K. Farha,J. Roberts, K. A. Scheidt, S. T. Nguyen and J. T. Hupp, *Chem. Soc. Rev.*, 2009, **38**, 1450–1459.

5 - D. Farrusseng, S. Aguado and C. Pinel, *Angew. Chem., Int. Ed.*, 2009, **48**, 7502– 7513.

6 - S. Hasegawa, S. Horike, R. Matsuda, S. Furukawa, K. Mochizuki, Y. Kinoshita and S. Kitagawa, *J. Am. Chem. Soc.*, 2007, **129**, 2607.

7 - H. Furukawa, K. E. Cordova, M. O'Keeffe, O. M. Yaghi, *Science*, 2013, **341**, 974.

8 - A. F.Cronstedt, *Akad Handl. Stockholm,* 1756*,* **17**, 120-132.

9 - H. De Sainte, C. Deville, *C. R. Acad Sci*. 1862, **54**, 324-327.

10 - D. H. Everett, Manual of Symbols and Terminology for Physicochemical Quantities and Units; IUPAC Council, 23 July 1971.

11 - O. M. Yaghi, G. Li and H. Li, *Nature*, 1995, **378**, 703; O. M. Yaghi and H. Li, *J. Am. Chem. Soc.*, 1995, **117**, 10401.

12 - C. Janiak, *Dalton Trans.*, 2003, 2781.

13 - W. L. Leong, J. J. Vittal, *Chem. Rev.*, 2001, **111**, 688–764.

14 - 1 G. Férey, *Chem. Soc. Rev.*, 2008, **37**, 191–214.

15 - J. Liu, P. K. Thallapally, B. P. McGrail, D. R. Brown, J. Liu, *Chem. Soc. Rev.*, 2012, **41**, 2308–2322.

16 - C. Janiak, J. K. Vieth, *New J. Chem.*, 2010, **34**, 2366–2388

17 - I. Bassanetti, *Ph. D Thesis*, XXV Cycle, Dipartimento di Chimica, Università di Parma, Italy.

18 - D. Dang, Y. Zheng, Bai, Y., X. Guo, J. Niu, Assembly of Polyoxometalate-Based Metal−Organic Frameworks with Silver(I)-Schiff Base Coordination Polymeric Chains as Building Blocks., Elsevier, 2012.

19 - Ni, J., Wei, K.-J., Liu, Y., Huang, X.-C. & Li, D. *Crystal Growth & Design*, 2010, **10**, 3964–3976.

20 - Eddaoudi, M. *et al.*, *Acc. Chem. Res.*, 2001, **34**, 319–330.

21 - Batten, S. R. & Robson, R. *Angew. Chem. Int. Ed.*, 1998, **37**, 1460–1494.

22 - Blake, A. J. *et al.*, *Coord. Chem. Rev.*, 1999, **183**, 117–138.

23 - J.-R. Li, R. J. Kuppler, H.-C. Zhou, *Chem. Soc. Rev.*, 2009, **38**, 1477–1504.

24 - R. Vaidhyanathan, S. S. Iremonger, G. K. H. Shimizu, P. G. Boyd, S. Alavi, T. K. Woo, *Science*, 2010, 330, 650.

25 - J. Park, J.-R. Li, Y.-P. Chen, J. Yu, A. A. Yakovenko, Z. U. Wang, L.-B. Sun, P. B. Balbuena and H.-C. Zhou, *Chem. Commun.*, 2012, **48**, 9995–9997.

# Chapter II

## *Silver complexes of functionalized $N_2$S-donor bispyrazolyl ligands as building blocks for coordination polymers.*

## 2.1 - Introduction

Hybrid metal-organic extended solids are called Metal-Organic Frameworks (MOFs), by some referred to as Porous Coordination Polymers (PCPs), since they are constituted by the infinite repetition of metal centres and organic ligands[1]. This class of compounds has been subject of a surprising large number of studies in the last fifteen years due to their numerous foreseeable applications[2] in the fields of gas adsorption[3,4], separation processes[5], drug delivery[6], catalysis[7] and, more recently, luminescent sensors[8–10] and magnetism[11].

MOFs have been shown to present the widest structural variability, due to the high number of possible structural combinations that can be employed by changing the coordination geometry of the metal ions, and the topology of the organic ligands used. The class of organic ligands that has been more extensively used to prepare the materials is undoubtedly the one of polycarboxilate ions. The design of their chelating geometry and of their spacer groups allows to obtain tailored ligands that form robust coordinative bonds. Moreover these ligands present an inherent structural rigidity, which useful in order to limit the formation of undesired topologies.

Although the ligand plays the major role in the variability of the fascinating architectures exhibited by MOFs, the structural topology can be influenced by numerous factors, such as counterions, temperature, solvent systems, metal/ligand ratios, templating agents and coordination abilities.

One of the key steps of a rational design of new multidimensional porous solids is thus represented by the prediction and control of the structures that can arise from the employment of specific synthons.

If the use of rigid and geometrically tailored organic ligands provides more reliable synthons towards the synthesis of the target supramolecular framework and increases the chances of successfully predicting the topology of the system that will be obtained, on the other hand it reduces the variability and limits the investigation of new structural motifs.

Another aspect that can provide more flexibility to supramolecular hybrid systems is the metal coordination; the use of metal ions that exhibit variable coordination geometries can produce greatly diverse structures by slight modifications on the ligands used or of minor factors such as crystallization solvents or temperature.

Ag(I) cationic complexes have been commonly used as building blocks for coordination polymers thanks to flexible coordination geometries. This ion is often used for coordination to soft bases such as ligands containing sulphur and nitrogen donor atoms.

We recently reported the preparation of Ag(I)-bis(pirazolyl)methane hexameric and toroidal supramolecules that self-assemble, at a higher hierarchical level, into a diversity of 3D supramolecular architectures as function of the anion used.[12,13] The counterions ($BF_4^-$, $PF_6^-$, $NO_3^-$, and $CF_3SO_3^-$) largely modulate the structure of the toroidal hexamers and have a profound impact on the crystal framework arrangement.

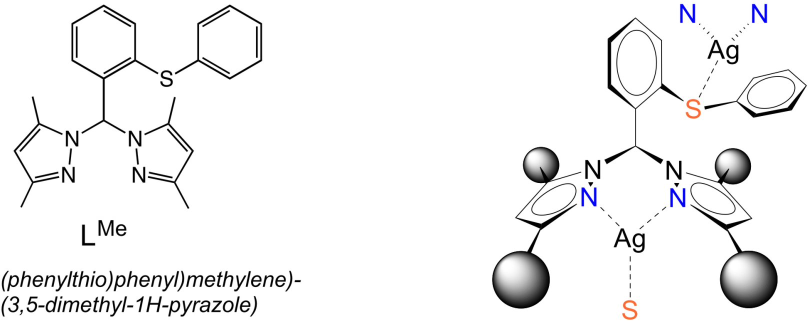

$L^{Me}$

*1,1'-((2-(phenylthio)phenyl)methylene)-bis(3,5-dimethyl-1H-pyrazole)*

**Fig. 2.1**: Scheme of the ligand $L^{Me}$ (left), which assembles in toroidal hexameric molecular structures and into supramolecular porous aggregates. Schematic representation of the conformation adopted by the ligand $L^{Me}$ when bridging two $Ag^+$ ions (right).

In all these architectures, the constituting synthons have analogous substructures, which are here described.

The ditopic $N_2S$ ligands bridge two different $Ag^+$ ions by coordinating to one of them using the chelating N,N' bispyrazolyl moiety and the other using the S-donor thioletheric side-arm (Fig. 2.1). The cyclic self-assembly of this motif generates cyclic hexamers with toroidal shape, measuring 26 Å in diameter, with a central hydrophobic pore of 5.1 Å. Hexamers respond to the general formula $[AgL]_6(A)_6$, where A = $BF_4^-$ or $PF_6^-$, they are isostructural and crystallize in the cubic space group Fd-3; furthermore, the crystal packing is determined by $BF_4^-$ or $PF_6^-$

counterions, which interact with two silver atoms belonging to two adjacent hexamers.

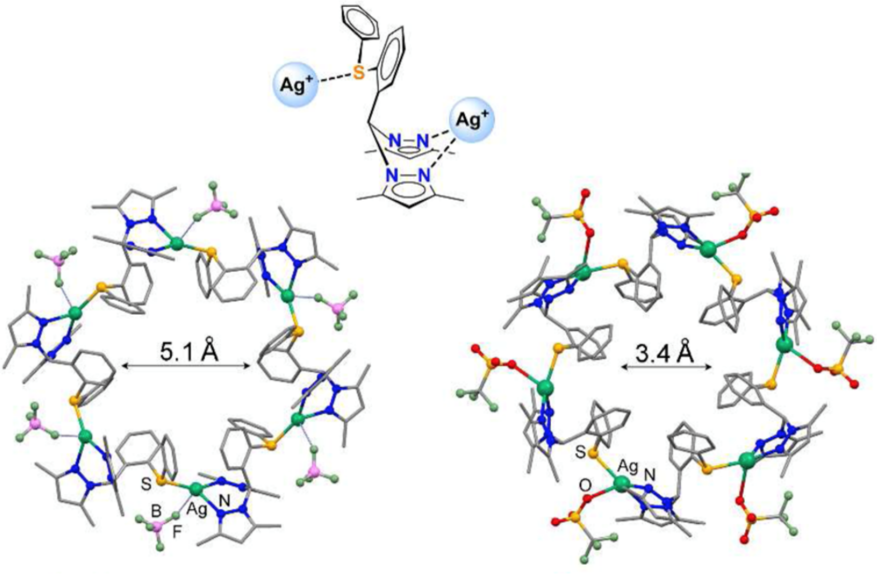

**Fig. 2.2**: Above, ligand structure; below, molecular structure of $[AgL^{Me}]_6(BF_4)_6$ (left), and of $[AgL^{Me}]_6(CF_3SO_3)_6$ (right). Colour scheme: Ag, light green; S, yellow; F, green; B, pink; N, blue; O, red; C, grey; H, white.

The halogenated bridges held together four hexamers, forming supramolecular spherical capsules. Each capsule contains an internal cavity with an approximate diameter of 6 Å (coloured in red in Fig. 2.3 and referred to as “intracapsular” cavity). At a higher degree of supramolecular packing, four nearby capsules generate a second kind of capsule, with an approximate diameter of 7 Å (coloured in yellow, referred to as “intercapsular” cavity).

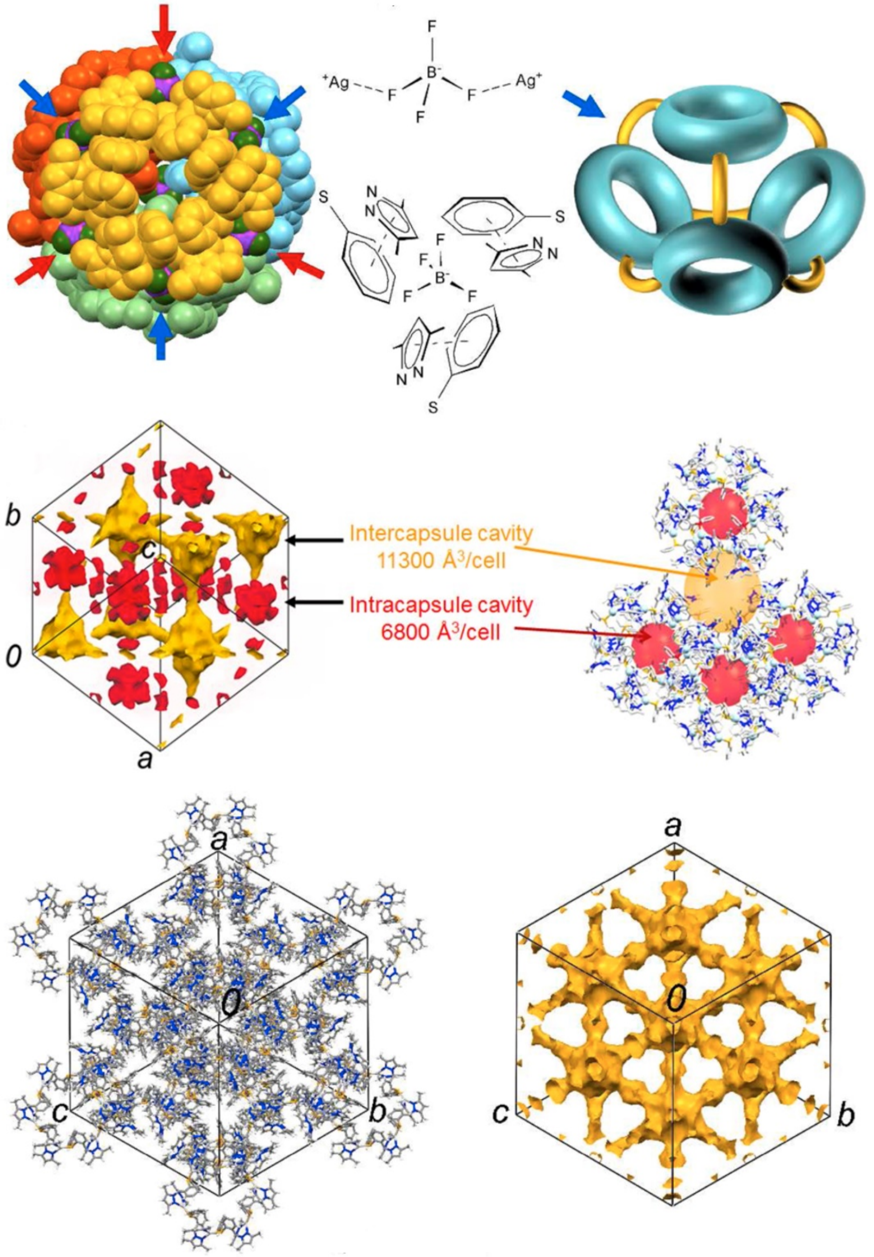

**Fig. 2.3**: Upper row, representation of the supramolecular disposition of toroidal hexamers to form capsules and description of the contacts between the $BF_4^-$ anions and the hexameric moieties. Middle row, the two different types of cavities are depicted in yellow (intercapsule) and red (intracapsule), respectively. Lower row, crystal packing of $[AgL^{Me}]_6$ depicting the rigid part of the structure in stick and the cavities in yellow.

The crystal structures of $[AgL^{Me}]_6(BF_4)_6$ and $[AgL^{Me}]_6(PF_6)_6$ are resistant to solvent evacuation and the different interconnected cavities form extended porous coordination polymers, whose permanent porosity were demonstrated by adsorption isotherms of different gases. $[AgL^{Me}]_6(BF_4)_6$ can adsorb 76 $cm^3$ (STP)/g of $CO_2$ at 195 K and 1 atm (15.1 wt %), whereas only 22 $cm^3$/g of methane were adsorbed under the same pressure and temperature conditions (Fig. 2.4). The measured $CO_2$ capacity, equal to 3.44 mmol/g, corresponds to an occupied volume of 9600 Å per unit cell ($d_{CO2}$ = 1.5 g/$cm^3$) which matches well with the open-pore capacity of the inter-capsular space, 11300 $Å^3$ per unit cell, determined with a sphere with a diameter of 3.3 Å (corresponding to the kinetic diameter of $CO_2$). Thus, this result indicates the virtually complete filling of the intercapsular space which is easily accessible to gas molecules via diffusion.

In the case of $[AgL^{Me}]_6(PF_6)_6$, the $CO_2$ adsorption isotherm at 195 K reaches the plateau value of 77 $cm^3$ (STP)/g at 1 atm, comparable to the value for the isostructural $[AgL^{Me}]_6(BF_4)_6$. These systems show a type I isotherm (Fig. 2.4) which is in agreement with the cavity size of these compounds, which is in the microporous range.

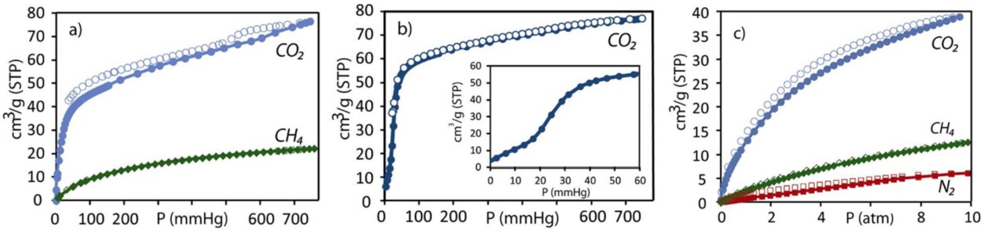

**Fig. 2.4**: (left) Adsorption/desorption isotherms for $CO_2$ and $CH_4$ into porous $[AgL^{Me}]_6(BF_4)_6$ at 195 K. (centre) $CO_2$ adsorption/desorption isotherm for the porous $[AgL^{Me}]_6(PF_6)_6$ compound at 195 K. Inset, enlargement of the low pressure region. (right) Adsorption/desorption isotherms for $CO_2$, $CH_4$ and $N_2$ into $[AgL^{Me}]_6(BF_4)_6$ at room temperature and up to 10 atm.

Furthermore, specific functionalizations to the $N_2S$ ligands were undertaken to investigate the dependence of the self-assembled architectures from the organic ligand structure.

It was observed that, while the introduction of substituents on the phenyl rings of the side arm changes the size of the intracapsular cavities, the removal of any of the two phenyl rings prevents the formation of the hexamers and of the porous structures.[13] Fig. 2.5 reports the four ligands that formed hexameric molecular structures and porous supramolecular aggregates; the different steric hindrance provided by the substituents on the phenyl ring influences the size of the intracapsular cavity (Fig. 2.6). It was also noted that the removal of both methyl groups from each pyrazole moiety led to the formation of 1D polymeric chains, packing into non-porous solid state structures (Fig. 2.7).

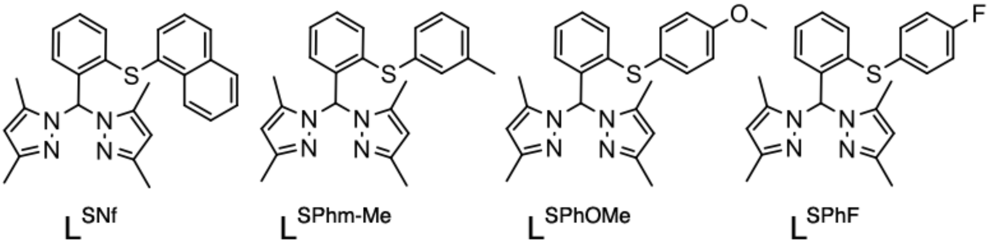

$L^{SNf}$ $L^{SPhm\text{-}Me}$ $L^{SPhOMe}$ $L^{SPhF}$

**Fig. 2.5**: Scheme of the $L^{Me}$-analogous ligands that provided hexameric molecular structures and porous supramolecular assemblies.[13]

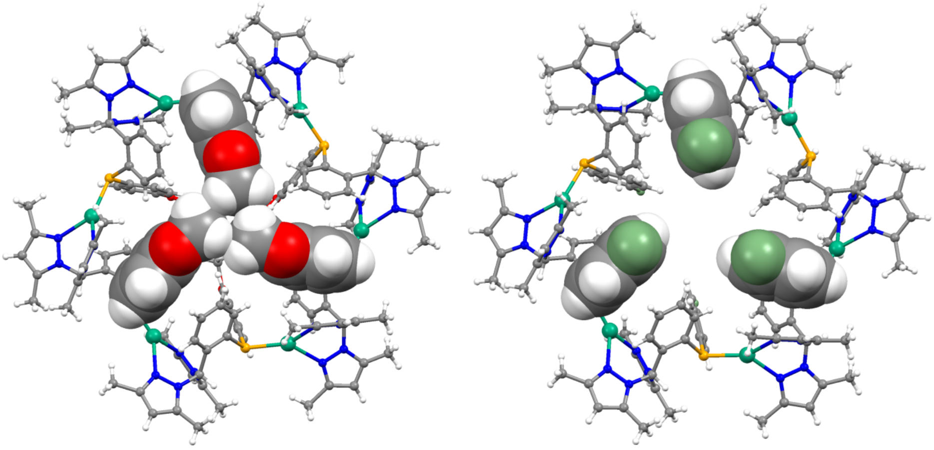

**Fig. 2.6**: Representation of the hexameric structures obtained from $L^{SPhOMe}$ (left) and $L^{SPhF}$ (right), the phenyl rings pointing towards the centre of the intracapsular cavity are represented in *spacefill*.[13] Colour scheme: Ag, light green; S, yellow; F, green; N, blue; O, red; C, grey; H, white.

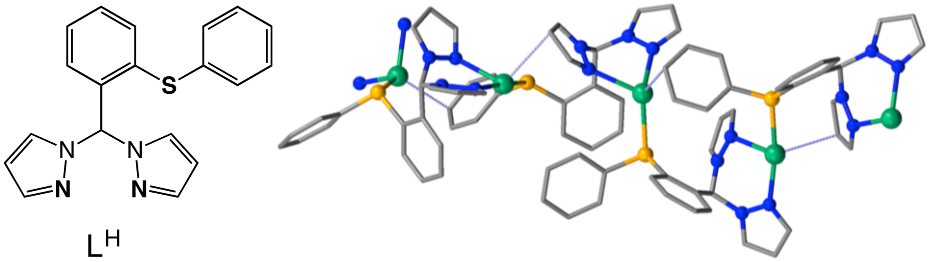

$L^{H}$

**Fig. 2.7**: Scheme of the ligand with no methyl groups on the pyrazolyl moieties $L^{H}$ (left), which provided only 1D chains; the monodimensional chain $[Ag(L^{H})]_n(BF_4)_n$ (right), counterions have been omitted for clarity. Colour scheme: Ag, light green; S, yellow; N, blue; C, grey; H, white.

Herein, we present a series of additional modifications of the pyrazolyl scaffold, in order to investigate the role of the bispyrazole moiety on the structural arrangement of the silver complexes and on the potential porosity. Specifically, we functionalized the pyrazoles by adding a bromine atom in position 4 ($\mathbf{L^{Br}}$), by substituting the methyl groups with trifluoromethyl groups ($\mathbf{L^{CF3}}$) and by removing selectively one of the two methyl groups. This last modification led to three bispyrazole isomers (indicated as $\mathbf{L^{5,5'Me}}$, $\mathbf{L^{3,3'Me}}$ and $\mathbf{L^{5,3'Me}}$).

Therefore we present five novel ligands with different electronic properties and steric hindrance (Fig. 2.8). Furthermore, to investigate the role of the counterions on the different topologies, geometries and packing arrangments of the coordination polymers, we report the use of three different anions in the synthesis of the Ag(I) complexes ($BF_4^-$, $PF_6^-$ and $CF_3SO_3^-$).

These complexes were fully characterized in solution and in the solid state and an analysis of the various structures is reported.

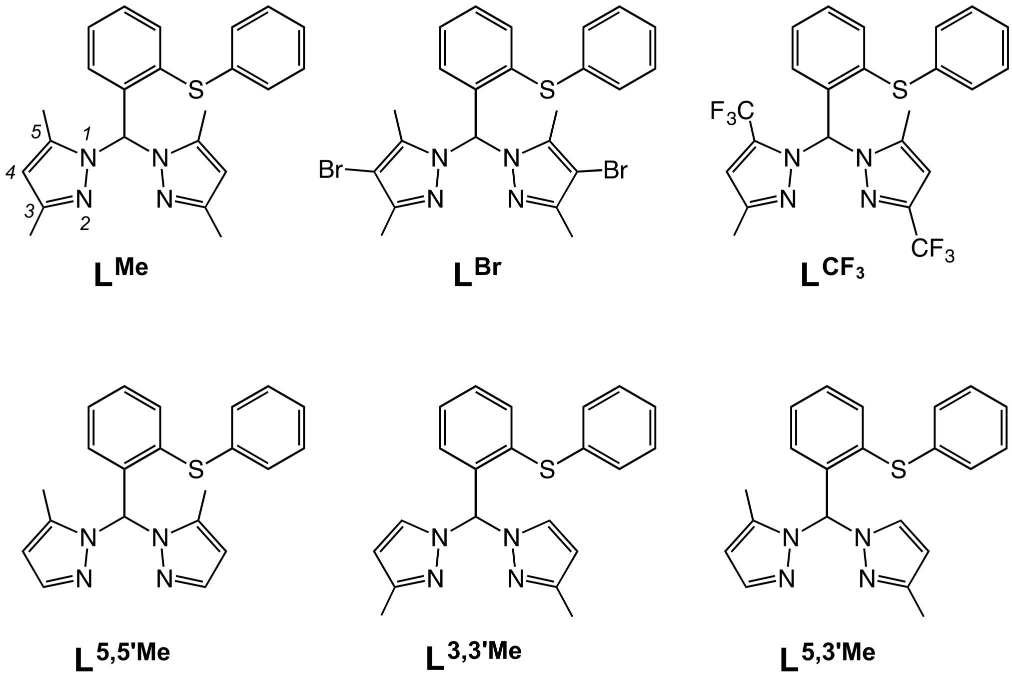

$\mathbf{L^{Me}}$ $\mathbf{L^{Br}}$ $\mathbf{L^{CF_3}}$

$\mathbf{L^{5,5'Me}}$ $\mathbf{L^{3,3'Me}}$ $\mathbf{L^{5,3'Me}}$

**Fig. 2.8**: Scheme of the ligands used. For comparison, the original **L**$^{\mathbf{Me},}$ which provides hexamers,[12] is reported.

## 2.2 - Experimental Section

### 2.2.1 - Materials and Methods

All reagents and solvents were commercially available, except for 2-(phenylthio)benzaldehyde and bis(3,5- dimethyl-1H-pyrazol-1-yl)methanone which were prepared as reported in the literature.[14,15] The synthesis of the $N_2S$ ligand followed a previously documented procedure.[16] $^1$H-NMR and $^{13}$C-NMR spectra were recorded on a Bruker Advance 300 and 400 spectrometer using standard Bruker pulse sequences. Chemical shifts are reported in parts per million (ppm) referenced to residual solvent protons. Infrared spectra were recorded from 4000 to 700 cm$^{-1}$ on a Perkin-Elmer FT-IR Nexus spectrometer equipped with a Smart Orbit HATR accessory with diamond crystal. Elemental analyses (C, H, and N) were performed with a Carlo Erba EA 1108 automated analyzer.

### 2.2.2 - Synthesis of the ligands

*Synthesis of 2-(phenylthio)benzaldehyde* (**1**). In dry and inert atmosphere ($N_2$), 2-chlorobenzaldehyde (2.40 ml, 21.30 mmol) was slowly added to a stirred solution of benzenethiol (2.73 mL, 26.71 mmol) and anhydrous $Na_2CO_3$ (3.48 g) in dry DMF (8 mL). The mixture was stirred at 90 °C for 3 hours. After cooling, the reaction mixture was poured into water (20 mL) and extracted with diethyl ether (20 mL). The extract was washed with water (2x20 mL), dried with anhydrous $Na_2SO_4$, and concentrated under vacuum. The resulting oil was triturated with hexane in an ultrasound bath for 20 min, filtered and dried under vacuum to afford a yellow solid (4.09 g, yield 89%). IR (cm$^{-1}$): 3334w, 3072w, 3048w, 2844w, 2819w, 2745w, 1940w, 1691w, 1667m, 1638w, 1580w, 1548m, 1499w, 1475w, 1454s, 1438s, 1393m, 1323w, 1303w, 1270w, 1258m, 1189m, 1123m, 1066m, 1041m, 1029m, 997w, 964w, 911w, 870w, 845m, 763s, 739s, 702m, 690m, 670s, 653s, 518w, 490w. $^1$H-NMR (300 MHz, $CDCl_3$): δ, 7.08-7.11 (dd, $J_1$ = 7.8 Hz, $J_2$ = 7.8 Hz, 1H, CH(Ph)), 7.30-7.45 (m, 7H, CH(Ph)), 7.86- 7.90 (dd, $J_1$ = 7.5 Hz, $J_2$ = 7.5 Hz, 1H, CH(Ph)), 10.39 (s, 1H, CHO).

*Synthesis of bis(4-bromo-3,5-dimethyl-1H-pyrazol-1-yl)methanone* (**2**). In dry and inert atmosphere ($N_2$), phosgene (3 mL, 5.72 mmol) was slowly added to a stirred mixture of 4-bromo-3,5-dimethyl-1H-pyrazole (2.00 g, 11.43 mmol), triethylamine (2.50 mL, 17.83 mmol) and dry diethyl ether (80 mL). The mixture was stirred at room temperature for 30 min, filtered under nitrogen and washed with diethyl ether (2x40 mL). The recovered solution was concentrated under vacuum, triturated with hexane in an ultrasound bath for 20 min, filtered and dried under vacuum to afford a white solid (1.56 g, 4.16 mmol, yield 73%). IR ($cm^{-1}$): 2993w, 1736s, 1585m, 1495m, 1446m, 1429w, 1397s, 1364s, 1348s, 1278m, 1229w, 1135w, 1127w, 1070m, 1029m, 1004m, 984s, 935s, 800w, 772s, 731s, 719s, 657m, 612m, 502m, 437w. $^1H$ NMR (300 MHz, $CDCl_3$): δ, 2.29 (s, 6H, $2CH_3$), 2.49 (s, 6H, $2CH_3$).

*Synthesis of bis(3-methyl-1H-pyrazol-1-yl)methanone* (**3**). In dry and inert atmosphere ($N_2$) phosgene (3.6 mL, 12.18 mmol) was slowly added to a stirred mixture of 3-methyl-1H-pyrazole (1.96 mL, 24.36 mmol), triethylamine (3.60 mL, 25.69 mmol) and dry diethyl ether (80 mL). The mixture was stirred at room temperature for 30 min, filtered under nitrogen and washed with diethyl ether (2x40 mL). The recovered solution was concentrated under vacuum, triturated with hexane in an ultrasound bath for 20 min, filtered and dried under vacuum to afford a white solid (1.23 g, 6.44 mmol, yield 53%). IR ($cm^{-1}$): 3179w, 3154w, 2999w, 2962w, 2925w, 1732m, 1556m, 1442w, 1413m, 1377m, 1344m, 1328m, 1278m, 1225m, 1213w, 1176m, 1070s, 1041w, 1017w, 980w, 948w, 849m, 792s, 768s, 723s, 690m, 669w, 653w, 612w, 596w, 580w. $^1H$ NMR (300 MHz, $CDCl_3$): δ, 2.38 (s, 6H, $2CH_3$), 6.32 (d, J = 3.0 Hz, 2H, CH(Pz)), 8.65 (d, J = 3.0 Hz, 2H, CH(Pz)).

*Synthesis of (5-methyl-3-(trifluoromethyl)-1H-pyrazol-1-yl)(3-methyl-5-(trifluoromethyl)-1H-pyrazol-1- yl)methanone* (**4**). In dry and inert atmosphere ($N_2$), phosgene (5,8 mL, 11.40 mmol) was slowly added to a stirred mixture of 3-methyl-5-(trifluoromethyl)-1H-pyrazole (3.27 g, 22.80 mmol), triethylamine (3.08mL, 22.80 mmol) and dry diethyl ether (80 mL). The mixture was stirred at room temperature for 30 min, filtered under nitrogen and washed with diethyl ether (2x40 mL). The recovered solution was concentrated under vacuum, triturated with hexane in an ultrasound bath for 20 min, filtered and dried under vacuum to afford a white solid (2.65 g, 8.12 mmol, yield 74%). IR ($cm^{-1}$): 3068w, 3051w, 2843w, 2819w, 1693m, 1670s, 1584m, 1551s, 1475m, 1455s, 1439s, 1395s, 1301m, 1256m, 1188s, 1123m, 1056m, 1041m, 910w, 849m, 757s, 698m, 677m, 654s, 519m, 492m. $^1$H NMR (300 MHz, $CDCl_3$): δ, 2.59 (s, 6H, 2 $CH_3$), 6.51 (s, 2H, CH(Pz)).

*Synthesis of 1,1'-((2-(phenylthio)phenyl)methylene)bis(4-bromo-3,5-dimethyl-1H-pyrazole)* (**L**$^{\mathbf{Br}}$). In dry and inert atmosphere ($N_2$), a mixture of bis(4-bromo-3,5-dimethyl-1H-pyrazol-1-yl)methanone (1.56 g, 4.16 mmol), 2-(phenylthio)-benzaldehyde (884 mg, 4.16 mmol) and $CoCl_2{\bullet}6H_2O$ (5 mg) was heated at 90°C for 2 hours with stirring. The solid mixture was then cooled at room temperature and stirred for 2 hours. Dichloromethane (30 mL) was added and the mixture was stirred for 20 minutes. The organic phase was washed withwater (50 mL) and brine (20 mL), then dried with anhydrous $Na_2SO_4$ and filtered. The crude product is a white powder which was purified through silica column chromatography (hexane:acetate 90:10; r.f. 0.3), yielding a white powder (1.26 g, 2.30 mmol, yield 30%). IR (cm$^{-1}$): 3060w, 2917w, 1581w, 1552w, 1479m, 1434, 1413m, 1372w, 1360w, 1335w, 1307m, 1278m, 1250m, 1209m, 1131w, 1127w, 1074m, 1041w, 1021w, 992w, 894w, 882w, 874w, 837w, 821w, 764s, 727s, 715s, 686s, 645w, 604w. $^1$H NMR (300 MHz, $CDCl_3$): δ, 2.07 (s, 6H, 2 $CH_3$), 2.16 (s, 6H, 2 $CH_3$), 6.99-7.01 (m, 1H, CH(Ph)), 7.08-7.11 (m, 2H, CH(Ph)), 7.16-7.22 (m, 3H, CH(Ph)), 7.30-7.35 (m, 2H, CH(Ph)), 7.39-7.35 (m, 1H, CH(Ph)). $^{13}$C NMR (300 MHz, $CDCl_3$): δ, 10.35 (2 $CH_3$), 12.64 (2 $CH_3$), 72.97 ($C_{central}$), 96.29 (2CBr), 126.83 (C(Ph)), 128.47 (C(Ph)), 128.82 (C(Ph)), 128.98 (C(Ph)), 129.74 (C(Ph)), 129,.77 (C(Ph)), 133.62 (C(Ph)), 134.46 (CS), 135.08 (CS), 136.85 (2C(Pz)), 138.13 (C(Ph)), 147.29 (2C(Pz)). ESI-MS (p.i., $CH_3OH$, m/z, I%): 197.07, [PhSPhNa] $^+$; 568.89, [LNa]$^+$. Anal. Calc. for C23H22Br2N4S (546.32): C: 50.56; H: 4.06; N: 10.26. Found: C: 50.86; H: 3.99; N: 10.47.

*Synthesis of 1,1'-((2-(phenylthio)phenyl)methylene)bis(5-methyl-1H-pyrazole) (**L**$^{\mathbf{5,5'Me}}$) , 1,1'-((2-(phenylthio)phenyl)methylene)bis(3-methyl-1H-pyrazole) (**L**$^{\mathbf{3,3'Me}}$) and 5-methyl-1-((3-methyl-1H-pyrazol-1-yl)(2-(phenylthio)phenyl)methyl)-1H-pyrazole (**L**$^{\mathbf{5,3'Me}}$).* The procedure is analogous to the synthesis of **L**$^{\mathbf{Br}}$, with a slight modification. In dry and inert atmosphere ($N_2$), a mixture of bis(3- methyl-1H-pyrazol-1-yl)methanone (870 mg, 4.57 mmol), 2-(phenylthio)benzaldehyde (985 mg, 4.57 mmol) and $CoCl_2{\bullet}6H_2O$ (5 mg) was heated at 90°C for 2 hours. The crude is a yellow oil which was purified through silica column chromatography (hexane:acetate; 80:20; r.f. 0.11), yielding a white powder of **L**$^{\mathbf{5,5'Me}}$ (226 mg, 0.62 mmol, yield 16%) and an oil with r.f. = 0.17 that consists of a mixture of **L**$^{\mathbf{5,3'Me}}$ and

**L**$^{3,3'Me}$ (820 mg, 2.27 mmol, yield 58%). By means of additional silica column purification (hexane:acetate 80:20; r.f. 0.17) we were able to purify approximately 90 mg for each species. IR **L**$^{5,5'Me}$ ($cm^{-1}$): 3101w, 3056w, 2978w, 2921w, 1581w, 1548w, 1466m, 1438m, 1372m ,1344w, 1315m, 1278w, 1250w, 1205w, 1131w, 1127w, 1058w, 1033w, 1021w, 997w, 980w, 919m, 866w, 820m, 809m, 780m, 743s, 686m, 645w, 617w, 551w, 531w, 498w, 461w, 441w, 412w. $^1H$ NMR (300 MHz, $CDCl_3$): **L**$^{5,5'Me}$ δ, 2.10 (s, 1H, $CH_{central}$), 6.06 (d, J = 0.6 Hz, 2H, CH(Pz)), 6.99-7.02 (m, 1H, CH(Ph), 7.16-7.25 (m, 3H, CH(Ph)), 7.48-7.49 (d, J = 1.5 Hz), 7.99 (s, 1H, $CH_{central}$); **L**$^{5,3'Me}$ δ, 2.32 (s, 3H, $CH_3$), 2.34 (s, 3H, $CH_3$), 6.03 (d, J = 0.9 Hz, 1H, CH(Pz)), 6.10 (d, J = 2.4 Hz, 1H, CH(Pz)), 6.83-6.86 (m, 1H, CH(Ph)), 7.14-7.22 (m, 7H, CH(Ph) + CH(Pz)), 7.22- 7.37 (m, 3H, CH(Ph)), 7.48 (d, J = 1.5 Hz, 1H, CH(Pz)), 8.02 (s, 1H, $CH_{central}$). **L**$^{3,3'Me}$ δ, 2.27 (s, 6H, $CH_3$), 6.04 (d, J = 2.4 Hz, 2H, CH(Ph)), 6.84-6.87 (m, 1H, CH(Ph)), 7.14 (d, J = 2.4 Hz, 2H, CH(Pz)), 7.19-7.29 (m, 8H, CH(Ph)), 8.01 (s, 1H, $CH_{central}$). $^{13}C$ NMR (400 MHz, $CDCl_3$): **L**$^{5,5'Me}$ δ, 10.90 (2 $CH_3$), 71.45 ($C_{central}$), 106.70 (2C(Pz)), 126.93 (C(Ph)), 128.36 (C(Ph)), 128.84 (C(Ph)), 129.18 (C(Ph)), 129.77 (C(Ph)), 133.80 (CS), 135.41 (CS), 139.31 (C(Ph)), 139.72 (2C(Pz)). **L**$^{5,3'Me}$ δ, 10.88 ($CH_3$), 13.50 ($CH_3$), 72.48 ($C_{central}$), 106.37 (C(Pz)), 106.72 (C(Pz)), 126.88 (C(Ph)), 128.03 (C(Ph)), 128.24 (C(Ph)), 129.08 (C(Ph)), 129.76 (C(Ph)), 130.01 (CS), 130.29 (CS), 133.79 (C(Pz)), 137.83 (2C(Pz)), 140.03 (C(Ph)), 149.56 (C(Pz)). **L**$^{3,3'Me}$ δ, 13.81 (2 $CH_3$), 75.42 ($C_{central}$), 106.12 (2C(Pz)), 127.20 (C(Ph)), 127.82 (C(Ph)), 129.09 (C(Ph)), 129.84 (C(Ph)), 130.25 (CS), 131.18 (CS), 133.15 (C(Pz)), 134.78 (C(Pz)), 135.29 (C(Ph)), 136.85(C(Ph)), 150.20 (2C(Pz)). ESI-MS (p.i., $CH_3OH$, m/z,I%): 196.81 $[PhSPhNa]^+$ ; 383.09, $[LNa]^+$. Anal. Calc. for C21H20N4S (360.48): C: 69.97; H: 5.59; N: 15.54. Found: C: 70.03; H: 5.41; N: 15.10.

*Synthesis of 1,1'-((2-(phenylthio)phenyl)methylene)bis(4-bromo-3,5-dimethyl-1H-pyrazole)* (**L**$^{CF3}$)*.* In dry and inert atmosphere ($N_2$), a mixture of (5-methyl-3-(trifluoromethyl)-1H-pyrazol-1-yl)(3-methyl-5- (trifluoromethyl)-1H-pyrazol-1-yl)-methanone (2.65 g, 8.12 mmol), 2-(phenylthio)benzaldehyde (1.74 g, 8.12 mmol) and $CoCl_2.6H_2O$ (5 mg) was heated at 90°C for 2 hours with stirring. The solid mixture was then cooled at room temperature and stirred for 2 hours. Dichloromethane (30 mL) was added and the mixture was stirred for 20 minutes. The organic phase was washed with water (50 mL) and brine (20 mL), then dried with anhydrous $Na_2SO_4$ and filtered. The crude product was poured in warm hexane and recrystallized at low temperature (-10°C) during a night, yielding white crystals

(2.01 g, 2.30 mmol, yield 49.8%). IR (cm$^{-1}$): 3064w, 2962w, 2925w, 1489m, 1466m, 1444m, 1343m, 1265m, 1226s, 1171s, 1119s, 1037m, 1015m, 967m, 829w, 739m, 689m, 664w. $^1$H NMR (400 MHz, $CDCl_3$): δ, 2.12 (s, 3H, $CH_3$), 2.24 (s, 3H, $CH_3$), 6.21 (s, 1H, CH(Pz)), 6.48 (s, 1H, CH(Pz)), 7.02-7.09 (m, 3H, CH(Ph)), 7.13-7.18 (m, 3H, CH(Ph)), 7.34-7.38 (m, 2H, CH(Ph)), 7.44-7.48 (m, 1H , CH(Ph)), 8.14 (s, 1H, $CH_{central}$). $^{13}$C NMR (400 MHz, $CDCl_3$): δ, 10.90 ($CH_3$), 13.73 ($CH_3$), 71.55 ($C_{central}$), 104.80 (C(Pz)), 109.10 (C(Pz)), 126.66 (2 $CF_3$), 128.87-129.22 (7C(Ph)), 130.18 (C(Ph)), 131.85 (C(Pz)), 135.05 (C(Ph)), 135.22 (C(Pz)), 136.82 (C(Ph)), 141.14 (C(Pz)), 149.03 (C(Pz)). ESI-MS (p.i., $CH_3OH$, m/z, I%): 197.01 $[PhSPhNa]^+$; 519.08, $[LNa]^+$. Anal. Calc. for C23H18F6N4S (496.12): C: 55.64; H: 3.65; N: 11.29. Found: C: 55.58; H: 3.66; N: 11,44.

### 2.2.3 - Synthesis of complexes

*Synthesis of [Ag(**L$^{Br}$**)]$_n$(PF$_6$)$_n$.* **L$^{Br}$** (393 mg, 0.72 mmol) and $AgPF_6$ (190 mg, 0.72 mmol) were mixed in acetone (10 mL), and the colourless solution was stirred for 15 min. The mixture was concentrated under vacuum and the crude was triturated with hexane in an ultrasound bath, from which a white solid precipitated. The solid was filtered and vacuum dried (550 mg, 0.68 mmol, yield 95%). The compound was recrystallized by stratifying diethyl ether over an acetone solution of the complex, yielding colourless crystals. IR (cm$^{-1}$): 3056w, 2921w, 1708w, 1581w, 1552w, 1475w, 1442w, 1417w, 1381w, 1362w, 1315w, 1274w, 1238w, 1184w, 1119w, 1082w, 1066w, 1021w, 997w, 890w, 874w, 825s, 764m, 731m, 706m, 686m, 645w, 600w, 551m, 527w, 490w, 461w, 416w. $^1$H NMR (300 MHz, $CDCl_3$): δ, 1.61 (s, 6H, 2 $CH_3$), 2.39 (s, 6H, 2$CH_3$), 7.02-7.04 (m, 2H, CH(PH)), 7.09-7.12 (m, 1H, CH(PH)), 7.22-7.29 (m, 3H, CH(PH)), 7.38-7.41 (m, 1H, CH(PH)), 7.44-7.47 (m, 2H, CH(Ph)), 7.63 (s, 1H, $CH_{central}$). ESI-MS (p.i., $CH_3CN$, m/z, I%): 197.07, $[PhSPhNa]^+$ ; 478.91 $[(PhSPh)_2Ag]^+$; 654.81, $[(L)Ag]^+$; 1200.86, $[(L)_2Ag]^+$. Anal. Calc. for C23H22AgBr2F6N4PS (795.86): C: 34.57; H: 2.77; N: 7.01. Found: C: 34.45; H: 2.18; N: 6.98.

*Synthesis of [Ag(**L$^{Br}$**)]$_n$(BF$_4$)$_n$.* **L$^{Br}$** (114 mg, 0.21 mmol) and $AgBF_4$ (42 mg, 0.21 mmol) were mixed in acetone (10 mL), and the colourless solution was stirred for 15 min. The mixture was concentrated under vacuum and the crude was triturated with hexane in an ultrasound bath, from which a white solid precipitated. The solid was filtered and vacuum dried (132 mg, 0.18 mmol, yield 85%). The compound can be recrystallized by stratifying diethyl ether over an acetone solution of the complex yielding colourless crystals. IR ($cm^{-1}$): 3052w, 2921w, 1585w, 1483w, 1438w, 1417w, 1389w, 1360w, 1311w, 1287w, 1246m, 1058s, 1021s, 996m, 886m, 849w, 759m, 727s, 711m, 686m, 657w, 645w, 625w, 608w, 596w, 518w, 486w, 457w, 433w, 408w. $^1H$ NMR (300 MHz, Acetone): δ, 1.652 (s, 6H, $2CH_3$), 2.566 (s, 6H, $2CH_3$), 7.050-7.087 (m, 2H, CH(Ph)), 7.157 (d, J = 7.5 Hz, 1H, CH(Ph)), 7.335-7.229 (m, 3H, CH(Ph)), 7.475-7.652 (m, 3H, CH(Ph)), 8.047 (s, 1H, $CH_{central}$).

*Synthesis of [Ag(***L**$^{Br}$*)]$_n$(CF$_3$SO$_3$)$_n$.* **L**$^{Br}$ (96 mg, 0.17 mmol) and $AgCF_3SO_3$ (45 mg, 0.17 mmol) were mixed in acetone (10 mL), and the colourless solution was stirred for 15 min. The mixture was concentrated under vacuum and the crude was triturated with hexane in an ultrasound bath, from which a white solid precipitated. The solid was filtered and vacuum dried (120 mg, 0.15 mmol, yield 85%). The compound was recrystallized by stratifying diethyl ether over an acetone solution of the complex, yielding colourless crystals. IR ($cm^{-1}$): 2978w, 2925w, 1581w, 1548w, 1475w, 1446w, 1409w, 1389w, 1315w, 1266w, 1246w, 1205w, 1127w, 1102w, 1037w, 1021w, 952w, 931w, 903w, 882w, 829s, 817s, 792w, 755m, 727m, 686m, 649w, 612w, 547s, 528w, 498w, 445w, 408w. $^1H$ NMR (300 MHz, Acetone): δ, 1.94 (s, 6H, $CH_3$), 2.56 (s, 6H, $CH_3$), 7.03-7.06 (m, 2H, CH(Ph)), 7.16 (d, J = 7.8 Hz, 1H, CH(Ph)), 7.22-7.30 (m, 3H, CH(Ph)), 7.47- 7.55 (m, 3H, CH(Ph)), 8.06 (s, 1H, $CH_{central}$). ESI-MS (p.i., $CH_3CN$, m/z, I%): 197.01, $[PhSPhNa]^+$ ; 478.91 $[(PhSPh)_2Ag]^+$; 654.81, $[(L)Ag]^+$; 1200.86, $[(L)_2 Ag]^+$. Anal. Calc. for C23H22AgBr2F3N4O3S2 (803.26): C: 42.23; H: 3.39; N: 8.56. Found: C: 42.45; H: 3.18; N: 8.98.

*Synthesis of [Ag(***L**$^{5,5'Me}$*)]$_2$(PF$_6$)$_2$.* **L**$^{5,5'Me}$ (100 mg, 0.28 mmol) and $AgPF_6$ (72 mg, 0.28 mmol) were mixed in acetone (10 mL), and the colourless solution was stirred for 15 min. The mixture was concentrated under vacuum and the crude was triturated with hexane in an ultrasound bath, from which a white solid precipitated. The solid was filtered and vacuum dried (113 mg, 0.18 mmol, yield 67%). The compound was recrystallized by stratifying hexane over a dichloromethane solution of the complex, yielding colourless crystals. IR ($cm^{-1}$): 3072w, 2925w, 1581w, 1548w, 1475w, 1446w, 1409w, 1389w, 1315w, 1266w, 1246w, 1205w, 1127w, 1102w, 1037w, 1021w, 952w, 931w, 903w, 882w, 829s, 817s, 792w, 755m, 727m, 686m, 649w, 612w, 547s, 528w, 498w, 445w, 408w. $^1$H NMR (300 MHz, Acetone): δ, 2.56 (s, 6H, $CH_3$), 6.36 (d, J = 0.9 Hz, 2H, CH(Pz)), 6.79 (d, J = 7.8 Hz, 1H, CH(Ph)), 7.21-7.24 (dd, $J_1$ = 8.1 Hz, $J_2$ = 7.5 Hz, 2H, CH(Ph)), 7.29-7.37 (m, 5H, CH(Ph)), 7.44 (d, J = 7.2 Hz, 1H, CH(Ph)), 7.50 (d, J = 1.2 Hz, 1H, CH(Pz)), 7.97 (s, 1H, $CH_{central}$). ESI-MS (p.i., $CH_3CN$, m/z, I%): 197.01, $[PhSPhNa]^+$ ; 384.95, $[(L)Na]^+$; 466.94, $[(L)Ag]^+$. Anal. Calc. for C20H19AgF6N4SP (600.29): C: 40.02; H: 3.19; N: 9.33. Found: C: 39.96; H: 3.18; N: 9.14.

*Synthesis of [Ag((**L**$^{5,5'Me}$))]$_2$(BF$_4$)$_2$.* **L**$^{5,5'Me}$ (124 mg, 0.34 mmol) and $AgBF_4$ (67 mg, 0.34 mmol) were mixed in acetone (10 mL), and the colourless solution was stirred for 15 min. The mixture was concentrated under vacuum and the crude was triturated with hexane in an ultrasound bath, from which a white solid precipitated. The solid was filtered and vacuum dried (161 mg, 0.29 mmol, yield 85%). The compound can be recrystallized by stratifying hexane over a dichloromethane solution of the complex yielding colourless crystals. IR (cm$^{-1}$): 3142w, 1581w, 1548w, 1483w, 1438w, 1385w, 1319w, 1283w, 1254w, 1217w, 1021s, 943m, 882w, 858w, 817, 788w, 764s, 751s, 686m, 666w, 617m, 571w, 518m, 498w, 469w, 437w, 408m $^1$H NMR (300 MHz, Acetone): δ, 2.555 (s, 6H, CH3), 6.372 (s, 2H, CH(Pz)), 6.792 (d, J = 7.8 Hz, 1H, CH(Ph)), 7.218-7.245 (m, 2H, CH(Ph)), 7.306-7.378 (m, 5H, CH(Ph)), 7.455 (d, J = 7.8 Hz, 1H, CH(Ph)), 7.526 (s,2H, CH(Pz)), 7.973 (s, 1H, $CH_{central}$).

*Synthesis of [Ag(**L**$^{5,5'Me}$)]$_2$(CF$_3$SO$_3$)$_2$.* **L**$^{5,5'Me}$ (128 mg, 0.35 mmol) and $AgCF_3SO_3$ (91 mg, 0.35 mmol) were mixed in acetone (10 mL), and the colourless solution was stirred for 15 min. The mixture was concentrated under vacuum and the crude was triturated with hexane in an ultrasound bath, from which a white solid precipitated. The solid was filtered and vacuum dried (200 mg, 0.32 mmol, yield 92%). The compound was recrystallized by stratifying hexane over a dichloromethane solution of the complex, yielding colourless crystals. IR (cm$^{-1}$): 3056w, 1577w, 1552w, 1479w, 1438w, 1389w, 1315w, 1270m, 1246m, 1213m, 1152m, 1025m, 939w, 866w, 837w, 817w, 792w, 747m, 682m, 572w, 514m, 457w. $^1$H NMR (300 MHz, Acetone): δ, 2.54 (s, 6H, $CH_3$), 6.37 (d, J = 0.9 Hz, 2H, CH(Pz)), 6.80 (d, J = 7.8 Hz, 1H, CH(Ph)), 7.22-7.25 (dd, $J_1$ = 8.1 Hz, $J_2$ = 7.5 Hz, 2H, CH(Ph)), 7.31-7.39 (m, 5H, CH(Ph)), 7.46 (d, J = 6.9 Hz, 1H, CH(Ph)), 7.51 (d, J = 1.8 Hz, 1H, CH(Pz)), 7.967 (s, 1H, $CH_{central}$). ESI-MS (p.i., $CH_3CN$, m/z, I%): 197.01, $[PhSPhNa]^+$ ; 384.88,

$[(L)Na]^+$; 469.01, $[(L)Ag]^+$; 829.04, $[(L)_2\ Ag]^+$. Anal. Calc. for C21H19AgF3N4O3S2 (604.39): C: 41.73; H: 3.17; N: 9.27. Found: C: 41.67; H: 3.09; N: 9.58.

*Synthesis of [Ag(***L**$^{\mathbf{5,3'Me}}$*)$_2$]PF$_6$.* **L**$^{\mathbf{5,3'Me}}$ (94 mg, 0.26 mmol) and $AgPF_6$ (66 mg, 0.26 mmol) were mixed in acetone (10 mL), and the colourless solution was stirred for 15 min. The mixture was concentrated under vacuum and the crude was triturated with hexane in an ultrasound bath, from which a white solid precipitated. The solid was filtered and vacuum dried (150 mg, 0.24 mmol, yield 94%). The compound was recrystallized by stratifying hexane over a dichloromethane solution of the complex, yielding colourless crystals. IR ($cm^{-1}$): 3148w, 3145w, 3059w, 2983w, 1557w, 1524m, 1479m, 1435m, 1397m, 1280m, 1131m, 1071m, 1042m, 1024m, 998w, 824vs, 724s, 688s, 666s, 552vs. $^1H$ NMR (300 MHz, $CDCl_3$): δ, 1.99 (s, 3H, $CH_3$), 2.46 (s, 3H, $CH_3$), 6.11 (d, J = 1.0 Hz, 1H, CH(Pz)), 6.23 (d, J = 2.4 Hz, 1H, CH(Pz)), 6.97 (d, J = 7.8 Hz, 1H, CH(Ph)), 7.11-7.32 (m, 8H, CH(Ph) + CH(Pz)), 7,75 (s, 1H, $CH_{central}$), 7.85 (s, 1H, CH(Pz)). ESI-MS (p.i., $CH_3CN$, m/z, I%): 197.07, $[PhSPhNa]^+$ ; 387.01, $[(L)Na]^+$; 469.01, $[(L)Ag]^+$. Anal. Calc. for C20H19AgF6N4SP (600.29): C: 40.02; H: 3.19; N: 9.33. Found: C: 40.21; H: 3.24; N: 9.78.

*Synthesis of [Ag(***L**$^{\mathbf{3,3'Me}}$*)$_2$]PF$_6$.* **L**$^{\mathbf{3,3'Me}}$ (94 mg, 0.26 mmol) and $AgPF_6$ (66 mg, 0.26 mmol) were mixed in acetone (10 mL), and the colourless solution was stirred for 15 min. The mixture was concentrated under vacuum and the crude was triturated with hexane in an ultrasound bath, from which a white solid precipitated. The solid was filtered and vacuum dried (150 mg, 0.24 mmol, yield 94%). The compound was recrystallized by stratifying hexane over a dichloromethane solution of the complex, yielding colourless crystals. IR ($cm^{-1}$): 3142w, 3066w, 2980w, 1524m, 1473m, 1438m, 1365m, 1280m, 1232w, 1128m, 1056m, 1014w, 830vs, 748s, 685m, 552vs. $^1H$ NMR (400 MHz, $CDCl_3$): δ, 2.14 (s, 3H, $CH_3$), 2.20 (s, 3H, $CH_3$), 6.16 (d, J = 0.4 Hz, 2H, CH(Pz)), 7.02-7.05 (m, 1H, CH(Ph)), 7.15-7.19 (m, 2H, CH(Ph)), 7.27-7.39 (m, 6H, CH(Ph)), 7.64 (d, J = 0.4 Hz, 2H, CH(Pz)), 7.97 (s, 1H, $CH_{central}$). ESI-MS (p.i., $CH_3CN$, m/z, I%): 197.01, $[PhSPhNa]^+$; 384.88, $[(L)Na]^+$; 468.94, $[(L)Ag]^+$; 829.04, $[(L)_2Ag]^+$. Anal. Calc. for C20H19AgF6N4SP (600.29): C: 40.02; H: 3.19; N: 9.33. Found: C: 40.10; H: 3.11; N: 9.34.

*Synthesis of [Ag(***L**$^{\mathbf{CF3}}$*)$_2$]PF$_6$.* **L**$^{\mathbf{CF3}}$ (156 mg, 0.31 mmol) and $AgPF_6$ (79 mg, 0.31 mmol) were mixed in acetone (10 mL), and the colourless solution was stirred for 15 min. The mixture was concentrated under vacuum and the crude was triturated with hexane in an ultrasound bath, from which a white solid precipitated. The solid was filtered and vacuum dried (190 mg, 0.25 mmol, yield 82%). The compound was recrystallized by stratifying hexane over a dichloromethane solution of the complex, yielding colourless crystals. IR (cm$^{-1}$): 3160w, 1581w, 1473m, 1444m, 1384w, 1330w, 1267m, 1245w, 1220s, 1178vs, 1128vs, 1099vs, 1045s, 995m, 969m, 824vs, 764s, 742s, 685m, 666m, 618m, 555vs $^1$H NMR (400 MHz, $CD_3CN$): δ,

2.13 (s, 3H, $CH_3$), 2.18 (s, 3H, $CH_3$), 6.41 (s, 1H, CH(Pz)), 6.68 (s, 1H, CH(Pz)), 6.91-6.95 (m, 1H, CH(Ph)), 7.06-7.09 (m, 2H, CH(Ph)), 7.21-7.24 (m, 3H, CH(Ph)), 7.40-7.52 (m, 3H, CH(Ph)), 8.15 (s, 1H, $CH_{central}$). ESI-MS (p.i., $CH_3CN$, m/z, I%): 196.94, $[PhSPhNa]^+$ ; 602.87, $[(L)Ag]^+$. Anal. Calc. for C23H18AgF12N4PS (794.30): C: 36.87; H: 2.42; N: 7.48. Found: C: 36.13; H: 2.56; N: 7.59.

*Synthesis of* $[Ag(\mathbf{L}^{CF3})]_n(CF_3SO_3)_n$. $\mathbf{L}^{CF3}$ (85 mg, 0.17 mmol) and $AgCF_3SO_3$ (44 mg, 0.17 mmol) were mixed in acetone (10 mL), and the colourless solution was stirred for 15 min. The mixture was concentrated under vacuum and the crude was triturated with hexane in an ultrasound bath, from which a white solid precipitated. The solid was filtered and vacuum dried (105 mg, 0.14 mmol, yield 82%). The compound was recrystallized by stratifying hexane over a dichloromethane solution of the complex, yielding colourless crystals. IR (cm$^{-1}$): 3141vw, 3060vw, 1467m, 1441m, 1220s, 1173s, 1120s, 1023s, 973m, 833m, 740m, 665w, 633s, 573m, 515m, 473w. $^1$H NMR (400 MHz, $CD_3CN$): δ, 2.17 (s, 3H, $CH_3$), 2.21 (s, 3H, $CH_3$), 6.44 (s, 1H, CH(Pz)), 6.71 (s, 1H, CH(Pz)), 6.69 (d, 1H, CH(Ph)), 7.10-7.12 (m, 2H, CH(Ph)), 7.23-7.29 (m, 3H, CH(Ph)), 7.42-7.55 (m, 3H, CH(Ph)), 8.17 (s, 1H, $CH_{central}$). ESI-MS (p.i., $CH_3CN$, m/z, I%): 197.01, $[PhSPhNa]^+$ ; 602.94, $[(L)Ag]^+$. Anal. Calc. for C24H18AgF9N4O3S2 (753.41): C: 38.26; H: 2.41; N: 7.44. Found: C: 38.08; H: 2.34; N: 7.21.

### 2.2.4 - Single Crystal X-ray Structures

Single crystal data were collected with a Bruker Smart APEXII area detector diffractometers (Mo $K_\alpha$; $\lambda = 0.71073$ Å). Cell parameters were refined from the observed setting angles and detector positions of selected strong reflections. Intensities were integrated from several series of exposure frames that covered the sphere of reciprocal space53. A multiscan absorption correction was applied to the data using the program SADABS54. The structures were solved by direct methods55 and refined with full-matrix least-squares (SHELXL-97)56, using the Wingx software package57. Graphical material was prepared with the Mercury58 3.0 program.

## 2.3 - Results

### 2.3.1 - Syntheses

The $N_2S$-donor ligands here described were generated by treating substituted bis(pyrazolyl)ketones with functionalized (phenylthio)acetaldehyde using in a solvent-free reaction catalysed by $CoCl_2$, run at 90 ºC for 2 hours, as depicted in Fig. 2.9. In order to investigate the influence of the pyrazole ring on the resulting structural arrangement, different pyrazoles were employed as starting reagents. Such variation did not provoke significant differences as much on the synthetic procedures as on the purification of the ligands. Actually, the ligand $\mathbf{L^{CF_3}}$ was easily purified by recrystallization in hexane, the ligand $\mathbf{L^{Br}}$ was purified by silica column chromatography, while the isomeric ligands $\mathbf{L^{5,5'Me}}$, $\mathbf{L^{5,3'Me}}$ and $\mathbf{L^{3,3'Me}}$ where much harder to purify with silica column chromatography, due to co-elution.

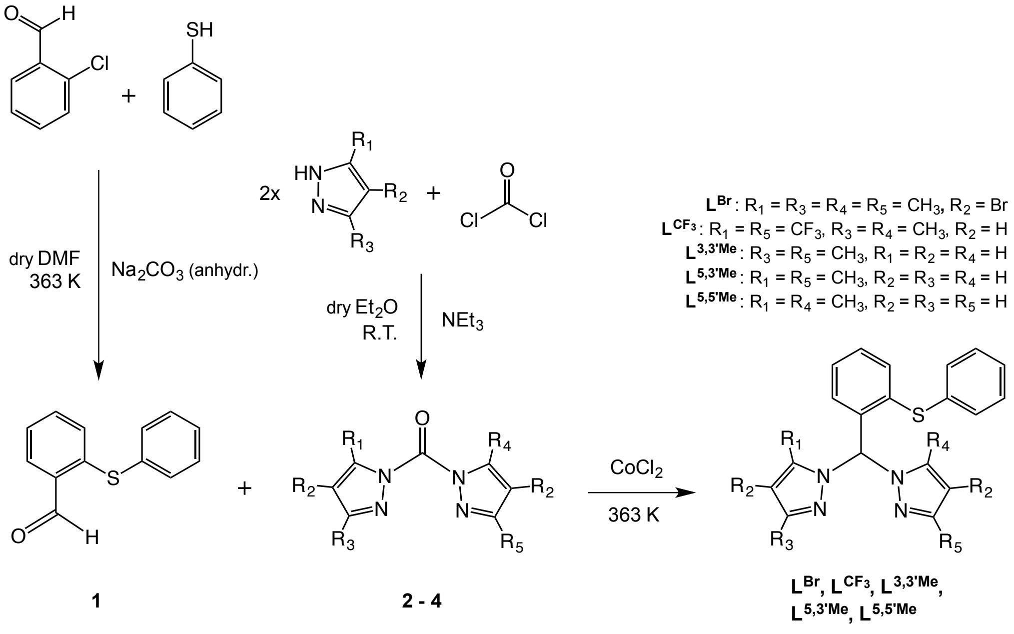

**Fig. 2.9**: Synthetic route followed for the preparation of the ligands.

Ligands $\mathbf{L}^{\mathbf{5,5'Me}}$, $\mathbf{L}^{\mathbf{5,3'Me}}$ and $\mathbf{L}^{\mathbf{3,3'Me}}$ are positional isomers and comprise the lone methyl groups either on position *3* or on position *5*. Interestingly, the synthesis of the intermediate **3** provided the symmetrical species *bis(3-methyl-1H-pyrazol-1-yl)methanone*, characterized by both methyl groups on the position *3* and *3'*, while the following catalysed reaction afforded the isomerization of the product, due to the displacement of one pyrazole moiety, according to the mechanism proposed by Peterson.[16]

Purification of the isomers was optimized by seeking the most proper technique; multiple recrystallizations and column chromatography separations were experimented. The optimized separation was pursued by the reiteration of column chromatography; firstly, a column chromatography separation was run with hexane/ethyl acetate 8/2, in order to isolate the aldehyde remained and the isomer $\mathbf{L}^{\mathbf{5,5'Me}}$. Secondly, partial separation between the co-eluting ligands $\mathbf{L}^{\mathbf{5,3'Me}}$ and $\mathbf{L}^{\mathbf{3,3'Me}}$ was achieved through a sequence of multiple chromatography columns with hexane/ethyl acetate 9/1. These two isomers proved to be very difficult to isolate, yielding about 90 mg of each species after 6 chromatographic columns.

Fig. 2.10 displays a scheme of the TLC related to the first separation step, run in hexane/ethyl acetate 8/2. Three spots were observed: the one at $R_f = 0.47$ corresponding to the starting aldehyde, a spot at $R_f = 0.17$ corresponding to the mixture of $\mathbf{L}^{\mathbf{5,3'Me}}$ and $\mathbf{L}^{\mathbf{3,3'Me}}$ and a spot at $R_f = 0.11$ corresponding to $\mathbf{L}^{\mathbf{5,5'Me}}$. The identification of the products associated to each spot was done by $^1$H-NMR (Fig. 2.11).

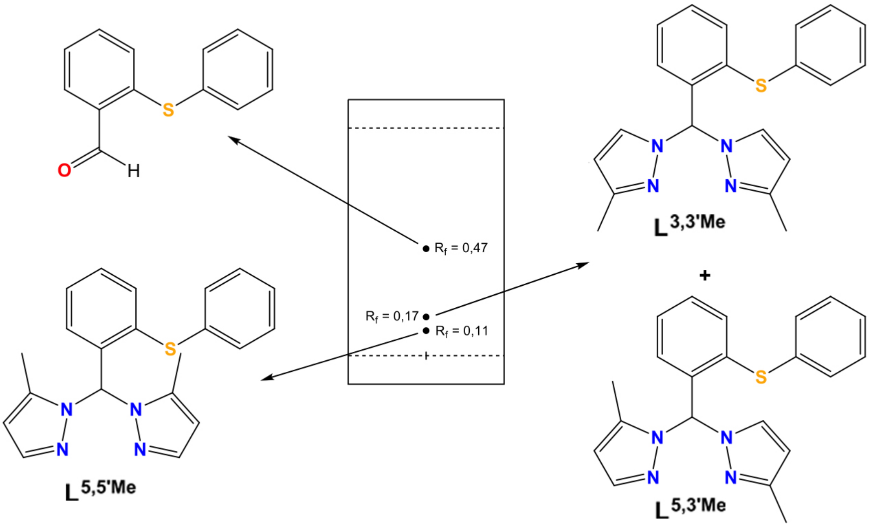

**Fig. 2.10**: Representation of the TLC run in hexane/ethyl acetate 8/2, corresponding to the crude mixture resulting from the synthesis of ligands **L$^{5,5'Me}$**, **L$^{5,3'Me}$** and **L$^{3,3'Me}$**.

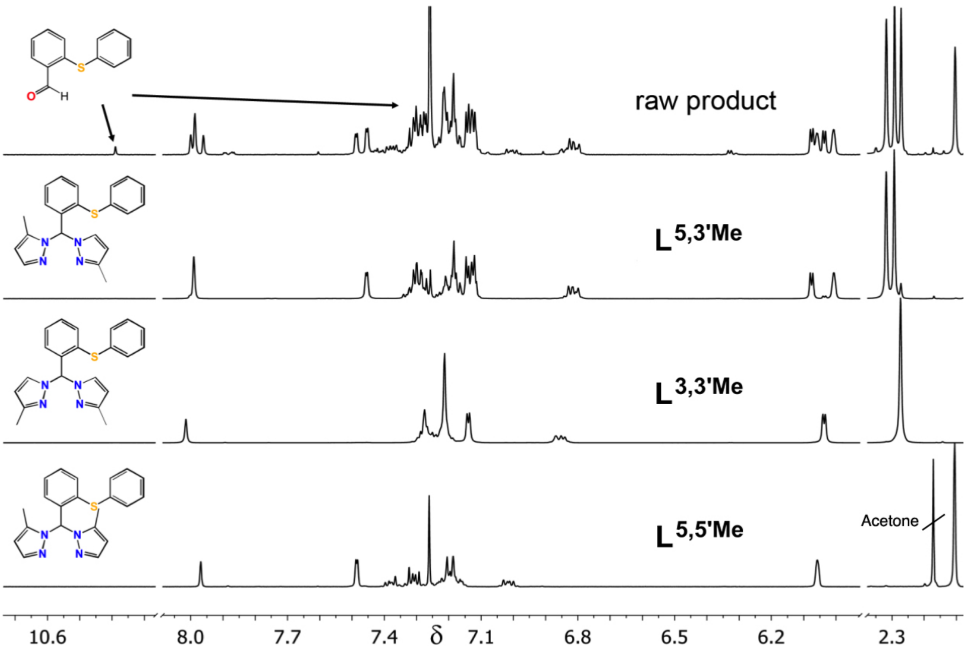

**Fig. 2.11**: Stacked $^1$H NMR spectra (ppm) of the crude product and of the three purified ligands.

The quantities of isolated isomers were nevertheless enough to prepare silver complexes that could be characterized by means of X-ray crystallography, confirming the structural assignments previously made on the base of the NMR spectra.

The complexes were prepared mixing equimolar amounts of the ligands with Ag(I) salts ($AgPF_6$, $AgBF_4$, $AgCF_3SO_3$) in acetone, in air at room temperature. Fig. 2.12 indicates the complexes that were isolated in the solid state and their specific stoichiometry. As can be noted, although the M:L ratio used in the synthesis was always 1:1, the structures obtained show different M:L ratios and different topologies. In particular, 7 structures show M:L 1:1, while 4 exhibit M:L 1:2 and just one structure is characterized by M:L 2:1.

Concerning the topology of the structures obtained, only 5 structures are extended polymers, while all other complexes form discrete molecular units (Fig. 2.13). As will be discussed further on, all the coordination polymers consist of monodimensional (1D) chains and do not provide supramolecular aggregates endowed with permanent porosity.

$L^{Br} + AgPF_6 \longrightarrow [Ag(L^{Br})]_n(PF_6)_n$
$L^{Br} + AgBF_4 \longrightarrow [Ag(L^{Br})]_n(BF_4)_n$
$L^{Br} + AgCF_3SO_3 \longrightarrow [Ag(L^{Br})]_n(CF_3SO_3)_n$
$L^{CF_3} + AgPF_6 \longrightarrow [Ag(L^{CF_3})_2]PF_6$
$L^{CF_3} + AgBF_4 \longrightarrow [Ag(L^{CF_3})_2]BF_4$
$L^{CF_3} + AgCF_3SO_3 \longrightarrow [Ag(L^{CF_3})]_n(CF_3SO_3)_n$
$L^{5,5'Me} + AgPF_6 \longrightarrow [Ag(L^{5,5'Me})]_2(PF_6)_2$
$L^{5,5'Me} + AgBF_4 \longrightarrow [Ag(L^{5,5'Me})]_2(BF_4)_2$
$L^{5,5'Me} + AgCF_3SO_3 \longrightarrow [Ag(L^{5,5'Me})]_2(CF_3SO_3)_2$
$L^{3,3'Me} + AgPF_6 \longrightarrow [Ag(L^{3,3'Me})_2]PF_6$
$L^{5,3'Me} + AgPF_6 \longrightarrow [Ag(L^{5,3'Me})_2]PF_6$
$L^{5,3'Me} + AgCF_3SO_3 \longrightarrow [Ag_2(L^{5,3'Me})]_n(CF_3SO_3)_{2n}$

**Fig. 2.12**: Complexes isolated in the solid state

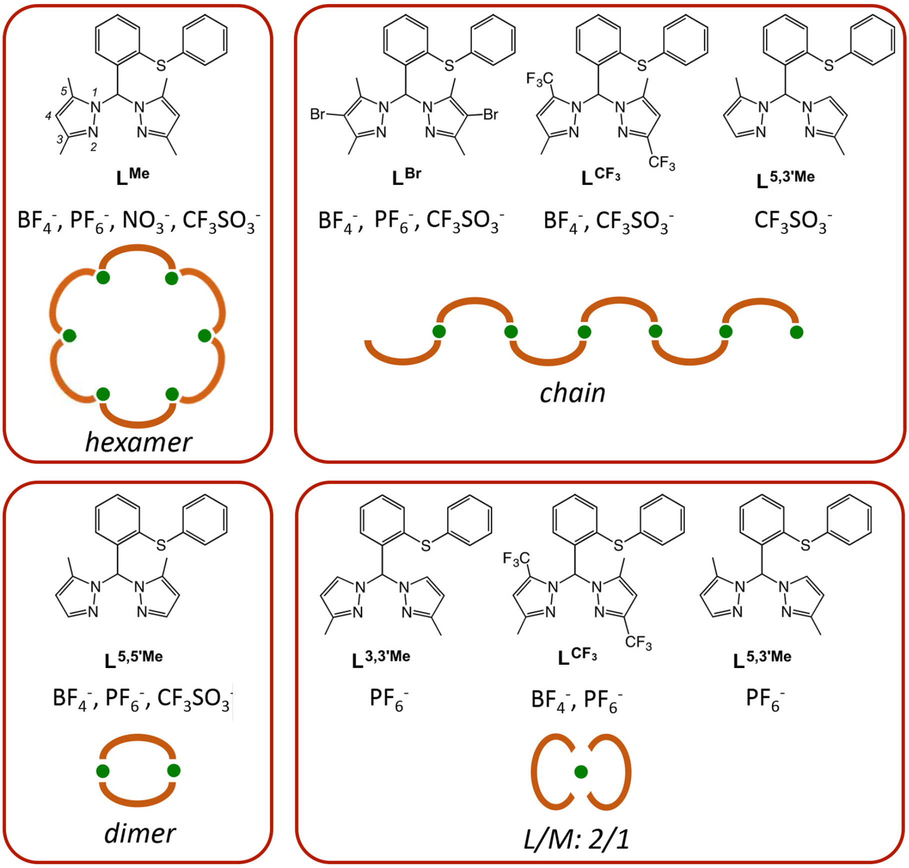

**Fig. 2.13**: Scheme of the topologies of the complexes obtained for the different functionalised ligands. The toroidal hexamer topology obtained with ligand $\mathbf{L}^{\mathbf{Me}}$ is reported for displaying purposes, although it was never observed in the current work.

## 2.4 - Discussion

### 2.4.1 - Silver Complexes Crystals Structures.

The presence of two bromine atoms on the bispyrazolyl scaffold gives polymeric silver complexes $[Ag(\mathbf{L}^{Br})]_n(PF_6)_n$, $[Ag(\mathbf{L}^{Br})]_n(BF_4)_n$, and $[Ag(\mathbf{L}^{Br})]_n(CF_3SO_3)_n$ which crystallize in the form of very similar molecular chains in the orthorhombic space group *P*bca. For all of these compounds the ligand acts as $N_2$ bidentate on a metal and bridges on another silver atom with the thioether group, with the central phenyl ring in a rigid geometry, Table 2.1. In the three complexes, the asymmetric unit comprises a $[Ag(\mathbf{L}^{Br})]_2(X)_2$ fragment (X= anion), with the two silver atoms and two different anions that interact differently but with the same overall geometry. The metal is in a trigonal planar environment, which is slightly distorted towards the tetrahedral according to presence of long contact with the fluorine atoms of $BF_4^-$ or $PF_6^-$ or the oxygen atoms of $CF_3SO_3^-$. In all structures, the metal is out of the trigonal plane to an extent that depends of the degree of the interaction exchanged with the anions. With $PF_6^-$ the metal lies out of the coordination plane of approximately 0.16-0.17 Å, whereas with $BF_4^-$ it lies out of approximately 0.17-0.22 Å. With $CF_3SO_3^-$ the metal lies out of 0.23-0.24 Å in agreement with the presence of a moderately short Ag-O contact (2.52 and 2.57 Å). The torsion angles (described as the angle between the bipyrazolyl scaffold and the phenyl linker) $\tau$ in Fig. 2.14 varies in the 0.0/-3.9° range confirming a conserved ligand conformational rigidity among the three complexes.

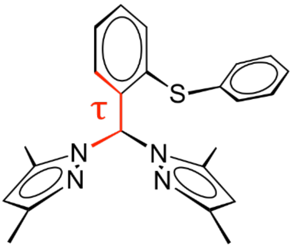

**Fig. 2.14**: Torsion angle of a generic bispyrazolyl analogue used to describe the conformational rigidity of the ligands.

The structures present a π stacking between the pyrazole ring and the peripheral phenyl ring with distances that vary in the 3.3-3.5 Å range. In fact, the two planar rings are almost parallels as confirmed by their dihedral angles (13.6-17.1° range). These molecular chains exhibit a helical arrangement (Fig. 2.15), both the left-handed and the right-handed are present in the crystal packing according to the fact that the structures are centrosymmetric. The exterior of the chains is defined by alternate anions and pyrazole rings, whereas in the interior are located the peripheral aromatic moieties of the thioether fragments. Contrarily to the toroidal hexamers described in the previous work,[12] the crystal packing of $[Ag(\mathbf{L}^{\mathbf{Br}})]_n(PF_6)_n$, $[Ag(\mathbf{L}^{\mathbf{Br}})]_n(BF_4)_n$, and $[Ag(\mathbf{L}^{\mathbf{Br}})]_n(CF_3SO_3)_n$ do not exhibit any cavity with permanent porosity, even though acetone molecules of crystallizations are present.

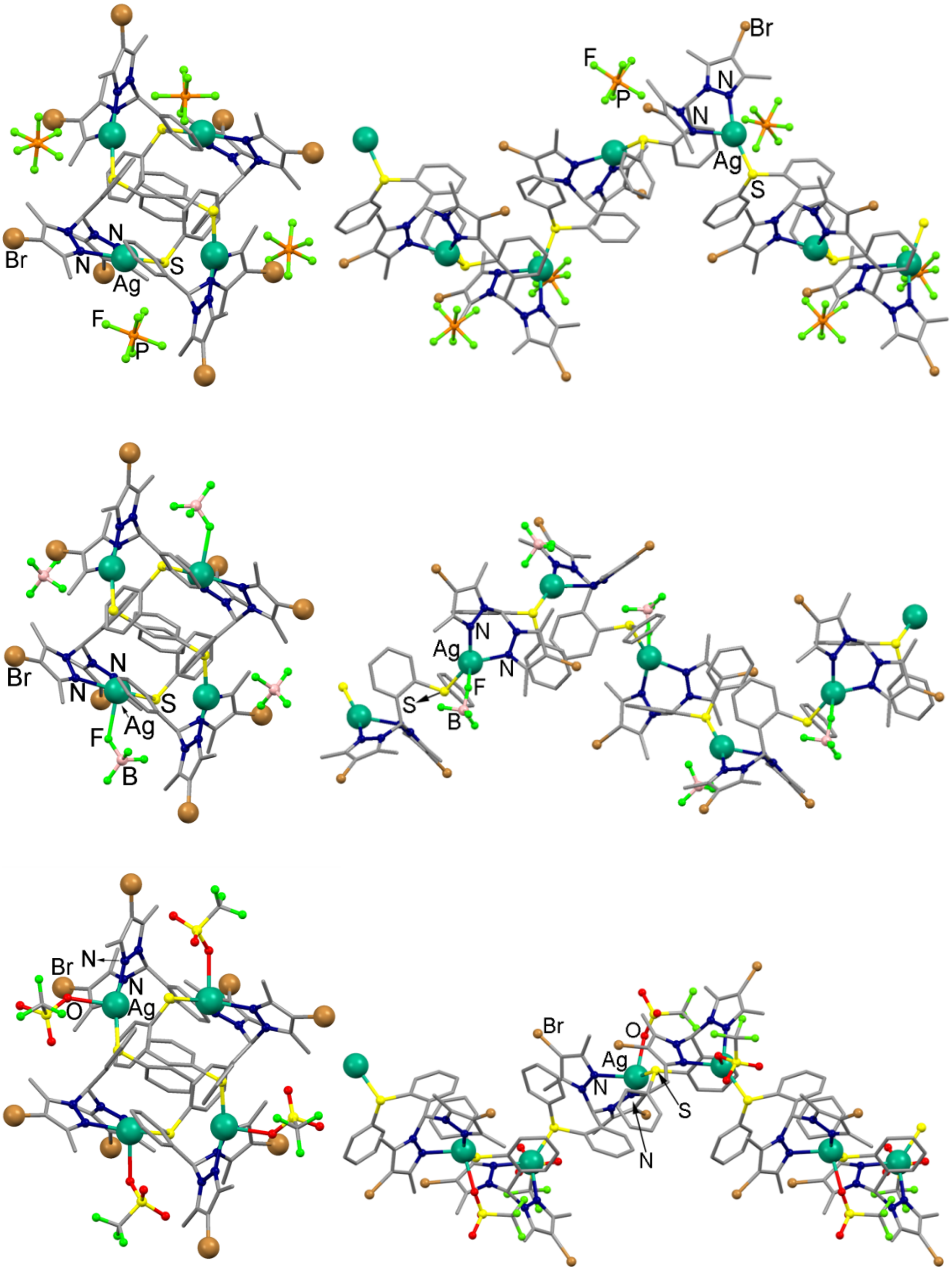

**Fig. 2.15**: Left, projection along the direction of propagation of the molecular chain of $[\mathrm{Ag}(\mathbf{L}^{\mathbf{Br}})]_n(\mathrm{PF}_6)_n$, $[\mathrm{Ag}(\mathbf{L}^{\mathbf{Br}})]_n(\mathrm{BF}_4)_n$, and $[\mathrm{Ag}(\mathbf{L}^{\mathbf{Br}})]_n(\mathrm{CF}_3\mathrm{SO}_3)_n$; right, side view of the molecular chain.

**Table 2.1**: Selected bond lengths (Å) and angles (°) for $[Ag(\mathbf{L}^{Br})]_n(PF_6)_n$, $[Ag(\mathbf{L}^{Br})]_n(BF_4)_n$ and $[Ag(\mathbf{L}^{Br})]_n(CF_3SO_3)_n$.

| | | | |
|---|---|---|---|
| $[Ag(\mathbf{L}^{Br})]_n(PF_6)_n$ | | | |
| Ag(1)-N(21) | 2.347(5) | N(22)-Ag(1)-N(21) | 84.8(2) |
| Ag(1)-N(22) | 2.241(5) | N(22)-Ag(1)-S(16)' | 158.6(1) |
| Ag(1)-S(16)' | 2.407(2) | N(21)-Ag(1)-S(16)' | 115.8(1) |
| Ag(1)-F(1) | 2.772(6) | N(24)-Ag(2)-N(25) | 84.6(2) |
| Ag(2)-N(24) | 2.254(5) | N(24)-Ag(2)-S(13) | 132.8(1) |
| Ag(2)-N(25) | 2.295(5) | N(25)-Ag(2)-S(13) | 140.8(1) |
| Ag(2)-S(13) | 2.405(2) | | |
| Ag(2)-F(7) | 2.91(2) | | |
| $[Ag(\mathbf{L}^{Br})]_n(BF_4)_n$ | | | |
| Ag(1)-N(21) | 2.249(4) | N(21)-Ag(1)-N(22) | 84.3(1) |
| Ag(1)-N(22) | 2.348(4) | N(21)-Ag(1)-(16)” | 156.5(1) |
| Ag(1)-S(16)” | 2.408(1) | N(22)-Ag(1)-S(16)” | 116.7(1) |
| Ag(2)-N(24) | 2.293(4) | N(24)-Ag(2)-N(25) | 85.3(1) |
| Ag(2)-N(25) | 2.249(4) | N(24)-Ag(2)-S(13) | 142.3(1) |
| Ag(2)-S(13) | 2.416(3) | N(25)-Ag(2)-S(13) | 129.2(1) |
| $[Ag(\mathbf{L}^{Br})]_n(CF_3SO_3)_n$ | | | |
| Ag-N(21) | 2.258(7) | N(21)-Ag(1)-N(22) | 84.9(3) |
| Ag-N(22) | 2.305(9) | N(21)-Ag(1)-S(16)’’’ | 131.1.(2) |
| Ag-S(16)''' | 2.416(3) | N(22)-Ag(1)-S(16)’’’ | 140.3(2) |
| Ag-O(37) | 2.57(1) | N(21)-Ag(1)-O(37) | 95.1(3) |
| Ag(2)-N(24) | 2.327(7) | N(22)-Ag(1)-O(37) | 101.4(4) |
| Ag(2)-N(25) | 2.284(7) | S(16)’’’-Ag(1)-O(37) | 92.4(3) |
| Ag(2)-S(13) | 2.449(2) | N(24)-Ag(2)-N(25) | 83.7(2) |
| Ag(2)-O(18) | 2.523(8) | N(25)-Ag(2)-S(13) | 156.2(2) |
| | | N(24)-Ag(2)-S(13) | 116.0(2) |
| | | N(25)-Ag(2)-O(18) | 93.9(3) |
| | | N(24)-Ag(2)-O(18) | 97.7(3) |
| | | S(13)-Ag(2)-O(18) | 96.2(2) |

Symmetry codes: ’ = x-½, ½-y, 1-z; ” = -x, ½+y, ½-z; ’’’ = ½+x, ½-y,-z

Ligand $\mathbf{L}^{CF_3}$ produced two different structural topologies depending on the counterion used in the synthesis. In presence of the more coordinating $CF_3SO_3^-$, a 1D coordination chain is obtained. This coordination polymer is analogous to the ones obtained with the ligand $\mathbf{L}^{Br}$ that were just described. When the less coordinating $BF_4^-$ and $PF_6^-$ counterions are employed, molecular units with M:L ratio of 1:2 are observed, despite the fact that the synthesis was conducted with a M:L 1:1 stoichiometry.

Concerning the structure of $[Ag(\mathbf{L}^{CF_3})]_n(CF_3SO_3)_n$, the monodimensional polymeric repetition is generated by one molecule of ligand chelating an $Ag^+$ ion with the $N_2$ bispyrazolyl moiety and bridging towards a second $Ag^+$ ion with the thioether arm (Fig. 2.16). The asymmetric unit is constituted by a $[Ag(\mathbf{L}^{CF_3})]CF_3SO_3$ fragment, with the silver ion chelated by the $N_2$ moiety and by the triflate counterion. The metal coordination is completed by the sulphur atom of the following ligand and the geometry established is a distorted tetrahedral, elongated towards the thioether moiety ($d_{Ag\text{-}S}$ = 2.62 Å), Table 2.2. The $CF_3SO_3^-$ ion is tightly bound to the silver atom, as underlined by the short bond distance $d_{Ag\text{-}O}$ = 2.30 Å, the shortest one of all the coordination bonds formed by the $Ag^+$ ($d_{Ag\text{-}N1}$ = 2.32 Å and $d_{Ag\text{-}N2}$ = 2.46 Å). The torsion angle $\tau$ accounts for -2.9°, comparable to the torsion angles of the monodimensional chains provided by $\mathbf{L}^{Br}$ (0.0/-3.9°), proving the structure preorganization is maintained for this type of structural arrangement.

One pyrazole moiety establishes a short C-H···π interaction with the terminal phenyl ring of the following ligand, with a distance of 3.13 Å. A moderately short halogen interaction is formed between a triflate ion and the trifluoromethyl moiety of a close by ligand ($d_{F\text{-}F}$ = 2.74 Å, VdW radius = 1.47 Å). The repetition of the asymmetric unit proceeds along a glide plane, thus the 1D chains are characterized by a hydrophobic side, where the aromatic moieties of the ligand are located, and by a hydrophilic side, which exposes the triflate counterions.

Crystal packing is afforded by multiple hydrogen bonds established between the ligand and $CF_3SO_3^-$ ions of a nearby chain. Thus, chains are packed in an alternate fashion, coupling the hydrophobic side with the hydrophilic one (Fig. 2.17).

As for the molecular chains observed with ligand $\mathbf{L}^{Br}$, the crystal lattice of $[Ag(\mathbf{L}^{CF_3})]_n(CF_3SO_3)_n$ does not exhibit any cavities.

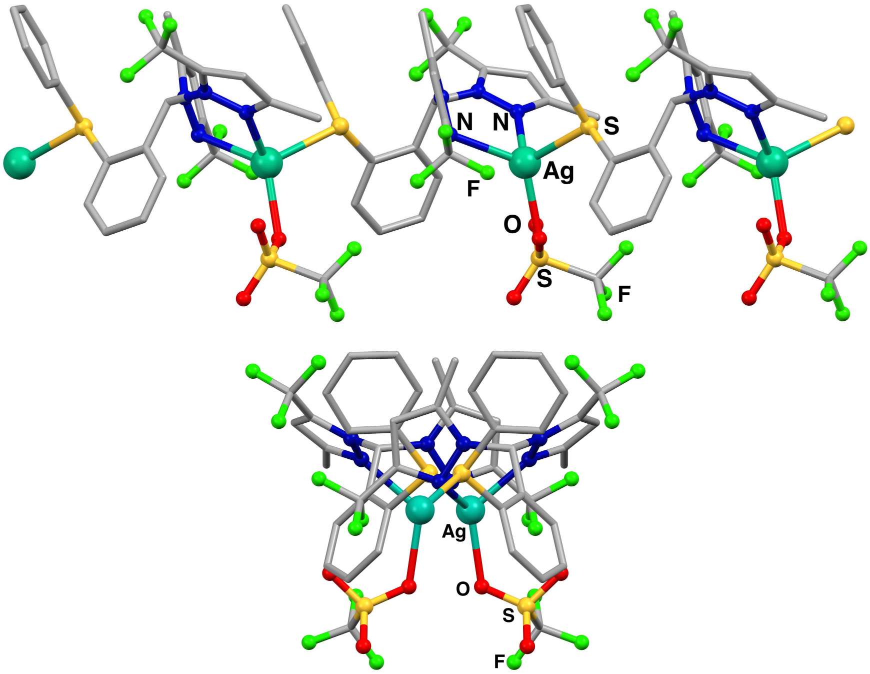

**Fig. 2.16**: Above, side view of the molecular chain along the *a* axes. Below, projection along the direction of propagation of the molecular chain (*b* axes) of $[Ag(\mathbf{L}^{CF_3})]_n(CF_3SO_3)_n$. Colour scheme: Ag, green; S, yellow; F, bright green; N, blue; O, red; C, grey.

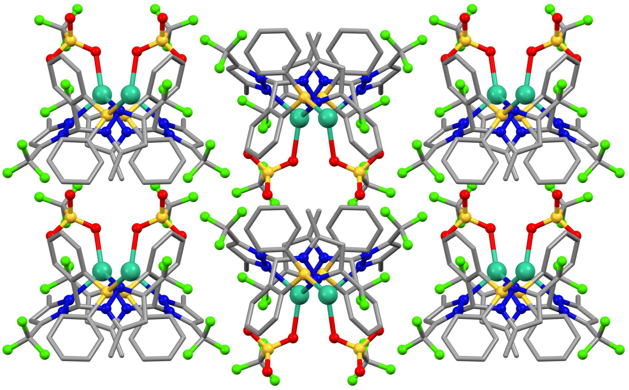

**Fig. 2.17**: Supramolecular packing of the 1D chains of $[Ag(\mathbf{L}^{CF_3})]_n(CF_3SO_3)_n$, viewed along the axes of propagation *b*. Colour scheme: Ag, green; S, yellow; F, bright green; N, blue; O, red; C, grey.

Complexes $[Ag(\mathbf{L}^{CF_3})_2]BF_4$ and $[Ag(\mathbf{L}^{CF_3})_2]PF_6$ exhibit structures characterized by M:L ratio of 1:2 despite the fact that the syntheses were conducted with M:L stoichiometry of 1:1. Both complexes comprise two ligand molecules chelating as $N_2$ on one $Ag^+$ ion. The thioether moieties are not coordinating, exposed outward from the molecular unit.

The structures possess metal ions of different coordination geometries, where the main difference is constituted by the role of the fluorinated counterion (Fig. 2.18).

The complex $[Ag(\mathbf{L}^{CF_3})_2]PF_6$ shows an $Ag^+$ ion with a distorted tetrahedral coordination geometry; the $PF_6^-$ ion is distant from the metal centre and does not interact with it. The ligand disposition shows two pyrazolyl units close to each other, interacting by their trifluoromethyl groups ($d_{F-F}$ = 3.21 Å).

The complex $[Ag(\mathbf{L}^{CF_3})_2]BF_4$ exhibits a trigonal bipyramidal metal coordination geometry instead. The unusual coordination number of five for $Ag^+$ is achieved by the two $N_2$ bidentate ligands and by the $BF_4^-$ ligand, which weakly interacts with the $Ag^+$ ion on its equatorial plane, with a distance of 2.89 Å. The apical positions are occupied by the other two pyrazolyl moieties, which are bound at the short distance of 2.19 Å. The distortion of the trigonal bipyramidal coordination geometry is underlined by the angle between the two apical coordination positions, which is of 167.5º. The two pyrazolyl moieties located on the equatorial positions are close to each other ($d_{Pz-Pz}$ = 4.0 Å), leaving more space for the other equatorial ligand, the isolated $BF_4^-$ counterion. The average torsion angle $\tau$ is -21.6º, much higher as absolute value than the torsion angles displayed by the molecular chains above described.

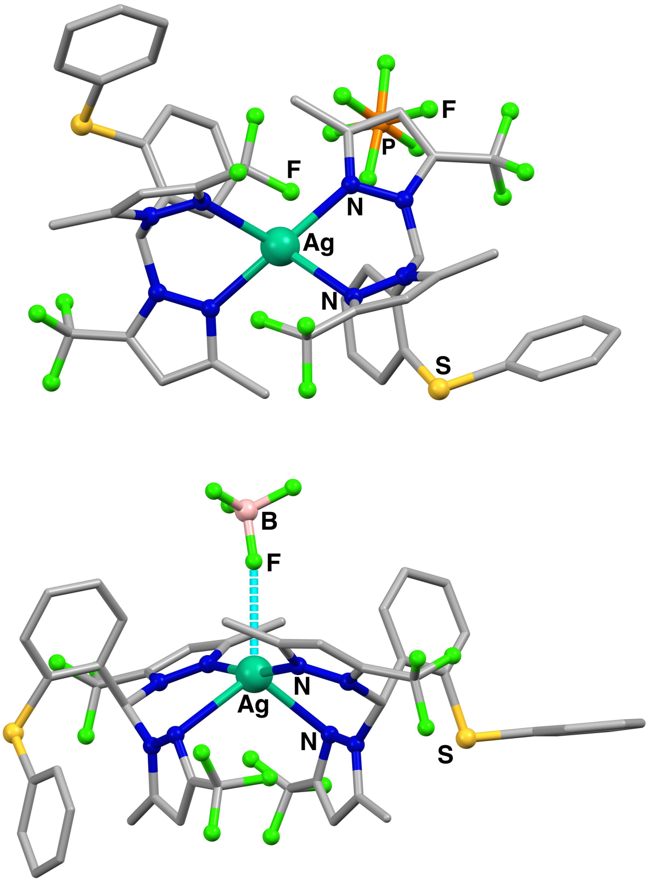

**Fig. 2.18**: Molecular structures of $[\mathrm{Ag}(\mathbf{L}^{\mathbf{CF3}})_2]\mathrm{PF}_6$ (above) and $[\mathrm{Ag}(\mathbf{L}^{\mathbf{CF3}})_2]\mathrm{BF}_4$ (below). Colour scheme: Ag, green; S, yellow; F, bright green; N, blue; C, grey.

In all the three complexes obtained with ligand $\mathbf{L}^{\mathbf{CF3}}$, a significant difference is noticeable between the coordination bonds established by the two asymmetric pyrazolyl moieties. Coordination bonds formed by the 5-trifluoromethylpyrazolil (*5*-$CF_3$-Pz) group are shorter (Table 2.2) and give rise to a more linear geometry when compared to the bonds formed by the 3-trifluoromethylpyrazolil unit (*3*-$CF_3$-Pz). Linearity of this coordination geometry is here expressed by the use of $\theta_{Pz}$, the angle formed between the pyrazolyl ring plane and the coordination bond axes (Fig. 2.19). Ideally, a linear coordination bond between the lone pair of the pyrazole N atom and the $Ag^+$ ion would entail a $\theta_{Pz}$ angle of 180º. When the observed $\theta_{Pz}$

values are significantly smaller than 180º, the coordination bond deviates from a σ-coordination bond towards a π Pz-Ag bond. As can be seen from Fig. 2.19, all three complexes involve a pyrazole group coordinating linearly (*5*-$CF_3$-Pz) and one pyrazole coordinating in a more tilted fashion (*3*-$CF_3$-Pz), with values ranging from 116º to 147º. Furthermore, a related difference in evident also in the bond lengths: the bond lengths established by the linear *5*-$CF_3$-Pz moieties are always shorter than the bonds provided by the *3*-$CF_3$-Pz groups (Fig. 2.19).

These considerations on the Pz-Ag bond lengths and $\theta_{Pz}$ angles are in agreement with the limited coordinating ability of the group *3*-$CF_3$-Pz, characterised by an electron withdrawal $CF_3$ fragment adjacent to the N-donor group, compared to the more coordinating *5*-$CF_3$-Pz.

The most significant example is complex [Ag($\mathbf{L}^{\mathbf{CF3}}$)$_2$]$BF_4$, which shows the smallest $\theta_{Pz}$ angles (avg. 119º) along with the biggest difference in bond lengths. In fact, the two more linear pyrazolyl groups form short N-Ag bonds of 2.19 Å (N21 and N24), typical of a $Ag_+$ ion with linear coordination geometry. The two more tilted pyrazoles (N22 and N25) form bonds *circa* 0.5 Å longer (avg. 2.64 Å). By taking into account the other long coordination bond established by the $BF_4^-$ counterion (2.89 Å) and the wide angle between the two linear pyrazoles (N21 and N24) of 167.5º, the coordination geometry of the silver ion in the complex [Ag($\mathbf{L}^{\mathbf{CF3}}$)$_2$]$BF_4$ can be described as trigonal bypiramidal significantly distorted towards linear with three short interactions.

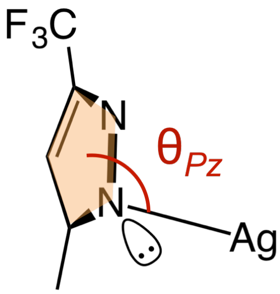

**Fig. 2.19**: Schematic representation of the angle between the pyrazolyl ring plane and the coordination bond $N_{Pz}$-Ag, referred to as $\theta_{Pz}$.

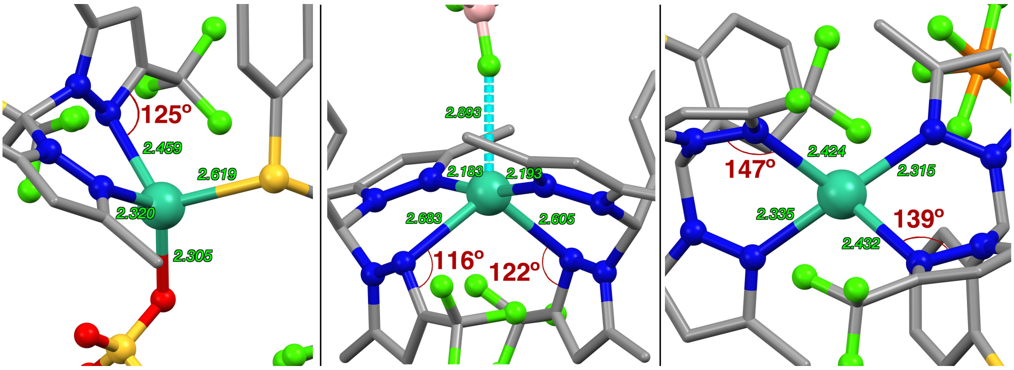

**Fig. 2.20**: Insets on the coordination environments for the complexes; bond distances are written in green (reported in Table 2.2), the angles $\theta_{Pz}$ for the three complexes are written in red. Colour scheme: Ag, green; S, yellow; F, bright green; O, red; N, blue; C, grey.

**Table 2.2**: Selected bond lengths (Å) and angles (°) for $[Ag(\mathbf{L}^{\mathbf{CF3}})]_n(CF_3SO_3)_n$, $[Ag(\mathbf{L}^{\mathbf{CF3}})_2]PF_6$ and $[Ag(\mathbf{L}^{\mathbf{CF3}})_2]BF_4$.

| $[Ag(\mathbf{L}^{\mathbf{CF3}})]_n(CF_3SO_3)_n$ | | | |
|---|---|---|---|
| Ag-O(14) | 2.305(6) | O(14)-Ag-N(21) | 123.52(19) |
| Ag-N(21) | 2.320(5) | O(14)-Ag-N(22) | 122.0(2) |
| Ag-N(22) | 2.459(6) | N(21)-Ag-N(22) | 84.70(19) |
| Ag-S(13)#1 | 2.619(2) | O(14)-Ag-S(13)#1 | 109.55(19) |
| | | N(21)-Ag-S(13)#1 | 102.82(13) |
| | | N(22)-Ag-S(13)#1 | 111.20(15) |
| $[Ag(\mathbf{L}^{\mathbf{CF3}})_2]PF_6$ | | | |
| Ag-N(21) | 2.315(3) | N(21)-Ag-N(24) | 156.03(10) |
| Ag-N(24) | 2.336(3) | N(21)-Ag-N(25) | 111.20(9) |
| Ag-N(25) | 2.424(3) | N(24)-Ag-N(25) | 79.85(9) |
| Ag-N(22) | 2.432(3) | N(21)-Ag-N(22) | 82.32(9) |
| | | N(24)-Ag-N(22) | 108.31(9) |
| | | N(25)-Ag-N(22) | 127.66(9) |
| $[Ag(\mathbf{L}^{\mathbf{CF3}})_2]BF_4$ | | | |
| Ag-N(21) | 2.183(3) | N(21)-Ag-N(24) | 167.49(13) |
| Ag-N(24) | 2.194(3) | N(21)-Ag-N(25) | 102.14(12) |
| Ag-N(25) | 2.605(3) | N(24)-Ag-N(25) | 87.04(12) |
| Ag-N(22) | 2.683 | N(21)-Ag-N(22) | 85.79 |
| Ag-F(2) | 2.893 | N(22)-Ag-N(25) | 108.22 |
| | | N(24)-Ag-N(22) | 99.52 |

Symmetry transformation: #1 -x+3/2,y,z+1/2.

By using the ligand $\mathbf{L}^{\mathbf{5,5'Me}}$, the isolated structures of the silver complexes present a different metal/ligand arrangement. In fact the complexes $[Ag(\mathbf{L}^{\mathbf{5,5'Me}})]_2(PF_6)_2$, $[Ag(\mathbf{L}^{\mathbf{5,5'Me}})]_2(BF_4)_2$, and $[Ag(\mathbf{L}^{\mathbf{5,5'Me}})]_2(CF_3SO_3)_2$ crystallize in a dimeric form. In $[Ag(\mathbf{L}^{\mathbf{5,5'Me}})]_2(PF_6)_2$, the ligand acts as a $N_2$ bidentate on a metal and bridges on a second silver atom with the thioether group. The silver atoms exhibit a distorted trigonal planar geometry (Figure 2.21) as a consequence of the $N_2$ bite angle of chelation; the torsion angle τ (Fig. 2.14) of the central phenyl ring is 19.1°. Furthermore, in the crystal packing the dimeric units assembles in supramolecular chains thanks to the π stacking between the peripheral aromatic rings. The closest distance occurs between the sulphur atom and a carbon atom of symmetry related phenyl rings (3.46 Å).

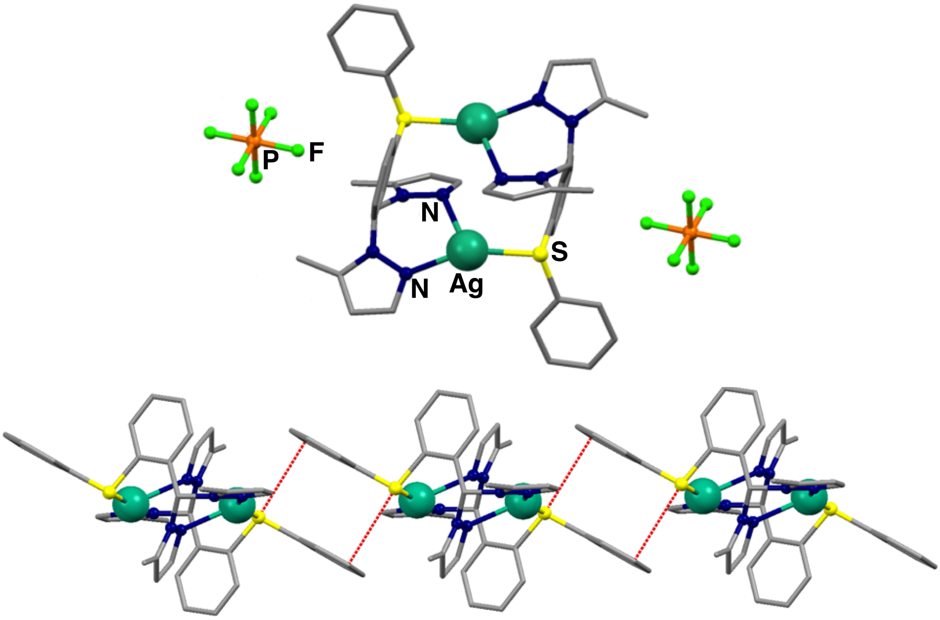

**Fig. 2.21**: Above, molecular structure of $[Ag(\mathbf{L}^{5,5'Me})]_2(PF_6)_2$; below, π stacking between the peripheral phenyl rings and portion of the supramolecular chain. Colour scheme: Ag, green; S, yellow; F, bright green; N, blue; C, grey.

The complexes $[Ag(\mathbf{L}^{5,5'Me})]_2(CF_3SO_3)_2$ and $[Ag(\mathbf{L}^{5,5'Me})]_2(BF_4)_2$ present a dimeric structure with the ligand that behaves as a bridging $N_2$ donor on two metal centres. The silver atom has a linear geometry, which is distorted by the interactions with the fluorine atom (from $BF_4^-$) or the oxygen atom (from $CF_3SO_3^-$), Figure 2.22. The τ angle is of -9.4° ($[Ag(\mathbf{L}^{5,5'Me})]_2(CF_3SO_3)_2$), and -1.4° ($[Ag(\mathbf{L}^{5,5'Me})]_2(BF_4)_2$). Differently from the structure of $[Ag(\mathbf{L}^{5,5'Me})]_2(PF_6)_2$, in these two complexes, the sulphur atom does not interact with the metal. The main characteristic of these structures is the presence of an argentophilic interaction between the two silver atoms. In fact, the distance between the metals is significantly shorter than the VdW radii sum (3.44 Å) being 2.94 Å in $[Ag(\mathbf{L}^{5,5'Me})]_2(BF_4)_2$ and 3.11 Å in $[Ag(\mathbf{L}^{5,5'Me})]_2(CF_3SO_3)_2$.

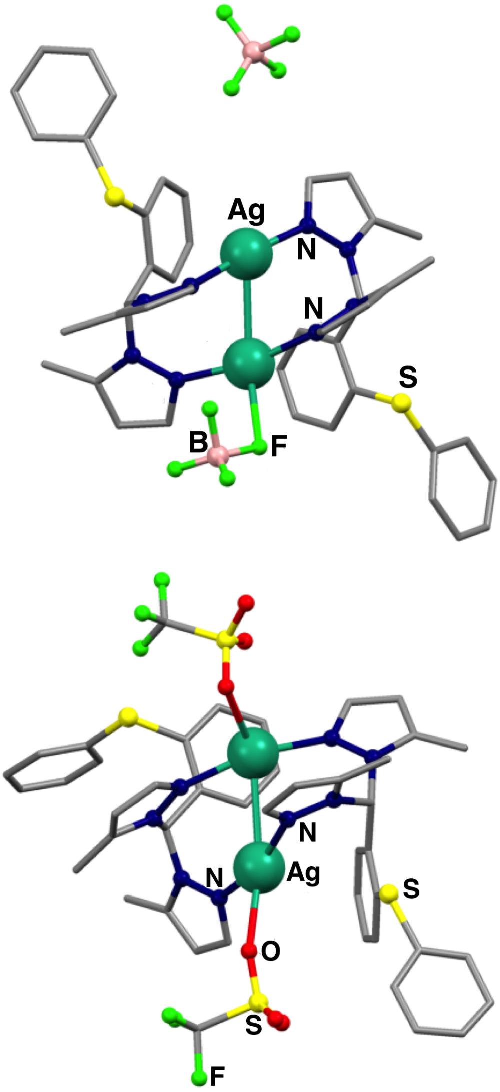

**Fig. 2.22**: Molecular structures of [Ag($\mathbf{L}^{5,5'Me}$)]$_2$(BF$_4$)$_2$ (above) and [Ag($\mathbf{L}^{5,5'Me}$)]$_2$(CF$_3$SO$_3$)$_2$ (below). Colour scheme: Ag, green; S, yellow; F, bright green; N, blue; O, red; C, grey.

**Table 2.3**: Selected bond lengths (Å) and angles (°) for $[\mathrm{Ag}(\mathbf{L}^{5,5'\mathrm{Me}})]_2(\mathrm{PF}_6)_2$, $[\mathrm{Ag}(\mathbf{L}^{5,5'\mathrm{Me}})]_2(\mathrm{BF}_4)_2$ and $[\mathrm{Ag}(\mathbf{L}^{5,5'\mathrm{Me}})]_2(\mathrm{CF}_3\mathrm{SO}_3)_2$.

| $[\mathrm{Ag}(\mathbf{L}^{5,5'\mathrm{Me}})]_2(\mathrm{PF}_6)_2$ | | | |
|---|---|---|---|
| Ag-N(21) | 2.210(3) | N(21)-Ag-N(22) | 85.42(1) |
| Ag-N(22) | 2.403(3) | N(21)-Ag-S(13)' | 155.72(8) |
| Ag-S(13)' | 2.451(1) | N(22)-Ag-S(13)' | 115.07(8) |
| $[\mathrm{Ag}(\mathbf{L}^{5,5'\mathrm{Me}})]_2(\mathrm{BF}_4)_2$ | | | |
| Ag(1)-N(24) | 2.125(5) | N(24)-Ag(1)-N(22) | 174.25(2) |
| Ag(1)-N(22) | 2.104(4) | N(24)-Ag(1)-Ag(2) | 108.77(1) |
| Ag(2)-N(21) | 2.164(5) | N(22)-Ag(1)-Ag(2) | 68.87(1) |
| Ag(2)-N(25) | 2.182(5) | N(21)-Ag(2)-N(25) | 169.26(2) |
| Ag(1)-Ag(2) | 2.9445(7) | N(21)-Ag(2)-Ag(1) | 101.76(1) |
| | | N(25)-Ag(2)-Ag(1) | 67.63(1) |
| $[\mathrm{Ag}(\mathbf{L}^{5,5'\mathrm{Me}})]_2(\mathrm{CF}_3\mathrm{SO}_3)_2$ | | | |
| Ag(1)-N(21) | 2.187(4) | N(21)-Ag(1)-N(25) | 166.05(1) |
| Ag(1)-N(25) | 2.200(4) | N(21)-Ag(1)-Ag(2) | 98.53(9) |
| Ag(2)-N(24) | 2.186(3) | N(25)-Ag(1)-Ag(2) | 67.60(1) |
| Ag(2)-N(22) | 2.216(3) | N(24)-Ag(2)-N(22) | 164.76(1) |
| Ag(2)-O(18) | 2.511(4) | N(24)-Ag(2)-O(18) | 87.28(1) |
| Ag(1)-Ag(2) | 3.1067(7) | N(22)-Ag(2)-O(18) | 104.26(1) |
| | | N(24)-Ag(2)-Ag(1) | 104.04(9) |
| | | N(22)-Ag(2)-Ag(1) | 61.99(9) |
| | | O(18)-Ag(2)-Ag(1) | 159.16(1) |

Symmetry codes: ‘ = -x, 1-y, -z

The complex $[\mathrm{Ag}(\mathbf{L}^{5,3'\mathrm{Me}})_2](\mathrm{PF}_6)$ presents a M:L 1:2 stoichiometry, despite the fact it was prepared with the 1:1 M:L ratio. In the complex, the two ligands act as $N_2$ bidentate on one metal atom. The silver atom exhibits a distorted tetrahedral geometry due to the bite angle of the ligands close to 90° (Figure 2.23). The $\tau$ angle of the central phenyl ring is 3.0°. The thioether arm does not partake in the metal coordination and is pointing outward from the molecular unit. The $\mathrm{PF}_6^-$ counterion does not interact with the metal centre.

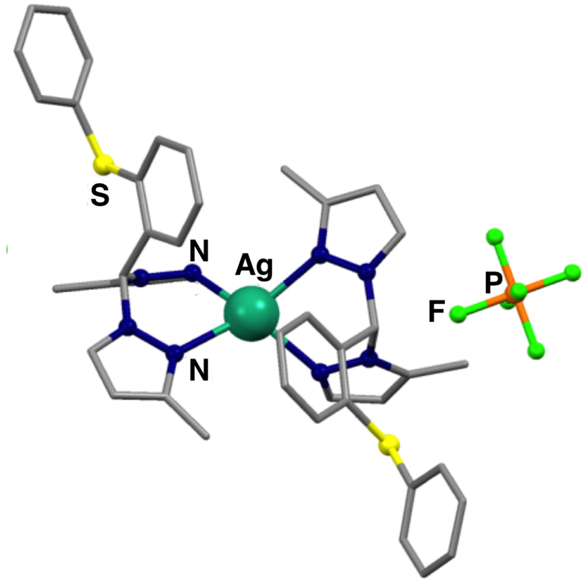

**Fig. 2.23**: Molecular structure of the complex $[Ag(\mathbf{L}^{5,3'Me})_2](PF_6)$. Colour scheme: Ag, green; S, yellow; F, bright green; N, blue; C, grey.

Complex $[Ag_2(\mathbf{L}^{5,3'Me})]_n(CF_3SO_3)_{2n}$ forms a monodimensional coordination polymer, with M:L ratio of 2:1, although the synthesis was conducted with a 1:1 M:L stoichiometry.

The asymmetric unit comprises the fragment $[Ag_2(\mathbf{L}^{5,3'Me})](CF_3SO_3)_2$. A single ligand molecule chelates $N_2$ the first silver ion, Ag1; at the meantime, one of the two pyrazolyl moieties is also coordinating on the second silver ion, Ag2. Thus, the two $Ag^+$ ions are bridged $\mu_2$-N15 by one pyrazolyl moiety and $\mu_2$-O23, on the opposite side, by a triflate ion (Fig. 2.24).

The two $Ag^+$ ions bridged by $\mu_2$-N15 and by $\mu_2$-O23 establish a marked argentophilic interaction, being the distance between the two ions significantly shorter than the sum of their Van der Waals radii (3.17 Å versus 3.44 Å). The $CF_3SO_3^-$ ion bridging $\mu_2$-O23 on Ag1 and Ag2 coordinates with a second oxygen atom (O13) on another Ag2' ion, belonging to the following asymmetric unit. The charge is balanced by a second triflate counterion bound to Ag2 in a monodentate fashion.

The coordination geometry of Ag1 is a distorted tetrahedral, presenting a wide N21-Ag1-S3’ angle of 147.1° and a narrow N15-Ag1-N21 bite angle of 85.4°, where coordination is achieved by the bidentate ligand, the bridging triflate μ$_2$-O23 and the thioether arm of the successive ligand (S3’). The long coordination bond between μ$_2$-O23 and Ag1 (d = 2.64 Å) and the sum of the angles between Ag and N21, N15 and S3, which accounts for 354°, underline a distortion towards the trigonal planar geometry.

Ag2 develops a distorted trigonal pyramidal coordination geometry, established by μ$_2$-N15, the two triflate ions and by a third triflate ion belonging to the following asymmetric unit. The τ torsion angle accounts for -16.4°.

The polymeric repetition is provided by the coordination of the thioether arm onto the Ag1 ion of the next molecular unit, establishing monodimensional molecular chains. Repetition along the second dimension is afforded by the bridging triflate ions, which connect two Ag2 ions of nearby chains, building an extended 2-dimensional coordination network (Fig. 2.25).

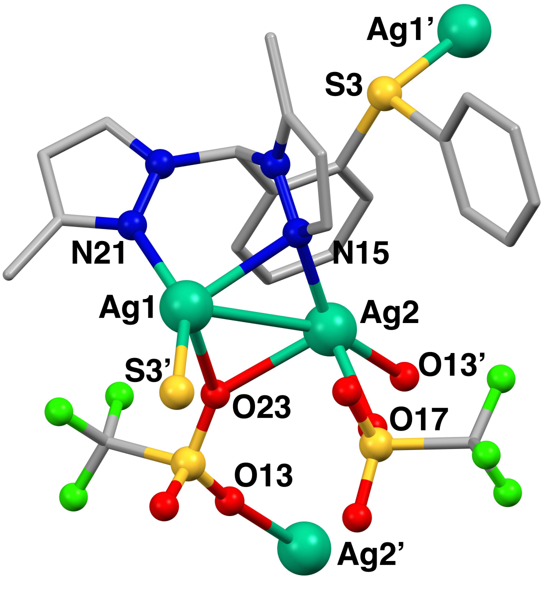

**Fig. 2.24**: Asymmetric unit of the structure [Ag$_2$(**L**$^{5,3'Me}$)]$_n$(CF$_3$SO$_3$)$_{2n}$. Two molecules of CH$_2$Cl$_2$ were omitted for clarity. Colour scheme: Ag, green; S, yellow; F, bright green; N, blue; O, red; C, grey.

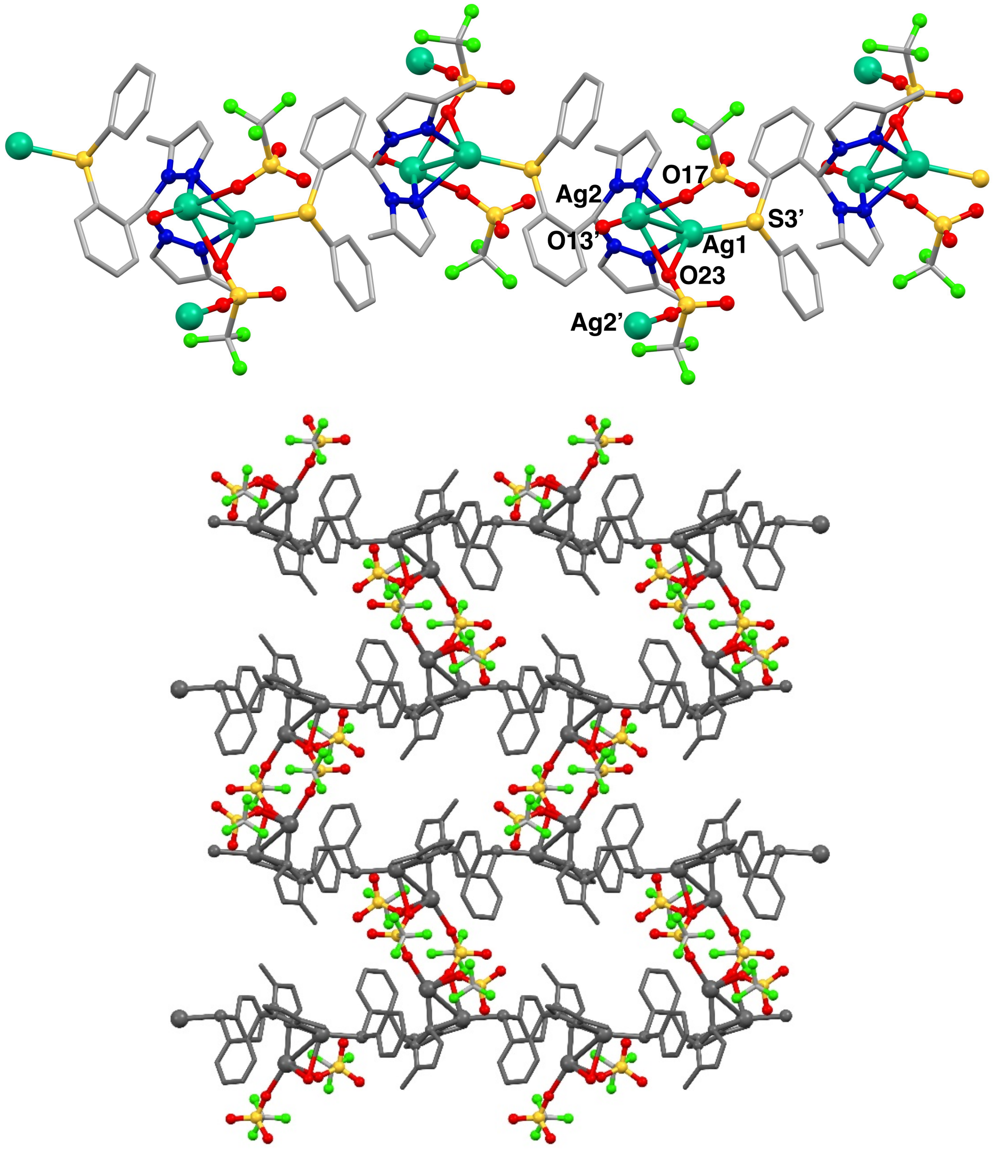

**Fig. 2.25**: Above, side view of the 1D molecular chain formed by complex $[Ag_2(\mathbf{L}^{5,3'Me})]_n(CF_3SO_3)_{2n}$, repetition along the second dimension is omitted for clarity. Colour scheme: Ag, green; S, yellow; F, bright green; N, blue; O, red; C, grey. Below, representation of the 2D coordination network of complex $[Ag_2(\mathbf{L}^{5,3'Me})]_n(CF_3SO_3)_{2n}$; the monodimensional chains formed by the bridging of ligand $\mathbf{L}^{5,3'Me}$ on silver ions Ag1 and Ag2 are displayed in grey, triflate counterions establishing the second dimensionality are standard-coloured.

The complex [Ag(**L**$^{3,3'Me}$)$_2$](PF$_6$) is characterized by a M:L ratio of 1:2, although the synthesis was performed with a M:L stoichiometry of 1:1. Two ligand units coordinate a silver ion as N$_2$ bidentate fashion. The coordination geometry displayed by the Ag$^+$ ion is a distorted tetrahedral, where the PF$_6^-$ counterion does not partake in the coordination and lays aside of the molecular unit. The structure is analogous to the one of [Ag(**L**$^{5,3'Me}$)$_2$](PF$_6$); both bispyrazolyl isomers provide the same complex topology, depicting a comparable behaviour of the two ligands. As can be noted from Table 2.4, coordination bond lengths and angles of complex [Ag(**L**$^{3,3'Me}$)$_2$](PF$_6$) are comparable to those of [Ag(**L**$^{5,3'Me}$)$_2$](PF$_6$). The $\tau$ torsion angle of the central phenyl ring is 6.7°.

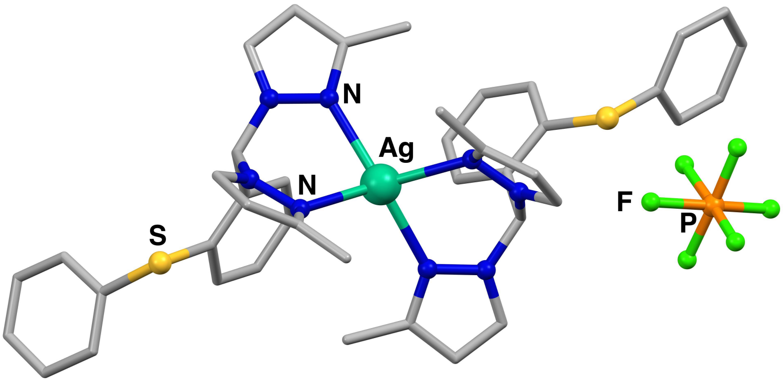

**Fig. 2.26**: Molecular structure of the complex [Ag(**L**$^{3,3'Me}$)$_2$](PF$_6$). Colour scheme: Ag, green; S, yellow; F, bright green; N, blue; O, red; C, grey.

**Table 2.4**: Selected bond lengths (Å) and angles (°) for $[Ag(\mathbf{L}^{5,3'Me})_2](PF_6)$, $[Ag_2(\mathbf{L}^{5,3'Me})]_n(CF_3SO_3)_{2n}$ and $[Ag(\mathbf{L}^{3,3'Me})_2](PF_6)$.

| | | | |
|---|---|---|---|
| $[Ag(\mathbf{L}^{5,3'Me})_2](PF_6)$ | | | |
| Ag-N(21) | 2.328(5) | N(21)-Ag-N(24) | 130.41(19) |
| Ag-N(24) | 2.332(6) | N(21)-Ag-N(22) | 83.66(17) |
| Ag-N(22) | 2.335(5) | N(24)-Ag-N(22) | 108.41(19) |
| Ag-N(25) | 2.345(6) | N(21)-Ag-N(25) | 114.04(18) |
| | | N(24)-Ag-N(25) | 83.1(2) |
| | | N(22)-Ag-N(25) | 145.59(18) |
| $[Ag_2(\mathbf{L}^{5,3'Me})]_n(CF_3SO_3)_{2n}$ | | | |
| Ag(1)-N(22) | 2.199(5) | N(22)-Ag(1)-S(13)#1 | 147.04(14) |
| Ag(1)-S(13)#1 | 2.4229(16) | N(22)-Ag(1)-N(21) | 85.43(18) |
| Ag(1)-N(21) | 2.500(5) | S(13)#1-Ag(1)-N(21) | 121.64(13) |
| Ag(1)-Ag(2) | 3.1733(8) | N(22)-Ag(1)-Ag(2) | 99.88(13) |
| Ag(2)-N(21) | 2.304(5) | S(13)#1-Ag(1)-Ag(2) | 112.41(5) |
| Ag(2)-O(35)#2 | 2.323(5) | N(21)-Ag(1)-Ag(2) | 46.06(12) |
| Ag(2)-O(14) | 2.409(5) | N(21)-Ag(2)-O(35)#2 | 148.7(2) |
| Ag(2)-O(15) | 2.461(6) | N(21)-Ag(2)-O(14) | 109.82(18) |
| | | O(35)#2-Ag(2)-O(14) | 85.5(2) |
| | | N(21)-Ag(2)-O(15) | 103.36(18) |
| | | O(35)#2-Ag(2)-O(15) | 103.8(2) |
| | | O(14)-Ag(2)-O(15) | 89.6(2) |
| | | N(21)-Ag(2)-Ag(1) | 51.37(13) |
| | | O(35)#2-Ag(2)-Ag(1) | 157.84(17) |
| | | O(14)-Ag(2)-Ag(1) | 94.05(14) |
| | | O(15)-Ag(2)-Ag(1) | 54.00(14) |
| $[Ag(\mathbf{L}^{3,3'Me})_2](PF_6)$ | | | |
| Ag-N(24) | 2.314(8) | N(24)-Ag-N(22) | 108.8(3) |
| Ag-N(22) | 2.325(8) | N(24)-Ag-N(25) | 83.2(3) |
| Ag-N(25) | 2.351(8) | N(22)-Ag-N(25) | 154.5(3) |
| Ag-N(21) | 2.354(8) | N(24)-Ag-N(21) | 125.5(3) |
| | | N(22)-Ag-N(21) | 83.9(3) |
| | | N(25)-Ag-N(21) | 107.9(3) |

Symmetry codes: #1 -x+1/2,y-1/2,-z+1/2; #2 -x+1/2,-y+1/2,-z+1

## 2.5 - Conclusions

In conclusion, a set of five new bispyrazolylmethane derivatives were synthesized to be employed as $N_2S$ ligands. The purpose was to investigate the possible formation of porous coordination polymers with $Ag^+$ ions. In particular, modifications were carried out on the previously reported ligand $\mathbf{L^{Me}}$, which forms hexamers in the solid state characterized by permanent porosity and by the ability to selectively absorb gases. The functionalization undertaken aimed at studying the influence of substituents on the pyrazolyl moieties over the structural arrangement, with specific focus on the investigation of their importance on the void cavities. Nevertheless, it was observed that none of the modifications realized brought to the formation of hexameric units and of any sort of structural cavities. Hence, it can be concluded that the nature of the two pyrazolyl moieties comprised in ligand $\mathbf{L^{Me}}$ is fundamental for the achievement of porous supramolecular architectures. The tendency of the more coordinating counterion $CF_3SO_3^-$ to establish coordination polymers with this type of systems was noted, with respect to the less coordinating anions $BF_4^-$ and $PF_6^-$, which tend to induce the formation of complexes of lower dimensionality. This behaviour is in agreement with what reported in a previous work[13] on the same type of complexes, where $BF_4^-$ and $PF_6^-$ provided molecular hexamers, while $CF_3SO_3^-$ afforded only molecular chains.

## 2.6 - Supporting Information

**Table S2.1**: Summary of X-ray crystallographic data for $[Ag(\mathbf{L}^{\mathbf{Br}})]_n(PF_6)_n$, $[Ag(\mathbf{L}^{\mathbf{Br}})]_n(BF_4)_n$, and $[Ag(\mathbf{L}^{\mathbf{Br}})]_n(CF_3SO_3)_n$.

| | $[Ag(\mathbf{L}^{\mathbf{Br}})]_n(PF_6)_n$ | $[Ag(\mathbf{L}^{\mathbf{Br}})]_n(BF_4)_n$ | $[Ag(\mathbf{L}^{\mathbf{Br}})]_n(CF_3SO_3)_n$ |
|---|---|---|---|
| Empirical formula | $C_{49}H_{50}Ag_2Br_4$ $F_{12}N_8OP_2S_2$ | $C_{49}H_{50}Ag_2B_2Br_4$ $F_8N_8OS_2$ | $C_{51}H_{50}Ag_2Br_4$ $F_6N_8O_7S_4$ |
| Formula weight | 1656.41 | 1540.09 | 1664.61 |
| Colour, habit | Colourless, block | Colourless, block | Colourless, block |
| Crystal size, mm | 0.21×0.12×0.11 | 0.28×0.19×0.09 | 0.17×0.10×0.09 |
| Crystal system | Orthorhombic | Orthorhombic | Orthorhombic |
| Space group | *P*bca | *P*bca | *P*bca |
| *a*, Å | 20.392(5) | 23.926(2) | 20.462(5) |
| *b*, Å | 24.173(5) | 20.500(2) | 24.654(5) |
| *c*, Å | 24.653(5) | 24.006(2) | 25.026(5) |
| α, deg. | 90 | 90 | 90 |
| β, deg. | 90 | 90 | 90 |
| γ, deg. | 90 | 90 | 90 |
| $V$, Å$^3$ | 12152(5) | 11775(2) | 12603(5) |
| $Z$ | 8 | 8 | 8 |
| $T$, K | 293(2) | 293(2) | 293(2) |
| $\rho$ (calc), Mg/m$^3$ | 1.811 | 1.738 | 1.755 |
| $\mu$, mm$^{-1}$ | 3.476 | 3.519 | 3.362 |
| $\theta$ range, deg. | 1.55 to 25.00 | 1.56 to 25.83 | 1.65 to 25.00 |
| No.of rflcn/independ. | 38957 / 10075 | 98439 / 11322 | 65780 / 11048 |
| GooF | 1.006 | 1.007 | 1.035 |
| $R1$ | 0.0533 | 0.0440 | 0.0731 |
| $wR2$ | 0.1013 | 0.0916 | 0.1573 |

$R1 = \Sigma||F_o|-|F_c||/\Sigma|F_o|$, $wR2 = [\Sigma[w(F_o^2-F_c^2)^2]/\Sigma[w(F_o^2)^2]]^{1/2}$ , $w = 1/[\sigma^2(F_o^2) + (aP)^2 + bP]$, where $P = [\max(F_o^2,0) + 2F_c^2]/3$

**Table S2.2**: Summary of X-ray crystallographic data for $[\mathrm{Ag}(\mathbf{L}^{\mathbf{CF3}})]_n(\mathrm{CF_3SO_3})_n$, $[\mathrm{Ag}(\mathbf{L}^{\mathbf{CF3}})_2]\mathrm{PF_6}$ and $[\mathrm{Ag}(\mathbf{L}^{\mathbf{CF3}})_2]\mathrm{BF_4}$.

| | $[\mathrm{Ag}(\mathbf{L}^{\mathbf{CF3}})_2]\mathrm{CF_3SO_3}$ | $[\mathrm{Ag}(\mathbf{L}^{\mathbf{CF3}})_2]\mathrm{PF_6}$ | $[\mathrm{Ag}(\mathbf{L}^{\mathbf{CF3}})_2]\mathrm{BF_4}$ |
|---|---|---|---|
| Empirical formula | $\mathrm{C_{24}H_{18}AgF_9N_4O_3S_2}$ | $\mathrm{C_{46}H_{35}AgF_{18}N_8PS_2}$ | $\mathrm{C_{47}H_{38}AgBCl_2F_{16}N_8S_2}$ |
| Formula weight | 753.41 | 1244.78 | 1272.55 |
| Colour, habit | Colourless, block | Colourless, block | Colourless, block |
| Crystal size, mm | 0.19 x 0.17 x 0.11 | 0.42 x 0.17 x 0.14 | 0.32 x 0.16 x 0.15 |
| Crystal system | Orthorhombic | Monoclinic | Monoclinic |
| Space group | Pca21 | P 21/n | P 21/n |
| *a*, Å | 20.562(3) | 14.589(2) | 18.380(3) |
| *b*, Å | 9.212(1) | 12.961(2) | 11.763(2) |
| *c*, Å | 15.038(2) | 27.820(5) | 24.684(4) |
| α, deg. | 90 | 90 | 90 |
| β, deg. | 90 | 101.570(3) | 92.869(3) |
| γ, deg. | 90 | 90 | 90 |
| $V$, Å$^3$ | 2848.5(6) | 5153.5(14) | 5330.1(15) |
| $Z$ | 4 | 4 | 4 |
| $T$, K | 293 (2) | 293 (2) | 293 (2) |
| $\rho$ (calc), Mg/m$^3$ | 1.757 | 1.604 | 1.586 |
| $\mu$, mm$^{-1}$ | 0.948 | 0.611 | 0.655 |
| $\theta$ range, deg. | 1.98 to 25.70 | 1.470 to 25.869 | 1.349 to 25.177 |
| No.of rflcn/independ. | 27291 / 5410 | 58479 / 9955 | 57340 / 9528 |
| GooF | 1.003 | 1.007 | 1.010 |
| $R1$ | 0.0479 | 0.0458 | 0.0513 |
| $wR2$ | 0.0866 | 0.1230 | 0.1355 |

$R1 = \Sigma||F_o|-|F_c||/\Sigma|F_o|$, $wR2 = [\Sigma[w(F_o^2-F_c^2)^2]/\Sigma[w(F_o^2)^2]]^{1/2}$, $w = 1/[\sigma^2(F_o^2) + (aP)^2 + bP]$, where $P = [\max(F_o^2,0) + 2F_c^2]/3$

**Table S2.3**: Summary of X-ray crystallographic data for [Ag(**L**$^{5,5'Me}$)]$_n$($PF_6$)$_n$, [Ag(**L**$^{5,5'Me}$)]$_n$($BF_4$)$_n$, and [Ag(**L**$^{5,5'Me}$)]$_n$($CF_3SO_3$)$_n$.

| | [Ag(**L**$^{5,5'Me}$)]$_2$($PF_6$)$_2$ | [Ag(**L**$^{5,5'Me}$)]$_2$($BF_4$)$_2$ | [Ag(**L**$^{5,5'Me}$)]$_2$($CF_3SO_3$)$_2$ |
|---|---|---|---|
| Empirical formula | $C_{49}H_{50}Ag_2Br_4$ $F_{12}N_8OP_2S_2$ | $C_{49}H_{50}Ag_2B_2Br_4$ $F_8N_8OS_2$ | $C_{51}H_{50}Ag_2Br_4$ $F_6N_8O_7S_4$ |
| Formula weight | 1656.41 | 1540.09 | 1664.61 |
| Colour, habit | Colourless, block | Colourless, block | Colourless, block |
| Crystal size, mm | 0.21×0.12×0.11 | 0.28×0.19×0.09 | 0.17×0.10×0.09 |
| Crystal system | Orthorhombic | Orthorhombic | Orthorhombic |
| Space group | *P*bca | *P*bca | *P*bca |
| *a*, Å | 20.392(5) | 23.926(2) | 20.462(5) |
| *b*, Å | 24.173(5) | 20.500(2) | 24.654(5) |
| *c*, Å | 24.653(5) | 24.006(2) | 25.026(5) |
| α, deg. | 90 | 90 | 90 |
| β, deg. | 90 | 90 | 90 |
| γ, deg. | 90 | 90 | 90 |
| *V*, Å$^3$ | 12152(5) | 11775(2) | 12603(5) |
| *Z* | 8 | 8 | 8 |
| *T*, K | 293(2) | 293(2) | 293(2) |
| $\rho$ (calc), Mg/m$^3$ | 1.811 | 1.738 | 1.755 |
| $\mu$, mm$^{-1}$ | 3.476 | 3.519 | 3.362 |
| $\theta$ range, deg. | 1.55 to 25.00 | 1.56 to 25.83 | 1.65 to 25.00 |
| No.of rflcn/independ. | 38957 / 10075 | 98439 / 11322 | 65780 / 11048 |
| GooF | 1.006 | 1.007 | 1.035 |
| *R*1 | 0.0533 | 0.0440 | 0.0731 |
| *wR*2 | 0.1013 | 0.0916 | 0.1573 |

$R1 = \Sigma||F_o|-|F_c||/\Sigma|F_o|$, $wR2 = [\Sigma[w(F_o^2-F_c^2)^2]/\Sigma[w(F_o^2)^2]]^{½}$, $w = 1/[\sigma^2(F_o^2) + (aP)^2 + bP]$, where $P = [\max(F_o^2,0) + 2F_c^2]/3$

**Table S2.4**: Summary of X-ray crystallographic data for [Ag($\mathbf{L}^{\mathbf{5,3'Me}}$)$_2$](PF$_6$), [Ag$_2$($\mathbf{L}^{\mathbf{5,3'Me}}$)]$_n$(CF$_3$SO$_3$)$_{2n}$ and [Ag($\mathbf{L}^{\mathbf{3,3'Me}}$)$_2$](PF$_6$).

| | [Ag($\mathbf{L}^{\mathbf{5,3'Me}}$)$_2$](PF$_6$) | [Ag$_2$($\mathbf{L}^{\mathbf{5,3'Me}}$)]$_n$(CF$_3$SO$_3$)$_{2n}$ | [Ag($\mathbf{L}^{\mathbf{3,3'Me}}$)$_2$](PF$_6$) |
|---|---|---|---|
| Empirical formula | $C_{43}H_{42}AgCl_2F_6N_8PS_2$ | $C_{25}H_{24}Ag_2Cl_4F_6N_4O_6S_3$ | $C_{48}H_{52}AgF_6N_8O_2PS_2$ |
| Formula weight | 1058.71 | 1044.20 | 1089.93 |
| Crystal size, mm | 0.15 x 0.13 x 0.12 | 0.21 x 0.15 x 0.15 | 0.23 x 0.15 x 0.15 |
| Crystal system | Monoclinic | Monoclinic | Triclinic |
| Space group | P21/n | C 2/c | P -1 |
| *a*, Å | 11.123(1) | 25.734(4) | 12.89(2) |
| *b*, Å | 27.831(3) | 15.979(2) | 14.31(2) |
| *c*, Å | 15.647(2) | 18.604(3) | 14.84(2) |
| α, deg. | 90 | 90 | 91.12(2) |
| β, deg. | 95.134(2) | 107.341(3) | 99.33(2) |
| γ, deg. | 90 | 90 | 96.74(2) |
| $V$, Å$^3$ | 4824.3(9) | 7302.3(19) | 2680(7) |
| $Z$ | 4 | 8 | 2 |
| $T$, K | 293(2) | 205(2) | 293(2) |
| $\rho$ (calc), Mg/m$^3$ | 1.458 | 1.900 | 1.350 |
| $\mu$, mm$^{-1}$ | 0.711 | 1.612 | 0.548 |
| $\theta$ range, deg. | 1.46 to 23.33 | 1.658 to 24.863 | 1.392 to 23.387 |
| No.of rflcn/independ. | 29675 / 6970 | 36860 / 6313 | 12158 / 7487 |
| GooF | 1.040 | 1.009 | 0.968 |
| *R*1 | 0.0617 | 0.0531 | 0.0751 |
| *wR*2 | 0.1598 | 0.1166 | 0.1471 |

$R1 = \Sigma||F_o|-|F_c||/\Sigma|F_o|$, $wR2 = [\Sigma[w(F_o^2-F_c^2)^2]/\Sigma[w(F_o^2)^2]]^{1/2}$, $w = 1/[\sigma^2(F_o^2) + (aP)^2 + bP]$, where $P = [\max(F_o^2,0) + 2F_c^2]/3$

## 2.7 - References

1 C. Janiak and J. K. Vieth, *New J. Chem.*, 2010, **34**, 2366–2388.

2 H. Furukawa, K. E. Cordova, M. O'Keeffe and O. M. Yaghi, *Sci. (Washington, DC, U. S.)*, 2013, **341**, 974.

3 D. Deanna M., B. Smit, J. R. Long, D. M. D'Alessandro, B. Smit and J. R. Long, *Angew. Chemie Int. Ed.*, 2010, **49**, 6058–6082.

4 J.-R. Li, R. J. Kuppler and H.-C. Zhou, *Chem. Soc. Rev.*, 2009, **38**, 1477.

5 S. Ma, D. Sun, M. Ambrogio, J. A. Fillinger, S. Parkin and H.-C. Zhou, *J. Am. Chem. Soc.*, 2007, **129**, 1858–1859.

6 C. Wang, D. Liu and W. Lin, *J. Am. Chem. Soc.*, 2013, **135**, 13222–13234.

7 J. Lee, O. K. Farha, J. Roberts, K. a Scheidt, S. T. Nguyen and J. T. Hupp, *Chem. Soc. Rev.*, 2009, **38**, 1450–1459.

8 M. Zhang, G. Feng, Z. Song, Y. P. Zhou, H. Y. Chao, D. Yuan, T. T. Y. Tan, Z. Guo, Z. Hu, B. Z. Tang, B. Liu and D. Zhao, *J. Am. Chem. Soc.*, 2014, **136**, 7241–7244.

9 D. F. Sava Gallis, L. E. S. Rohwer, M. A. Rodriguez and T. M. Nenoff, *Chem. Mater.*, 2014, **26**, 2943–2951.

10 Z. Hu, B. J. Deibert and J. Li, *Chem. Soc. Rev.*, 2014, **43**, 5815–5840.

11 M. Kurmoo, *Chem. Soc. Rev.*, 2009, **38**, 1353.

12 I. Bassanetti, F. Mezzadri, A. Comotti, P. Sozzani, M. Gennari, G. Calestani and L. Marchiò, *J. Am. Chem. Soc.*, 2012, **134**, 9142–9145.

13 I. Bassanetti, A. Comotti, P. Sozzani, S. Bracco, G. Calestani, F. Mezzadri and L. Marchiò, *J. Am. Chem. Soc.*, 2014, **136**, 14883–14895.

14 K. I. Thé and L. K. Peterson, *Can. J. Chem.*, 1973, **51**, 422–426.

15 I. Bassanetti and L. Marchiò, *Inorg. Chem.*, 2011, **50**, 10786–10797.

16 L. K. Peterson, E. Kiehlmann, a. R. Sanger and K. I. Thé, *Can. J. Chem.*, 1974, **52**, 2367–2374.

# Chapter III

## *Introduction on Metallacrowns*

## 3.1 - Introduction on Metallacrowns

Metallacrowns (MCs) are a class of metallamacrocycles that was discovered by Pecoraro and Lah in 1989[1,2] and has so far studied because it exhibits astonishing structural variability,[3] great stability in solution, and remarkable functional properties.[4] Metallacrowns possess electron rich coordinating scaffolds analogous to those of the parent crown ethers. The structural similarity between crown ethers and MCs is known as the "crown analogy"; the cyclic repetition of $(CH_2)_nO$ units constituting crown ethers is replaced in MCs by the propagation of a $(M\text{-}N\text{-}O)_n$ motif, where the oxygen atoms are usually also engaged into a supplementary coordination towards a central guest.

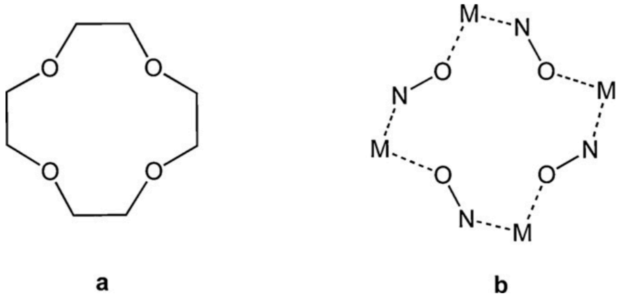

**Fig. 3.1**: Scheme representing the generic structure of a 12-C-4 crown ether (left) and a 12-MC-4 metallacrown (right).

The dimensions of the MCs central cavities are generally comparable to the ones of crown ethers[5] and, like the organic counterparts, MCs can encapsulate a variety of guests within their oxygen-rich rings, from alkaline metals, to transition metal ions, to lanthanide ions. Due to the many similarities between the two families of molecules, MCs adopt a nomenclature deriving from the one of crown ether. For example, just as 12-C-4 indicates a crown ether constituted of 12 atoms, of which 4 coordinating oxygen atoms pointing to the centre of the cavity, the analogous 12-MC-4 is formed by 12 ions constituting the ring, of which 4 are the coordinating oxygen atoms (Fig. 3.1).

The most common class of ligands used to assemble metallacrowns is that of hydroxamic acids, in particular amino- or hydroxyhydroxamic acids. They feature an hydroxamic function and an additional $NH_2$ or OH coordinating group. Depending on the length of the spacer between the two groups, they acquire the prefix α, β and γ (one, two or three carbon atoms in the spacer, respectively). Depending on their degree of deprotonation, aminohydroxamic acids can bind metal cations in three main fashions, displayed in Fig. 3.2. The bridging coordination mode (N, $N^-$)-(O, $O^-$) (Fig. 3.2**c**) is the one giving rise to the peculiar ligand disposition that is typical of metallacrowns. By cyclic repetition (and ring closure) of the bridging unit, the scaffold of the MC is obtained, into which a cation is incapsulated. The hydroximate (O,$O^-$) moiety creates always a five-member chelation ring, whilst the additional $NH_2$ or OH group can form a five-, six- or seven-member chelation ring, depending on the spacer length (respectively α, β or γ, as discussed).

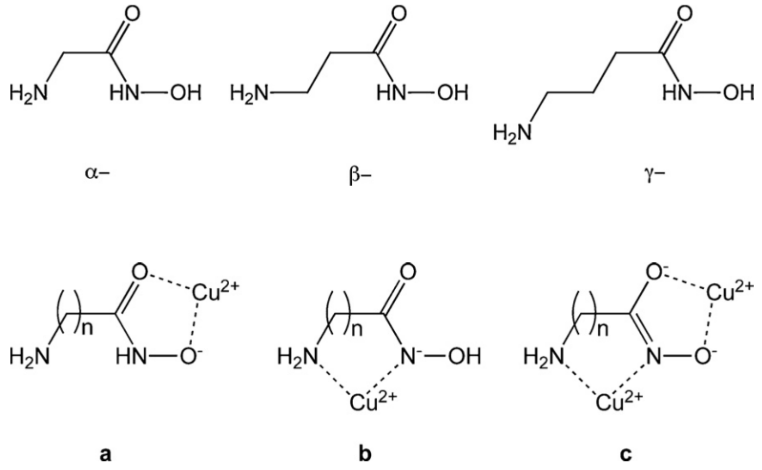

**Fig. 3.2**: Scheme representing the generic structure of α, β or γ-aminohydroxamic acids (upper row) and their coordination modes (lower row), respectively **a**: (O, $O^-$), **b**: (N, $N^-$) and **c**: (N, $N^-$)-(O, $O^-$).

The length of the spacer, thus the size of the chelation ring, influences the topology and the symmetry of the MC obtained. In particular, it was noticed that β-aminohydroxamic acids form 12-MC-4 complexes, of four-fold symmetry, while α--aminohydroxamic acids tend to give rise to 15-MC-5 complexes, with five-fold symmetry. In fact, the first ligands ascribe an angle between the chelation bisectors of 90º, providing a square motif, while the latter ones create an angle between the chelation bisectors of 108º, which is the internal angle of a pentagon (Fig. 3.3). This set of geometric requirements is defined as the "Metallacrown Structural Paradigm", which represent the most useful paradigm for the design and isolation of planar MC species.

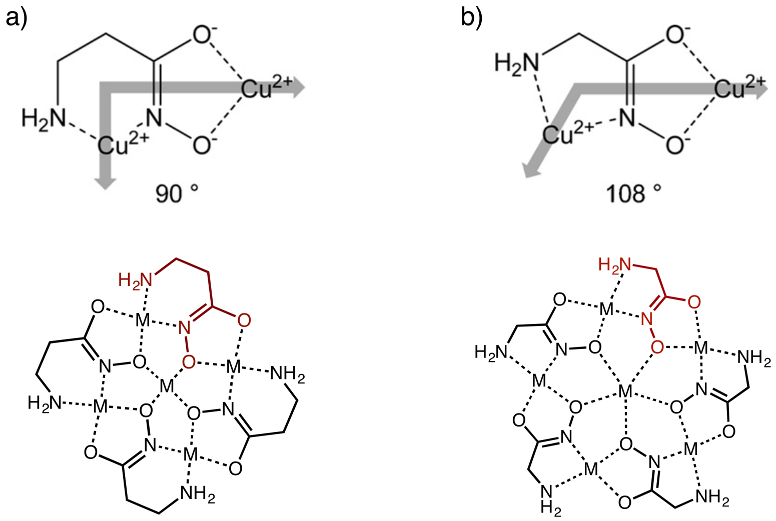

**Fig. 3.3**: Scheme depicting the geometric relation between the length of the spacer, the angles between the bisectors of the chelating systems and the topology of the metallacrowns obtained. (a) a β-aminohydroxamic acid originates a 12-MC-4; (b) an α-aminohydroxamic acid originates a 15-MC-5.

Numerous metallacrowns that respect the metallacrown structural paradigm have been isolated and presented in literature. These complexes showed very interesting properties as hosts for anions and cations, as complexes capable to interact with biomolecules, and as building blocks of porous materials. However, in recent years, significant research has focused on MCs which represent exceptions to the paradigm, as these complexes have been found to possess interesting luminescent and magnetic properties. However, while the MCs that observe the MC structural paradigm are in general planar, the ones constituting exceptions often adopt non-planar geometries, and in some cases have peculiar stoichoimetries.

Just as examples, the α-aminohydroxamic ligand picolinehydroxamic acid (Picha) forms 15-MC-5 complexes such as $[EuZn_5(picHA)_5]^{3+}$ (Fig. 3.4), $[EuCu_5(picHA)_5]^{3+}$ or $[EuNi_5(picHA)_5]^{3+}$ species, which differ for the nature of the peripheral metal ion. On the other hand, salicylhydroxamic acid can form 12-MC-4 species such as $[Cu_5(Shi)_4]^{2-}$ or $[Mn_5(Shi)_4]^{3+}$. All these species are paradigm-allowed metallacrowns, they exhibit rather planar structures, and they allow the proper fitting of either a lanthanide ion or a transition metal ion within their cavities of 5- or 4-fold symmery, respectively.

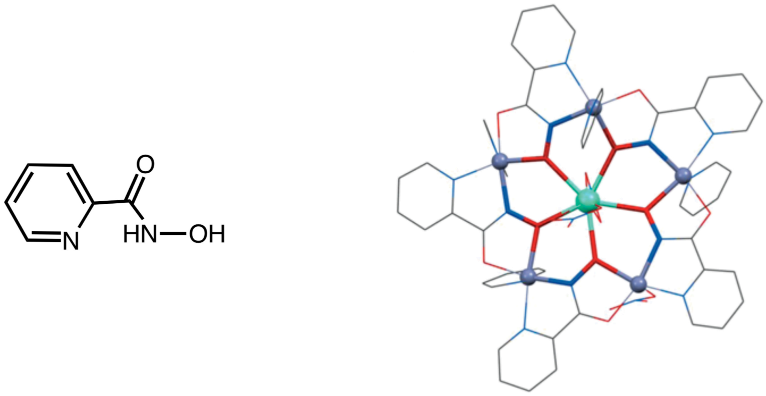

**Fig. 3.4**: Left, the α-aminohydroxamic ligand picolinehydroxamic acid (PicHA; right, the complex Eu(III)[15-MC$_{Zn(II),\ PicHA}$-5]$(NO_3)_3(Py)_4$.[6,7] The coordination ring is highlighted in bold. Colour scheme: aqua, Eu(III); purple; Zn(II); O, red; N, blue.

In fact, like their organic counterparts, MCs posses cavities of different size, and similarly to what happens for crown ethers, different cavity sizes induce selectivity towards metal guest of appropriate radius or, more often, as a function of the coordination preferences of the core metal.[8] This principle is best observed in 15-MC-5 complexes: the 15-MC-5 scaffolds appear frequently planar or almost planar, with all five of the hydroximate oxygen atoms on the same plane. With five hydroximate oxygen atoms in one plane, transition metal ions such as Cu(II) or Ni(II) are not ideally suited for the central cavity due to their smaller ionic radii and their preference towards only four ligand atoms on the equatorial plane. Therefore, this provides a benefit for lanthanide and actinide ions, which, due to their larger ionic radii, can accommodate within larger cavities. For example, the 15-$MC_{Cu(II)}$-5 structures with picHA are very well known complexes that bind cations such as Eu(III), Gd(III), $(U^{VI}O_2)^{2+}$, Y(III), Ag(I), Hg(II), and Pb(II). Similar 15-$MC_{Ni(II)}$-5 complexes have shown to bind Ln(III) ions such as Ce(III), Pr(III), Sm(III), Dy(III), Er(III)[9]. The inclusion of lanthanide ions within the scaffold is what triggers the interesting functional properties of MCs, such as luminescence and magnetism, and for these reasons that of lanthanide-metallacrowns is nowadays perhaps the most studied subclass of metallacrowns.

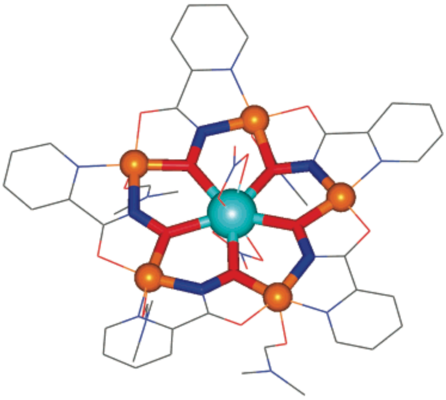

**Fig. 3.5**: Crystal structure of $Eu^{III}(NO_3)_2[15\text{-}MC_{Cu(II),\ PicHA}\text{-}5]^+(DMF)_4$.[3,10] The structure is the Cu(II)-based analogous of the complex reported in Fig. 3.4. Colour scheme: aqua - Eu(III), orange - Cu(II), red - oxygen, blue - nitrogen, grey - carbon. Hydrogen atoms and a $NO_3^-$ free counterion have been omitted for clarity.

Zinc(II) metallacrowns are just examples of MCs that do not follow the metallacrowns structural paradigm. Some zinc(II) MCs that do not respect the paradigm were isolated in the solid state: *i.e.* the homometallic species $[Zn_5(picHA)_4]^{2+}$ (Fig. 3.6) comprises an α-aminohydroxamate that gives rise to a 12-MC-4 species.[11] Furthermore, the interesting heterometallic analogue $[DyZn_4(picHA)_4]^{3+}$ and its sandwich relative $[DyZn_8(picHA)_8]^{3+}$,[11] are also species based on the 12-MC-4 scaffold constituted by the α-aminohydroxamic acid picHA and, thus, they infringe the "metallacrown structural paradigm" (Fig. 3.7). Notably, the complexes $[DyZn_4(picHA)_4]^{3+}$ and $[DyZn_8(picHA)_8]^{3+}$ show deeply domed structures, due to the side-on coordination they develop towards the lanthanide ion, whose larger ionic radius prevents the metal from penetrating into the cavity. Thus, the Dy(III) ion completes its 8-memeber square antiprismatic coordination geometry with 4 DMF molecules

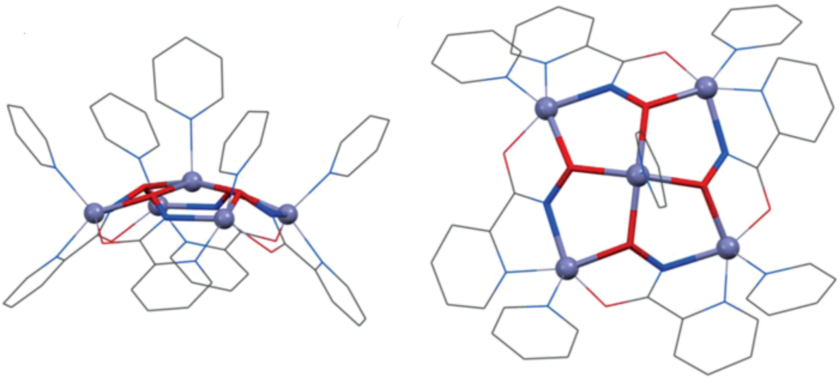

**Fig. 3.6**: Left, side view of the species $[Zn_5(picHA)_4]^{2+}$; right, top view.[11,12] Hydrogen atoms, counterions and unbound solvent molecules have been omitted. Colour scheme: purple - Zn(II), red - oxygen, blue - nitrogen, grey - carbon. Figure taken from reference [12].

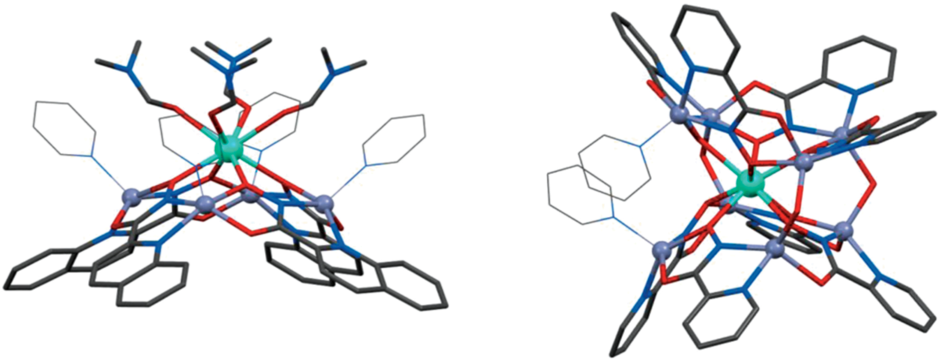

**Fig. 3.7**: Left, molecular structure of the complex $[DyZn_4(picHA)_4]^{3+}(DMF)_4(Py)_4$; right, crystal structure of the sandwich analogue $[DyZn_8(picHA)_8]^{3+}(DMF)_2$.[11] Hydrogen atoms, unbound counterions and solvent molecules were omitted for clarity. Colour scheme: aqua, Dy(III); purple, Zn(II); O, red; N, blue; C, grey. Figure taken from reference [12].

A wide range of metal ions can partake in the formation of MCs, from alkali metals to transition metals to lanthanides.[9] For this reason, MCs express a great potential as functional materials, as they can entail attractive features deriving from the electronic and nuclear properties of the enclosed metal species. Indeed, in the last decade MCs have shown interesting applications in the fields of ion sensing,[13–16] lanthanide luminescence[17,18] and molecular magnetism.[19] Although several of these systems are *3d-only* homometallic MCs[19–21], the encapsulation of lanthanides into MC scaffolds represents a potent tool to enhance or tailor functional abilities of the compounds, due to the peculiar luminescence and magnetic properties of *4f* ions. In fact, the class of *3d-4f* heterometallic MCs has so far shown interesting abilities, both for their luminescent and magnetic properties. For instance, heterometallic MC species of outstanding luminescence abilities were obtained with Ln(III)/Zn(II), where the emission characteristics were modulated by substituting the encapsulated Ln(III) ions.[17,18] Furthermore, several heterometallic 15-MC-5 species exhibited SMM properties, thanks to the great magnetoanisotropy possessed by lanthanide ions, which can boost magnetic behaviour (Fig. 3.8).[12]

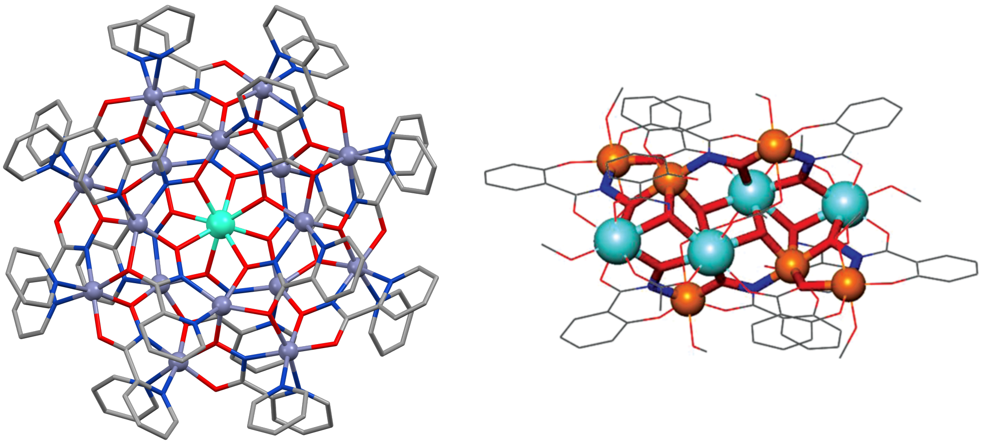

**Fig. 3.8**: Left, crystal structure of the luminescent complex $Tb^{III}[12\text{-}MC_{Zn(II),\ PicHA}\text{-}4]_2[24\text{-}MC_{Zn(II),\ PicHA}\text{-}8]^{3+}$.[17] Colour scheme: aqua, Tb(III); purple, Zn(II); O, red; N, blue; C, grey. Right, crystal structure of the SMM metallacrown $Ho^{III}{}_4Mn^{III}{}_6(H_2Shi)_2(Shi)_6(Sal)_2(OAc)_4(OH)_2(OMe)_8$.[22] Colour scheme: aqua, Ho(III); orange, Mn(III); O, red; N, blue; C, grey.

For instance, very recently two interesting *3d-4f* heterometallic systems were reported to form coordination polymers endowed with i) SMM metallacrown,[23] exhibiting a energy barrier of *circa* 40 K, or with ii) luminescence properties, able of differentiating small organic molecules.[24] Hence, heterometallic MC represent one of the widest and most promising classes of SMM yet known. A thorough review covering structural and functional aspects of *3d-4f* MCs was recently published by Pecoraro *et al*.[12]

The first heterometallic MC species was isolated back in 1996 and consisted in a fascinating *3d-5f* MC of Cu(II) and uranyl ion ($U^{VI}O_2^{2+}$).[25] The discovery of this first species led the way for the synthesis of all following *3d-4f* MCs compounds, after it was noticed in 1996 that Ln(III) would fit neatly within the core of 15-MC-5s, with the observation of a $Nd^{III}[15\text{-}MC_{Cu(II)}\text{-}5]$[26]. Since then, a large amount of mixed 3d-4f 15-MC-5 structures have been presented, leading this type of structure to being the most well studied of all MC topologies principally because, as discussed previously. they contain lanthanide ions.

Overall, we may state that the main reason behind the interest for metallacrowns goes beyond the mere solid state structural investigation of a complicated but highly symmetric class of molecules, but it rather lies in the confinement of several metal ions within a compact scaffold, ions that can be exploited for their numerous peculiar properties like magnetism and luminescence, which will be discussed here.

## 3.2 - Porous metallacrowns

The field of supramolecular chemistry has attracted great attention in the last three decades for the enormous number of applications foreseeable when a careful design of selective and robust interactions between active substrates is achieved. Thus, the focus of supramolecular chemistry ranges from the study of the interactions developed “beyond molecules”, to the design of new synthons and the exploitation of selected interactions, to finally obtain new functional materials and systems. Actually, by controlling the way and the forces through which substrates interact, supramolecular chemists focus their attentions on applications that range from molecular sensing, to electronics, to molecular machines. The general aim is to obtain substrates that exert specific task only when a target species is detected, from emitting radiations, to releasing compounds entrapped into their elaborate architectures, to promoting a desired reaction.

In the field of the supramolecular chemistry of MCs for obtaining porous materials, perhaps the most fascinating metallacrown typology has so far been that of Ln(III)[15-MC$_{Cu(II),(S\text{-}pheHA)}$-5]. In fact, metallacrowns often exhibited a particular type of chirality, deriving from the iso-orientation of the chiral R-aminohydroxamic acids ligands, to form the molecular scaffold. The disposition of chiral ligands around the metallacrown scaffold places all R groups on the same face of the merallacrown, providing what is known as “face differentiation” (Fig. 3.9). This R group orientation is enforced by the scaffold strict geometric requirements. An eventual flipping of the ligands is not allowed by the (M-N-O)$_n$ repetition. Therefore, by choosing enantiopure chiral ligands, enantiopure chiral face-differentiated metallacrowns can be synthesized.

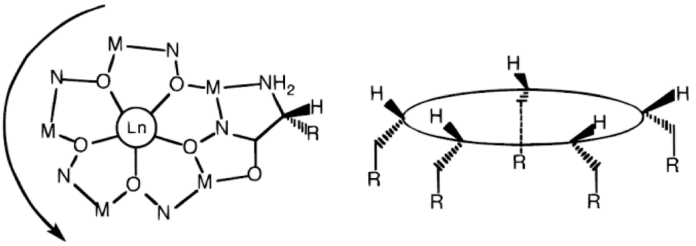

**Fig. 3.9**: Representation of the concept of face differentiation in 15-MC-5 complexes based on L-α-aminohydroxamic ligands.

Regarding the Ln(III)[15-MC$_{\text{Cu(II),(S-pheHA)}}$-5] metallacrowns, they can assemble in the solid state into different supramolecular architectures depending on the core lanthanide ion or on the crystallization solvents used. For instance, Ln$(NO_3)_{3-x}(OH)_x$[15-MC$_{\text{Cu(II), S-pheHA}}$-5] complexes crystallize in two different polymorphs, depending on solvent conditions. Using a 5:1 methanol:water solvent mixture is used for crystallization, a helical chain of MCs can be obtained.[27] In this helical structure, MCs are linked to each other by the carbonyl oxygen atom of a pheHA binding to a ring Cu$^{II}$ ion of an adjacent MC. The exterior of the helix is composed of the peripheral phenyl rings of the ligands side chains, and the interior surface of helix is composed of the hydrophilic MC coordination scaffold. Interestingly, the use of S-pheHA leads to the plus (P) helix, while the use of R-pheHA leads to a minus (M) helical chain (Fig. 3.10).

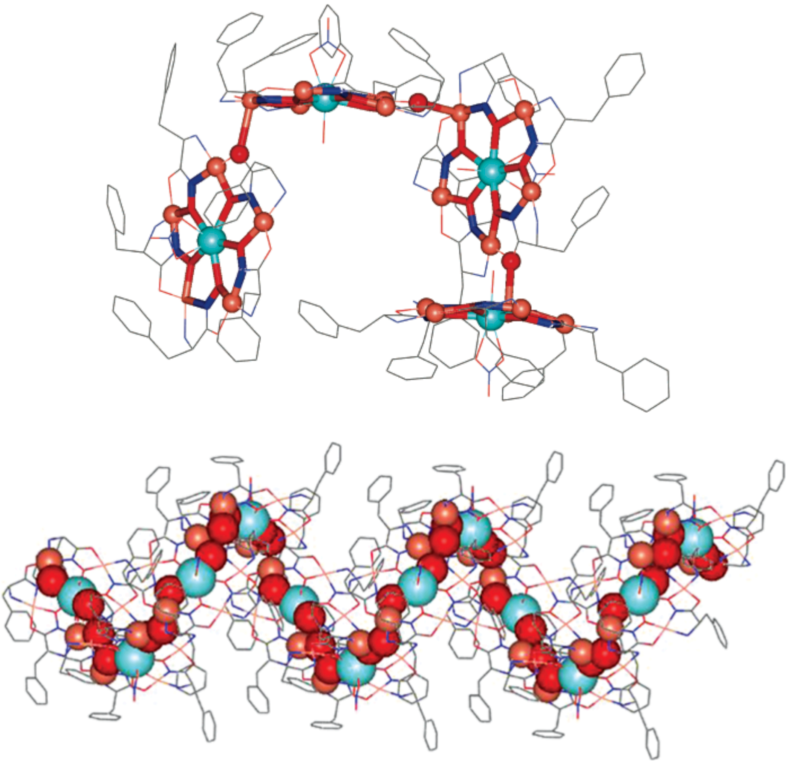

**Fig. 3.10**: Crystal structure of the complex Gd(III)$(NO_3)$[15-MC$_{\text{Cu(II), S-pheHA}}$-5]$^{2+}$.[28] above, the MC connectivity establishing the chain is shown; below, view of the helical chain. Hydrogen atoms, counterions and lattice solvent have been removed.

Colour scheme: aqua, Gd(III); orange, Cu(II); red, O; blue, N; grey, C. Figure taken from reference [3].

On the contrary, using water as the crystallization solvent, a second polymorph can be produced, constituting a dimer of MCs where the phenyl rings of the two MCs are directed toward each other and form a hydrophobic pocket. This so-called “hands-hands” compartment is capable of selectively binding guests.[15,16,29–31] Anion recognition is observed with such dimers, since aromatic dicarboxylates interact with the dimers in a different way with respect to saturated carboxylates. In general, aromatic carboxylates bind to the available axial positions of the metals on the hydrophobic face of the MC, while apliphatic ones preferentially bint to the hydrophilic face. As an example, aromatic dicarboxylate guests such as terephthalate bind to the central Ln(III) of two adjacent Ln(III)[15-$MC_{Cu(II),\ S\text{-}pheHA}$-5] from within the hydrophobic pocket, whereas bridging saturated dicarboxylates coordinate adjacent MCs from the hydrophilic face.[30]

However, a completely different behavior is observed when the pimelate anion (7-carbon extended saturated dicarboxylate) is used as the counter-anion for Ln-containing copper 15-MC-5. When reacting with Dy(III)[15-$MC_{Cu(II),\ S\text{-}pheHA}$-5], pimelate anion binds exceptionally in the hydrophobic compartment.[32] Interestingly, when the lanthanide ion is changed from Dy(III) to La(III) and La(III)[15-$MC_{Cu(II),\ S\text{-}pheHA}$-5] is reacted with a 7- or 8-carbon saturated dicarboxylate (respectively, pimelate or suberate), non-permanently porous MC architectures can be crystallized. In these structures, the saturated dicarboxylate guests bind selectively to the hydrophilic faces of the MCs, to form terameric aggregates. These tetramers hierarchically interact to form dimers of tetramers (octameric capsules), which in turn aggregate into trimers of octamers that represent the vertices of a honeycomb assembly (Fig. 3.11). In this architecture, 1D void channels of 24 Å section, which occupy 43% of the total unit cell volume, are present.

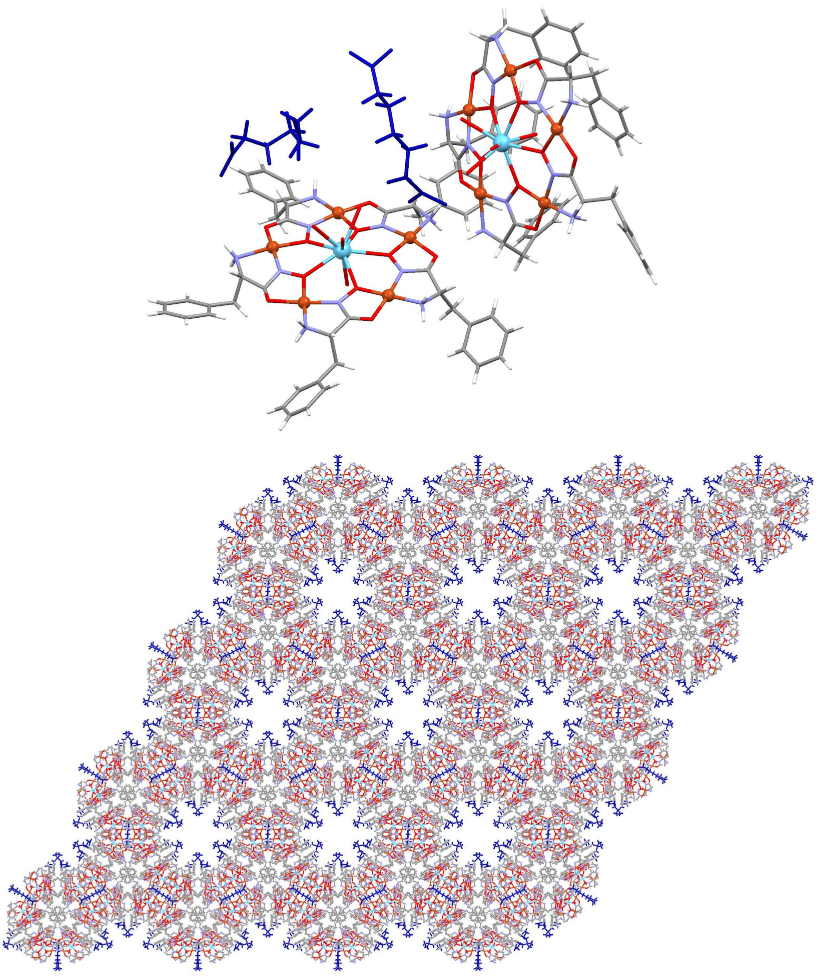

**Fig. 3.11**: Above, asymmetric unit of the compound $La^{III}(NO_3)_{2.5}$[15-$MC_{L\text{-}pheHA}$-5]$(pimelate)_2(OH)_{0.5}(H_2O)_{3.5}$,[32] which assembles supramolecularly to form the mesoporous honeycomb-like aggregate, represented below. The pimelate anions are coloured in purple. Colour scheme: aqua, La(III); orange, Cu(II); red, O; blue, N; grey, C.

## 3.3 - References

1 M. S. Lah and V. L. Pecoraro, *J. Am. Chem. Soc.*, 1989, **111**, 7258–7259.

2 V. L. Pecoraro, *Inorganica Chim. Acta*, 1989, **155**, 171–173.

3 G. Mezei, C. M. Zaleski, V. L. Pecoraro, G. Mezei†, C. M. Zaleski\textsection and V. L. Pecoraro*†, *Chem. Rev.*, 2007, **107**, 4933–5003.

4 M. Tegoni and M. Remelli, *Coord. Chem. Rev.*, 2012, **256**, 289–315.

5 B. R. Gibney, D. P. Kessissoglou, J. W. Kampf and V. L. Pecoraro, *Inorg. Chem.*, 1994, **33**, 4840–4849.

6 C. Y. Chow, H. Bolvin, V. E. Campbell, R. Guillot, J. W. Kampf, W. Wernsdorfer, F. Gendron, J. Autschbach, V. L. Pecoraro and T. Mallah, *Chem. Sci.*, 2015.

7 J. Jankolovits, J. W. Kampf and V. L. Pecoraro, *Polyhedron*, 2013, **52**, 491–499.

8 M. . Tegoni, M. . Furlotti, M. . Tropiano, C. S. . Lim and V. L. Pecoraro, *Inorg. Chem.*, 2010, **49**, 5190–5201.

9 G. Mezei, C. M. Zaleski and V. L. Pecoraro, *Chem. Rev.*, 2007, **107**, 4933–5003.

10 A. J. Stemmler, J. W. Kampf, M. L. Kirk, B. H. Atasi and V. L. Pecoraro, *Inorg. Chem.*, 1999, **38**, 2807–2817.

11 J. Jankolovits, J. W. Kampf and V. L. Pecoraro, *Inorg. Chem.*, 2014, **53**, 7534–7546.

12 C. Y. Chow, E. R. Trivedi, V. Pecoraro and C. M. Zaleski, *Comments Inorg. Chem.*, 2015, **35**, 214–253.

13 S. Rochat, Z. Grote and K. Severin, *Org. Biomol. Chem.*, 2009, **7**, 1147–1153.

14 J. Gao, Sè. Rochat, X. Qian and K. Severin, *Chem. - A Eur. J.*, 2010, **16**, 5013–5017.

15 J. T. Grant, J. Jankolovits and V. L. Pecoraro, *Inorg. Chem.*, 2012, **51**, 8034–8041.

16 J. Jankolovits, A. D. Cutland Van-Noord, J. W. Kampf and V. L. Pecoraro, *Dalton Trans.*, 2013, **42**, 9803–8.

17 J. Jankolovits, C. M. Andolina, J. W. Kampf, K. N. Raymond and V. L. Pecoraro, *Angew. Chemie Int. Ed.*, 2011, **50**, 9660–9664.

18 E. R. Trivedi, S. V Eliseeva, J. Jankolovits, M. M. Olmstead, S. Petoud and V. L. Pecoraro, *J. Am. Chem. Soc.*, 2014, **136**, 1526–1534.

19 P. Happ, C. Plenk and E. Rentschler, *Coord. Chem. Rev.*, 2015, **289-290**, 238–260.

20 C. M. Zaleski, E. C. Depperman, C. Dendrinou-Samara, M. Alexiou, J. W. Kampf, D. P. Kessissoglou, M. L. Kirk and V. L. Pecoraro, *J. Am. Chem. Soc.*, 2005, **127**, 12862–72.

21 C. M. Zaleski, S. Tricard, E. C. Depperman, W. Wernsdorfer, T. Mallah, M. L. Kirk and V. L. Pecoraro, *Inorg. Chem.*, 2011, **50**, 11348–52.

22 C. M. Zaleski, J. W. Kampf, T. Mallah, M. L. Kirk and V. L. Pecoraro, 2007, **45**, 1954–1956.

23 S. Zhang, H. Li, E. Duan, Z. Han, L. Li, J. Tang, W. Shi and P. Cheng, *Inorg. Chem.*, 2016, acs.inorgchem.5b02378.

24 G. Zeng, S. Xing, X. Wang, Y. Yang, D. Ma, H. Liang, L. Gao, J. Hua, G. Li, Z. Shi and S. Feng, *Inorg. Chem.*, 2016, acs.inorgchem.5b02193.

25 A. J. Stemmler, J. W. Kampf and V. L. Pecoraro, *Angew. Chemie Int. Ed. English*, 1996, **35**, 2841–2843.

26 A. J. Stemmler, A. Barwinski, M. J. Baldwin, V. Young and V. L. Pecoraro, *J. Am. Chem. Soc.*, 1996, **118**, 1196211963.

27 A. D. C.-V. Noord, J. W. Kampf and V. L. Pecoraro, *Angew. Chemie {(International} ed. English)*, 2002, **41**, 4667–4670.

28 C. M. Zaleski, E. C. Depperman, J. W. Kampf, M. L. Kirk and V. L. Pecoraro, *Inorg. Chem.*, 2006, **45**, 10022–10024.

29 J. Jankolovits, J. W. Kampf, S. Maldonado and V. L. Pecoraro, *Chemistry*, 2010, **16**, 6786–96.

30 A. D. Cutland, J. A. Halfen, J. W. Kampf and V. L. Pecoraro, *J. Am. Chem. Soc.*, 2001, **123**, 6211–6212.

31 J. Jankolovits, C.-S. Lim, G. Mezei, J. W. Kampf and V. L. Pecoraro, *Inorg. Chem.*, 2012, **51**, 4527–4538.

32 C.-S. Lim, J. Jankolovits, J. Kampf and V. Pecoraro, *Chem. Asian J.*, 2010, **5**, 46.

# Chapter IV

## *Metallacrowns as supramolecular building blocks for coordination polymers*

## 4.1 - Introduction

The chemistry of porous coordination polymers (PCPs), often referred to as metal-organic frameworks (MOFs), is a subject of extensive investigation due to interesting applications in gas absorption or purification, catalysis, luminescence and magnetism.[1–4] The use of metal-rich entities as building blocks in the assembly of PCPs is an approach that imparts solid structure functional properties which are derived from the specific molecular units (e.g. luminescence or slow magnetic relaxation).[5] In particular, PCPs are emerging as new sensing agents due to their porosity and to the convenient tunability of the metal or ligand-induced luminescence.[6,7]

Metallacrowns (MCs) can be described as self-assembled metallamacrocycles, and are the inorganic analogues of crown ethers. Both classes of compounds have the ability to coordinate various metal ions in their central cavity, ranging from transition to main group metals to larger lanthanide ions.[8,9] Due to the confinement of a large number of metal ions within a stable molecular environment, MCs are promising precursors of advanced materials and probes, which utilize the electronic, optical and magnetic properties of the metal ions contained. For instance, MCs containing NIR-emitting lanthanides have been shown to display outstanding quantum yields and lifetimes, which opens up the possibility for applications such as *in-vivo* imaging.[10,11] Additionally, in the field of magnetism, several MCs have been reported to exhibit single-molecule magnet behaviour.[12–19] With this in mind, we were attracted by the possibility of combining the versatile properties of MC scaffolds together with the functional chemistry of PCPs. The resulting hybrid solids may potentially have interesting properties suitable for applications ranging from the field of guest-responsive luminescent sensors and materials to the field of advanced magnetic materials.

MCs are solution stable in a wide range of conditions,[8,20,21] and can be easily isolated in the solid state. Nevertheless, only a few examples of extended frameworks[22–28] or supramolecular architectures[29–32] composed of MC units have been reported to date. Furthermore, none of these compounds display the permanently porosity which is typical of porous coordination polymers. One reason for the lack of porosity is the fact that MCs are often linked through ditopic bridging ligands (*e.g.* dicarboxylates), which coordinate to the axial position of the metal ions in the MC framework.[24,29,33,34] This type of connection favors the formation of chains of MC, which tend to come in close proximity to each other, therefore reducing the void space necessary for significant porosity (Fig. 4.1).

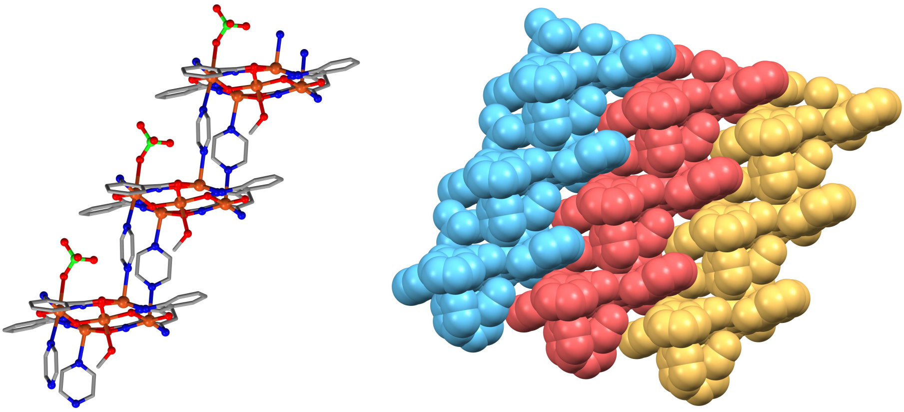

**Fig. 4.1**: Left, monodimensional molecular chain of $\{[Cu_5(L)_4(pz)_2(MeOH)_3](ClO_4)_2MeOH\}_n$, where L = 2-(amino)phenylhydroxamic acid and pz = pyrazine;[24] the unbound perchlorate ion was removed for clarity. Colour scheme: Cu(II), orange; Cl, green; N, blue; O, red; C, grey. Right, supramolecular packing of the 1D-chains represented in *spacefill* view; each chain is represented in a different colour; no voids are present in the packing.

Two examples are known of multidimensional coordination polymers formed by the linkage of MCs through functions placed on the periphery of the molecular framework, although no porosity has been observed for either one of the lattices.[22,23] On the other hand, lattices with porous-like features have been shown in a few examples of supramolecular aggregates of MCs that are held together by weak interactions.[30–32] Despite the pseudo-porosity of these assemblies, the interactions established in these architectures do not provide wide pores or sufficient structural stabilization for the lattices to exhibit significant gas uptake properties. Also, the pseudo-porous nature of these extended frameworks followed from a quite unpredicted spatial arrangement of the MC units, rather than from the rational design and control of the interactions established between the building blocks.

The idea of constructing 2D networks by linking MC units using metal ions as spacers coordinated to the peripheral side arms was first introduced by Pecoraro and co-workers back in 2000.[35] The design was conceived after the isolation of 1D chains of {Cu(II)[12-MC$_{\text{Cu(β-Pheha)}}$-4]}$^{2+}$ connected by a paddlewheel [Cu(II)(benzoate)$_4$] unit to the peripheral carbonyl oxygens of two neighbouring metallacrowns (Fig. 4.2).[22]

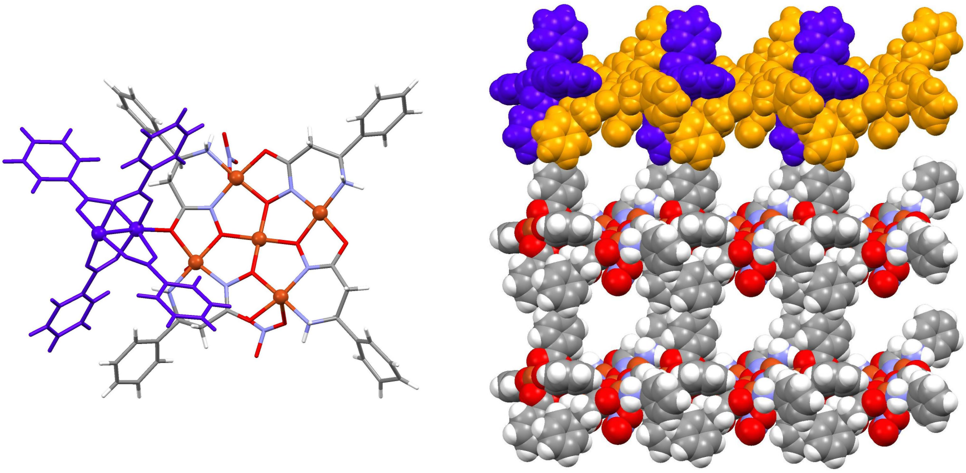

**Fig. 4.2**: Left, asymmetric unit of the compound {Cu(II)[12-MC$_{\text{Cu(II), β-PheHA}}$-4][Cu$_2$(benzoate)$_2$]}$_n$, where β-PheHA = β-phenylalaninehydroxamic acid.[22] The *paddlewheel* unit is coloured in violet. Right, supramolecular packing of the 1D chains obtained by the polymeric repetition of the asymmetric unit. One chain is highlighted (violet = *paddlewheel*, yellow = 12-MC-4). Colour scheme: Cu(II), orange; N, light blue; O, red; C, grey; H, white.

It was suggested that 2D networks could be generated by connecting MC units using solely metals as bridges between properly functionalized peripheral side arms (Fig. 4.3).[35] However, to the best of our knowledge, only one example of an extended structure where the MC units are bridged by a metal ion has been published.[23] Unfortunately, this example resulted in a tightly packed, non-porous structure. In this assembly, the donor atom on the MC is the carboxylato group of the malonohydroxamic acid required for the formation of the MC scaffold, which only serendipitously coordinates potassium countercations. Therefore, the rational design and the isolation of porous extended structures where MCs are linked by metal ions through intended heteroatom ligands on the MC periphery has been elusive.

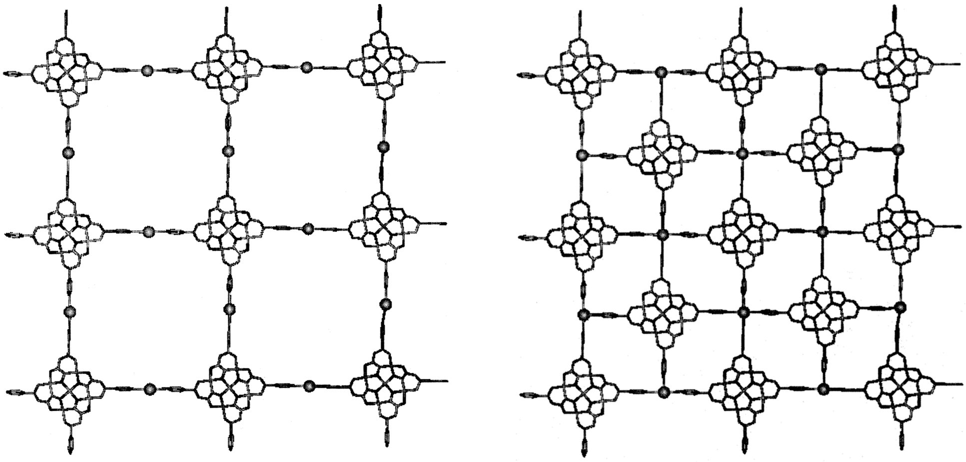

**Fig. 4.3**: Scheme of two-dimensional coordination networks made of metallacrowns linked by two-coordinate (left) or four-coordinate square planar (right) metal ions, conceived by Bodwin in the early 2000's.[35]

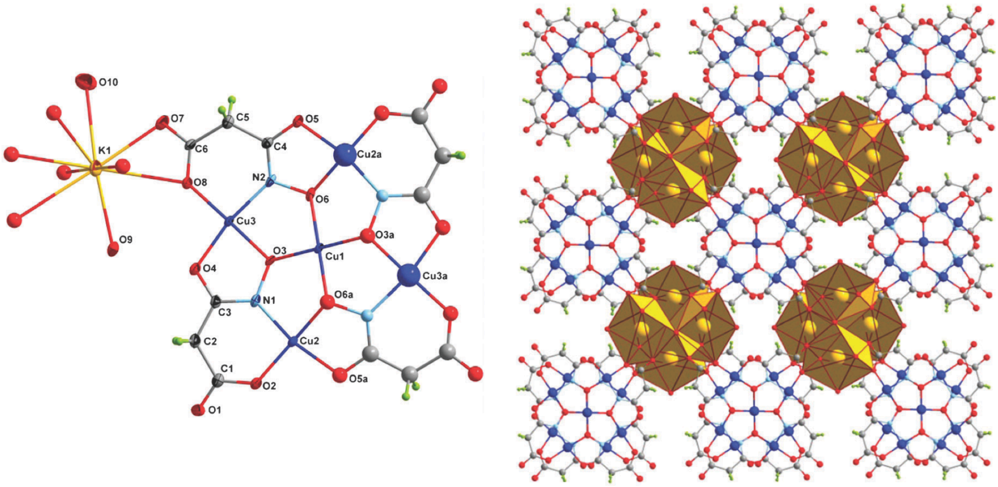

**Fig. 4.4**: Left, monomeric unit of compound $\{[K(H_2O)_2]_2[Cu_5(mmh)_4]\}_n$, where mmh = malonomonohydroxamic acid. Right, the 2D coordination network formed by the crystal packing of the complex, viewed along *c* axis.

Herein, we present two novel MC networks, one of which constitutes the first permanent PCP made of metallacrowns, resistant to solvent evacuation and capable of absorbing gas.[36] In this architecture, 12-MC-4 units were assembled using copper(II) and a pyridinic analogue of salicylhydroxamic acid as ligand (Fig. 4.5**a**). We aimed to connect these MC units to metal ion bridges in a chessboard-like four-fold arrangement, through in-plane coordination bonds (Fig. 4.5**b**). Hence, the ligand was designed to provide the MC with pyridine-like moieties pointing towards the exterior of the scaffold, apt to form peripheral coordination bonds. These interactions were sought to impose proper distance between MC units in order to generate voids within the lattice.

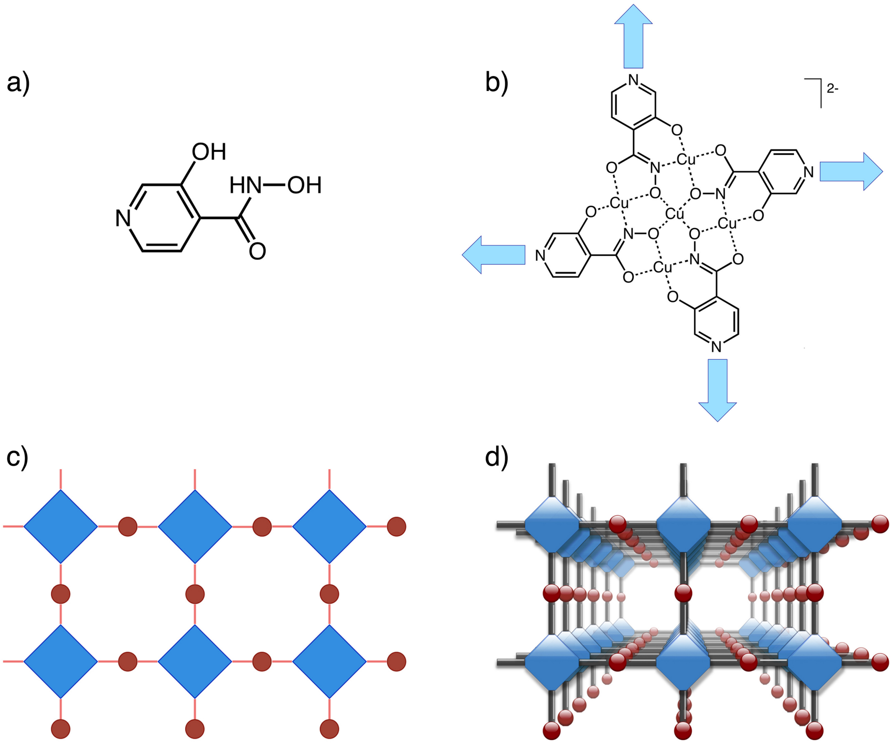

**Fig. 4.5**: (a) Scheme of the designed ligand hinHA; (b) scheme of the resulting $\{Cu(II)[12\text{-}MC_{Cu(II),\ hinHA}\text{-}4]\}^{2-}$, the blue arrows display the directions of secondary coordination, through which extended architectures sought for; (c) scheme of the idealized *chessboard-like* 2D network obtained with connecting metal nodes (blue squares: MC units; red dots: connecting metal ions); (d) scheme of a porous architecture formed by three-dimensional assembly of single layers of network.

## 4.2 - Experimental Section

### 4.2.1 - Materials and methods

All reagents and solvents were obtained from commercially available sources and were used without further purification. Inert atmosphere was achieved in $N_2$ using Schlenk techniques. Flash column chromatography was performed using silica gel (230-400 mesh) from Sigma-Aldrich. $^1H$ and $^{13}C$ NMR spectra were recorded on Varian MR400 and Vnmrs500 spectrometers using standard pulse sequences. Chemical shifts were referenced to residual solvent protons. Infrared spectra were recorded on a Perkin-Elmer FTIR Nexus spectrometer using a Smart Orbit HATR accessory equipped with a diamond crystal. Electrospray ionization mass spectra (ESI-MS) were collected on a Micromass LCT TOF electrospray ionization mass spectrometer. Capillary voltage 3.0 V and negative cone voltage of -40 V (ESI- ion mode) were used. Desolvation temperatures were set at 150 °C for methanolic solutions, and 200 °C for solutions in DMF. Samples (40 µM) were injected through direct infusion using a syringe pump at 10 µl/min, and the spectra recorded in full scan analysis mode in the range 100-2000 m/z. Elemental analysis (C, H, N) were performed by Atlantic Microlab, Inc. (Atlanta, GA, United States). Thermogravimetric analysis was performed on a Perkin-Elmer TGA-7 thermogravimetric analyzer using a temperature ramp rate of 5 °C/min from 50 to 700 °C, under a $N_2$ flow of 20.0 mL/min. Differential scanning calorimetry was performed on a Perkin-Elmer DSC-6000 analyzer equipped with Intracooler, with a temperature ramp rate of 5 °C/min from 20.0 °C to either 200 or 400°C, under a $N_2$ flow of mL/min.

### 4.2.2 - X-ray Crystal Determination

Crystals of dimensions 0.23 × 0.23 × 0.16 mm of **1**, or crystals of dimensions 0.10 × 0.10 × 0.02 mm of **2** were mounted on a Rigaku Saturn944+ CCD-based X-ray diffractometer equipped with a low-temperature device and fine-focus Cu-target

X-ray tube (λ = 1.54187 Å). The X-ray intensities were measured at 85(2) K; A total of 107642 and 80642 reflections were collected for **1** and **2**, respectively. The frames were integrated with the CrystalClear-SM Expert 2.0 Rigaku software package. The structures were solved and refined with the Bruker SHELXTL (version 2008/3) software package.[37] In **1**, the data collection was considerably affected by the poor crystal quality, and several restraints were used to model the hydroxamate moieties. The pyridine ring bound to the central metal was found disordered in two positions. The pyridine and acetate moieties of the peripheral copper atom were also statically disordered over two sites. The disordered fragments were refined with isotropic thermal parameters. The residual electron density found into the structural cavities was treated with the SQUEEZE program.[38] In **2**, on one of the metal centers a dmso/pyridine moiety was found disordered. These coordinated molecules were refined with site occupancy factors (s.o.f.) of 0.7 (dmso) and 0.3 (pyridine). In the lattice, solvent of crystallization was present and it could be tentatively located from the difference fourier map as pyridine and dmso molecules. The hydrogen atoms placed in idealized positions. Additional details are presented in Table S1 and are given as supporting information in a CIF file.

### 4.2.3 - Ligand synthesis

The synthesis of hinHA was modified from a previously reported route for the synthesis of hydroxamic acids.[39]

*Synthesis of N-(benzyloxy)-3-hydroxyisonicotinamide (**BzOhinHA**):*
3-hydroxy-4-pyridinecarboxylic acid (5.42 g, 38.99 mmol) and *N,N*-diisopropylethylamine (13.58 mL, 77.98 mmol) were mixed in 150 mL of dry $CH_2Cl_2$ in a two-necked round bottom flask under nitrogen atmosphere. Solid carbonyldiimidazole (6.64 g, 40.94 mmol) was added and the solution was kept stirring under nitrogen atmosphere for 3h at room temperature. Solid *O*-benzylhydroxylamine hydrochloride (6.53 g, 40.94 mmol) was added and the solution heated under reflux for 8 hours under stirring. The solvent was evaporated *in vacuo* yielding a dark red oil, which was diluted with 10 mL of distilled water. The solution was acidified to pH = 5 with a 5 M solution of acetic acid, and left at 4 °C overnight. The pink precipitate was filtered, washed with 5 mL of cold water, and dried under vacuum. The product was purified through silica column

chromatography using $CH_2Cl_2$/MeOH 95/5 as the eluent. The pure product was isolated as a yellow powder (6.45 g, 68%). $^1$H NMR (500 MHz, $CD_3OD$) δ: 8.20 (s, 1H), 8.04 (d, J = 5.2 Hz, 1H), 7.72 (d, J = 5.2 Hz, 1H), 7.52 – 7.46 (m, 2H), 7.44 – 7.33 (m, 3H), 4.87 (s, 3H). IR (cm$^{-1}$): 3086w, 3025w, 2926w, 2860w, 1634m, 1579m, 1524m, 1493m, 1454m, 1438m, 1377m, 1352m, 1310s, 1237m, 1218m, 1203m, 1160m, 1139w, 1096w, 1080w, 1004s, 916m, 870m, 830s, 781s, 754s, 699s, 683s. Anal. calc. for $C_{14}H_{13}N_2O_3$: C, 63.93; H, 4.95; N, 11.47; found: C, 63.8; H, 4.9; N, 11.5%. ESI+: *m/z* calc. for [M - H$^+$] = 243.1; found = 243.0.

*Synthesis of 3-hydroxyisonicotine hydroxamic acid (***hinHA***)*:
*N*-(benzyloxy)-3-hydroxyisonicotinamide, **BzOhinHA**, (1.00 g, 4.09 mmol) was dissolved in 5 mL of $CH_2Cl_2$, diluted with 350 mL of degassed MeOH, and hydrogenated in the presence of Pd/C (10%, 200 mg) under $H_{2(g)}$ ($p_{H2}$ = 1 atm) for 24 hours. The product precipitated out, and it was separated from the catalyst by washing the solid with 150 mL of hot methanol. The solvent was removed *in vacuo* and the product purified by recrystallization in 8 mL of 2:1 acetone:methanol, affording a white precipitate (0.50 g, 80%). $^1$H NMR (400 MHz, $D_2O$) δ: 7.60 (s, 1H), 7.36 (d, J = 5.1 Hz, 1H), 7.20 (d, J = 5.1 Hz, 1H). IR (cm$^{-1}$): 3126w, 3080w, 2572s(br), 2111m, 1646s, 1619s, 1591m, 1506s, 1444s, 1380s, 1310m, 1252s, 1182s, 1154m, 1080m, 1050m, 1016s, 959m, 901s, 870s, 836m,818s, 769s, 705m, 638s, 583s, 573s, 543s. Anal. calc. for $C_6H_6N_2O_3$: C, 46.76; H, 3.92; N, 18.18; found: C, 46.8; H, 4.0; N, 18.0%. ESI- (negative ion mode): *m/z* calc. for [M - H$^+$] = 153.0; found = 153.0.

*Synthesis of network* $\{[Cu(II)(AcO)Py]_2\{Cu(II)[12\text{-}MC_{Cu(II),\ hinHA}\text{-}4]\}\}_n$ (**1**):
The ligand **hinHA** (20 mg, 0.13 mmol, 4 eq.) was dissolved in a 2:1 DMF:pyridine (20:10 mL) mixture. A solution of copper(II) acetate monohydrate (45 mg, 0.23 mmol, 7 eq.) in 2:1 DMF:pyridine (20:10 mL) was added under stirring. The mixture immediately turned green, due to the formation of the 12-MC-4 species. After 30 minutes under stirring, the suspension was filtered to remove insoluble impurities, and the product left to crystallize by slow evaporation into test tubes in a fume hood. Green rods suitable for single-crystal X ray diffraction were obtained over the course of two weeks. IR (cm$^{-1}$): 3284w(br), 1652m, 1564s, 1487m, 1420s, 1380s, 1331s, 1236s, 1191m, 1111w, 1072m, 1026s, 959s, 888m, 815m, 702s, 680s, 656s, 607s. ESI-MS (on mother solution): *m/z* calc. for $\{Cu(II)[12\text{-}MC_{Cu(II),\ hinHA}\text{-}4]\}^{2-}$ = 460, found = 460; *m/z* calc. for $[\{Cu(II)[12\text{-}MC_{Cu(II),\ hinHA}\text{-}4]\}^{2-} + Na^+]^-$ = 943, found = 943.

### *Synthesis of* $\{(NEt_4)_2\{Cu(II)[12\text{-}MC_{Cu(II),\ hinHA}\text{-}4](DMSO)_{1.4}(Py)_{0.6}\}(DMSO)_{0.4}(Py)_{0.6}\}_n$ (**2**):

ligand **hinHA** (40 mg, 0.26 mmol, 4 eq.) was dissolved in 6 mL of a 3:2:1 DMSO:DMF:pyridine solution. Solid tetraethylammonium acetate (204 mg, 0.78 mmol, 12 eq.) and copper(II) triflate (106 mg, 0.32 mmol, 1.25 eq.) were added under stirring. Insoluble impurities were removed by filtration and the solution was left in a closed vessel at 0 °C yielding green crystalline plates of the product over the course of three weeks. Crystals have low stability out of the mother liquors. X-ray diffraction data were collected at low temperature. ESI-MS: *m/z* calc. for $\{Cu(II)[12\text{-}MC_{Cu(II),\ hinHA}\text{-}4]\}^{2-}$ = 460, found = 460.

## 4.3 - Results and Discussion

The ligand $H_3$hinHA (3-hydroxyisonicotine hydroxamic acid), was synthesized in moderate yields from a commercially available carboxylic acid precursor using activation-deprotection strategies, Fig. 4.6 (see Supporting Information). The reaction of copper(II) salts with $H_3$hinHA selectively provided a $\{Cu(II)[12\text{-}MC_{Cu(II),\ hinHA}\text{-}4]\}^{2-}$ species (Fig. 4.7), as observed by ESI-MS (Fig. 4.8).

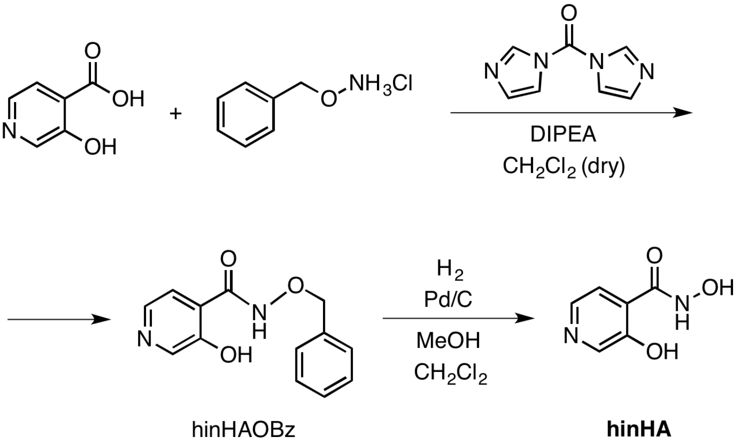

**Fig. 4.6**: Synthetic strategy for the synthesis of hinHA.

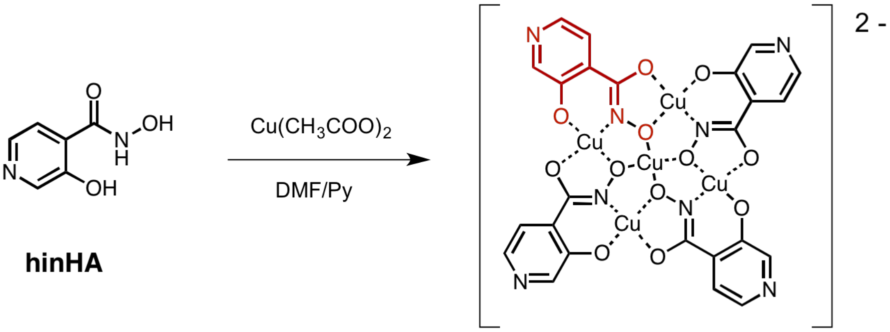

**Fig. 4.7**: Scheme of the synthesis of $\{Cu(II)[12\text{-}MC_{Cu(II),\ hinHA}\text{-}4]\}^{2-}$.

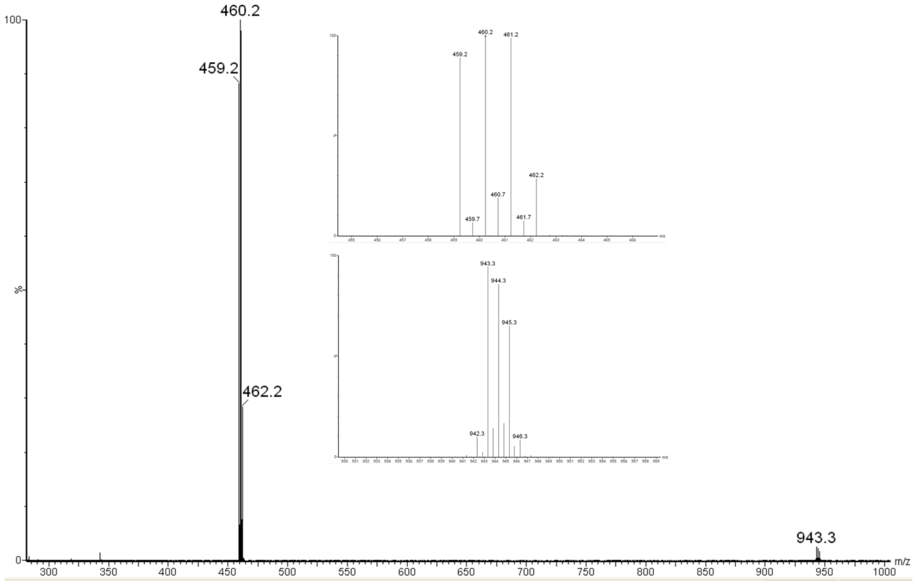

**Fig. 4.8**: Negative-ion ESI-MS spectrum of the mother solution of **1**, before crystallization. $\{Cu(II)[12\text{-}MC_{Cu(II),\ hinHA}\text{-}4]\}^{2-}$: *m/z* 460.2; $Na\{Cu(II)[12\text{-}MC_{Cu(II),\ hinHA}\text{-}4]\}^{-}$: 943.3 *m/z*. The observed isotopic distribution of the signals is reported in the insect.

Network **1** was isolated by reacting $H_3$hinHA with copper(II) acetate in a 1:1.75 ratio in a dilute 2:1 DMF:Pyridine solution, followed by slow evaporation of the solvent. The structure is composed of stacked two-dimensional coordination networks with the formula $\{[Cu(II)(AcO)Py]_2\{Cu(II)[12\text{-}MC_{Cu(II),\ hinHA}\text{-}4]\}\}_n$. As shown in Fig. 4.9, single units of the $\{Cu(II)[12\text{-}MC_{Cu(II),\ hinHA}\text{-}4]\}^{2-}$ metallacrown are bridged by additional Cu(II) ions coordinated to the peripheral pyridinic moieties of two neighbouring MC units. The bridging Cu(II) nodes have the formula $[Cu(II)(AcO)Py]^{+}$; with their coordination geometry being described as distorted square planar, where the two MC pyridinic moieties coordinate in a *trans* fashion with the first coordination sphere completed by a monodentate acetate ion and a solvent pyridine molecule (Fig. 4.9**a**). The result is the formation of a chessboard-like arrangement of 12-MC-4 units, in which the voids have a rectangular shape. Interestingly, each layer is not planar, but rather has a wave-like appearance as the result of the bowl-shaped MC subunits. In the MC unit, each of the five Cu(II) ions is coordinated apically by one solvent molecule of pyridine ($d_{Cu\text{-}Py}$ = 2.30 Å), and exhibits a distorted square pyramidal coordination geometry (Fig. 4.10). Due to steric interactions, the four ring ions are all coordinated by the pyridine molecules on the MC convex face, while the central copper(II) ion is coordinated by the fifth pyridine on the opposite face (Fig. 4.10**b**).

Although no comparison with similar structures is possible, it is intriguing to note that the zinc(II) and nickel(II) 12-MC-4 with Picha and Quinha present coordinated pyridines.[40] While for nickel the number of coordinated pyridines is nine (two for each peripheral metal, one for the core metal), in the zinc(II) complexes all metals are five coordinated with one bound pyridine. However, in the latter MC all pyridines are on the same side of the MC resulting into a very bowl-shaped complex.[40] On the contrary, in **1** the central pyridine coordinated to the core copper on the opposite face with respect to the remaining four mitigates this distortion from planarity.

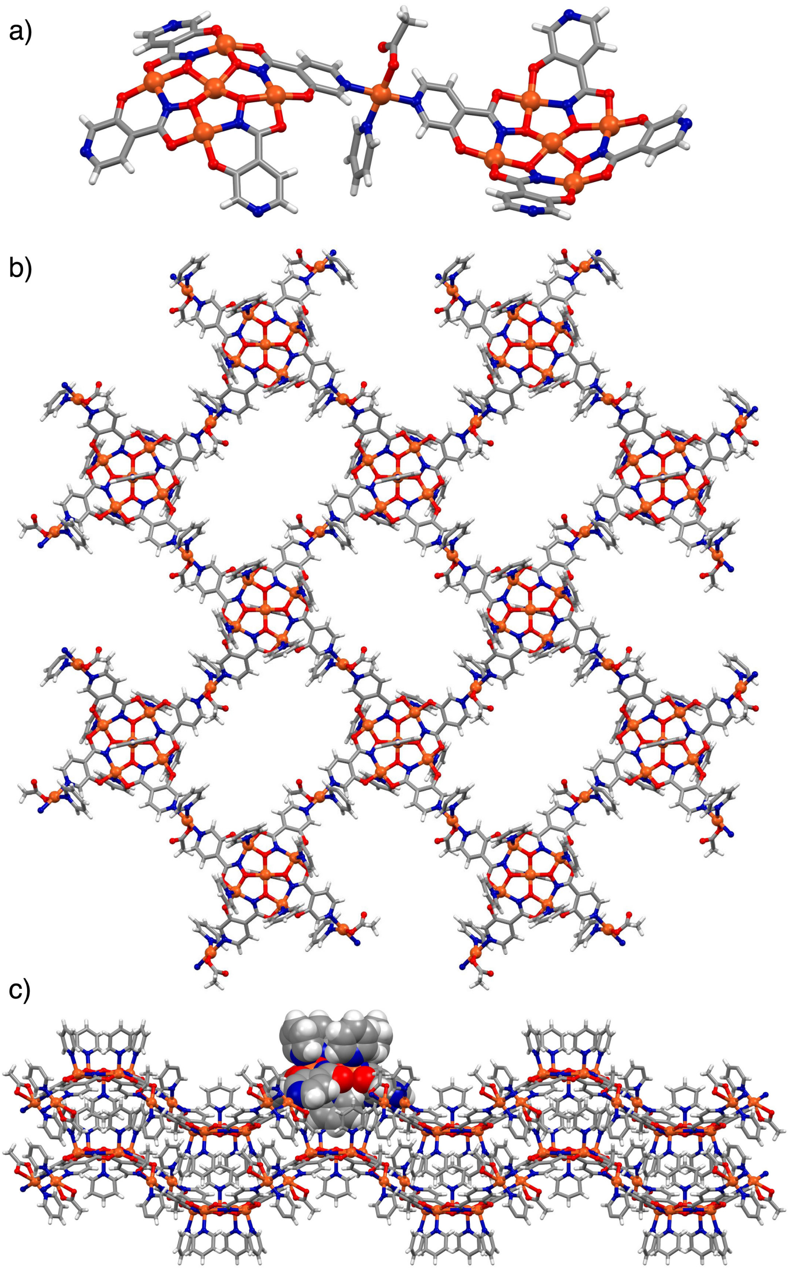

**Fig. 4.9**: (a) Ball and stick viewed of two $\{Cu(II)[12\text{-}MC_{Cu(II),\ hinHA}\text{-}4]\}^{2-}$ units connected by a bridging $[Cu(II)(AcO)Py]^{+}$ unit (solvent molecules on the 12-MC-4 scaffold have been omitted for clarity). (b) One layer of the porous network, viewed along the c-axis. (c) Side view along *a,b* plane of the wave-like network; one MC unit is shown in spacefill representation. Colour scheme: Cu(II), orange; N, blue; O, red; C, grey.

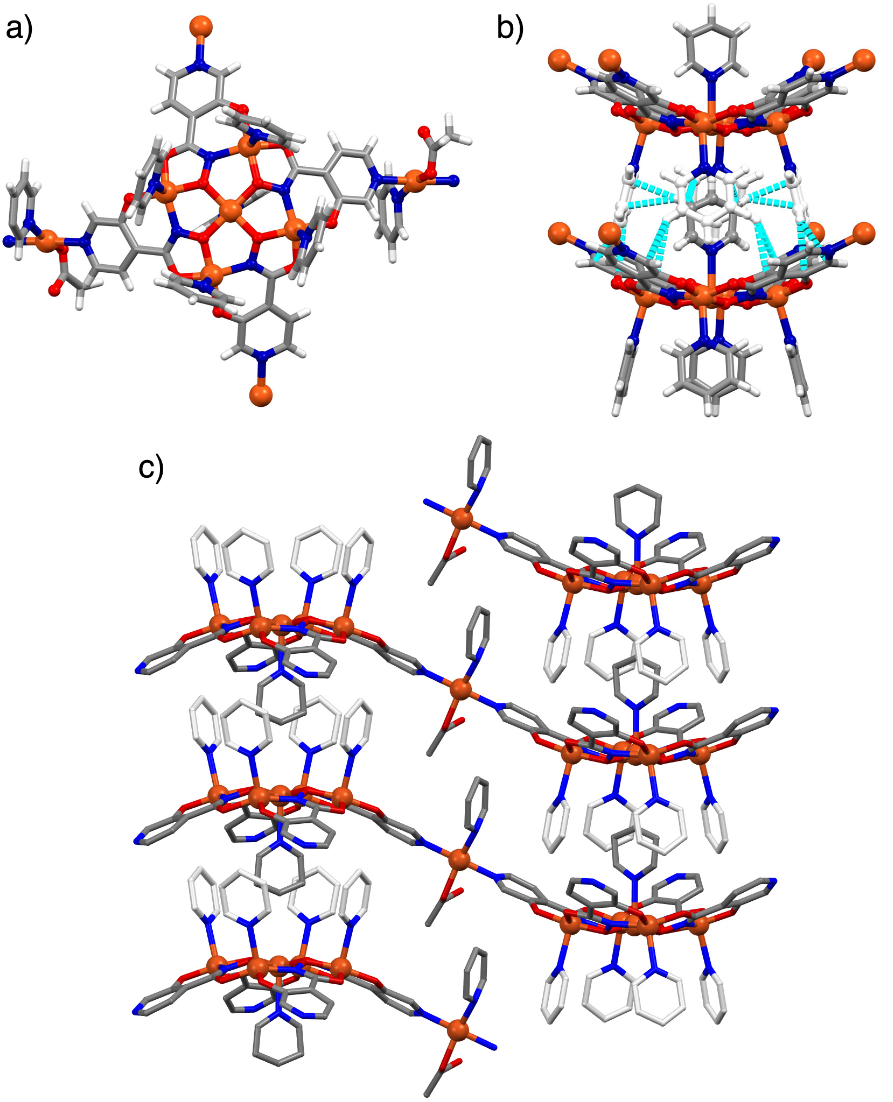

**Fig. 4.10**: (a) Representation of a single MC unit showing the peripheral Cu(II) ions acting as linkers between the units, viewed along the *c* crystallographic axis. Copper ions are represented as orange spheres; (b) Hydrophobic interactions (cyan) between two stacked MC units. The encapsulation of a coordinated pyridine molecule within the hydrophobic pyridinic pocket of a neighbouring MC is represented; (c) Representation of stacked MCs of different layers, view parallel to the c axis. Colour scheme: Cu(II), orange; N, blue; O, red; C, grey; H, white.

One structural consequence of this pyridine distribution is the disruption of planarity, leading, as discussed, to the bowl shape of the MC units. Furthermore, by removal of planarity, the prochiral MC units become chiral as one can distinguish the rotation of the MC ring $(Cu\text{-}O\text{-}N)_4$ cyclic repetition with respect to the concave or convex face of the molecule, leading to the observation of a "clockwise" and of an "anticlockwise" isomer.[41] Since the crystal lattice is formed by the wave-like repetition of only one of the two so formed enantiomers (Fig. 4.11), this gives rise to a homochiral coordination polymer, which crystallizes in the chiral space group $P42_12$.

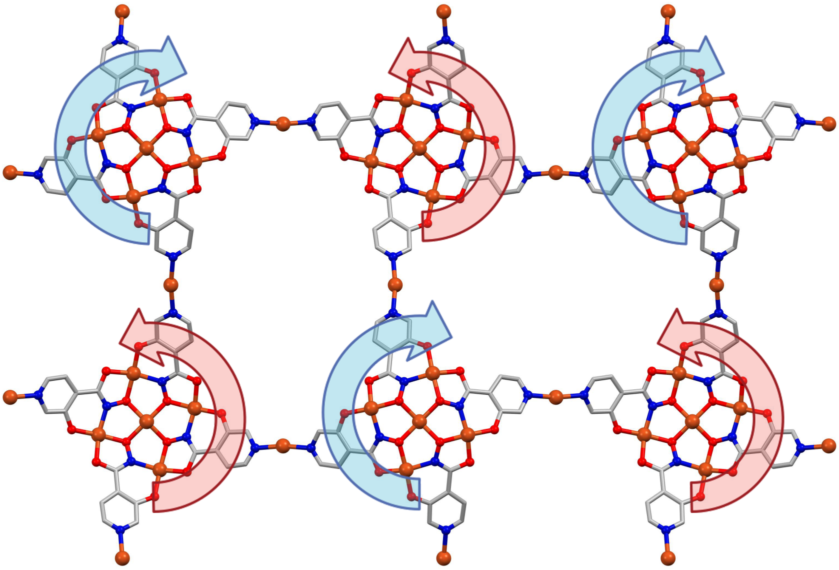

**Fig. 4.11**: Representation of the 2D layer of metallacrowns. Clockwise (blue) or anticlockwise (red) repetition of the Cu-O-N connectivity is represented. Colour scheme: Cu(II), orange; N, blue; O, red; C, grey; H, white.

The most important consequence of the solvent arrangement is that the four pyridine molecules coordinated to the same face of one MC form an aromatic pocket which encapsulates the lone pyridine of the neighbouring 2D layer (Fig. 4.10**b**). The columnar stacking of interpenetrated pyridines creates π -π pillars, which provide stability to the assembly and allow the rectangular void spaces of each layer to be perfectly stacked, one above the other, to form void channels that run along the entire crystal (Fig. 4.13). Since the charge balance is provided by the bridging [Cu(II)(AcO)Py]$^+$ units, no extra counter ions, which potentially may occupy the void spaces, are required. By taking into consideration the Van der Waals radii, the estimated channel cross section measures 12.6 x 8.9 Å$^2$, accounting for 36% of the total unit cell volume, as estimated by PLATON.[42] Channels are filled by disordered solvent molecules, which can be removed by thermal treatment of the solid at moderate temperature, without loss of crystallinity.

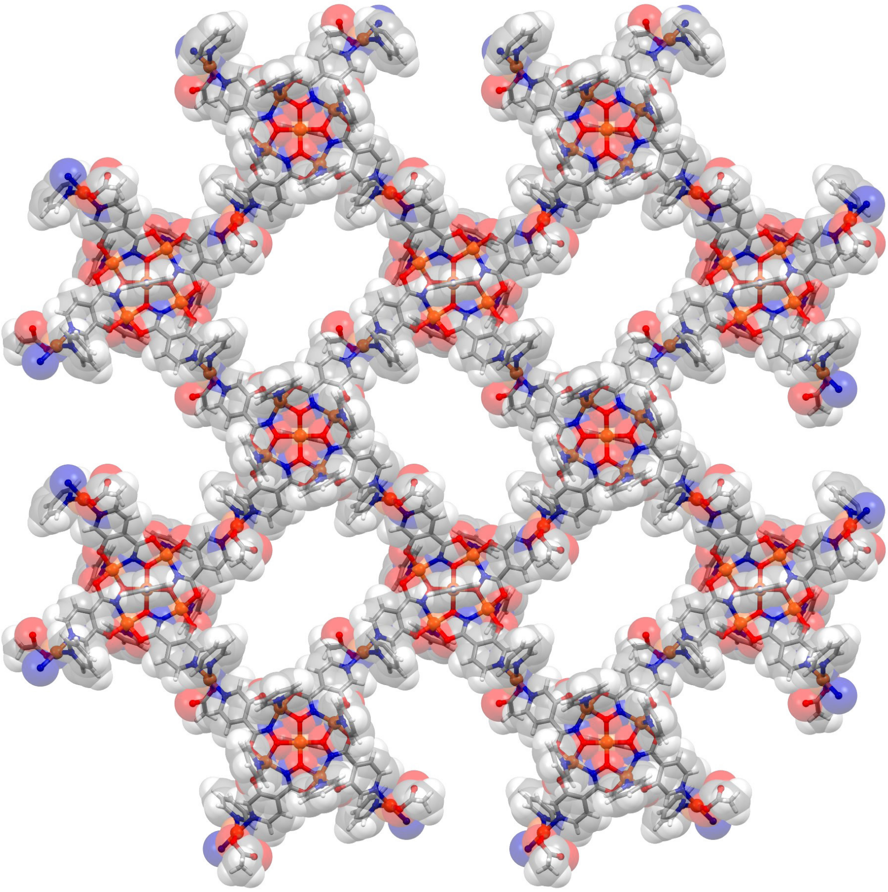

**Fig. 4.12**: *Spacefill* representation of one layer of the porous network **1**, viewed along the *c*-axis. Taking into consideration Van der Waals radii, the 2D pore section measures 12.6 x 8.9 Å$^2$, accounting for 36% of the total cell volume. Colour scheme: Cu(II), orange; N, blue; O, red; C, grey; H, white.

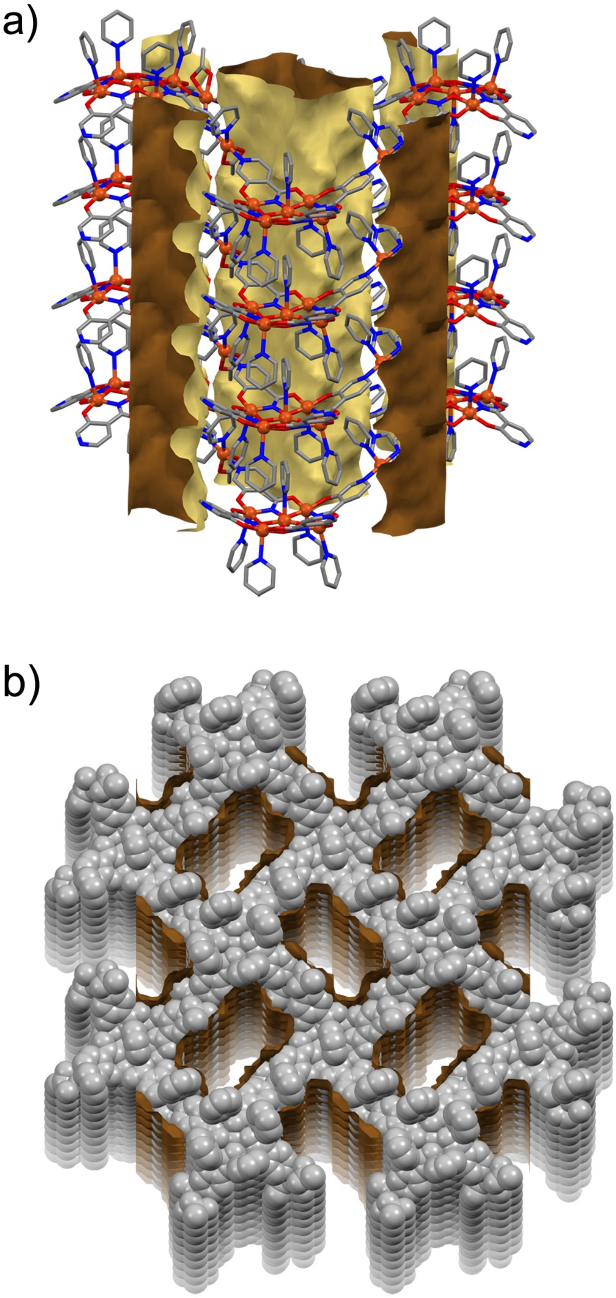

**Fig. 4.13**: Representation of the void channels formed by stacking of the network layers, in (a) ball and stick and (b) *spacefill* visualizations.

The thermal stability of the crystalline network **1** was investigated through thermogravimetric analysis (TGA) and variable-temperature powder-XRD (Fig. 4.14**a** and 4.14**b**) on a solvent-exchanged batch of crystals ($CH_2Cl_2$, three times over three days). The TGA curve displayed a sharp weight loss of 15% between 50-65 °C, corresponding to the loss of absorbed solvent in the void channels (Fig. 4.14**a**). The plateauing of the TGA curve between 65-320 °C suggests that the network is thermally stable over this temperature range; at higher temperatures, decomposition of the organic matrix takes place. No loss of crystallinity is observed below 225 °C, as shown in the PXRD patterns in Fig. 4.14**b**. The results suggest high thermal resistance of the crystal lattice to degradation.

Porosity of compound **1** was studied by isothermal nitrogen adsorption at 77 K on crystals activated by solvent exchange ($CH_2Cl_2$, three times over three days) followed by heating at 110 °C under vacuum for 6 hours. The isotherm shows a behaviour intermediate to Type-I and II with a pronounced hysteresis due to capillary condensation (Fig. 4.14**c**).[43,44] The surface area was determined to be 515 $m^2/g$ and 568 $m^2/g$ according to BET and Langmuir methods, respectively, with a total pore volume of 0.583 $cm^3/g$. The activated network was also tested for isothermal $CO_2$ absorption up to 1 atm at 195 K and at 273 K (Fig. 4.14**d**), showing a $CO_2$ uptake capacity of 23.3 wt% (118.64 $cm^3\ g^{-1}$, 5.31 mmol $g^{-1}$) and of 7.3 wt% (37.27 $cm^3\ g^{-1}$, 1.66 mmol $g^{-1}$), respectively. These values are comparable to the $CO_2$ adsorption capacities of other reported porous MOFs.[45–51] Hence, we can conclude that network **1** is the first permanently porous coordination polymer made of MCs, capable of reversible gas absorption.

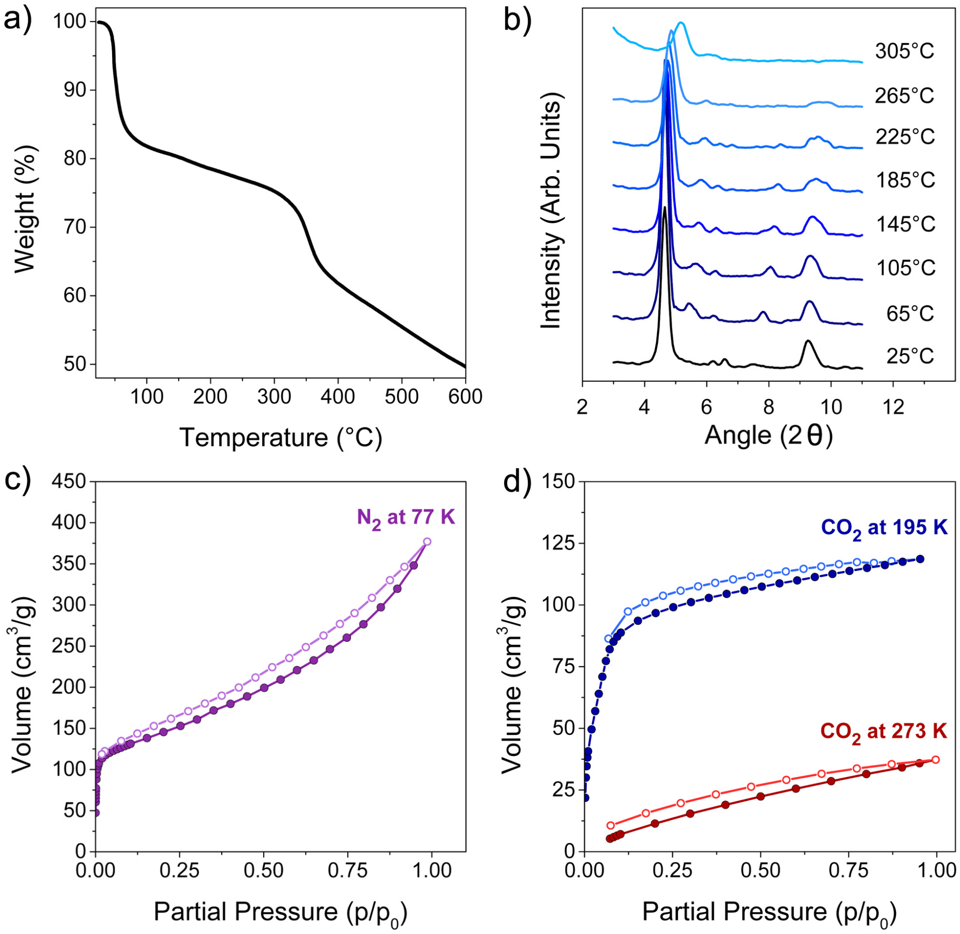

**Fig. 4.14**: (a) Thermogravimetric analysis of solid **1**, run under a $N_2$ atmosphere up to 400 °C; (b) Variable-temperature powder-XRD spectra of **1** in the 20-260 °C interval; (c, d) Isothermal gas absorption of **1**, respectively $N_2$ at 77 K and $CO_2$ at 195 K and 273 K

A detailed description of the coordination polymers based on metallacrowns has been reported recently.[52] Compared to the compounds known to date, network **1,** with its average calculated pore diameter of 1.2 nm and 36% total void volume, possesses the second widest pores of all MC-based systems, behind the mesoporous aggregate La(III)/Cu(II) 15-MC-5 (average pore diameter of 2.4 nm with 43% of unit cell voids).[30] Nevertheless, the aforementioned mesoporous material does not withstand solvent evacuation and, therefore, does not show permanent porosity due to structural collapse upon solvent removal. A few other MC-based supramolecular assemblies have exhibited good uptake capacities towards alcohols.[31,32] However, such sorption properties are not caused by the presence of porous lattices, but rather by compact, non-porous structures undergoing uptake mechanisms known as “gate-opening”.[53,54] Compound **1** is the first MC-based coordination polymer characterized by wide structured pores and by a crystal lattice resistant to solvent evacuation, attributes that effectively classify the framework as a porous material.

Reacting $H_3$hinHA, copper(II) triflate and tetraethylammonium ($NEt_4^+$) acetate (1:1.25:3 ratio) in a solution of 3:2:1 DMSO:DMF:pyridine led to the isolation of a different network (**2**), which corresponds to the formula $\{(NEt_4)_2\{Cu(II)[12\text{-}MC_{Cu(II),\ hinHA}\text{-}4]\}(DMSO)_2\}_n$. Single-crystal XRD revealed that compound **2** consists of a different 2D coordination polymer based on the same $\{Cu(II)[12\text{-}MC_{Cu(II),\ hinHA}\text{-}4]\}^{2-}$ unit, where the MCs are directly linked together, while bridging metal ions are absent. Cross-linking between MCs is established by the coordination of peripheral pyridinic moieties to available axial positions of the Cu(II) ions of a neighbouring MC unit (Fig. 4.15). The result is the formation of a net of MC units, with adjoined building blocks situated almost perpendicular to each other. The four ring Cu(II) ions exhibit a square pyramidal coordination geometry, where the axial positions are occupied alternately either by a nearby MC pyridinic moiety or by a DMSO molecule. The charge of each MC unit is balanced with two bulky $NEt_4^+$ ions, which occupy the rectangular interstices created between the linked MCs, generating a non-porous solid (Fig. 4.15b). Interestingly, also in **2**, the MC units arrange into layers: single 2D reticular frameworks, parallel to the *bc* crystallographic plane, are stacked by means of weak interactions between $NEt_4^+$ ions and the aromatic residues of adjacent MCs (Fig. 4.18, Supplementary Information).

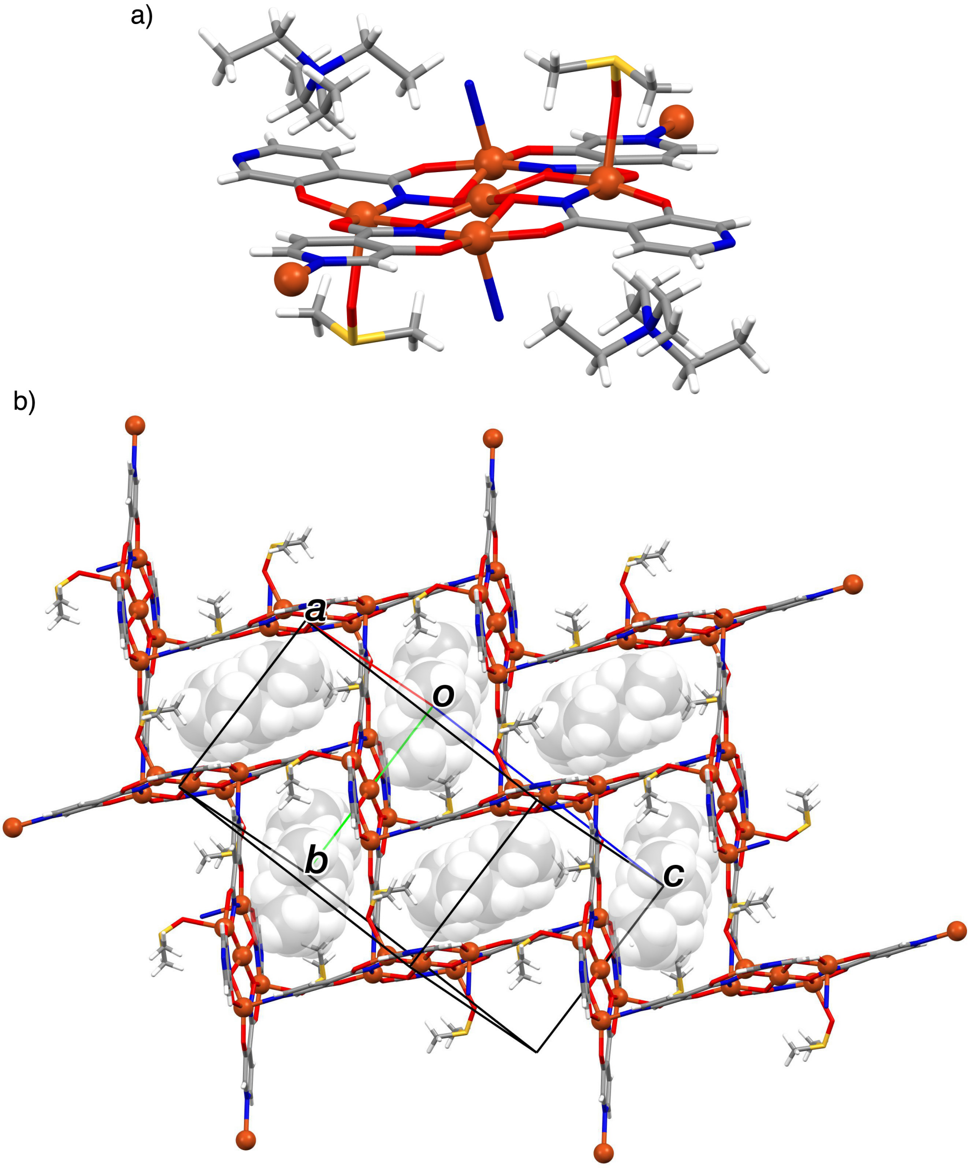

**Fig. 4.15**: Representation of the structure of **2**. (a) Single MC unit, with two coordinated DMSO molecules and two tetraethylammonium counter-ions; (b) 2D network established by cross-coordinated MC units, encapsulating tetraethylammonium in the interstices (shown in *spacefill* view and partial transparency). Colour scheme: Cu(II), orange; N, blue; O, red; C, grey; H, white.

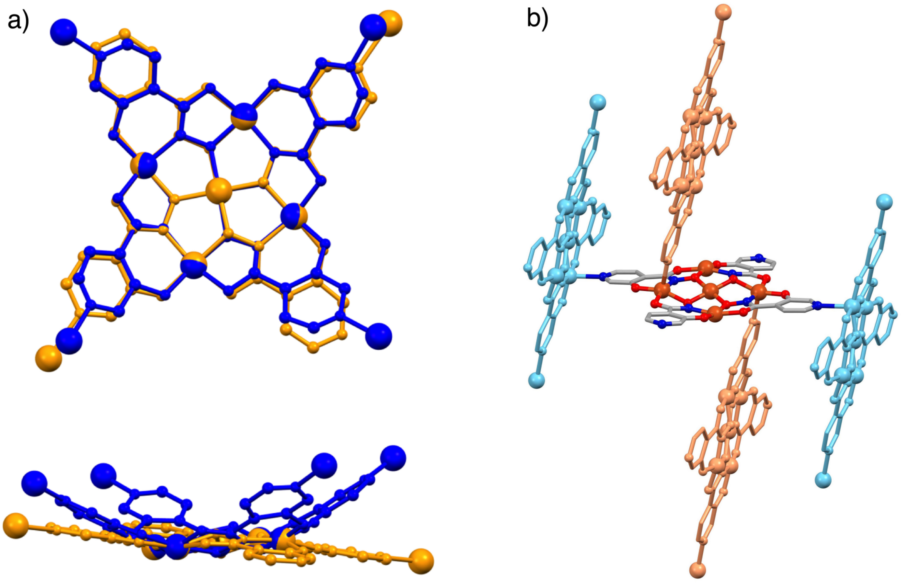

**Fig. 4.16**: (a) Overlap between the MC units of **1** (blue) and **2** (yellow) derived by the X-ray analysis. The overlap was realized by minimizing the RMSD between the five metal atoms of the MCs. (b) Detail of the cross-coordination established by the MC units in **2**; solvent molecules and counterions have been omitted for clarity.

Interestingly, a 1D coordination polymer of 15-MC-5 made of pyrazinohydroxamic acid, a close analog of $H_3$hinHA, was previously reported in the literature.[29] The connectivity between MCs is achieved by coordination from a peripheral pyridinic nitrogen onto a Cu(II) ring ion of a nearby MC (Fig. 4.17). However, no 2D or 3D assemblies were generated, possibly due to the five-fold symmetry of 15-MC-5, which complicates the establishment of such frameworks.

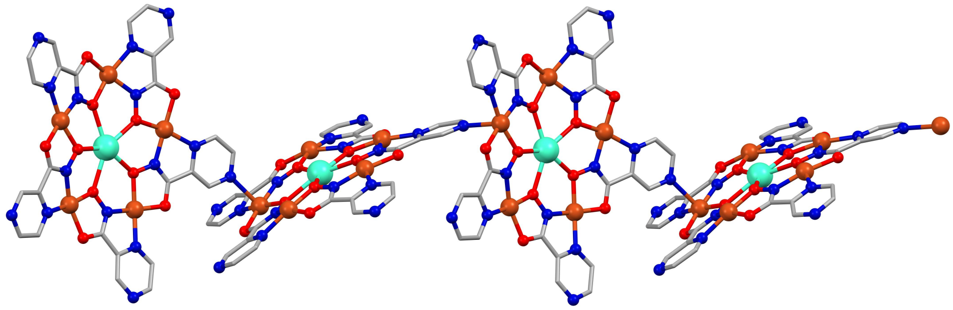

**Fig. 4.17**: Representation of the 1D coordination polymer formed by Gd(III)[15-$MC_{Cu(II),\ pizHA}$-5]$(NO_3)_3(DMF)_2(H_2O)$, counterions and solvent molecules have been omitted for clarity.[29] Colour scheme: Cu(II), orange; Gd, aqua; N, blue; O, red; C, grey; H, white.

Here, the capacity of $hinHA^{3-}$ to assemble stable, four-fold symmetrical 12-MC-4 and to provide donor atoms for the linkage of MC units through the coordination of bridging metal ions is fully exploited in **1**. Network **2**, although not porous, further demonstrates the tendency of 12-MC-4 of $hinHA^{3-}$ to form coordination polymers, opening at the possibility to further devise new materials using this ligand and different metals.

By comparing the solid state structures of **1** and **2**, a notable difference between the two networks is the nature of the counterions. In both structures, the overall charge of the MC node is 2- (3- per each deprotonated ligands, 2+ for each copper(II) ions). In **1**, the charge balance is provided by the four bridging $[Cu(II)(AcO)Py]^+$ cations, thus making not needed the presence of extra counterions which may occupy the void space unnecessary. On the contrary, in **2** two $NEt_4^+$ cations for each MC are present in the structure as needed for charge balance, which interpose between different MC planes.

Based on these observations, we attempt to rationalize the reasons that underpin the isolation of such different networks starting from the same precursors. A critical observation is that in both **1** and **2** the aromatic nitrogen of $hinHA^{3-}$ is involved in coordination interactions. This occurs in **1**, with the coordinatively unsaturated $[Cu(II)(AcO)Py]^+$ fragment, while in **2** coordination is achieved through the axial position of a ring Cu(II) atom of an adjacent MC.. We conclude that a metal is always bound to the peripheral nitrogen atoms of the templating ligand (in this case in $hinHA^{3-}$) in MCs and that by changing the metal:ligand ratio of ($hinHA:Cu^{2+}$) and employing different countercations ($NEt_4^+$) one may control the solid topology.

## 4.4 - Conclusions

In conclusion, the newly designed $H_3$hinHA proved to be a versatile and reliable organic ligand for the production of extended networks. We isolated two novel 2-dimensional coordination networks based on the unit $\{Cu(II)[12\text{-}MC_{Cu(II),\ hinHA}\text{-}4]\}^{2-}$ employed as building block. With the design and isolation of network **1,** we succeeded in obtaining the first homochiral MC-based permanently porous coordination polymer, which shows good gas absorption capacity both for $N_2$ and for $CO_2$. This network represent a proof-of-concept of how the rational design of MC units may lead the way for a new class of functional porous materials based on high interest MC synthons. We now aim at exploiting the porosity of new MC-based frameworks to realize functional guest-responsive materials, with applications ranging from luminescent sensors to advanced magnetic materials, to catalysis.

## 4.5 - Supporting Information

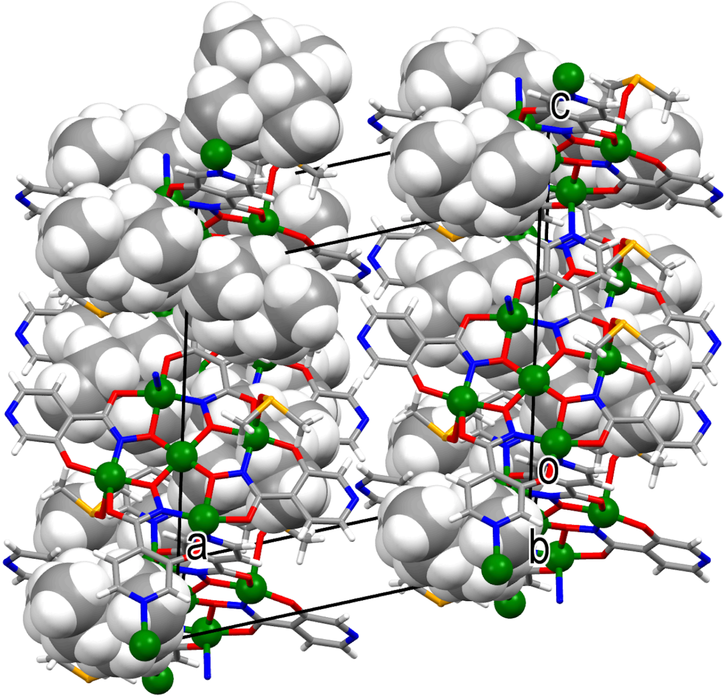

**Fig. 4.18**: Depiction of the reticular framework originated by the interacting MCs in **2** as viewed along the *b* axis. The interacting MC platforms are arranged nearly perpendicularly to each other forming a polymeric MC grid hosting $Et_4N^+$ cations (in spacefill representation). The grids are arranged in layers that are parallel to the *bc* crystallographic plane. The solvent of crystallization (pyridine and DMSO, not shown) is located in the interstices formed by the approaching layers.

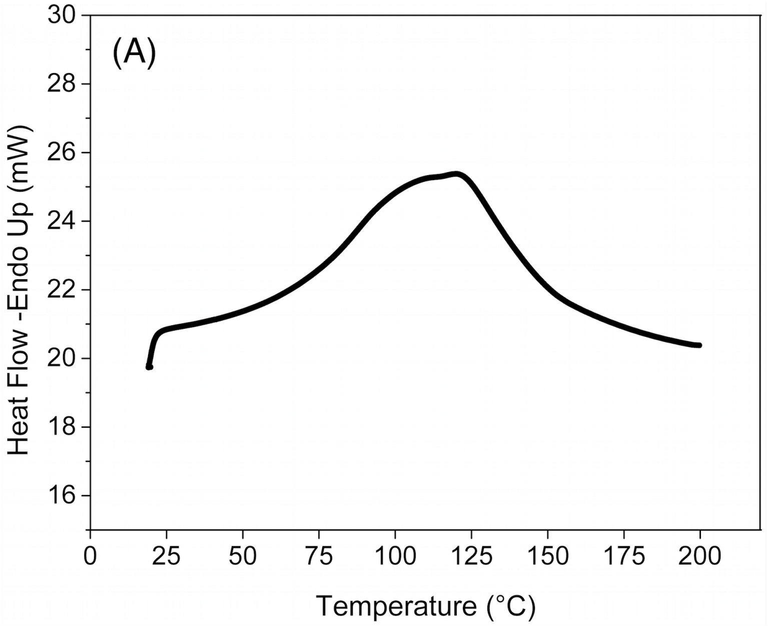

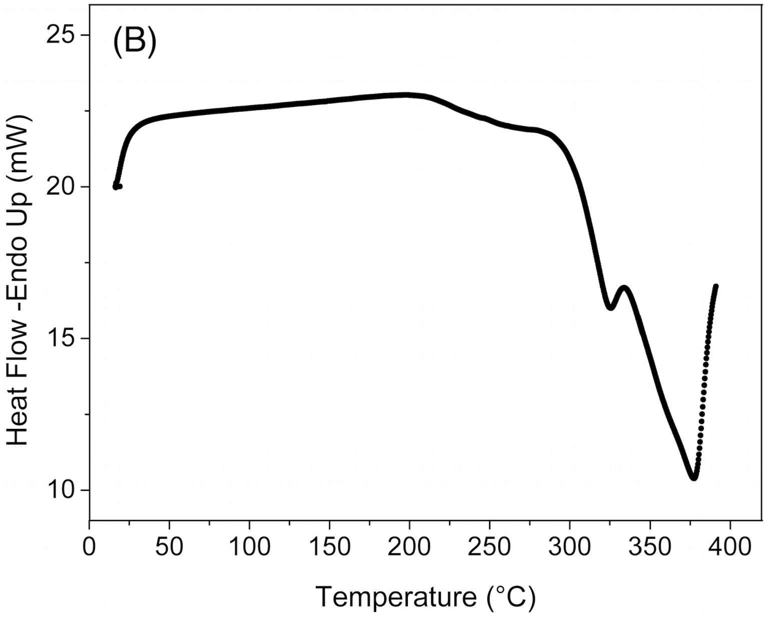

**Fig. 4.19**: Differential Scanning Calorimetry analysis on a 24 h air-dried sample of crystals of **1**. Loss of crystallization solvent is evidenced around 110 °C during a first run (A), while subsequent two-step decomposition of the material occurred above 300 °C during a second run (B).

**Table 4.1**: Summary of X-ray crystallographic data for networks **1** and **2**.

| | **1** | **2** |
|---|---|---|
| Empirical formula | $C_{63}H_{53}Cu_7N_{15}O_{16}$ | $C_{53.36}H_{74.21}Cu_5N_{11.79}O_{14.21}S_{2.21}$ |
| Formula weight | 1720.98 | 1496.80 |
| Colour, habit | Dark green, rods | Dark green, plates |
| Crystal size, mm | 0.16 x 0.02 x 0.02 | 0.100 x 0.100 x 0.020 |
| Crystal system | Tetragonal | Monoclinic |
| Space group | P 4 21 2 | P 21/c |
| $a$, Å | 25.3614(6) | 15.9549(3) |
| $b$, Å | 25.3614(6) | 11.5822(2) |
| $c$, Å | 8.6031(6) | 16.8627(12) |
| α, deg. | 90 | 90 |
| β, deg. | 90 | 105.274(7) |
| γ, deg. | 90 | 90 |
| $V$, Å$^3$ | 5533.5(5) | 3006.0(2) |
| $Z$ | 2 | 2 |
| $T$, K | 85 (2) | 85 (2) |
| F(000) | 1734 | 1542 |
| $r$ (calc), Mg/m$^3$ | 1.033 | 1.654 |
| $m$, mm$^{-1}$ | 1.859 | 3.296 |
| $q$ range, deg. | 3.897 to 68.209 | 6.651 to 68.249 |
| No.of rflcn/independ. | 107642/5079 | 80642/5486 |
| GooF | 1.008 | 1.042 |
| $R1$ | 0.1120 | 0.0605 |
| $wR2$ | 0.2727 | 0.1778 |

$R1 = \Sigma||F_o|-|F_c||/\Sigma|F_o|$, $wR2 = [\Sigma[w(F_o^2-F_c^2)^2]/\Sigma[w(F_o^2)^2]]^{½}$ , $w = 1/[\sigma^2(F_o^2) + (aP)^2 + bP]$, where $P = [\max(F_o^2,0) + 2F_c^2]/3$

## 4.6 - References

1 G. Férey, *Chem. Soc. Rev.*, 2007, **37**, 191–214.

2 Y. Cui, F. Zhu, B. Chen and G. Qian, *Chem. Commun.*, 2015, **51**, 7420–7431.

3 X.-G. Liu, H. Wang, B. Chen, Y. Zou, Z.-G. Gu, Z. Zhao and L. Shen, *Chem. Commun.*, 2015, **51**, 1677–1680.

4 M. Kurmoo, *Chem. Soc. Rev.*, 2009, **38**, 1353.

5 C. Wang, D. Liu and W. Lin, *J. Am. Chem. Soc.*, 2013, **135**, 13222–13234.

6 L. V. Meyer, F. Schönfeld and K. Müller-Buschbaum, *Chem. Commun.*, 2014, **50**, 8093.

7 Z. Hu, B. J. Deibert and J. Li, *Chem. Soc. Rev.*, 2014, **43**, 5815–5840.

8 M. Tegoni and M. Remelli, *Coord. Chem. Rev.*, 2012, **256**, 289–315.

9 G. Mezei, C. M. Zaleski and V. L. Pecoraro, *Chem. Rev.*, 2007, **107**, 4933–5003.

10 J. Jankolovits, C. M. Andolina, J. W. Kampf, K. N. Raymond and V. L. Pecoraro, *Angew. Chemie Int. Ed.*, 2011, **50**, 9660–9664.

11 E. R. Trivedi, S. V Eliseeva, J. Jankolovits, M. M. Olmstead, S. Petoud and V. L. Pecoraro, *J. Am. Chem. Soc.*, 2014, **136**, 1526–1534.

12 C. Dendrinou-Samara, M. Alexiou, C. M. Zaleski, J. W. Kampf, M. L. Kirk, D. P. Kessissoglou and V. L. Pecoraro, *Angew. Chemie {(International} ed. English)*, 2003, **42**, 3763–3766.

13 C. M. Zaleski, E. C. Depperman, J. W. Kampf, M. L. Kirk and V. L. Pecoraro, *Angew. Chemie Int. Ed.*, 2004, **43**, 3912–3914.

14 C. M. Zaleski, E. C. Depperman, C. Dendrinou-Samara, M. Alexiou, J. W. Kampf, D. P. Kessissoglou, M. L. Kirk and V. L. Pecoraro, *J. Am. Chem. Soc.*, 2005, **127**, 12862–12872.

15 C. M. Zaleski, E. C. Depperman, J. W. Kampf, M. L. Kirk and V. L. Pecoraro, *Society*, 2006, **45**, 10022–10024.

16 C. M. Zaleski, J. W. Kampf, T. Mallah, M. L. Kirk and V. L. Pecoraro, *Inorg. Chem.*, 2007, **46**, 1954–1956.

17 T. T. Boron, J. W. Kampf and V. L. Pecoraro, *Inorg. Chem.*, 2010, **49**, 9104–9106.

18 C. M. Zaleski, S. Tricard, E. C. Depperman, W. Wernsdorfer, T. Mallah, M. L.

Kirk and V. L. Pecoraro, *Inorg. Chem.*, 2011, **50**, 11348–52.

19 F. Cao, S. Wang, D. Li, S. Zeng, M. Niu, Y. Song and J. Dou, *Inorg. Chem.*, 2013, **52**, 10747–10755.

20 M. Tegoni, M. Remelli, D. Bacco, L. Marchiò and F. Dallavalle, *Dalton Trans.*, 2008, 2693–2701.

21 L. Marchiò, N. Marchetti, C. Atzeri, V. Borghesani, M. Remelli and M. Tegoni, *Dalt. Trans.*, 2015, **44**, 3237–3250.

22 J. J. Bodwin and V. L. Pecoraro, *Inorg. Chem.*, 2000, **39**, 34343435.

23 A. B. Lago, J. Pasán, L. Cañadillas-Delgado, O. Fabelo, F. J. M. Casado, M. Julve, F. Lloret and C. Ruiz-Pérez, *New J. Chem.*, 2011, **35**, 1817–1822.

24 C. McDonald, T. Whyte, S. M. Taylor, S. Sanz, E. K. Brechin, D. Gaynor and L. F. Jones, *CrystEngComm*, 2013, **15**, 6672–6681.

25 M. Moon, I. Kim and M. S. Lah, *Inorg. Chem.*, 2000, **39**, 2710–2711.

26 K. Wang, H.-H. Zou, Z.-L. Chen, Z. Zhang, W.-Y. Sun and F.-P. Liang, *Dalton Trans.*, 2014, **43**, 12989–95.

27 L. Han, L. Qin, X. Z. Yan, L. P. Xu, J. Sun, L. Yu, H. B. Chen and X. Zou, *Cryst. Growth Des.*, 2013, **13**, 1807–1811.

28 D. Moon and S. L. Myoung, *Inorg. Chem.*, 2005, **44**, 1934–1940.

29 E. V. Govor, A. B. Lysenko, A. N. Chernega, J. A. K. Howard, A. A. Mokhir, J. Sieler and K. V. Domasevitch, *Polyhedron*, 2008, **27**, 2349–2356.

30 C.-S. Lim, J. Jankolovits, J. Kampf and V. Pecoraro, *Chem. Asian J.*, 2010, **5**, 46.

31 A. V Pavlishchuk, S. V Kolotilov, M. Zeller, L. K. Thompson, I. O. Fritsky, A. W. Addison and A. D. Hunter, *Eur. J. Inorg. Chem.*, 2010, **2010**, 4851–4858.

32 A. V Pavlishchuk, S. V Kolotilov, M. Zeller, O. V Shvets, I. O. Fritsky, S. E. Lofland, A. W. Addison and A. D. Hunter, *Eur. J. Inorg. Chem.*, 2011, **2011**, 4826–4836.

33 J. Jankolovits, C.-S. Lim, G. Mezei, J. W. Kampf and V. L. Pecoraro, *Inorg. Chem.*, 2012, **51**, 4527–4538.

34 G. Mezei, J. W. Kampf, S. Pan, K. R. Poeppelmeier, B. Watkins and V. L. Pecoraro, *Chem. Commun.*, 2007, 1148.

35 J. J. Bodwin, A. D. Cutland, R. G. Malkani and V. L. Pecoraro, *Coord. Chem. Rev.*, 2001, **216-217**, 489–512.

36 C. Atzeri, M. Tegoni, L. Marchiò, J. W. Kampf and V. L. Pecoraro, 2013, 1057331.

37 G. M. Sheldrick, *Acta Crystallogr.*, 2008, **A64**, 112–122.

38 A. Spek, *J. Appl. Cryst.*, 2003, **36**, 7–13.

39 T. Haemers, J. Wiesner, D. Gießmann, T. Verbrugghen, U. Hillaert, R. Ortmann, H. Jomaa, A. Link, M. Schlitzer and S. Van Calenbergh, *Bioorg. Med. Chem.*, 2008, **16**, 33613371.

40 J. Jankolovits, J. W. Kampf and V. L. Pecoraro, *Inorg. Chem.*, 2013, **52**, 5063–76.

41 V. L. Pecoraro, A. J. Stemmler, B. R. Gibney, J. J. Bodwin, H. Wang, J. W. Kampf and A. Barwinski, *Metallacrowns: a new class of molecular recognition agents*, 1997, vol. 45.

42 A. L. Spek, *PLATON, A Multipurpose Crystallographic Tool*, Utrecht University, Utrecht, The Netherlands, 2003.

43 S. Storck, H. Bretinger and W. F. Maier, *Appl. Catal. A Gen.*, 1998, **174**, 137–146.

44 G. Leofanti, M. Padovan, G. Tozzola and B. Venturelli, *Catal. Today*, 1998, **41**, 207–219.

45 Y. E. Cheon and M. P. Suh, *Chem. - A Eur. J.*, 2008, **14**, 3961–3967.

46 S. R. Miller, G. M. Pearce, P. a. Wright, F. Bonino, S. Chavan, S. Bordiga, I. Margiolaki, N. Guillou, G. Férey, S. Bourrelly and P. L. Llewellyn, *J. Am. Chem. Soc.*, 2008, **130**, 15967–15981.

47 Y. E. Cheon, J. Park and M. P. Suh, *Chem. Commun. (Camb).*, 2009, 5436–5438.

48 Y. E. Cheon and M. P. Suh, *Chem. Commun.*, 2009, 2296.

49 E. Neofotistou, C. D. Malliakas and P. N. Trikalitis, *Chem. - A Eur. J.*, 2009, **15**, 4523–4527.

50 A. Demessence, D. M. D'Alessandro, M. L. Foo and J. R. Long, *J. Am. Chem. Soc.*, 2009, **131**, 8784–8786.

51 H.-S. Choi and M. P. Suh, *Angew. Chemie {(International} ed. English)*, 2009, **48**, 6865–6869.

52 A. V. Pavlishchuk, Y. . Satska, S. V. Kolotilov and I. Fritsky, *Curr. Inorg. Chem.*, 2015, **5**, 5–25.

53 R. Kitaura, K. Seki, G. Akiyama and S. Kitagawa, *Angew. Chemie - Int. Ed.*, 2003, **42**, 428–431.

54 D. Tanaka, K. Nakagawa, M. Higuchi, S. Horike, Y. Kubota, T. C. Kobayashi, M. Takata and S. Kitagawa, *Angew. Chemie - Int. Ed.*, 2008, **47**, 3914–3918.

# Chapter V

## *Isolation and characterization of a new Manganese(II)/(III) metallacryptate*

## 5.1 - Introduction

Different families of SMMs have been synthesized since the discovery of the peculiar magnetic behaviour of the first SMM by Sessoli *et al.* in 1991, a species referred to as $Mn_{12}(OAc)$,[1] comprised of four Mn(IV) and eight Mn(III) ions. In particular, lanthanide bis-phthalocyanine[2] complexes and lanthanide polyoxometallates[3] are amongst the most famous classes of SMMs, showing high blocking-temperatures and ground states of great total spin value.

Despite the variety of transition metal ions that can constitute SMMs, such as iron[4–6], cobalt[7] and nickel,[8,9] the most widely studied 3d metal ion for this purpose is manganese. Mn(III) shows indeed a ground state spin of S=2, due to its four unpaired electrons, and large anisotropy caused by its Jahn-Teller axial distortion. In the past, large manganese clusters accounting up $Mn_{84}$ to have been studied for their SMM behaviour.[10]

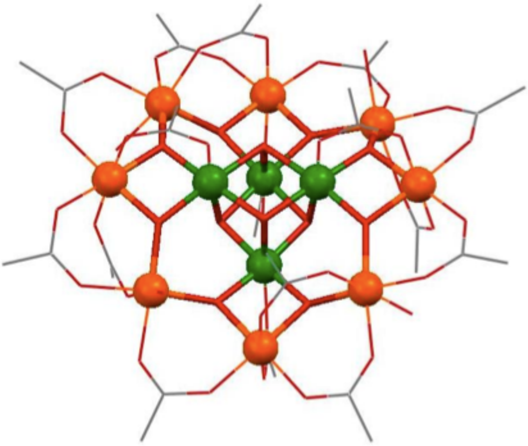

**Fig. 5.1**: Structure of compound $M(III)_8Mn(IV)_4O_{12}(CH_3COO)_{16}(H_2O)_4$.[11] Solvent molecules have been omitted for clarity. Colour scheme: orange - Mn(III), green - Mn(IV), red - oxygen, grey - carbon.

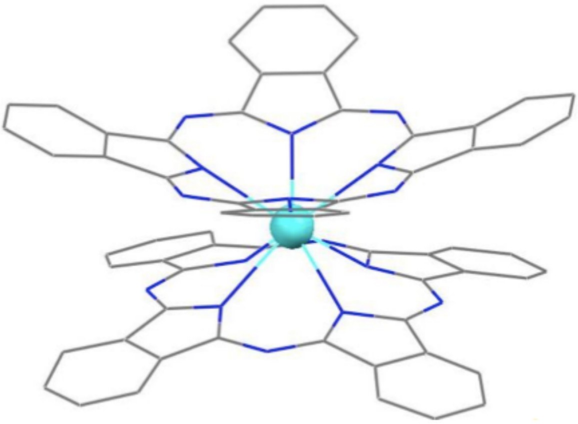

**Fig. 5.2**: Structure of the bisphthalocyanine Gd(III) complex [Pc2Gd]-TBA+.[12] The TBA+ cation has been removed for clarity. Colour scheme: aqua - Gd(III), grey - carbon, blue - nitrogen.

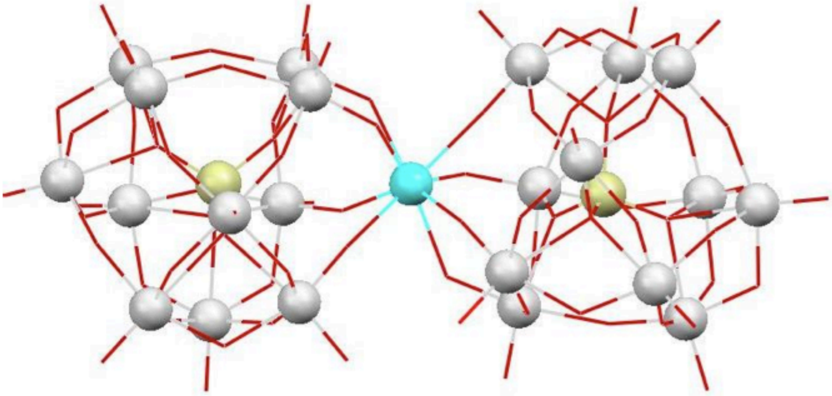

**Fig. 5.3**: Structure of the $[Er(\beta\text{-}SiW_{11}O_{39})_2]^{13-}$ polyoxometallate.[3] Only the core of the polyoxometallate is shown for clarity. Colour scheme: aqua - Er(III), light grey sphere - W(VI), gold - silicon, red - oxygen.

Numerous homometallic and heterometallic MCs showing interesting SMM behaviour have been reported in literature in the last fifteen years.[13,14] MCs possess peculiar features that contribute to their interesting SMM behaviour. They can be assembled using different metal ions and can encapsulate several paramagnetic metals including lanthanides. Therefore, the magnetic properties can derive from a single paramagnetic ion in the cavity, or from a high number of transition metal ions confined in small molecular scaffolds. In the latter case, several paramagnetic ions contribute into providing a large total spin state for the molecule.[15] Furthermore, while the structures of most SMMs approach spherical symmetry, cancelling out the individual anisotropy components of each metal ions, the planar structure of MCs and their *n*-fold axial symmetry impose the metal anisotropy axes to stay almost parallel to each other, summing into greater values of total molecular spin.[15,16]

Most of these MC-based SMMs entail manganese(III) ions as the principal constituents of the inorganic scaffold. Three important examples of homometallic manganese metallacrowns with marked SMM properties were reported by C. Zaleski, namely one 12-MC-4 and two metallacryptates (Fig. 5.4 and Fig. 5.5).[16–18] All of the three structures possess manganese ions in the oxidation states +2 and +3. Interestingly, despite its relatively low S=1/2 total ground spin state, the $\mathrm{Mn^{II}(AcO)_2[12\text{-}MC_{Mn(III),\ Shi}\text{-}4]}$ complex presented by Zaleski is one of the first examples of SMM behaviour originated by a convenient alignment of the single ion magnetoanisotropy, which leads to an increased molecular anisotropy. This compound shows an energy barrier to magnetic reorientation of the total spin angular momentum (usually referred to as $U_{eff}$) of 21 K and a relaxation time at infinite temperature of $1.4 \times 10^{-7}$, demonstrating effective SMM properties.

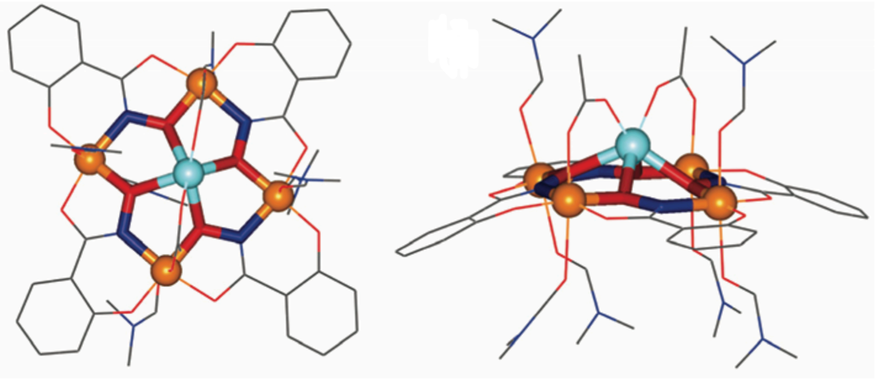

**Fig. 5.4**: Structure of $\mathrm{Mn^{II}(AcO)_2[12\text{-}MC_{Mn(III),\ Shi}\text{-}4](DMF)_6}$.[16] Colour scheme: orange - Mn(III), aqua - Mn(II), red - oxygen, blue - nitrogen, grey - carbon.

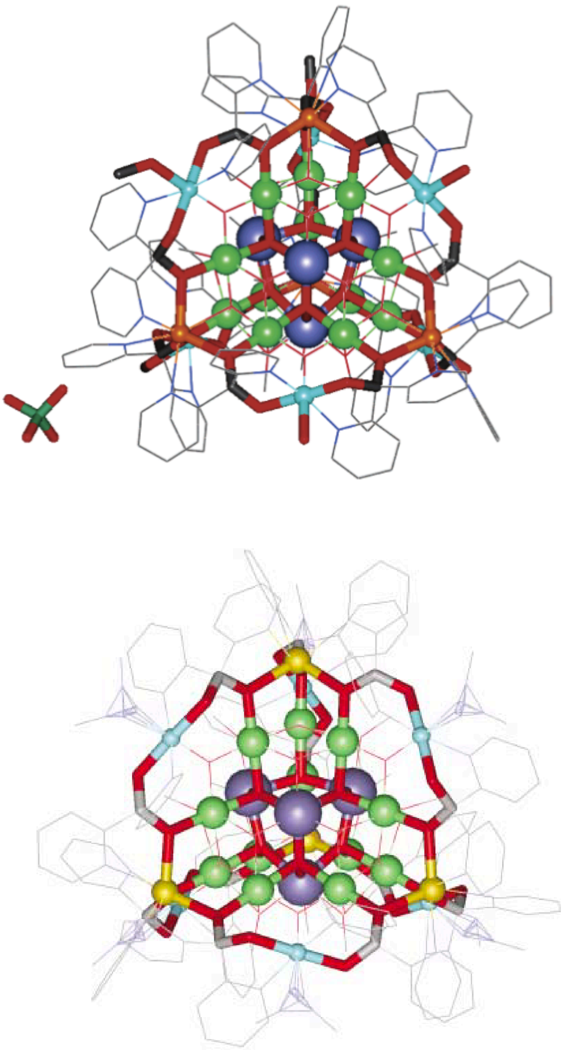

**Fig. 5.5**: Above, $[\mathrm{Mn^{II}}_4\mathrm{Mn^{III}}_{22}(\mathrm{pdol})_{12}(\mu_3\text{-}\mathrm{OCH_3})_{12}(\mu_3\text{-}\mathrm{O})_6(\mu_4\text{-}\mathrm{O})_{10}(\mathrm{OH})_2(\mathrm{H_2O})\text{-}(\mathrm{OCH_3})_3]\cdot\mathrm{ClO_4}\cdot5\mathrm{CH_3OH}$.[18] Twelve manganese ions of the $\{\mathrm{Mn_{16}}(\mathrm{O^{2-}})_{12}(\mathrm{MeO^-})_{16}\}$ core consist of the chemically equivalent Mn1, Mn4, Mn6, and Mn8 and are directly bonded to the metallacryptand. Colour scheme: orange - Mn2 and Mn5; green - Mn3 and Mn7; aqua - Mn1, Mn4, Mn6, and Mn8, navy blue - Mn9 and Mn10, grey - carbon, red - oxygen; dark green - chlorine. Below, the analogous $\mathrm{Mn_{26}}$ metallacryptate of formula $[\mathrm{Mn^{II}}_4\mathrm{Mn^{III}}_{22}(\mathrm{pdol})_{12}(\mathrm{OCH_3})_{12}(\mathrm{O})_{16}(\mathrm{N_3})_6]$;[17] colour scheme: gold - Mn1; aqua - Mn2; green - Mn3; blue - Mn4; grey - C; red - O. The core and ring connectivity are highlighted with thick tubes. Hydrogen atoms and lattice solvent are omitted for clarity.

Current strategies to increase blocking temperature and therefore the SMM behaviour operate on maximizing two key factors: to increase the total ground spin state, and to increase the magnetic anisotropy of the metal ions.

A higher total ground spin state can ideally be obtained by increasing of the number of paramagnetic metal ions in the molecular scaffold (possibly having a high spin state), and by optimizing the spin exchange interactions. However, a large total ground spin state in the absence of a significant magnetoanisotropy results into a poor SMM behaviour. Therefore, the design of the molecular architecture, perhaps in combination with the use of metals that show magnetic anisotropy, must be pursued.

An interesting development of homometallic (i.e. manganese) MCs consists in using different transition metals within the same MC scaffold. The general approach followed consisted in the preparation of heterometallic species where the central Mn(II) is substituted by more magnetically active transition metal or lanthanide ions. In fact, the inclusion of lanthanide ions within magnetically interesting metal complexes has been exploited to increase the SMM behaviour of MCs, thanks to the large spin states and the large anisotropies of lanthanide ions (with the exception of La(III), Gd(III) and Lu(III) for which J = 0). Although mixed 3d/4f complexes showing SMM behaviour had been presented earlier,[19,20] the ability of lanthanides to induce SMM behaviour into *3d-only* complexes that would otherwise not behave as SMMs, was proven for the first time in 2009 by Ako, who selectively substituted a Mn(II) ion with a Dy(III) ion in a $Mn_{19}$ aggregate.[21] Interestingly, the unusual coordination environment of the central Mn(II) in the $Mn_{19}$ aggregate allowed for site-selective substitution with a Dy(III) ion. The obtained $Mn_{18}Dy$ complex exhibited remarkable large anisotropy and magnetic hysteresis. Since then great results have also been obtained and reported in literature using mixed 3d/4f metallacrowns where Mn(III) and Ln(III) ions are present.[14]

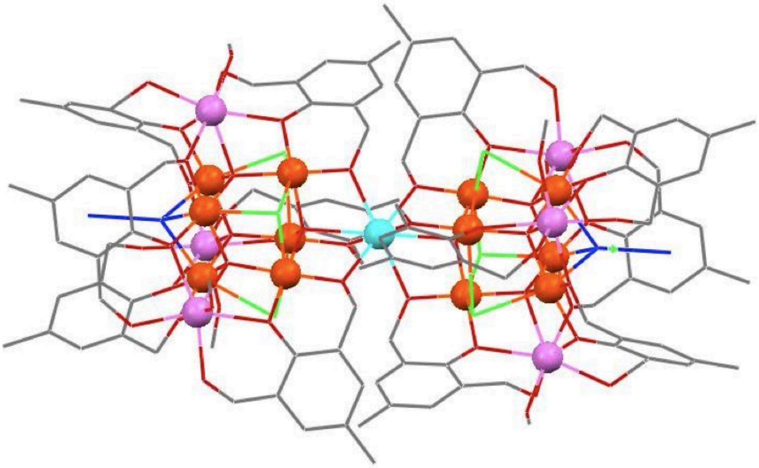

**Fig. 5.6**: Structure of the $Mn_{18}Dy$ complex presented by Ako in 2009.[21] Colour scheme: aqua - Dy(III), violet - Mn(II), orange - Mn(III), red - oxygen, blue - nitrogen, grey - carbon, green - chlorine.

As far as *3d*-only MC-based SMMs are concerned, less results have been presented and just a few 3*d*-only MC compounds have been reported to date to show SMM properties and are mainly manganese[16–18] (Fig. 4 and Fig. 5) and cobalt-based[13] (Fig. 7). Interesting Mn(III) structures endowed with a central Ni(II) were reported by T. Boron in his doctoral thesis, but have yet to be published; Ni(II) was used to replace the only Mn(II) ion within {Mn(II)[12-$MC_{Mn(III), Shi}$-4]} structures hoping to improve the SMM behaviour, thanks to the relatively similar coordination chemistry of the two ions and the excellent anisotropy showed by Ni(II). In fact, single-ion anisotropies ($D_{si}$) showed by octahedral Ni(II) complexes can be as large as -10 $cm^{-1}$,[22] compared to the typical $D_{si}$ of octahedral Mn(II) which are ca. 0.1-0.2 $cm^{-1}$.[23] Ni(II) is an anisotropic high spin $d^8$ ion with S=1 and a radius of 0.690 Å, smaller than that of high spin Mn(II), of 0.830 Å.[24]

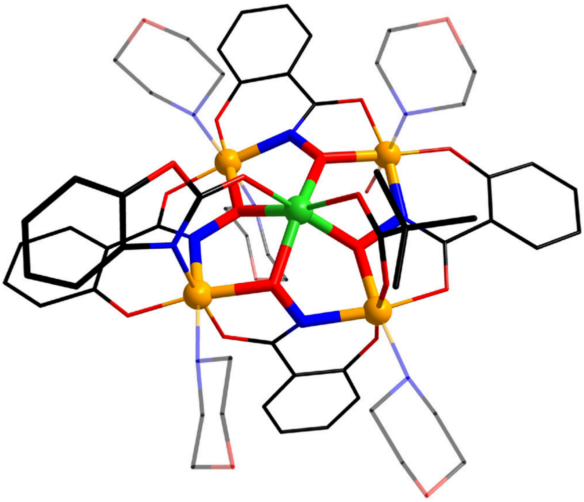

**Fig. 5.7**: Structure of the cobalt 3d-only metallacrown of formula Co(II)(Boa)(Piv)[12-$MC_{Co(III),\ Shi}$-4]$(Morph)_5$(MeOH), where Boa = 2-benzoxazolinonate, Piv = pivalate and Morph = morpholine, exhibiting SMM behaviour[13]. Colour scheme: orange - Co(III), green - Co(II), red - oxygen, blue - nitrogen, black - carbon.

An interesting *3d-only* heterometallic 12-MC-4, namely Cu(II)$(DMF)_2Cl_2$[12-$MC_{Fe(III)N(Shi)}$-4]$(DMF)_4$·2DMF,[25] represents the first purposeful selective substitution of the central metal ion in order to optimize magnetic properties of this class of compounds. In fact, 12-MC-4s have so far shown limited applications in the field of magnetic materials. The reason for this is related to the general absence of a high spin ground state. In fact, the intrinsic molecular connectivity and the antiferromagnetic radial magnetic interactions lead the ring ions to couple antiferromagnetically (negative $J_2$ values) and cancel out the ring contribution to the total ground state spin. Therefore, the use of a “magnetic director” approach, inserting a strongly coupling Cu(II) ion, was pursued by Happ in 2014 for a 12-$MC_{Fe(III)}$-4 metallacrown.[25] The stronger magnetic coupling provided between Cu(II) and Fe(III), with respect to weaker Fe(III)-Fe(III) interactions (i.e. $|J_1| > |J_2|$), could enforce the ground state spin of the ring Fe(III) ions to adopt a ferromagnetic orientation (i.e. positive $J_2$ values) and maximize the final total ground state spin.

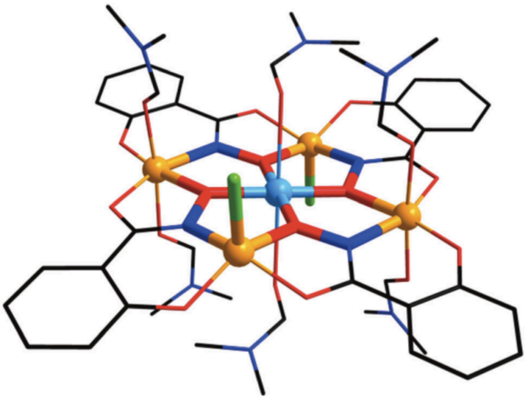

**Fig. 5.8**: Crystal structure of Cu(II)(DMF)$_2$Cl$_2$[12-MC$_{Fe(III)N(Shi)}$-4](DMF)$_4$..[25] Colour scheme: light blue - Cu(II), orange - Fe(III), red - oxygen, blue - nitrogen, black - carbon, green - chlorine.

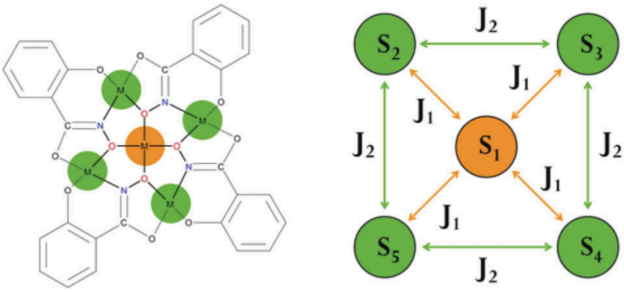

**Fig. 5.9**: General 12-MC-4 motif with different metal-binding sites (core - orange, ring - green) and a corresponding simplified square magnetic model with a radial (J$_1$) and tangential (J$_2$) coupling constant.

In our work, we decided of exploring the field of *3d-only* metallacrowns with SMM behaviour and we focused on the production of new Mn-based MCs. Furthermore, we decided to try isolating new mixed 3*d*-3*d* MC species by inserting a Cu(II) guest within a manganese 12-MC-4 scaffold, to investigate the effect of a “magnetic director” on the magnetically interesting 12-MC$_{Mn(III)}$-4 scaffold.

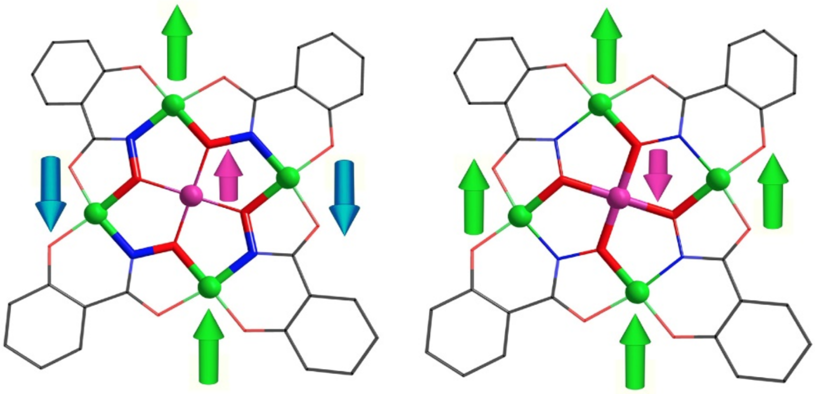

**Fig. 5.10**: Schematic representation of the “magnetic director” approach. On the left, the ground state spin alignment of a general 12-MC-4 in the case of dominantly tangential antiferromagnetic interactions; on the right, the case of radial antiferromagnetic interactions between a “magnetic director” and the ring ions, which increases the total molecular ground state spin. The superior coupling pathways are graphically highlighted

Herein, we discuss what was done to try encapsulating a Cu(II) ion in a 12-$MC_{Mn(III)}$-4 and the serendipitous result obtained. In particular, a Mn-only metallacryptate was obtained, having a complex solid state structure. The molecular unit is described by analysing its structural motives, which are compared with different previously reported MC scaffolds. Notably, the compound appears to be an interesting arrangement of three peculiar MC motifs, generating at the meantime a fascinating symmetrical architecture.

## 5.2 - Experimental Section

### 5.2.1 - Materials and methods

All reagents and solvents were obtained from commercially available sources (Sigma Aldrich and Carlo Erba) and were used without further purification. Salicylhydroxamic acid was purchased from Alfa-Aesar. $^1$H NMR spectra were recorded on a Brüker Avance 400 MHz spectrometer using standard pulse sequences. Chemical shifts (δ) are reported in parts per million (ppm) and referenced to residual solvent protons. Infrared spectra were recorded from 4000 to 400 cm$^{-1}$ on a Perkin-Elmer FTIR Nexus spectrometer equipped with a Smart Orbit HATR accessory with diamond crystal. ESI-MS mass spectra were recorded on a Waters instrument equipped with an electrospray ionization source and single quadrupole analyser. Working parameters were set as follows: capillary voltage, 3.0 V; cone voltage -40 V (negative ion mode). Samples were injected via flow-injection as 30 ppm methanolic solutions and spectra were recorded in full scan analysis mode in the range 100-2000 m/z.

### 5.2.2 - Synthesis

$Na_4\{O \subset [(MCryp_{Mn(II)Mn(III)(\mu\text{-}O)N(Shi)})(OAc)_6(DMF)_3]\}(DMF)_{1.5}(H_2O)_9$, (**$Mn_{11}L_6$**). Manganese(II) acetate tetrahydrate (0.40 g, 1.63 mmol), salicylhydroxamic acid (Shi$^{3-}$, L, 0.10 g, 0.65 mmol) and sodium acetate trihydrate (0.01 g, 0.11 mmol) were dissolved in 15 mL of DMF obtaining a dark brown solution that was kept under magnetic stirring for four hours. The solution was filtered and crystallized by slow evaporation. Dark brown block crystals, suitable for single crystal XRD, were obtained over the course of four weeks. Alternatively to slow evaporation, crystallization by toluene stratification over the filtered solution was used, affording high yields of aesthetically rougher crystals, formed over the course of ten days. $^1$H-NMR (400 MHz, MeOD, ppm): δ 39.21 (br, 3H, OAc core); 8.45 (br, 1H, HShi), -4.45 (br, 1H, Shi), -10.82 (br, 1H, Shi), -13.59 (br, 1H, Shi). FT-IR (cm$^{-1}$): 1653s, 1594s, 1573s, 1525s, 1447s, 1408s, 1377s, 1339m, 1312m, 1258s, 1150w, 1101m, 1026m, 934s, 863w, 759m, 688s, 633s, 537m. ESI-MS (m/z): 1796 $\{O \subset [(MCryp_{Mn(II)Mn(III)(\mu\text{-}O)N(Shi)})(OAc)_3(OH)_3]\}^+$, 1810 $\{O \subset [(MCryp_{Mn(II)Mn(III)(\mu\text{-}O)N(Shi)})(OAc)_3(OH)_2(OMe)_1]\}^+$, 1824 $\{O \subset [(MCryp_{Mn(II)Mn(III)(\mu\text{-}O)N(Shi)})(OAc)_3(OH)_1(OMe)_2]\}^+$, 1838 $\{O \subset [(MCryp_{Mn(II)Mn(III)(\mu\text{-}O)N(Shi)})(OAc)_3(OMe)_3]\}^+$.

### 5.2.3 - Single crystal X-ray structures

Single crystal data were collected with a Brüker Smart 1000 and on a Brüker Smart APEXII area detector diffractometers (Mo Ka; l = 0.71073 Å). Cell parameters were refined from the observed setting angles and detector positions of selected strong reflections. Intensities were integrated from several series of exposure frames that covered the sphere of reciprocal space. A multiscan absorption correction was applied to the data using the program SADABS. The structures were solved by direct methods SIR97 and SIR2004 and refined with full-matrix least-squares (SHELXL- 97), using the Wingx software package. Graphical material was prepared with the Mercury 3.0 program. Crystallographic data are reported in Appendix I - II.

## 5.3 - Results and Discussion

### 5.3.1 - Synthesis

The species **$Mn_{11}L_6$** was serendipitously isolated while trying to isolate the heterometallic metallacrown of formula Cu(II)[12-$MC_{Mn(III), Shi}$-4]. In fact, the first time the complex was isolated, the synthesis was conducted with different stoichiometric ratios and order of additions than from what is reported in paragraph 5.2.2 (see Supplementary Information, paragraph 5.4.1, for more details). Equimolar amounts of Mn(II) acetate and $H_3Shi$ were added initially, along with sodium acetate, in order to promote the formation of the previously reported manganese-only $Mn^{II}(AcO)_2$[12-$MC_{Mn(III), Shi}$-4]$(DMF)_6$ scaffold. Then, the stoichiometric amount of Cu(II) acetate was added, in order to displace the more labile Mn(II) guest. Instead, Cu(II) did not insert within the Mn(III) scaffold; Cu(II) might establish the kinetically and thermodynamically favoured Cu(II)[12-$MC_{Cu(II)}$-4][26], which lowers the amount of available $Shi^{3-}$ for the Mn(III), leading to the formation of a $Mn_{11}L_6$ complex, where L = $Shi^{3-}$. Interestingly, no copper-containing metallacrown was produced from crystallization of the mother liquor, but a different species was isolated, the previously reported **$Na_2Mn_4L_4$** (Fig. 5.11).[27]

After the isolation of the species **$Mn_{11}L_6$**, the synthesis was reproduced and optimized to maximize the yield of crystalline **$Mn_{11}L_6$**.

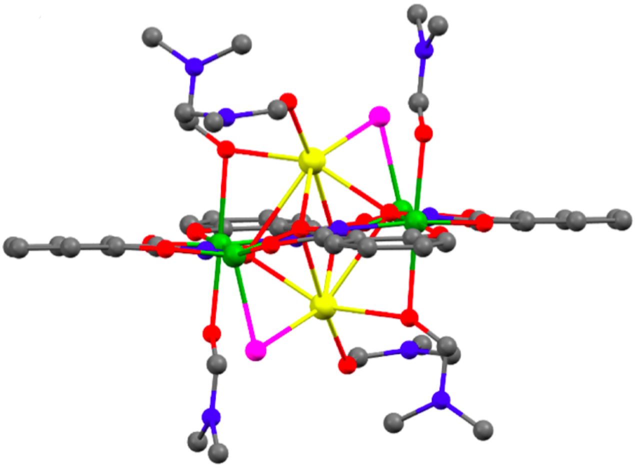

**Fig. 5.11**: compound $Na_2(OAc)_2[12\text{-}MC_{MnIII(N)shi}\text{-}4](DMF)_6{\cdot}2DMF{\cdot}1.60H_2O$ (referred to as **$Na_2Mn_4L_4$**)[27]. Colour scheme: yellow - Na(I), green - Mn(III), red - oxygen, blue - nitrogen, grey - carbon.

## 5.3.2 - Crystal structure

The isolated compound (**$Mn_{11}L_6$**) has the formula $Na_4\{O \subset [(MCryp_{Mn(II)Mn(III)(\mu\text{-}O)N(Shi)})(OAc)_6(DMF)_3]\}(DMF)_{1.5}(H_2O)_9$ (Fig. 5.12).

It crystallizes in the cubic space group *I*-43d, with a large elemental cell of 35.53 Å and 44864 $Å^3$ of volume. The complex can be described as a {2}-metallacryptate (MCrypt) (Fig. 5.13), made of two 16-MC-6 rings fused together (Fig. 5.14). The complex possesses a $C_3$ symmetry, with the crystallographic $C_3$ axis passing through the centre of the unit. Due to the three-fold symmetry, the structure resembles a three-blade propeller, bearing an intrinsic Λ or Δ chirality (Fig. 5.15); both the chiral systems are present in the crystal lattice, since the space group *I*-43d is centrosymmetric.

Each one of the three identical blades constitutes half of the 16-MC-6 scaffold. The two 16-MC-6 scaffolds merge onto two shared Mn(II) ions, situated on the C3 axis, which act as the propeller hub around which the three blades pivot.

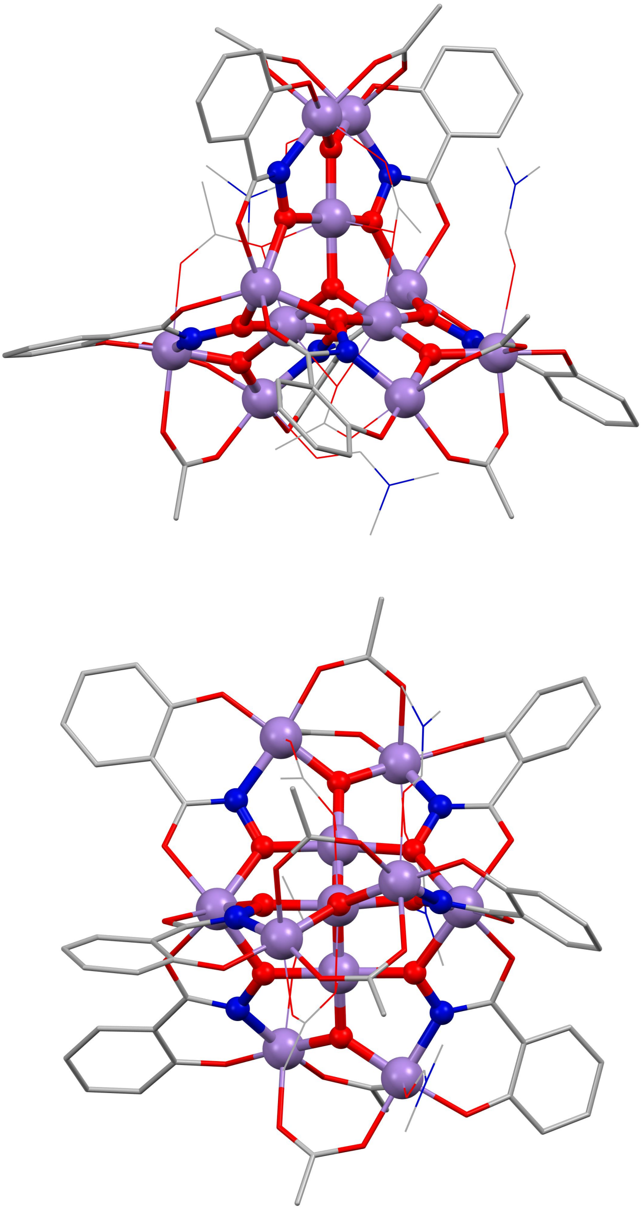

**Fig. 5.12**: Views of the molecular structure of the complex $\mathbf{Mn_{11}L_6}$, of formula $Na_4\{O \subset [(MCryp_{Mn(II)Mn(III)(\mu\text{-}O)N(Shi)})(OAc)_6(DMF)_3]\}(DMF)_{1.5}(H_2O)_9$. The propeller blades are represented in *capped stick* style, while the two 16-MC-6 coordination scaffolds are represented as *ball and stick*; additional solvent molecules and acetate ions are represented as *wireframe* for clarity. Colour scheme: violet - $Mn^{n+}$, red - oxygen, blue - nitrogen, grey - carbon.

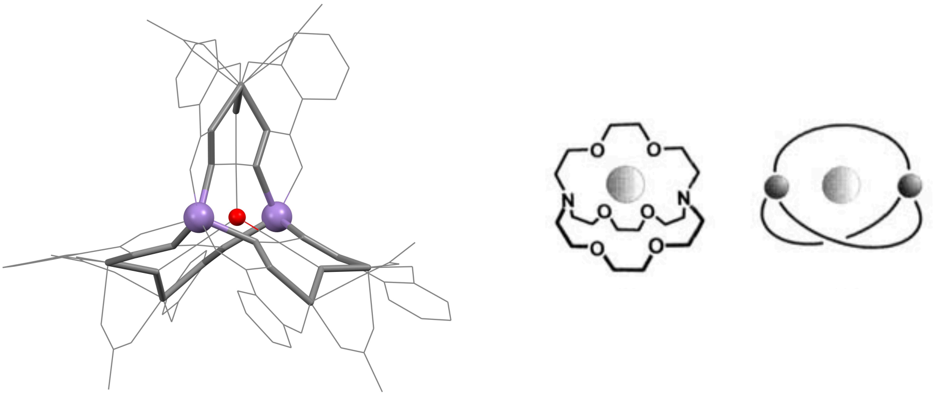

**Fig. 5.13**: The {2}-metallacryptate topology of $\mathbf{Mn_{11}L_6}$ (left); generic schemes of a {2}-cryptate (centre) and of a {2}-metallacryptate (right).[28] All atoms are coloured in grey for displaying purposes, besides the two pivoting Mn(II) ions (violet) and the cryptate $\mu_3$-$O^{2-}$ ion (red).

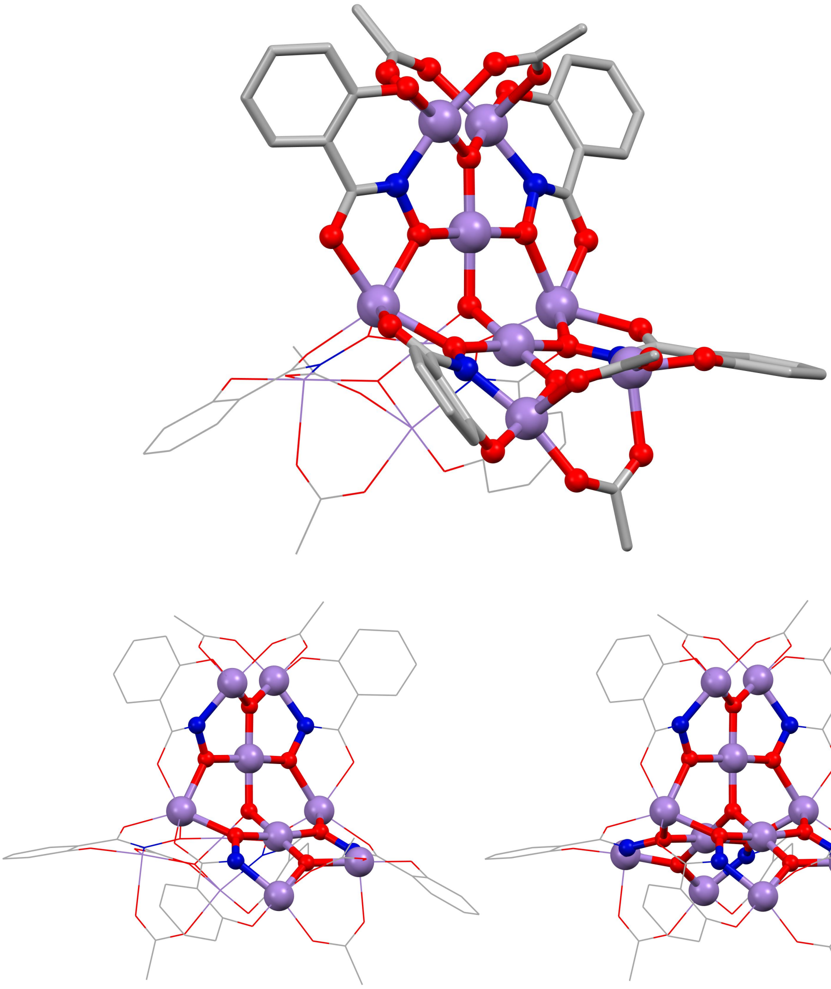

**Fig. 5.14**: Above, structure of one 16-MC-6 scaffold is highlighted, the fraction of the second connected 16-MC-6 is displayed as *wireframe*; below left, the coordination ring of one 16-MC-6 is highlighted; below right, the complete coordination scaffold is shown, constituted by the two fused 16-MC-6. Colour scheme: violet - $Mn^{n+}$, red - oxygen, blue - nitrogen, grey - carbon.

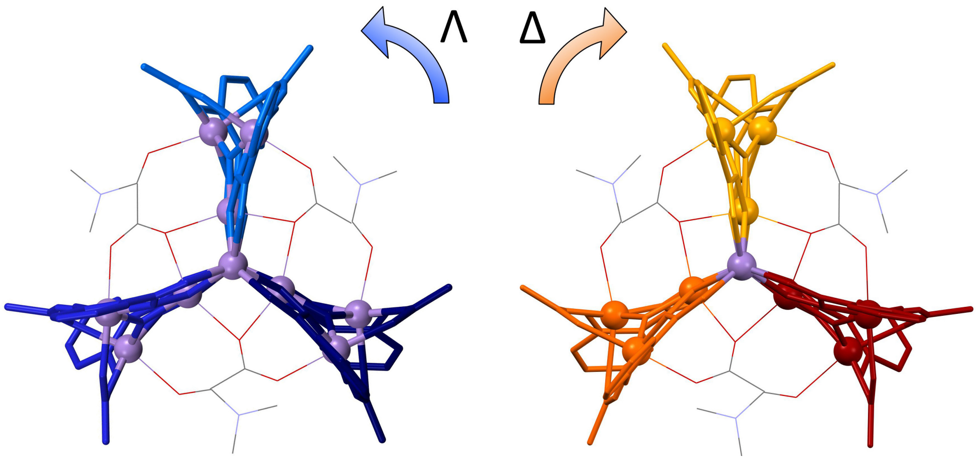

**Fig. 5.15**: Propeller-like structure of the complex **$Mn_{11}L_6$**; Λ or Δ chirality of the objects is shown. Colours have been customized for displaying purposes, each blade is represented in a different colour, manganese ions are coloured in violet, DMF and three acetate ions are shown as *wireframe*.

The compound comprises 11 manganese ions, 6 fully deprotonated Shi ligands, 9 acetate ions and 4 oxide ions $O^{2-}$, which will be discussed more in detail further on (Fig. 5.16 and Fig. 5.17). Of the 11 manganese ions, 9 are in the +3 oxidation state (namely Mn1, Mn4 and Mn5), as testified by the pronounced Jahn-Teller distortion on the apical positions, and 2 are in the +2 oxidation state (Mn2 and Mn3), and show a peculiar trigonal prismatic coordination geometry (selected coordination bond lengths are reported in Table 5.1, the complete crystallographic tables are reported in the Supplementary Information). The latter Mn(II) ions (Mn2 and Mn3) connect the three blades, while the 9 Mn(III) ions (Mn1, Mn4 and Mn5) form the blades. Two molecules of Shi and two acetate ions concur in the formation of each tilted blade of the MCrypt, together with the three Mn(III) ions Mn1, Mn4 and Mn5 and with the two shared Mn(II) ions. The $Mn^{III}1$ ion has a peculiar coordination, since it is coordinated by two independent $\mu_3$-oxide ions, namely $\mu_3$-O19 and $\mu_3$-O29 (described more in detail further on). The octahedral coordination of Mn1 is completed by 2 $Shi^{3-}$ oxygen atoms and 2 oxygen atoms from the acetate ions.

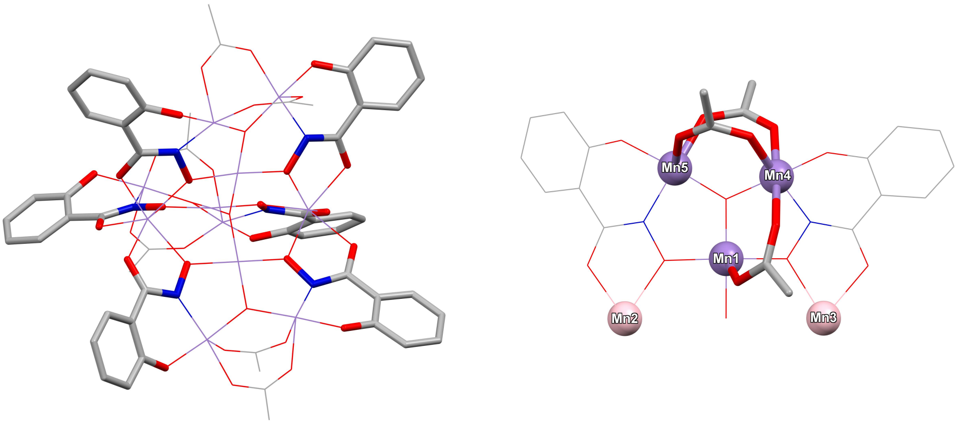

**Fig. 5.16**: Left, representation of the six salicylhydroximate ligands; right, the three different acetate ions present on each blade of the propeller, the other 6 ions are symmetry-related. Colour scheme: violet - Mn(III), pink - Mn(II), red - oxygen, blue - nitrogen, grey - carbon.

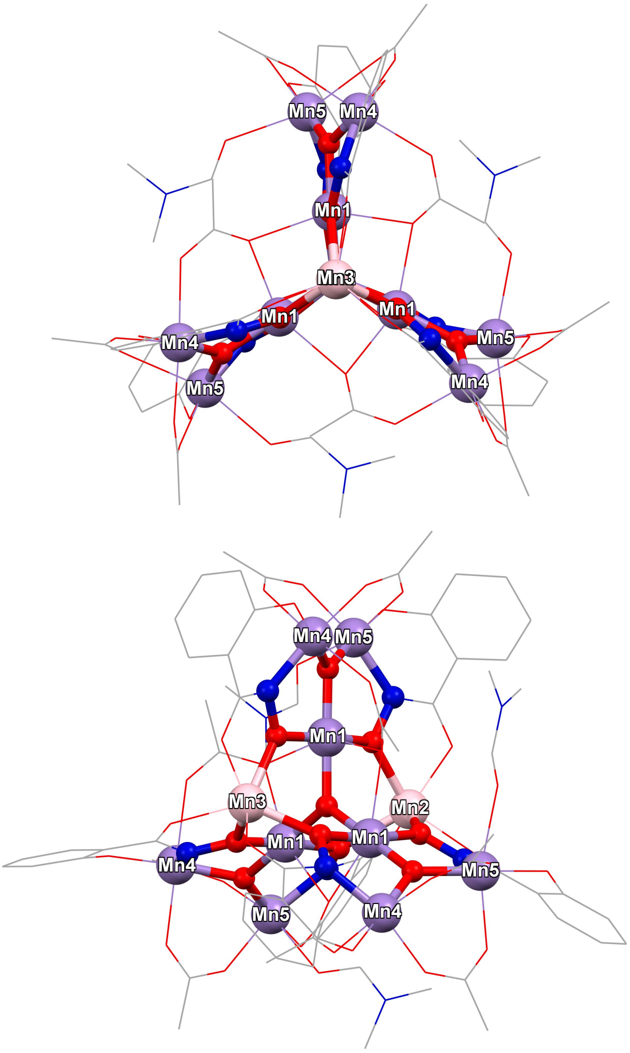

**Fig. 5.17**: Representation of the 11 manganese ions contained in the molecular structure of **$\mathbf{Mn_{11}L_6}$**. The 2 Mn(II) ions (Mn2 and Mn3) are coloured in pink, the 9 Mn(III) ions are coloured in violet. Colour scheme: red - oxygen, blue - nitrogen, grey - carbon.

**Table 5.1**: Coordination bond lengths for the complex **$Mn_{11}L_6$**. Refer to Supplementary Information for the complete list of bond lengths and angles.

| **$Mn_{11}L_6$** - Lengths (Å) | | | |
|---|---|---|---|
| Mn(1)-O(19) | 1.8651(10) | Mn(4)-O(31) | 1.862(5) |
| Mn(1)-O(29) | 1.866(5) | Mn(4)-O(29) | 1.887(5) |
| Mn(1)-O(21) | 1.909(5) | Mn(4)-N(11) | 1.975(6) |
| Mn(1)-O(22) | 1.922(5) | Mn(4)-O(25) | 2.005(5) |
| Mn(1)-O(14) | 2.251(5) | Mn(4)-O(26) | 2.191(6) |
| Mn(1)-O(14)#1 | 2.401(5) | Mn(4)-O(24) | 2.321(6) |
| Mn(2)-O(12) | 2.173(5) | Mn(5)-O(29) | 1.873(5) |
| Mn(2)-O(12)#2 | 2.173(5) | Mn(5)-O(32) | 1.881(5) |
| Mn(2)-O(12)#1 | 2.173(5) | Mn(5)-N(12) | 1.967(6) |
| Mn(2)-O(22)#1 | 2.186(5) | Mn(5)-O(16) | 1.995(6) |
| Mn(2)-O(22)#2 | 2.186(5) | Mn(5)-O(15) | 2.142(5) |
| Mn(2)-O(22) | 2.186(5) | Mn(5)-O(17) | 2.383(7) |
| Mn(3)-O(11) | 2.166(6) | | |
| Mn(3)-O(11)#1 | 2.166(6) | | |
| Mn(3)-O(11)#2 | 2.166(6) | | |
| Mn(3)-O(21) | 2.192(5) | | |
| Mn(3)-O(21)#2 | 2.192(5) | | |
| Mn(3)-O(21)#1 | 2.192(5) | | |

Symmetry codes: #1 = -y+1, z-1/2, -x+3/2; #2 = -z+3/2, -x+1, y+1/2.

The architecture of each blade is similar to that observed for the compound $Dy^{III}(OAc)(NO_3)_2[14\text{-}MC_{Mn(III)Dy(III)(\mu\text{-}O)(\mu\text{-}OH)N(Shi)}\text{-}5]\cdot(C_3H_7NO)_3\cdot(C_5H_5N)_7\cdot H_2O$[29] (Fig. 5.18), although in **$Mn_{11}L_6$** each blade is featured in a more complex metallacryptate structure.

By comparing these two solid state structures (Fig. 5.19), it is evident that the presence of the larger Dy(III) ion in the first compound widens the coordination ring, by imposing more distance between the two Mn1 ions ($d_{Mn1\text{-}Mn1}$ = 7.16 Å), compared to the structure of **$Mn_{11}L_6$**, where Mn2 and Mn3 are kept closer to each other ($d_{Mn2\text{-}Mn3}$ = 6.23 Å). This structural feature influences the distance between the two Mn2 ions on the opposite side of the Dy(III)[14-MC$_{Mn(III)Dy(III)}$-5] scaffold, which are 2.80 Å apart, compared with the ions Mn4 and Mn5 of **$Mn_{11}L_6$**, which are distanced by 3.33 Å. Hence, due to the shorter distance between the Mn2 ions, the first structures is characterized by a $\mu_2$-OH (O8) bridge, while **$Mn_{11}L_6$** exhibits two bridging acetate ions (Fig. 5.19).

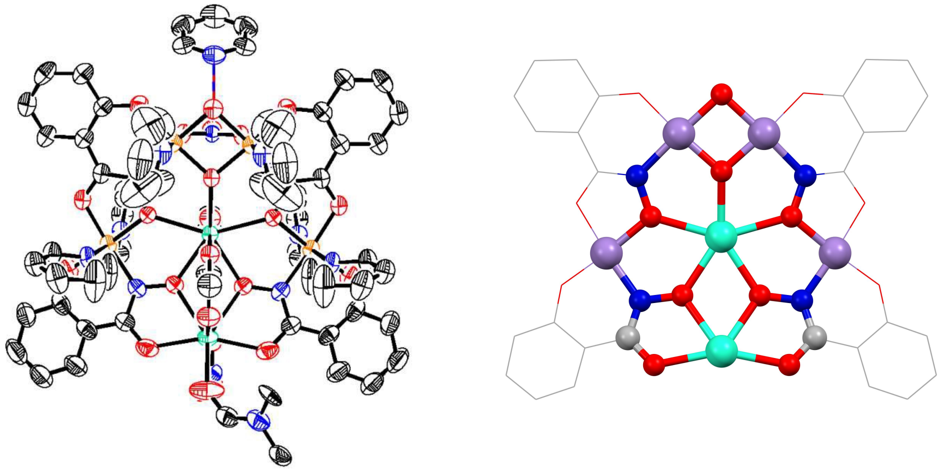

**Fig. 5.18**: Structure of the complex $Dy^{III}(OAc)(NO_3)_2[14\text{-}MC_{Mn(III)Dy(III)(\mu\text{-}O)(\mu\text{-}OH)N(Shi)}\text{-}5]\cdot(C_3H_7NO)_3\cdot(C_5H_5N)_7\cdot H_2O$;[29] the metallacrown coordination scaffold is highlighted. Colour scheme: violet - Mn(III), aqua - Dy(III), red - oxygen, blue - nitrogen, grey - carbon. On the right, solvent molecules and counterions are omitted for clarity.

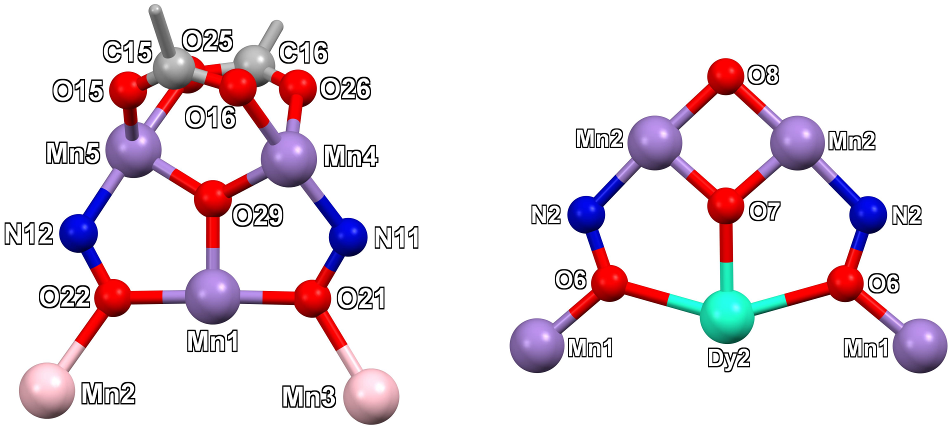

**Fig. 5.19**: Comparison between the analogous coordination scaffolds of complexes **$Mn_{11}L_6$** and of $Dy^{III}(OAc)(NO_3)_2[14\text{-}MC_{Mn(III)Dy(III)(\mu\text{-}O)(\mu\text{-}OH)N(Shi)}\text{-}5]\cdot(C_3H_7NO)_3\cdot(C_5H_5N)_7\cdot H_2O$.[29]

**Table 5.2**: Selected bond lengths of the two coordinating scaffolds of **$Mn_{11}L_6$** and of Dy(III)(OAc)($NO_3$)$_2$[14-MC$_{\text{Mn(III)Dy(III)}}$-5].

| Bond lengths (Å) | | | |
|---|---|---|---|
| **$Mn_{11}L_6$** | | Dy(III)[14-MC$_{\text{Mn(III)Dy(III)}}$-5] | |
| Mn(3)-O(21) | 2.192(5) | Mn(1)-O(6) | 1.937(4) |
| O(21)-N(11) | 1.419(8) | O(6)-N(2) | 1.427(6) |
| Mn(4)-N(11) | 1.975(6) | N(2)-Mn(2) | 1.998(5) |
| O(29)-Mn(4) | 1.887(5) | O(7)-Mn(2) | 1.878 |
| O(29)-Mn(5) | 1.873(5) | O(7)-Mn(2) | 1.878 |
| Mn(5)-N(12) | 1.967(6) | Mn(2)-N(2) | 1.998(5) |
| N(12)-O(22) | 1.412(7) | N(2)-O(6) | 1.427(6) |
| O(22)-Mn(2) | 2.186(5) | O(6)-Mn(1) | 1.937(4) |
| O(22)-Mn(1) | 1.922(5) | O(7)-Dy(2) | 2.223 |
| Mn(1)-O(29) | 1.866(5) | O(6)-Dy(2) | 2.414 |
| O(21)-Mn(1) | 1.909(5) | Dy(2)-O(6) | 2.414 |
| O(21)-O(22) | 3.826(7) | O(6)-O(6) | 4.647(5) |

One μ$_3$-oxide ion (O19) is situated in the very centre of the structure, laying on the C3 axis, and represents the anionic guest included in the metallacryptate (a more detailed description of the metallacryptate motif will be given further on). The second μ$_3$-oxide (O29) is found within the blades, between Mn4 and Mn5, and Mn1. Thus, while only one cryptate O19 ion is contained in the whole MCrypt unit, three symmetry equivalent O29 ions can be found in the cryptate blades (Fig. 5.20).

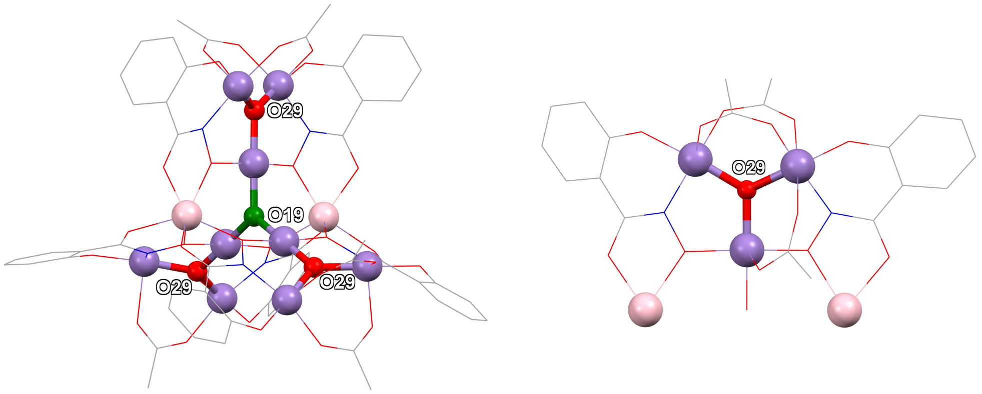

**Fig. 5.20**: Left, the four $\mu_3$-O$^{2-}$ ions are highlighted along with the 11 manganese ions; the three $\mu_3$-O29 ions contained in the blades are coloured in red, while the central $\mu_3$-O19 ion guest is coloured in green for clarity. Right, focus on the $\mu_3$-O29 found in each blade. Colour scheme: violet - Mn(III), pink - Mn(II), red - oxygen, blue - nitrogen, grey - carbon.

The two Mn4 and Mn5 ions are bridged by $\mu_3$-O29 and by two peripheral acetate ions. The presence of these two bridging acetates, generates another structural motif, called inverse MC, which is repeated four times within **Mn$_{11}$L$_6$**. Inverse MCs were previously illustrated by Pecoraro and coworkers.[15] Inverse MCs consist of metallamacrocycles that, as opposed to regular MCs, possess electron-poor scaffolds that bind anionic guest such as $\mu_3$-oxides, through Lewis acids (i.e. metal ions of the cavity) pointing inwards from the coordination ring. The $\mu_3$-oxide ion O29 can be envisaged as the anionic guest of an inverse 10-MC-3, bound to three Mn(III) ions (Mn1, Mn4 and Mn5), where the coordination ring is completed by one of the two bridging acetate residues. The *inv*10-MC-3 scaffold here described resembles other 9-MC-3 structures previously reported in literature.[15] Each blade of the propeller comprises one *inv*10-MC-3, accounting for three symmetrically equivalent inverse MCs of the total four contained within the structure.

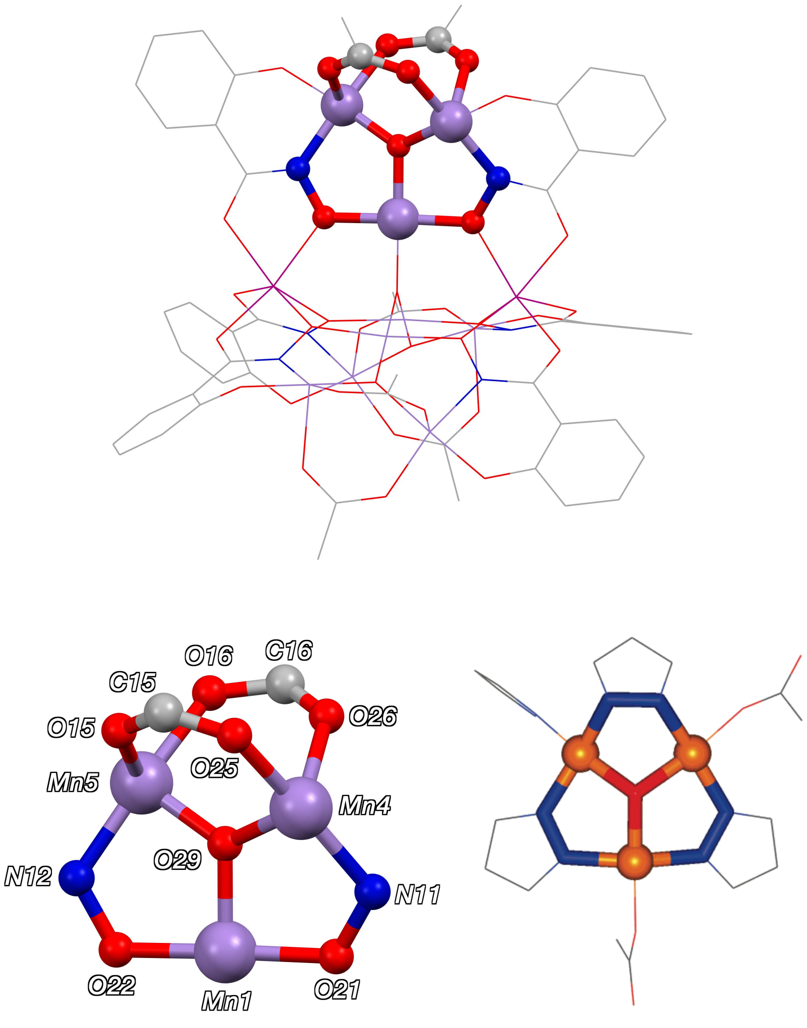

**Fig. 5.21**: Above, the *inv*10-MC-3 structure is highlighted as *ball and sticks* within the molecular structure. Below, focus on the *inv*10-MC-3 (left) and on the analogous *inv*9-MC-3 aza($\mu_3$-OH)[9-MC$_{\mathrm{Cu(II)}}$-3] (right).

This alternative description of the system, conceived by considering inverse MCs, requires the metallic guest ion Mn1 to become part of the inverse MC ring, while the $\mu_3$-oxide of the blade becomes the anionic guest of the *inv*10-MC-3.

By looking at the Mn$_{11}$L$_6$ assembly from a different supramolecular perspective, **Mn$_{11}$L$_6$** represents a {2}-metallacryptate. Metallacryptands are three-dimensional metallamacrocycles and, as metallacrowns are considered the inorganic analogs of crown ethers, metallacryptands are the inorganic equivalents of cryptands.[28] Ideally, the nitrogen atoms responsible of connecting crown ethers together to form cryptands, must be substituted by metal centres in order to give rise to metallacryptands. In general, cryptands and metallacryptands have electron-rich atoms pointing inward towards the centre of their cavity, allowing them to bind neutral or ionic guests stronger and with better selectivity then their two-dimensional equivalents.[30] When a guest molecule or ion is bound to the scaffold, the structure becomes a cryptate or a metallacryptate.

**Fig. 5.22**: Simplified scheme displaying the structural analogies between cryptands, interconnected crown ethers, and metallacryptands.

The $\mu_3$-O19 oxide ion is the guest of the metallacryptate **Mn$_{11}$L$_6$**, which is in fact an inverse-metallacryptate, since three Lewis acid ions point toward the centre of the scaffold and are bound to an anionic species. The $O^{2-}$ ion is located in the centre of the cryptand and is bound to the three symmetry equivalent Mn1 ions. Three $\mu_2$-O14 oxygen atoms belonging to "core" acetate ions link the three Mn1 ions, establishing a second inverse metallacrown. The so formed *inv*6-MC-3 is a subunit of the metallacryptate cage.

The cage within which the $\mu_3$-O19 is encapsulated is a $Mn_5O_9$ cluster and is the central core of the **Mn$_{11}$L$_6$** structure. It is formed from the three Mn(III) (Mn1) and two Mn(II) (Mn2 and Mn3), bridged by six hydroximate oxygen atoms of the six different Shi ligands (O22 and O21) and by the three acetate oxygen ions (O14).

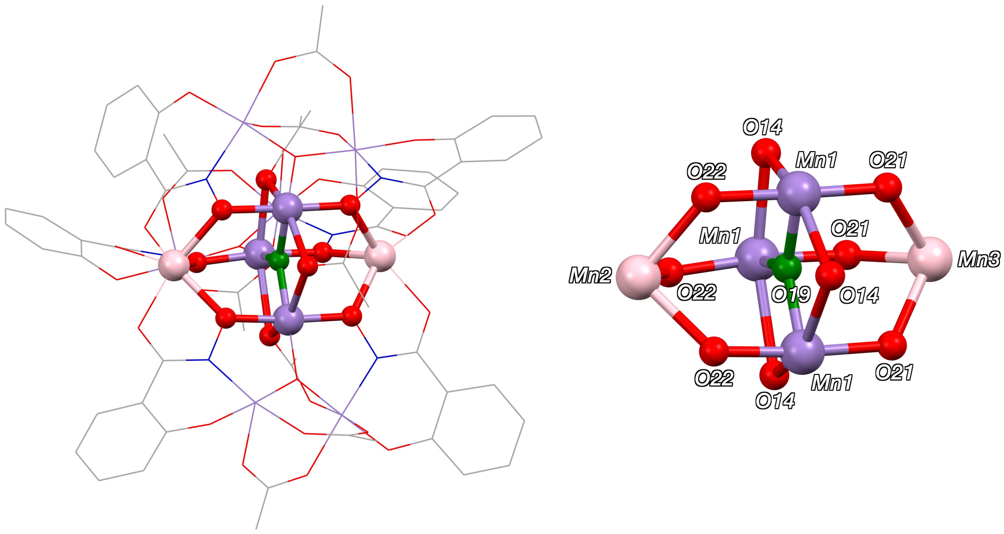

**Fig. 5.23**: Representation of the metallacryptate scaffold within the molecular unit, the coordinating cage is highlighted. The central $\mu_3$-O19 oxide ion is coloured in green for displaying purposes. Colour scheme: violet - Mn(III), pink - Mn(II), red - oxygen, blue - nitrogen, grey - carbon.

The total charge of the so far described structure is -4. Charge balance is achieved with 4 $Na^+$ ions, occupying eight different positions within the molecular structure, all with a partial occupancy of 0.5.

On every blade of the propeller, two symmetry-equivalent $Na^+$ ions (Na1) are located near Mn4 and Mn5 acting as coordination bridges, each one of them linking the MCrypt with another MCrypt unit. Partial occupancy of the $Na^+$ ions is motivated by the fact that each ion is shared by two adjacent MCrypt units.

In fact, the coordination of Na1 is established with two Shi phenolic oxygen atoms and two oxygen atoms of two peripheral acetate ions, all belonging to two different MCrypt units, and with a DMF and a water molecule (Fig. 5.24).

Through the $Na^+$ bridges, each MCrypt is surrounded by six indentical MCrypt units; such coordination links between MCrypt units effectively establish a 3D coordination framework of **$Mn_{11}L_6$** metallacryptates. Since each MCrypt unit lays on a $C_3$ axis of a cubic crystal cell, the units are disposed at 60° from each other along the bisectors of the cell angles, as can be observed along the direction 1,1,1 in Fig. 5.25.

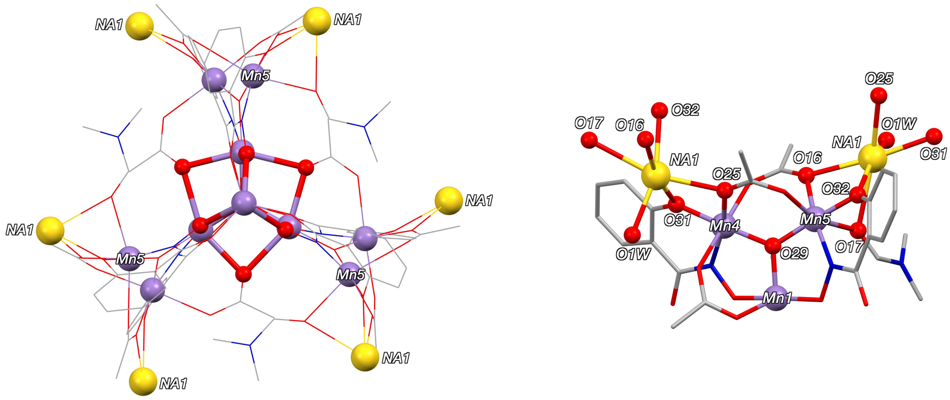

**Fig. 5.24**: Left, view along the $C_3$ symmetry axis of the two symmetry-equivalent Na1 ions, bridging two MCrypt units. Having a partial occupancy of 0.5, each MCrypt unit is bound to three other cryptate units. Right, Detail of the coordination of the symmetry-equivalents Na1 ions. Colour scheme: yellow - Na(I), violet - $Mn^{n+}$, red - oxygen, blue - nitrogen, grey - carbon.

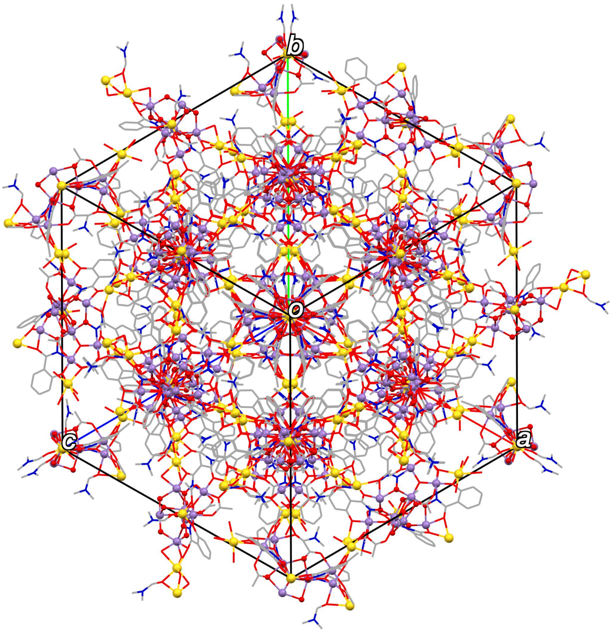

**Fig. 5.25**: Crystal packing of the structure of **$Mn_{11}L_6$**, view along the crystallographic direction 1,1,1. Colour scheme: yellow - Na(I), violet - $Mn^{n+}$, pink - Mn(II), red - oxygen, blue - nitrogen, grey - carbon.

An additional fourth $Na^+$ ion is present in the MCrypt structure for charge balance. This ion is found with a 0.5 partial occupancy in two different positions, near $Mn^{II}2$ and $Mn^{II}3$ (adopting the label Na3 and Na2 respectively).

Both six-coordinate Na2 and Na3 are bound to three carbonyl oxygen atoms of three $Shi^{3-}$ ligands; their coordination is completed by three DMF molecules (Na2) or three water molecules (Na3) having a partial occupancy of 0.5.

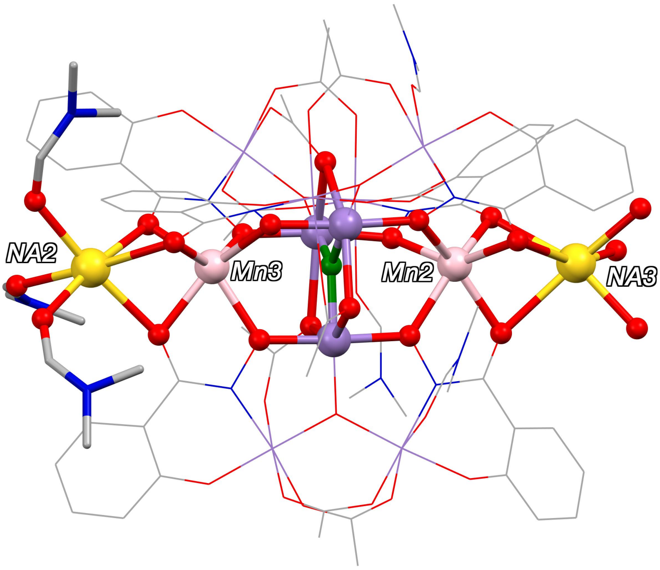

**Fig. 5.26**: Representation of the two Na(I) ions with partial occupancy of 0.5 located next to Mn2 and Mn3. Three molecules of DMF and three water molecules of 0.5 partial occupancy coordinated to Na2 and Na3 are shown; the metallacryptate scaffold is highlighted. Colour scheme: yellow - Na(I), green - $\mu_3$-O19, violet - Mn(III), pink - Mn(II), red - oxygen, blue - nitrogen, grey - carbon.

Although the structural repetition of **$Mn_{11}L_6$** units within the crystal designs a well-defined 3D network and narrow 1D dimensional channels that run parallel to each of the three crystallographic axes, such channels are occupied by DMF and water molecules. Therefore, the structure cannot be described as a porous coordination polymer or framework, as the structure lacks voids within the lattice. The voids within the structure, calculated through a probe of radius 1.2 Å, account for just 1.6% of the total cell volume.

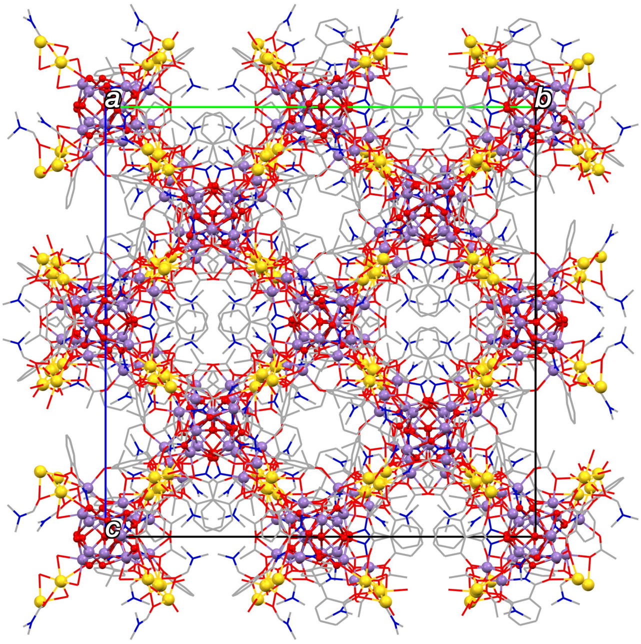

**Fig. 5.27**: Crystal packing of the structure of **$Mn_{11}L_6$**, view along the *a*-axes. Colour scheme: yellow - Na(I), violet - $Mn^{n+}$, pink - Mn(II), red - oxygen, blue - nitrogen, grey - carbon.

## 5.4 - Conclusions

A novel manganese-based metallacryptate system was isolated in the solid state and characterized. Its synthesis was optimized and the compound is obtainable in high yields.

The compound is characterized by a M:L:A ratio of 11:6:9, where M is manganese, L is salicylhydroximate and A is acetate. Of the 11 manganese ions, nine are in the +3 oxidation state and two in the +2 state.

The structure is composed of two16-MC-6 fused together and it coordinates a central $\mu_3$-$O^{2-}$ ion in a stable and closed *inv*9-MC-3 environment, thus it is defined as a metallacryptate.

The complex topology was compared to a three-blade propeller, with the three blades (consisting of half of 16-MC-6 unit each) merge on two pivotal Mn(II) ions, located on a $C_3$ symmetry axis. Hence, the blades confer to the propeller an intrinsic Λ or Δ chirality. Both isomers are present in the crystal structure.

Furthermore, each of the blades entails a *inv*10-MC-3 scaffold, where three Mn(III) ions are bound to a central $\mu_3$-$O^{2-}$ ion. Thus, the structure coordinates a total of four $\mu_3$-$O^{2-}$ ions within four separated *inverse* metallacrown scaffolds.

The large number of manganese ions within the metallacryptate might confer interesting magnetic properties to the solid. In the future, magnetic characterization will be pursued on the solid to seek for a magnetic, possibly SMM, behaviour. Due to the different coordination environments of the manganese ions and to the limited degree of symmetry of the structure, a complete magnetic characterization, in order to investigate a possible SMM behaviour, might be difficult to accomplish.

## 5.5 - Supplementary Information

### 5.4.1 - Synthesis

The first time this synthesis was conducted, the intended goal was to isolate a Mn(III) 12-MC-4 bearing a Cu(II) ion in the central position, of theoretical formula Cu(II)[12-MC$_{Mn(III)N(Shi)}$-4]. Therefore, the synthetic procedure followed had different stoichiometry with respect to the optimized synthesis of $Mn_{11}L_6$ reported in paragraph 5.2.2.

**Table 5.3**: Equivalents of reagents used in the attempts to prepare the elusive product Cu(II)[12-MC$_{Mn(III)N(Shi)}$-4], and the optimization of the synthesis to produce $Mn_{11}L_6$.

| | Mn(II | Cu(II) | Salt | $H_3$Shi | Na(I) | Salt |
|---|---|---|---|---|---|---|
| $Cu^{II}$[12-MC$_{Mn(III)}$-4] | 4 | 1 | $Cu(OAc)_2$ | 4 | 8 | NaOAc |
| | 4 | 0.25 | $Cu(OAc)_2$ | 4 | 0.25 | NaOAc |
| | 4 | 1 | $Cu(NO_3)_2$ | 4 | 8 | NaOAc |
| | 4 | 0.25 | $Cu(NO_3)_2$ | 4 | 8 | NaOAc |
| | 4 | 0.25 | $Cu(NO_3)_2$ | 4 | 8 | NaOBz |
| | 4 | 0.25 | $Cu(NO_3)_2$ | 4 | 8 | NaOSal |
| | 4 | 0.25 | $Cu(NO_3)_2$ | 4 | 8 | NaOTer |
| | 4 | 0.25 | $Cu(NO_3)_2$ | 4 | 8 | NaOH |
| | 4 | 0.25 | $Cu(NO_3)_2$ | 4 | 8 | KOBz |
| | 11 | 0 | | 6 | 8 | NaOBz |
| | 4 | 0 | | 4 | 8 | NaOSal |
| | 11 | 0 | | 6 | 8 | NaOSal |
| | 11 | 0 | | 6 | 8 | NaOTer |
| | 11 | 0 | | 6 | 8 | NaOH |
| | 11 | 0 | | 6 | 8 | KOBz |
| | 11 | 0 | | 6 | 5.5 | $NaNO_3$ |
| | 11 | 0 | | 6 | 1.2 | $NaNO_3$ |
| | 11 | 0 | | 6 | 0.5 | $NaNO_3$ |

| | | | | | | |
|---|---|---|---|---|---|---|
| | 11 | 0 | | 6 | 8 | NaOAc |
| | 11 | 0 | | 6 | 4 | NaOAc |
| | 11 | 0 | | 6 | 2 | NaOAc |
| | 11 | 0 | | 6 | 0.5 | NaOAc |
| | 15 | 0 | | 6 | 1 | NaOAc |
| | 22 | 0 | | 9 | 1.5 | NaOAc |
| | | | | | | |
| Optimized synth.<br>**$Mn_{11}L_6$** | 15 | 0 | | 6 | 1 | NaOAc |
| | 2.5 | 0 | | 1 | 0.17 | |
| | Equivalents | | | | | |

The order in which the reagents were added was also different in the two reactions. While in the synthesis of $Mn_{11}L_6$ all the reagents are added as solids at the same time, the procedure for Cu(II)[12-$MC_{Mn(III)N(Shi)}$-4] followed a different order. Since the species Cu(II)-only 12-MC-4, of formula Cu(II)[12-$MC_{Cu(II)N(Shi)}$-4], is a well-document stable and kinetically favoured compound[26], the adding order had to avoid the formation of such species. The kinetic advantage of the Cu(II)[12-$MC_{Cu(II)}$-4] over the manganese counterpart was supported by a specific synthesis, where the two metals were added simultaneously: what was observed was the instantaneous formation of a deep green solution, typical of Cu(II)[12-$MC_{Cu(II)}$-4] species, which turned brown just much later, after about 10 minutes of stirring; this was observed despite the quantity of added Cu(II) was notably smaller, just one fourth of the total amount of added Mn(II). We therefore proceeded by adding manganese(II) acetate tetrahydrate to a solution of $H_3Shi$ and sodium acetate trihydrate in DMF. Copper(II) nitrate was finally added after 20 minutes of stirring, during which the Mn(II)[12-$MC_{Mn(III)N(Shi)}$-4] should have already formed. This way, we hoped to induce the displacement of the more labile central Mn(II) ion, in favour of the Cu(II) ion and obtain the heterometallic compound Cu(II)[12-$MC_{Mn(III)N(Shi)}$-4].

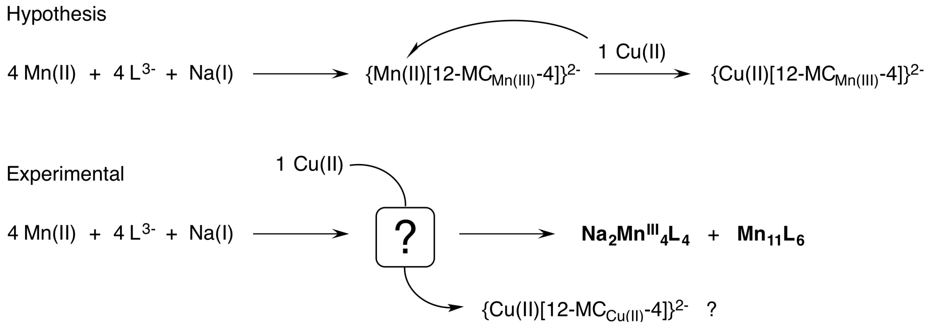

**Fig. 5.28**: Scheme of the theoretic synthetic approach and of the species experimentally formed.

Nevertheless, by slow evaporation of the obtained solution, two crystalline phases were formed:

1. $Na_2(OAc)_2[12\text{-}MC_{MnIII(N)shi}\text{-}4](DMF)_6 \cdot 2DMF \cdot 1.60H_2O$
   (referred to as $\mathbf{Na_2Mn_4L_4}$);
2. $Na_4\{O \subset [(MCryp_{Mn(II)Mn(III)(\mu\text{-}O)N(Shi)})(OAc)_6(DMF)_3]\}(DMF)_{1.5}(H_2O)_9$
   (referred to as $\mathbf{Mn_{11}L_6}$).

Compound $\mathbf{Na_2Mn_4L_4}$ was reported in literature[27] and is characterized by the replacement of the central guest ion by two sodium ions laying above and below the MC plane, with the coordinating oxygen atoms of the MC establishing a *side-on* coordination on the sodium ions. No Cu(II) ions were contained within this structure.

Compound $\mathbf{Mn_{11}L_6}$ does not comprise Cu(II) ions either and possesses a M:L ratio which is significantly different from the ratio used. Such results were found to be reproducible, and the synthesis was then optimized as described in Table 5.3.

By analysing the peculiar outcome of such a synthesis, we developed the following hypothesis:

1. The straightforward synthetic approach followed did not allow the isolation of any heterometallic Cu(II)/Mn(III) metallacrown species, possibly due to a thermodynamically and kinetically favoured $Cu(II)[12\text{-}MC_{Cu(II)}\text{-}4]$ species, although this was never isolated in our procedure, maybe due to its high solubility in the crystallization solvents used;
2. The formation of such $Cu(II)[12\text{-}MC_{Cu(II)}\text{-}4]$ species possibly reduces the available amount of ligand, inducing an excess of metal equivalents, giving rise to the $Mn_{11}L_6$ species of odd M:L ratio.

3. The $Mn_{11}L_6$ structure denotes a higher stability compared to the other possible reaction products.

## 5.4.2 - Crystal Structure

**Table 5.4**: Summary of X-ray crystallographic data for **$Mn_{11}L_6$**.

| | **$Mn_{11}L_6$** |
|---|---|
| Empirical formula | $Mn_{11}C_{73.5}H_{100.5}N_{10.5}Na_4O_{53.5}$ |
| Formula weight | 2683.44 |
| Colour, habit | Brown, block |
| Crystal size, mm | 0.34x0.30x0.30 |
| Crystal system | Cubic |
| Space group | I -4 3 d |
| *a*, Å | 35.533(2) |
| *b*, Å | 35.533(2) |
| *c*, Å | 35.533(2) |
| α, deg. | 90 |
| β, deg. | 90 |
| γ, deg. | 90 |
| $V$, Å$^3$ | 44864(8) |
| *Z* | 16 |
| *T*, K | 293(2) K |
| *r* (calc), Mg/m$^3$ | 1.589 |
| *m*, mm$^{-1}$ | 1.303 |
| *q* range, deg. | 1.40 to 25.67 |
| No.of rflcn/independ. | 185176 / 7104 |
| GooF | 1.004 |
| *R*1 | 0.0596 |
| *wR*2 | 0.1353 |

$R1 = \Sigma||F_o|-|F_c||/\Sigma|F_o|$, $wR2 = [\Sigma[w(F_o^2-F_c^2)^2]/\Sigma[w(F_o^2)^2]]^{½}$, $w = 1/[\sigma^2(F_o^2) + (aP)^2 + bP]$, where $P = [\max(F_o^2,0) + 2F_c^2]/3$

**Table 5.5**: Selected bond lengths (Å) for **Mn$_{11}$L$_{6}$**.

| **Mn$_{11}$L$_{6}$** - Lengths (Å) | | | |
|---|---|---|---|
| Mn(1)-O(19) | 1.8651(10) | Mn(4)-O(31) | 1.862(5) |
| Mn(1)-O(29) | 1.866(5) | Mn(4)-O(29) | 1.887(5) |
| Mn(1)-O(21) | 1.909(5) | Mn(4)-N(11) | 1.975(6) |
| Mn(1)-O(22) | 1.922(5) | Mn(4)-O(25) | 2.005(5) |
| Mn(1)-O(14) | 2.251(5) | Mn(4)-O(26) | 2.191(6) |
| Mn(1)-O(14)#1 | 2.401(5) | Mn(4)-O(24) | 2.321(6) |
| Mn(1)-Mn(4) | 3.1642(14) | Mn(4)-Na(1) | 3.474(4) |
| Mn(1)-Mn(5) | 3.2301(14) | Mn(5)-O(29) | 1.873(5) |
| Mn(1)-Mn(1)#2 | 3.2302(17) | Mn(5)-O(32) | 1.881(5) |
| Mn(1)-Mn(1)#1 | 3.2303(17) | Mn(5)-N(12) | 1.967(6) |
| Mn(2)-O(12) | 2.173(5) | Mn(5)-O(16) | 1.995(6) |
| Mn(2)-O(12)#2 | 2.173(5) | Mn(5)-O(15) | 2.142(5) |
| Mn(2)-O(12)#1 | 2.173(5) | Mn(5)-O(17) | 2.383(7) |
| Mn(2)-O(22)#1 | 2.186(5) | Mn(5)-Na(1)#3 | 3.200(3) |
| Mn(2)-O(22)#2 | 2.186(5) | | |
| Mn(2)-O(22) | 2.186(5) | | |
| Mn(2)-Na(3) | 3.027(17) | | |
| Mn(3)-O(11) | 2.166(6) | | |
| Mn(3)-O(11)#1 | 2.166(6) | | |
| Mn(3)-O(11)#2 | 2.166(6) | | |
| Mn(3)-O(21) | 2.192(5) | | |
| Mn(3)-O(21)#2 | 2.192(5) | | |
| Mn(3)-O(21)#1 | 2.192(5) | | |
| Mn(3)-Na(2) | 3.088(11) | | |

Symmetry codes: #1 -y+1,z-1/2,-x+3/2; #2 -z+3/2,-x+1,y+1/2;
#3 y-1/4,-x+5/4,-z+7/4.

**Table 5.6**: Selected bond angles (°) for **Mn$_{11}$L$_6$**.

| **Mn$_{11}$L$_6$** - Angles (°) | | | |
|---|---|---|---|
| O(19)-Mn(1)-O(29) | 179.0(2) | O(11)#2-Mn(3)-Na(2) | 52.23(15) |
| O(19)-Mn(1)-O(21) | 89.1(3) | O(21)-Mn(3)-Na(2) | 122.20(14) |
| O(29)-Mn(1)-O(21) | 91.3(2) | O(21)#2-Mn(3)-Na(2) | 122.20(14) |
| O(19)-Mn(1)-O(22) | 88.6(3) | O(21)#1-Mn(3)-Na(2) | 122.20(14) |
| O(29)-Mn(1)-O(22) | 91.2(2) | O(12)-Mn(2)-O(12)#2 | 90.4(2) |
| O(21)-Mn(1)-O(22) | 174.0(2) | O(12)-Mn(2)-O(12)#1 | 90.4(2) |
| O(19)-Mn(1)-O(14) | 77.90(13) | O(12)#2-Mn(2)-O(12)#1 | 90.4(2) |
| O(29)-Mn(1)-O(14) | 101.1(2) | O(12)-Mn(2)-O(22)#1 | 146.5(2) |
| O(21)-Mn(1)-O(14) | 88.6(2) | O(12)#2-Mn(2)-O(22)#1 | 117.0(2) |
| O(22)-Mn(1)-O(14) | 96.4(2) | O(12)#1-Mn(2)-O(22)#1 | 71.62(19) |
| O(19)-Mn(1)-O(14)#1 | 74.09(12) | O(12)-Mn(2)-O(22)#2 | 117.0(2) |
| O(29)-Mn(1)-O(14)#1 | 106.9(2) | O(12)#2-Mn(2)-O(22)#2 | 71.62(19) |
| O(21)-Mn(1)-O(14)#1 | 86.8(2) | O(12)#1-Mn(2)-O(22)#2 | 146.5(2) |
| O(22)-Mn(1)-O(14)#1 | 87.2(2) | O(22)#1-Mn(2)-O(22)#2 | 91.18(18) |
| O(14)-Mn(1)-O(14)#1 | 151.66(18) | O(12)-Mn(2)-O(22) | 71.62(19) |
| O(19)-Mn(1)-Mn(4) | 147.0(2) | O(12)#2-Mn(2)-O(22) | 146.5(2) |
| O(29)-Mn(1)-Mn(4) | 32.74(15) | O(12)#1-Mn(2)-O(22) | 117.0(2) |
| O(21)-Mn(1)-Mn(4) | 63.85(14) | O(22)#1-Mn(2)-O(22) | 91.18(18) |
| O(22)-Mn(1)-Mn(4) | 120.13(14) | O(22)#2-Mn(2)-O(22) | 91.19(18) |
| O(14)-Mn(1)-Mn(4) | 82.72(13) | O(12)-Mn(2)-Na(3) | 55.03(15) |
| O(14)#1-Mn(1)-Mn(4) | 119.62(13) | O(12)#2-Mn(2)-Na(3) | 55.03(15) |
| O(19)-Mn(1)-Mn(5) | 149.7(2) | O(12)#1-Mn(2)-Na(3) | 55.03(15) |
| O(29)-Mn(1)-Mn(5) | 30.32(15) | O(22)#1-Mn(2)-Na(3) | 124.42(13) |
| O(21)-Mn(1)-Mn(5) | 119.42(15) | O(22)#2-Mn(2)-Na(3) | 124.42(13) |
| O(22)-Mn(1)-Mn(5) | 62.01(14) | O(22)-Mn(2)-Na(3) | 124.42(13) |
| O(14)-Mn(1)-Mn(5) | 110.61(14) | O(29)-Mn(5)-O(32) | 176.1(2) |
| O(14)#1-Mn(1)-Mn(5) | 95.92(12) | O(29)-Mn(5)-N(12) | 87.8(2) |
| Mn(4)-Mn(1)-Mn(5) | 62.73(3) | O(32)-Mn(5)-N(12) | 88.4(2) |
| O(19)-Mn(1)-Mn(1)#2 | 30.006(5) | O(29)-Mn(5)-O(16) | 94.1(2) |
| O(29)-Mn(1)-Mn(1)#2 | 149.01(17) | O(32)-Mn(5)-O(16) | 89.9(2) |
| O(21)-Mn(1)-Mn(1)#2 | 90.21(15) | N(12)-Mn(5)-O(16) | 165.9(2) |
| O(22)-Mn(1)-Mn(1)#2 | 90.54(14) | O(29)-Mn(5)-O(15) | 93.6(2) |
| O(14)-Mn(1)-Mn(1)#2 | 47.96(13) | O(32)-Mn(5)-O(15) | 86.1(2) |
| O(14)#1-Mn(1)-Mn(1)#2 | 104.09(12) | N(12)-Mn(5)-O(15) | 102.6(2) |
| Mn(4)-Mn(1)-Mn(1)#2 | 125.80(5) | O(16)-Mn(5)-O(15) | 91.3(2) |
| Mn(5)-Mn(1)-Mn(1)#2 | 145.21(4) | O(29)-Mn(5)-O(17) | 100.8(2) |

|  |  |  |  |
|---|---|---|---|
| O(19)-Mn(1)-Mn(1)#1 | 30.005(3) | O(32)-Mn(5)-O(17) | 80.3(2) |
| O(29)-Mn(1)-Mn(1)#1 | 150.96(17) | N(12)-Mn(5)-O(17) | 89.3(2) |
| O(21)-Mn(1)-Mn(1)#1 | 89.25(14) | O(16)-Mn(5)-O(17) | 76.6(2) |
| O(22)-Mn(1)-Mn(1)#1 | 85.93(14) | O(15)-Mn(5)-O(17) | 161.7(2) |
| O(14)-Mn(1)-Mn(1)#1 | 107.90(13) | O(29)-Mn(5)-Na(1)#3 | 136.98(18) |
| O(14)#1-Mn(1)-Mn(1)#1 | 44.14(12) | O(32)-Mn(5)-Na(1)#3 | 46.60(18) |
| Mn(4)-Mn(1)-Mn(1)#1 | 151.24(3) | N(12)-Mn(5)-Na(1)#3 | 122.19(19) |
| Mn(5)-Mn(1)-Mn(1)#1 | 131.67(5) | O(16)-Mn(5)-Na(1)#3 | 49.34(19) |
| Mn(1)#2-Mn(1)-Mn(1)#1 | 60 | O(15)-Mn(5)-Na(1)#3 | 106.95(18) |
| O(11)-Mn(3)-O(11)#1 | 86.4(2) | O(17)-Mn(5)-Na(1)#3 | 54.78(18) |
| O(11)-Mn(3)-O(11)#2 | 86.4(2) | O(29)-Mn(5)-Mn(1) | 30.18(14) |
| O(11)#1-Mn(3)-O(11)#2 | 86.4(2) | O(32)-Mn(5)-Mn(1) | 146.79(17) |
| O(11)-Mn(3)-O(21) | 71.0(2) | N(12)-Mn(5)-Mn(1) | 60.81(17) |
| O(11)#1-Mn(3)-O(21) | 121.5(2) | O(16)-Mn(5)-Mn(1) | 116.79(18) |
| O(11)#2-Mn(3)-O(21) | 141.5(2) | O(15)-Mn(5)-Mn(1) | 111.08(17) |
| O(11)-Mn(3)-O(21)#2 | 121.5(2) | O(17)-Mn(5)-Mn(1) | 86.78(17) |
| O(11)#1-Mn(3)-O(21)#2 | 141.5(2) | Na(1)#3-Mn(5)-Mn(1) | 139.90(8) |
| O(11)#2-Mn(3)-O(21)#2 | 71.0(2) | O(31)-Mn(4)-O(29) | 176.2(3) |
| O(21)-Mn(3)-O(21)#2 | 94.24(18) | O(31)-Mn(4)-N(11) | 89.7(2) |
| O(11)-Mn(3)-O(21)#1 | 141.5(2) | O(29)-Mn(4)-N(11) | 89.4(2) |
| O(11)#1-Mn(3)-O(21)#1 | 71.0(2) | O(31)-Mn(4)-O(25) | 82.4(2) |
| O(11)#2-Mn(3)-O(21)#1 | 121.5(2) | O(29)-Mn(4)-O(25) | 99.3(2) |
| O(21)-Mn(3)-O(21)#1 | 94.25(18) | N(11)-Mn(4)-O(25) | 165.3(3) |
| O(21)#2-Mn(3)-O(21)#1 | 94.24(18) | O(31)-Mn(4)-O(26) | 90.6(2) |
| O(11)-Mn(3)-Na(2) | 52.24(15) | O(29)-Mn(4)-O(26) | 85.9(2) |
| O(11)#1-Mn(3)-Na(2) | 52.23(16) | N(11)-Mn(4)-O(26) | 100.5(3) |
| O(25)-Mn(4)-O(26) | 92.0(2) | Mn(1)-O(29)-Mn(5) | 119.5(3) |
| O(31)-Mn(4)-O(24) | 89.9(2) | Mn(1)-O(29)-Mn(4) | 114.9(2) |
| O(29)-Mn(4)-O(24) | 93.7(2) | Mn(5)-O(29)-Mn(4) | 124.5(2) |
| N(11)-Mn(4)-O(24) | 83.6(2) | C(31)-C(21)-C(71) | 117.9(8) |
| O(25)-Mn(4)-O(24) | 84.0(2) | C(31)-C(21)-C(11) | 118.8(8) |
| O(26)-Mn(4)-O(24) | 175.9(2) | C(71)-C(21)-C(11) | 123.3(7) |
| O(31)-Mn(4)-Mn(1) | 148.75(18) | C(11)-N(11)-O(21) | 111.1(6) |

| | | | |
|---|---|---|---|
| O(29)-Mn(4)-Mn(1) | 32.32(14) | C(11)-N(11)-Mn(4) | 130.4(5) |
| N(11)-Mn(4)-Mn(1) | 62.71(17) | O(21)-N(11)-Mn(4) | 115.6(4) |
| O(25)-Mn(4)-Mn(1) | 120.70(17) | C(71)-O(31)-Mn(4) | 129.1(5) |
| O(26)-Mn(4)-Mn(1) | 107.85(17) | C(71)-O(31)-Na(1) | 119.4(5) |
| O(24)-Mn(4)-Mn(1) | 73.56(14) | Mn(4)-O(31)-Na(1) | 110.4(3) |
| O(31)-Mn(4)-Na(1) | 39.43(19) | C(15)-O(25)-Mn(4) | 131.6(5) |
| O(29)-Mn(4)-Na(1) | 143.20(17) | C(15)-O(25)-Na(1) | 128.4(5) |
| N(11)-Mn(4)-Na(1) | 122.70(19) | Mn(4)-O(25)-Na(1) | 99.6(2) |
| O(25)-Mn(4)-Na(1) | 45.69(18) | O(26)-C(16)-O(16) | 124.5(7) |
| O(26)-Mn(4)-Na(1) | 103.40(18) | O(26)-C(16)-C(26) | 119.7(9) |
| O(24)-Mn(4)-Na(1) | 74.49(15) | O(16)-C(16)-C(26) | 115.8(9) |
| Mn(1)-Mn(4)-Na(1) | 146.59(8) | N(11)-O(21)-Mn(1) | 117.8(4) |
| C(12)-O(12)-Mn(2) | 116.7(5) | N(11)-O(21)-Mn(3) | 117.2(4) |
| C(12)-O(12)-Na(3) | 151.8(5) | Mn(1)-O(21)-Mn(3) | 122.5(2) |
| Mn(2)-O(12)-Na(3) | 80.0(3) | O(15)-C(15)-O(25) | 126.7(7) |
| C(16)-O(16)-Mn(5) | 130.5(5) | O(15)-C(15)-C(25) | 117.8(7) |
| C(16)-O(16)-Na(1)#3 | 131.3(5) | O(25)-C(15)-C(25) | 115.5(7) |
| Mn(5)-O(16)-Na(1)#3 | 92.1(3) | C(14)-O(14)-Mn(1) | 121.5(5) |
| N(12)-O(22)-Mn(1) | 116.5(4) | C(15)-O(15)-Mn(5) | 130.7(5) |
| N(12)-O(22)-Mn(2) | 115.7(4) | Mn(1)-O(19)-Mn(1)#2 | 119.989(8) |
| Mn(1)-O(22)-Mn(2) | 125.9(2) | Mn(1)-O(19)-Mn(1)#1 | 119.989(8) |
| C(11)-O(11)-Mn(3) | 117.6(5) | Mn(1)#2-O(19)-Mn(1)#1 | 119.989(8) |
| C(11)-O(11)-Na(2) | 158.6(5) | Mn(1)-O(29)-Mn(5) | 119.5(3) |
| Mn(3)-O(11)-Na(2) | 83.6(3) | C(14)-O(14)-Mn(1)#2 | 131.1(5) |
| C(12)-N(12)-O(22) | 112.8(5) | Mn(1)-O(14)-Mn(1)#2 | 87.90(17) |
| C(12)-N(12)-Mn(5) | 130.6(5) | C(16)-O(26)-Mn(4) | 131.5(5) |
| O(22)-N(12)-Mn(5) | 116.0(4) | C(72)-O(32)-Mn(5) | 121.6(5) |
| C(15)-O(15)-Mn(5) | 130.7(5) | C(72)-O(32)-Na(1)#3 | 140.6(5) |
| Mn(1)-O(19)-Mn(1)#2 | 119.989(8) | C(14)-O(14)-Mn(1)#2 | 131.1(5) |
| Mn(1)-O(19)-Mn(1)#1 | 119.989(8) | Mn(1)-O(14)-Mn(1)#2 | 87.90(17) |
| Mn(1)#2-O(19)-Mn(1)#1 | 119.989(8) | C(16)-O(26)-Mn(4) | 131.5(5) |

Symmetry codes: #1 -y+1,z-1/2,-x+3/2; #2 -z+3/2,-x+1,y+1/2; #3 y-1/4,-x+5/4,-z+7/4.

## 5.6 - References

1 A. Caneschi, D. Gatteschi and R. Sessoli, *J. Am. Chem. Soc.*, 1991, **113**, 5873–5874.

2 N. Ishikawa, M. Sugita, T. Ishikawa, S. Koshihara and Y. Kaizu, *J. Am. Chem. Soc.*, 2003, **125**, 8694.

3 M. A. Al Damen, S. Cardona-Serra, J. M. Clemente-Juan, E. Coronado, A. Gaita-Ariño, C. Martí-Gastaldo, F. Luis and O. Montero, *Inorg. Chem.*, 2009, **48**, 3467.

4 A. Bouwen, A. Caneschi, D. Gatteschi, E. Goovaerts, D. Schoemaker, L. Sorace and M. Stefan, *J. Phys. Chem. B*, 2001, **105**, 2658–2663.

5 A. Cornia, A. C. Fabretti, P. Garrisi, C. Mortalò, D. Bonacchi, D. Gatteschi, R. Sessoli, L. Sorace, W. Wernsdorfer and A.-L. Barra, *Angew. Chemie Int. Ed.*, 2004, **43**, 1136–1139.

6 D. Gatteschi, R. Sessoli and A. Cornia, *Chem. Commun.*, 2000, 725–732.

7 M. Murrie, S. J. Teat, H. Stœckli-Evans and H. U. Güdel, *Angew. Chemie Int. Ed.*, 2003, **42**, 4653–4656.

8 H. Andres, R. Basler, A. J. Blake, C. Cadiou, G. Chaboussant, C. M. Grant, H.-U. Güdel, M. Murrie, S. Parsons, C. Paulsen, F. Semadini, V. Villar, W. Wernsdorfer and R. E. P. Winpenny, *Chem. Eur. J.*, 2002, **8**, 4867–4876.

9 S. T. Ochsenbein, M. Murrie, E. Rusanov, H. Stoeckli-Evans, C. Sekine and H. U. Güdel, *Inorg. Chem.*, 2002, **41**, 5133–40.

10 A. J. Tasiopoulos, A. Vinslava, W. Wernsdorfer, K. Abboud and G. Christou, *Angew. Chemie - Int. Ed.*, 2004, **43**, 2117–2121.

11 T. Lis, *Acta Crystallogr.*, 1980, **B36**, 2042.

12 N. Koike, H. Uekusa, Y. Ohashi, C. Harnoode, F. Kitamura, T. Ohsaka and K. Tokuda, *Inorg. Chem.*, 1996, **35**.

13 P. Happ, C. Plenk and E. Rentschler, *Coord. Chem. Rev.*, 2015, **289-290**, 238–260.

14 C. Y. Chow, E. R. Trivedi, V. Pecoraro and C. M. Zaleski, *Comments Inorg. Chem.*, 2015, **35**, 214–253.

15 G. Mezei, C. M. Zaleski, V. L. Pecoraro, G. Mezei, C. M. Zaleski, V. L. Pecoraro, *Chem. Rev.*, 2007, **107**, 4933–5003.

16 C. M. Zaleski, S. Tricard, E. C. Depperman, W. Wernsdorfer, T. Mallah, M. L.

Kirk and V. L. Pecoraro, *Inorg. Chem.*, 2011, **50**, 11348–52.

17 C. Dendrinou-Samara, M. Alexiou, C. M. Zaleski, J. W. Kampf, M. L. Kirk, D. P. Kessissoglou and V. L. Pecoraro, *Angew. Chemie Int. Ed.*, 2003, **42**, 3763–3766.

18 C. M. Zaleski, E. C. Depperman, C. Dendrinou-Samara, M. Alexiou, J. W. Kampf, D. P. Kessissoglou, M. L. Kirk and V. L. Pecoraro, *J. Am. Chem. Soc.*, 2005, **127**, 12862–72.

19 C. M. Zaleski, E. C. Depperman, J. W. Kampf, M. L. Kirk and V. L. Pecoraro, *Angew. Chemie Int. Ed.*, 2004, **43**, 3912–3914.

20 C. M. Zaleski, J. W. Kampf, T. Mallah, M. L. Kirk and V. L. Pecoraro, *Inorg. Chem.*, 2007, **46**, 1954–1956.

21 A. M. Ako, V. Mereacre, R. Clérac, W. Wernsdorfer, I. J. Hewitt, C. E. Anson and A. K. Powell, *Chem. Commun.*, 2009, 544–546.

22 G. Rogez, J.-N. Rebilly, A.-L. Barra, L. Sorace, G. Blondin, N. Kirchner, M. Duran, J. van Slageren, S. Parsons, L. Ricard, A. Marvilliers and T. Mallah, *Angew. Chemie Int. Ed.*, 2005, **44**, 1876–1879.

23 J. Krzystek, A. Ozarowski and J. Telser, *Coord. Chem. Rev.*, 2006, **250**, 2308–2324.

24 R. D. Shannon, *Acta Crystallogr.*, 1976, **A32**, 751–767.

25 P. Happ and E. Rentschler, *Dalt. Trans.*, 2014, **43**, 15308–15312.

26 B. R. Gibney, D. P. Kessissoglou, J. W. Kampf and V. L. Pecoraro, *Inorg. Chem.*, 1994, **33**, 4840–4849.

27 M. R. Azar, T. T. Boron, J. C. Lutter, C. I. Daly, K. a. Zegalia, R. Nimthong, G. M. Ferrence, M. Zeller, J. W. Kampf, V. L. Pecoraro and C. M. Zaleski, *Inorg. Chem.*, 2014, **53**, 1729–1742.

28 R. W. Saalfrank, A. Dresel, V. Seitz, S. Trummer, F. Hampel, M. Teichert, D. Stalke, C. Stadler, J. Daub, V. Schunemann and A. X. Trautwein, 1997, 2058–2062.

29 T. T. Boron, J. W. Kampf and V. L. Pecoraro, *Inorg. Chem.*, 2010, **49**, 9104–9106.

30 B. Dietrich, *Cryptands*, Elsevier, Oxford, 1996, vol. 1.

# Chapter VI

## *$^1$H-NMR characterization of heterotrimetallic metallacrown complexes.*

## 6.1 - Introduction

Heterometallic compounds are coordination complexes that combine different metallic species together in a single molecular scaffold; thus, they are generally endowed with the peculiar properties ascribed to the metal ions they contain. The simultaneous presence of different metal ions can provide heterometallic compounds with a wider range of properties compared to homometallic species. It is clear that by combining the features of various and different metal ions one may unlock complementary physico-chemical properties and have access to a fascinating multivalent class of compounds. For these reasons, in the last decades, much effort has been put into synthesizing new heterometallic complexes, leading to several reports of heterometallic complexes with applications in catalysis,[1,2] luminescence[3] and magnetism[2,4–6].

Although the vast majority of heterometallic MCs is indeed characterized by a 15-MC-5 structural topology, because of the wider cavity able of encapsulating larger ions like lanthanides, interesting heterometallic complexes adopt smaller 12-MC-4 scaffolds, formed either as single MC units[7] or as more complex structures characterized by multiple MC rings fused together.[8] Here we present the study of a series of isostructural $\mathrm{Ln^{III}}$[12-$\mathrm{MC_{Mn(III),\ Shi}}$-4] complexes, reported by Zaleski in 2014,[7] represents the first heterotrimetallic MC complexes, where 12-MC-4 scaffolds comprise at the mean time Mn(III), a Ln(III) ion and a Na(I) ion (Fig. 6.1).

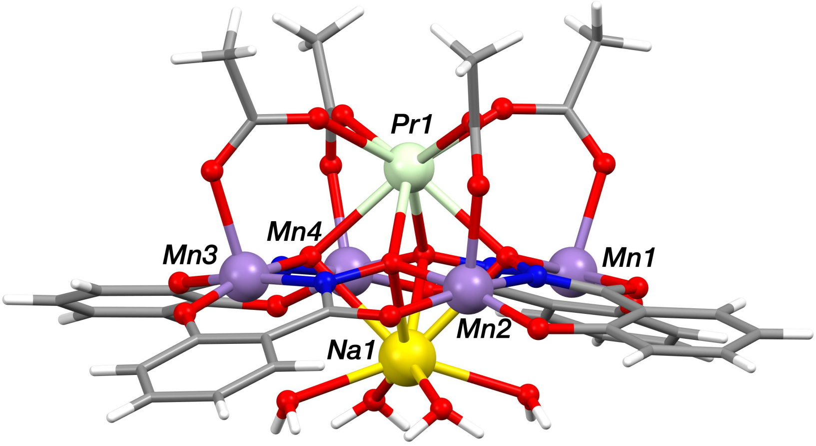

**Fig. 6.1**: Crystal structure of $Pr^{III}Na^{I}(OAc)_4[12\text{-}MC_{Mn(III),\ Shi}\text{-}4](H_2O)_4\cdot 6DMF$. Colour scheme: light green - Pr(III), purple - Mn(III), yellow - Na(I) red - oxygen, blue - nitrogen, gray - carbon, white - hydrogen.

The original work presented by Zaleski in 2014, in which these complexes are reported, provides a thorough investigation on the solid state structures of such heterotrimetallic complexes.[7]

The practical interest behind this class of isostructural heterotrimetallic metallacrowns resides within its similarity with the first homometallic transition metal 12-MC-4 of single-molecule magnetic behaviour, the species $Mn(II)(OAc)_2[12\text{-}MC_{Mn(III),\ Shi}\text{-}4](DMF)_6$, presented by Pecoraro in 1989[9] and studied for magnetic behaviour by Zaleski in 2011 (Fig. 6.2).[10] The SMM property of this compound is proved by its magnetic relaxation energy barrier ($U_{eff}$), which accounts for 21 K. Significanty, only a few homometallic 12-MC-4 complexes have shown SMM behaviour,[11] due to the common presence of low-spin ground states generated by the antiferromagnetic interactions between the ring MC metal ions. Indeed, the complex $Mn(II)(OAc)_2[12\text{-}MC_{Mn(III),\ Shi}\text{-}4](DMF)_6$ possesses a low-spin S = 1/2 ground state, which is though counterbalanced by the high magnetoanisotropy provided by the planar MC arrangement and by the central Mn(II) single-ion anisotropy.

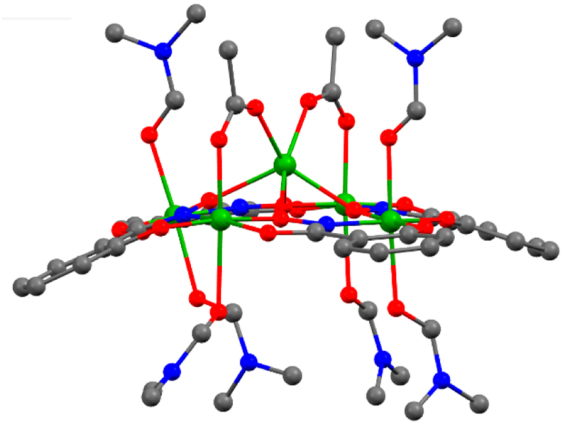

**Fig. 6.2**: Crystal structure of Mn(II)(OAc)$_2$[12-MC$_{\mathrm{Mn(III),\ Shi}}$-4](DMF)$_6$.[7,10] Colour scheme: green - Mn$^{2+/3+}$, red - oxygen, blue - nitrogen, gray - carbon.

The class of Ln(III)Na(I)(OAc)$_4$[12-MC$_{\mathrm{Mn(III),\ Shi}}$-4](H$_2$O)$_4$·6DMF complexes represents a functional evolution of the Mn-only MC SMM, since it succeeds in combining the typical asymmetric scaffold with lanthanide ions of higher magnetic anisotropy (*D*), constituting a family of promising tunable SMM candidates.

The series of Ln(III)Na(I)(OAc)$_4$[12-MC$_{\mathrm{Mn(III),\ Shi}}$-4](H$_2$O)$_4$·6DMF metallacrowns was thoroughly analysed from the solid state point of view in the first report by Zaleski from 2014 and much is known about the compounds behaviour in the solid state. To date, much less is known about their behaviour in solution, since no data have been reported regarding their solution stability. Herein, we describe the characterization in solution that was pursued by means of $^1$H-NMR on the 12 isostructural metallacrowns, which were investigated in order to complement the solid state description and gain an exhaustive picture of the chemistry of this class of heterotrimetallic metallacrowns. $^1$H NMR was employed to evaluate the stability in solution, the ligand (acetate) and metal exchange processes and, finally, to get insight on the magnetic properties of the compounds. With this regard, the paramagnetism of the compounds determines their NMR features, namely the bandwidth, chemical shifts and longitudinal relaxation rates, which have been analysed and interpreted.

## 6.2 - Experimental Section

### 6.2.1 - Materials and methods

All reagents and solvents were purchased by Sigma aldrich and were used without further purification. Salicylhydroxamic acid was purchased from Alfa-Aesar. The metallacrown complexes of formula Ln(III)M(I)$(OAc)_4$[12-MC$_{Mn(III),\ Shi}$-4]$(H_2O)_4$·6DMF were provided by the group of Dr. Zaleski at Shippensburg University, Shippensburg, PA, United States, and prepared following the synthetic procedure reported elsewhere.[7] $^1$H NMR spectra were recorded on Bruker Avance 300 and 400 MHz spectrometer using standard pulse sequences. Deuterated methanol was used as the solvent. The spectral window ranged from -60 to +60 ppm. Acquisition parameters are reported as Supporting Information. Variable temperature experiments were performed between -70 to +50 K using steps of 15 K. Standard inversion recovery experiments were performed using delay time values between the 180º and 90º deg pulses ranging from $10^{-4}$ and $5x10^{-2}$ s. Chemical shifts (δ) are reported in parts per million (ppm) and referenced to residual solvent protons. All NMR spectra analyses was performed using MestreNova 8.0.

Inversion recovery experiments were performed using delay time values ranging from $10^{-4}$ and $5x10^{-2}$ s. The integrals of each signal were employed with the relationship

$$I = I_0(1 - p \cdot e^{(-\tau/T_1)})$$

where $\tau$ is the relaxation delay time, I is the integral for a specific value of $\tau$, $I_0$ is the reference integral, obtained when no delay time $\tau$ is applied and p an empirical fitting parameter, ranging from 1 to 2, which resulted above 1.5 for all signals.

## 6.3 - Results and Discussion

### 6.3.1 - Solid state structures

The complexes have the general formula Ln(III)Na(I)(OAc)$_4$[12-MC$_{\mathrm{Mn(III),\ Shi}}$-4](H$_2$O)$_4$·6DMF, comprising a Mn(III) based 12-MC-4 metallacrown ring coordinating the Ln(III) guest above the ring, in a side-on coordinative fashion, and coordinating the Na(I) ion below the ring. The Ln(III) guest consists of Pr$^{III}$, Nd$^{III}$, Sm$^{III}$, Eu$^{III}$, Gd$^{III}$, Tb$^{III}$, Dy$^{III}$, Ho$^{III}$, Er$^{III}$, Tm$^{III}$, Yb$^{III}$, and Y$^{III}$ (a transition metal ion with a radius that is close to that of Ho$^{III}$[12]). The solid state structures of these complexes were reported and discussed in the original work by Zaleski[7], and are here briefly summarized.

The Ln(III) first coordination sphere is completed by four acetate ions acting as bridges with the Mn(III) ring ions, establishing an 8-coordinate square antiprismatic geometry. The charge-balancing alkaline metal ion embraced on the opposite side of the molecular unit possesses a distorted square antiprismatic first coordination sphere completed by four bound water molecules.

The central Ln$^{III}$ ions possess calculated crystal radii ranging from 1.03 Å for the smaller Yb$^{III}$ and Y$^{III}$ to 1.15 Å for the larger Pr$^{III}$. This system shows size selectivity regarding the binding of different lanthanide ions; when the largest ions, La$^{III}$ and Ce$^{III}$, or the smallest one, Lu$^{III}$, are used in the synthesis, a different complex is formed, responding to the formula Na$_2$(OAc)$_2$[12-MC$_{\mathrm{Mn(III),\ Shi}}$-4](DMF)$_6$, which does not enclose the trivalent Ln$^{III}$ ion.

Although minor variations on the MC conformations are noticeable, unit cell parameters are almost identical throughout the whole series of complexes, with the largest deviation on the unit cells *c*-axes of 0.162 Å, corresponding to the 0.93% of the *c*-axis length, and the largest deviation between the unit cells γ angles (formed between the cell axes *a* and *b*) accounting for 0.34% of the total γ angle value.

Thus, the 12 structures can effectively be considered as isostructural, depicting how *3d-4f* compounds can provide valuable panels of analogous compounds, by simple substitution of the central guest, as lanthanides are often dimensionally interchangeable. Further enlargement of this panel of isostructural compounds can be achieved by substitution of the carboxylate ligands and of the alkali metal ion, as testified by the structures of Ca$^{II}$(benzoate)$_2$[12-MC$_{\mathrm{Mn(III),\ Shi}}$-4] and Dy$^{III}$K(OAc)$_4$[12-

MC$_{\text{Mn(III), Shi}}$-4](DMF)$_4$·DMF, providing an even wider set of analogous compounds, useful for an exhaustive investigation on molecular properties, such as luminescence or magnetism.

Some solid state structure considerations were drawn concerning the role of the alkali metal on the structure conformation. Replacement of the Na$^+$ with K$^+$ led to the synthesis of Dy$^{\text{III}}$K(OAc)$_4$[12-MC$_{\text{Mn(III), Shi}}$-4](DMF)$_4$·DMF. Despite having similar Dy$^{\text{III}}$ crystal radius, this structure showed a less domed structure compared to the sodium analogue Dy$^{\text{III}}$Na(OAc)$_4$[12-MC$_{\text{Mn(III), Shi}}$- 4](H$_2$O)$_4$·6DMF, perhaps as a reflection of the larger ionic radius of the K$^+$ ion. However, it was determined that the presence of an alkali metal cation is not necessary for a domed structure. In fact, in the previously reported complex Ca$^{\text{II}}$(benzoate)$_2$[12-MC$_{\text{Mn(III), Shi}}$-4],[13] the MC contains only a central Ca(II) ion and the MC structure is domed without the presence of a coordinated alkali ion (Fig. 6.3).

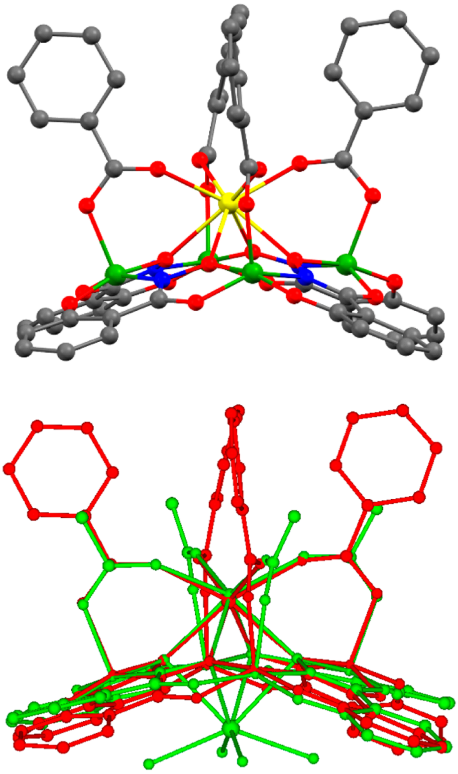

**Fig. 6.3**: Crystal structure of the complex Ca$^{\text{II}}$(benzoate)$_2$[12-MC$_{\text{Mn(III), Shi}}$-4].[7,13] Above, molecular structure. Colour scheme: green - Mn(III), yellow - Ca(II), red -

oxygen, blue - nitrogen, gray - carbon. Below, overlay between the crystal structures of $Ca^{II}$(benzoate)$_2$[12-$MC_{Mn(III), Shi}$-4] (red) and of Pr(III)Na(I)(OAc)$_4$[12-$MC_{Mn(III), Shi}$-4]($H_2O$)$_4$ (green). The overlay was realized by minimizing the RMSD between the oxime oxygen atoms.[7] Hydrogen atom and solvent molecules were omitted for clarity.

The metallacrown Y(III)Na(I)(OAc)$_4$[12-$MC_{Mn(III), Shi}$-4]($H_2O$)$_4$·6DMF, is the only compound containing a diamagnetic lanthanide-analog in the cavity. In fact, the analogous compounds of La(III) and Lu(III), *i.e.* the lanthanides with respectively the largest and shortest radii, were never isolated. Noteworthy, similarly to La(III), also the Ce(III) metallacrown could not be crystallized.

Several factors possibly make the MCs with the largest and smallest radii relatively less stable compared with those of lanthanides in the centre of the series. On one hand, La(III) and Ce(III), due to their larger ionic radii, might interact in a less favourably with both the MC scaffold and the capping acetate ions at the meantime. Significant geometric variations might be required to accommodate such ions within the MC scaffold, resulting into energetically unfavourable structures. On the other hand, an interplay between the small ionic radius and a higher charge/radius ratio might be at the origin of a lower stability of the complex with Lu(III). We expect in fact that the smallest lanthanide would tend to penetrate deeper within the coordinating scaffold, causing the bridging acetates to tilt inward, producing a destabilization of the structure by steric and charge repulsion.

As the radius of the lanthanide decreases, one would expect the absolute value of $\Delta H_{solvation}$ of the lanthanide to increase and the p$K_a$ of the coordinated water molecules to decrease. The first fact would cause the displacement of solvent molecules by coordinating ligands to be unfavourable, while the latter would increase the stability of hydrolytic species in solution. According to Piguet[14], $\Delta H_{solvation}$ for Lu(III) is however not higher than that of Yb(III), as would be expected, Fig. 6.4. Also, although lower than that of Yb(III), the pKa of coordinated water molecules for Lu(III) is not so low to suggest a much different coordination behaviour for Lu(III) compared to Yb(III) ($Lu^{3+}$: 7.41, $Yb^{3+}$: 7.45, for comparison $Pr^{3+}$: 8.32).[15] These values suggest that, from these points of view, the chemistry of Lu(III) does not differ excessively from that of Yb(III). Hence, in our opinion, the unsuccessful synthesis of the species Lu-MC is not attributable solely to one of the factors here analysed. Rather, it is the result of the interplay of all these factors that reduces the stability of the resulting metallacrown and make its crystallization less favourable than for the other lanthanide ions. Perhaps more importantly, from our analysis we do not envision elements that would however exclude the isolation of Lu-MC under appropriate conditions.

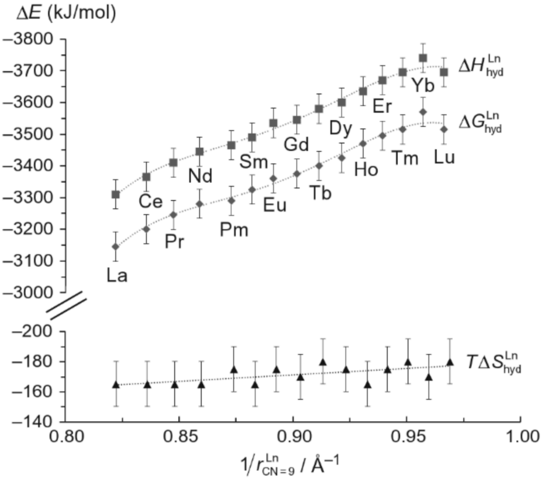

**Fig. 6.4**: Standard molar Gibb's free energy $\Delta G_{hydr}$, enthalpy $\Delta H_{hydr}$ and entropy $T\Delta S_{hydr}$ relative to hydration for trivalent lanthanides.[14]

### 6.3.2 - Paramagnetically shifted $^1$H-NMR

In this work, we present the solution studies of this series of twelve isostructural heterometallic metallacrowns, of general formula Ln(III)Na(I)($CH_3COO$)$_4$[12-$MC_{Mn(III), Shi}$-4]($H_2O$)$_4$·6DMF, which was analysed by monodimensional $^1$H Nuclear Magnetic Resonance spectrophotometry and UV-Vis spectrophotometry. The main difference in the twelve structures is the nature of the Ln(III) ion, which varies between $Pr^{3+}$, $Nd^{3+}$, $Sm^{3+}$, $Eu^{3+}$, $Gd^{3+}$, $Tb^{3+}$, $Dy^{3+}$, $Ho^{3+}$, $Er^{3+}$, $Tm^{3+}$, $Yb^{3+}$ and $Y^{3+}$ (a transition metal ion of comparable charge/radius ratio).

All the metallacrown complexes, abbreviated as Ln-MC depending on the Ln(III) ion present, were studied by standard monodimensional $^1$H-NMR and by T1 Inversion Recovery NMR. Complexes Y-MC and Dy-MC were also analysed by variable-temperature $^1$H NMR. Furthermore, the four complexes M(III)Na(I)(BzO)$_4$[12-MC$_{\text{Mn(III),(N)Shi}}$-4](H$_2$O)$_4$·6DMF, M(III)Na(I)(HSalO)$_4$[12-MC$_{\text{Mn(III),(N)Shi}}$-4](H$_2$O)$_4$·6DMF (M = Y and Dy, BzO$^-$ = benzoate, HSalO$^-$ = salicylate) were analysed. Carboxylate ligand exchange was also studied for the Y(III)Na(I)(CH$_3$COO)$_4$[12-MC$_{\text{Mn(III), Shi}}$-4](H$_2$O)$_4$·6DMF by $^1$H-NMR titration.

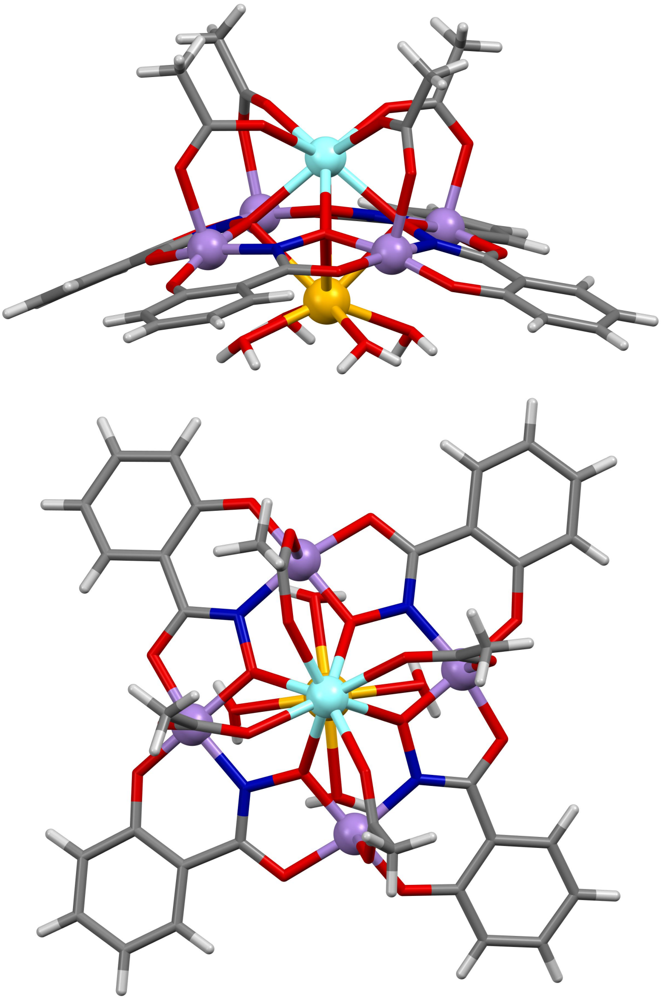

**Fig. 6.5**: Crystal structure of the Y(III)Na(I)(CH$_3$COO)$_4$[12-MC$_{\text{Mn(III), Shi}}$-4](H$_2$O)$_4$·6DMF complex. DMF solvent molecules have been omitted for clarity. Above, side-view of the complex; below, top-down view. Colour scheme: aqua - Y(III), yellow - Na(I), purple - Mn(III), red - oxygen, blue - nitrogen, gray - carbon, light grey - hydrogen.

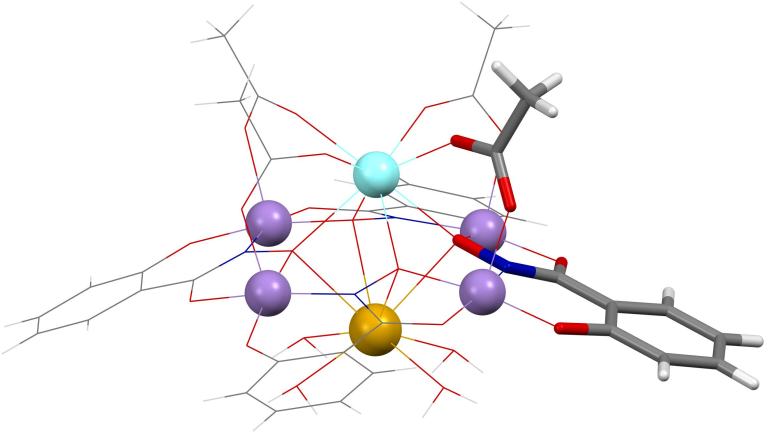

**Fig. 6.6**: Crystal structure of the species Y(III)Na(I)$(CH_3COO)_4$[12-$MC_{Mn(III),\ Shi}$-4]$(H_2O)_4$·6DMF, where one molecule of ligand salycilhydroximate and one molecule of ligand acetate have been highlighted. DMF solvent molecules have been omitted for clarity. Colour scheme: aqua - Y(III), yellow - Na(I), purple - Mn(III), red - oxygen, blue - nitrogen, gray - carbon, white - hydrogen.

With the aim of studying the integrity in solution of these complexes, an initial screenening of the spectral properties of these complexes was carried out. ElectroSpray Ionization (ESI) mass spectrometry was performed on a few selected compounds (Y-MC, Sa-MC and Yb-MC), providing spectra with multiple peaks. The bridging acetates proved to be labile and their partial dissociation/exchange with $OH^-$, $MeO^-$ or $H_2O$ in various ratios was always observed to some extent. A number of signals, likely associated to different ionic species, were observed at the different cone voltages employed. The $Na^+$ ion was often present, although many species appear to be adducts with two $Na^+$ ions. Overall, the spectrometric data showed however that the {Ln(III)[12-$MC_{Mn(III),\ Shi}$-4]}$^{3+}$ scaffold is stable under ESI-MS conditions.

UV-Vis spectra of a few selected compounds (Y-MC, Eu-MC) were also registered. The spectra present an indistinctive absorption profile, with an absorption band at circa 330 nm (with a minor shoulder at ca. 370 nm) and a second minor absorption band at around 420 nm. The spectra did not show differences respective of the different Ln(III) ions present in the metallacrown.

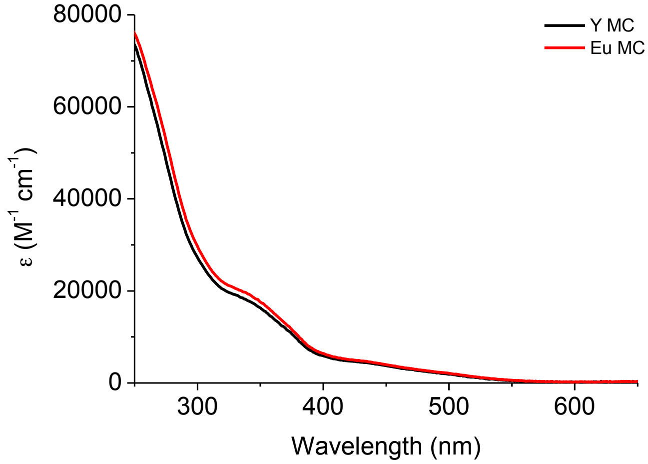

**Fig. 6.7**: Representative molar UV-Vis spectra of the Y MC and Eu MC complexes in acetonitrile.

We decided therefore to use $^1$H-NMR to characterize the MC complexes with the hope that different lanthanides could give rise to different spectra. We previewed actually that the Lanthanide Induced Shifts ($\delta_{para}$, LIS) could provide important information in particular on spin delocalization, coupling between paramagnetic centres and magnetic anisotropies.

Despite their paramagnetic nature, we expected $^1$H-NMR to be a suitable technique for the study of this class of compounds, thanks to the relaxation times of both Mn(III) and of Ln(III), which are orders of magnitude faster than the NMR timescale (ca. $3\times10^{-8}$ s) and that induce a limited peak broadening that does not preclude high-resolution NMR characterization of small molecular systems[16]. Interestingly, had Mn(II) ($\tau_s = 10^{-8}$ s) been present in the structure, the resulting spectra would have shown much broader peaks, preventing the acquisition of NMR signals with acceptable resolution. Also, we expected the Gd(III)-containing MC as the only exception to the mild peak broadenings induced by lanthanides in our complexes as the relaxation time of the lanthanide was expected in a range ($\tau_s = 10^{-8} - 10^{-9}$ s) which could provide with a substantial peak enlargement. Such signal broadening (expected for Mn(II) and Gd(III)) are motivated by the fact that an NMR-active nucleus possessing a spin rotating at the Larmor frequency ω has the highest probability of undergoing spin-lattice relaxation if it can release energy to dipoles that are fluctuating at the same ω frequency.

**Table 6.1**: Parameters valid at 500 MHz, T = 298 K.[17] *Calculated values for 400 MHz, T = 298 K.

| Ion | Conf. | Spin | $\tau_s$ (s) | Broad. (Hz) | Broad. (ppm)* |
|---|---|---|---|---|---|
| **$Mn^{3+}$** | $d^4$ | 2 | $10^{-10}$ - $10^{-11}$ | 150 - 1'500 | 0.4 - 4 |
| **$Mn^{2+}$** | $d^5$ | 5/2 | $10^{-8}$ | 100'000 | 250 |
| **$Ln^{3+}$** | $f^n$ | - | $10^{-12}$ - $10^{-13}$ | 1 - 1000 | 0.25 |
| **$Gd^{3+}$** | $f^7$ | 7/2 | $10^{-8}$ - $10^{-9}$ | $10^5$ - $10^6$ | 50 - 500 |

The monodimensional $^1$H spectrum of Y-MC is reported in Fig. 6.8. This spectrum shows a limited number of peaks, of which some denote a marked widthline, due to the paramagnetic character of the analysed species. In the solid state, the complex possess a pseudo-$C_4$ axis passing through the Y(III) and the Na(I) ions, although the molecules are not properly symmetrical due to the slightly tilted conformation they adopt. We might assume here, in a first approximation, that the pseudo axial symmetry exhibited in the solid state is maintained in the presence of an effective $C_4$ symmetry when the complex is in solution, as the result of small structural rearrangment. This approximation is consistent with the NMR data and the DFT structure optimization of the Y(III)(OAc)$_4$[12-MC$_{\text{Mn(III), Shi}}$-4]$^-$ anion in vacuo (see below). We believe these considerations can be applied to the entire series of complexes with the different Ln(III) ions in the cavity.

If we analyse the $^1$H-NMR spectrum of the Y-MC (Fig. 6.8), besides the peaks of the solvents (DMF at 2.86, 2.99, 7.97 ppm, MeOH at 3.31 ppm and $H_2O$ at 4.87 ppm), only five signals are present. In the spectrum, the calculated $T_1$ values and the peak bandwidths at half-height (indicated with ν½) for each peak are reported. Four signals in the spectrum (δ = 10.4, -24.3, -20.6, -16.9 ppm), accounting for one proton each, have been assigned to the four protons of the Shi$^{3-}$ ligands, while the broader peak at δ = +27.9 ppm, has been assigned to the acetate methyl group, although its integral accounts for just 2.8 instead of 3.0, possibly due to the significant broadness of the signal. Three peaks are significantly broad, due to the paramagnetic character of the four Mn(III) ions forming the metallacrown scaffold.

These assignements are consistent with the hypothesis of an actual 4-fold axial symmetry of the complex in solution.

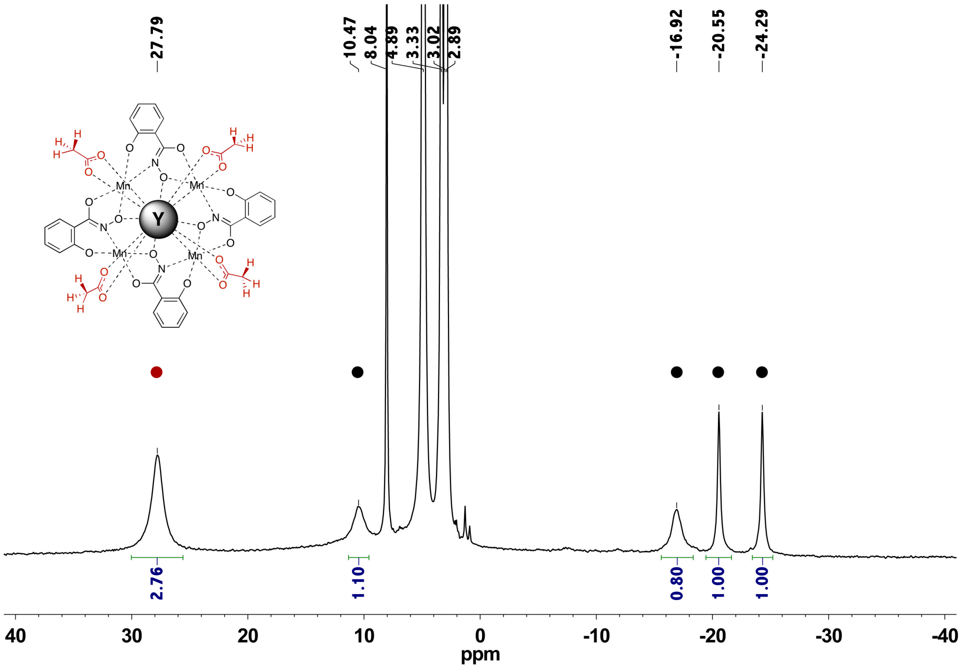

**Fig. 6.8**: $^1$H NMR spectrum of the species Y-MC in methanol-$d^4$; the scheme of the molecular structure of Y-MC is reported. Acetate ligands are coloured in red, Shi ligands in black.

Fig. 6.8 shows the stacking of the twelve spectra recorded for the isostructural Ln-MC compounds. As can be observed, the general appearance of the spectra is maintained along the series; all spectra show two sets of signals, ascribed to $Shi^{3-}$ and to the acetates ligands. The three peaks at negative ppm values belong to $Shi^{3-}$, with the fourth $Shi^{3-}$ peak being located in the positive region of the spectra, close to the solvent signals. Lastly, the single peak of the acetate protons falls always in the positive side of the spectra and is usually the most upfield-shifted signal (a part from the case of $Dy^{3+}$ and $Tb^{3+}$). Unfortunately, it was not possible to fully assign the $Shi^{3-}$ signals to the relative protons, due to the lack of information provided by the monodimensional experiments.

The first six spectra, from Y(III) to Gd(III), are closely similar in terms of chemical shifts, while the peak width is notably different for the acetate signals. The remaining six spectra, from Dy(III) to Yb(III), exhibit widely different chemical shifts, which can vary of ± 15 ppm, or more. A detailed description of such behaviours is reported further on. Although the appreciable differences in chemical shifts for these six spectra, the general appearance of the spectra and peaks distribution is retained, as discussed. The biggest differences are visible in the spectrum of Tm-MC, where two signals of $Shi^{3-}$ are merged together and another signal is not assuredly attributable, due to the poor resolution of the spectrum, and in the spectrum of Er-MC, where one peak is missing, fallen within the solvent signals. Furthermore, the spectrum of Dy-MC displays two signals partially combined, one belonging to $Shi^{3-}$, the other one to the acetate ions. By deconvolution of the merged signals, two independent peaks accounting for approximately 1:3 protons can be obtained, confirming the identity of the signals. Overall these spectra prove the stability of the MC scaffold in solution, and are consistent with the hypothesis of an actual $C_4$ axial symmetry of all compounds, obtained likely through a dynamical symmetrization of the structure in solution.

Since the 12-$MC_{Mn(III), Shi}$-4 scaffold remains unaltered along the whole series of compounds, any changes in the $^1H$-NMR spectra can be ultimately attributed to the paramagnetic properties of the encapsulated Ln(III) ions. We will see more in detail below that the Mn(III)-related paramagnetic contribution to the chemical shifts can reasonably be considered constant throughout the whole panel of compounds. Under this circumstance, being Y(III) diamagnetic the chemical shifts exhibited by the spectrum of Y-MC can be approximately described as those determined by the presence of a tripositive cation encapsulated in the Mn(III) coordination scaffold and the presence of the Mn(III) ions. Under this approximation, the spectrum of Y-MC can be treated as the reference spectrum of the series. Therefore, the difference in chemical shift between the spectrum of a give Ln(III) ion and that of Y(III) will be the result of the lanthanide-induced paramagnetic shifts, which in turn is composed by a contact and a dipolar contribution (see below). It is however necessary to point out that our data support the integrity of the MC scaffold in solution, the encapsulation of the Ln(III) and the presence of coordinated acetate ions, but no information is provided either on the presence of a coordinated sodium ion on the concave face of the metallacrown, or on its possible dissociation.

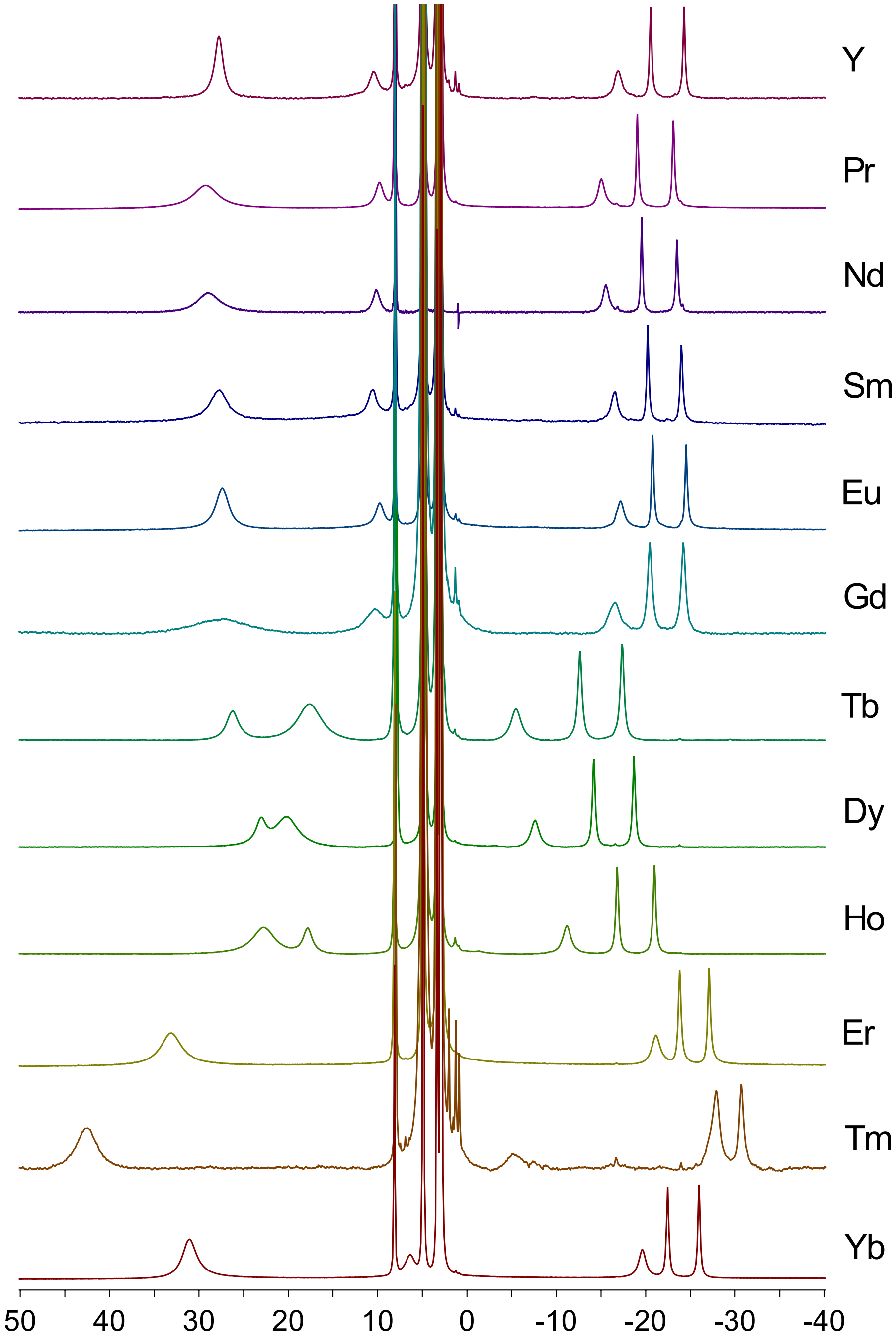

**Fig. 6.9**: Stacking of the spectra of the twelve heterometallic metallacrowns analysed. All spectra were recorded in methanol-$d^4$ at 298.2 K.

Seeking a possible further 2D NMR characterization, we carried out standard inversion recovery experiments, in order to investigate the longitudinal relaxation rates ($T_1$) of the protons in the complexes. Inversion Recovery spectra were registered on each sample to study the longitudinal relaxation times ($T_1$), also known as spin-lattice relaxation times, for each proton. Besides the mere investigation on the relaxation times, knowing $T_1$ was intended to determine whether bidimensional experiments could have been executed on the samples, Actually, if relatively long relaxation times were observed, 2D-NMR experiments such as DOSY (**D**iffusion **O**redered **S**pettroscop**Y**) or NOE (**N**uclear **O**verhauser **E**nhancement **S**pectroscop**Y**) could provide valuable information on eventual aggregation processes or on the molecular conformations adopted in solution.

The values of $T_1$ and of bandwidth obtained for each peak of the analysed compounds are reported in Table 6.2. The values of $T_1$ for partially overlapping peaks (e.g. Dy-MC) were determined using the integral of the tails of the signals, in order to minimize the effect of the overlap. Whenever possible, the bandwidth of these overlapping signals was determined, using the software MestreNova 8.0. It can be noticed that all relaxation times are extremely short, all accounting for less then 10 ms, extremely short if compared to spin-lattice relaxation times for protons of diamagnetic molecules, which are of the order of magnitude of seconds. As expected, the shortest values are shown by the Gd-MC complex, due to the metal long electronic relaxation times ($10^{-8}$ - $10^{-9}$ s). As a result, no bidimensional NMR experiment could be conducted, since the relaxation times of the protons were much shorter than the mixing times ($\tau_m$) behind the execution of any bidimensional experiment (around $10^2$ ms).

The peak bandwidths at half-height are also reported together with $T_1$ values in Table 6.2. Quite expectedly, the narrower peaks most upfield shifted (attributed to two protons of the Shi ligands), which are characterized by the longest relaxation times, while the opposite was actually observed for the acetate ions. No correlations with the chemical shifts was observed.

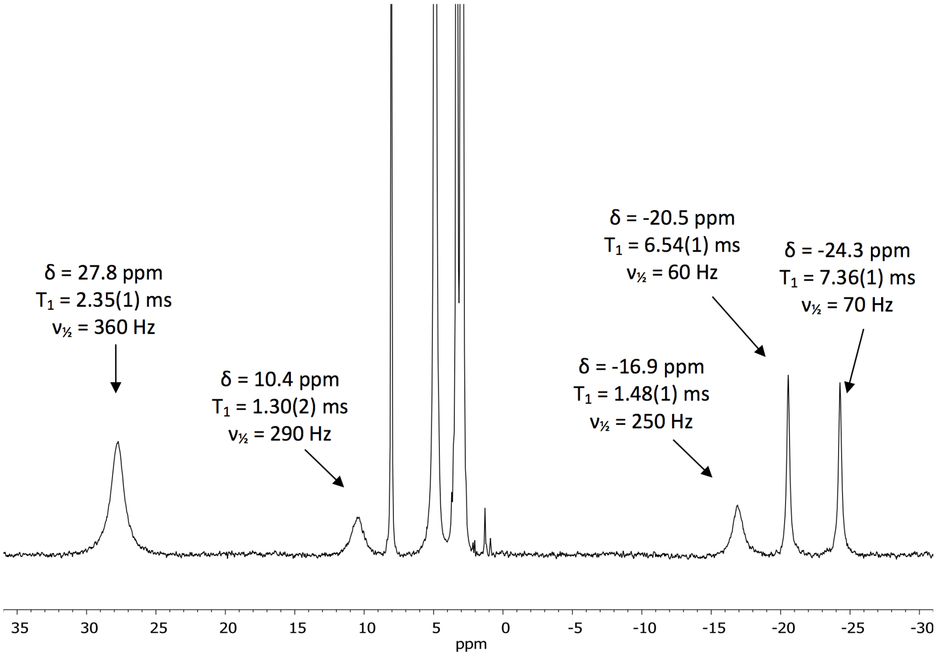

**Fig. 6.10**: Spectrum of the complex Y-MC, reporting the chemical shifts δ (ppm), the experimental $T_1$ relaxation times (ms) and the bandwidths at half-height (ν½, Hz).

**Table 6.2**: The calculated $T_1$ spin-lattice relaxation rates and the relative peak bandwidths are reported for each peak in the spectra of the isostructural compounds. Peaks are generically indicated as $H_{Ac}$, $H_A$, $H_B$, $H_C$ and $H_D$ with respect to their order, from higher (positive ppm) to lower chemical shifts (negative ppm).

| **$Ln^{3+}$** | | $H_{Ac}$ | $H_A$ | $H_B$ | $H_C$ | $H_D$ |
|---|---|---|---|---|---|---|
| Y-MC | δ , ppm | 27.8 | 10.4 | -16.9 | -20.5 | -24.3 |
| | $T_1$, ms | 2.35(1) | 1.30(2) | 1.48(1) | 6.54(1) | 7.36(1) |
| | ν½, Hz | 360 | 290 | 250 | 60 | 70 |
| Pr-MC | δ , ppm | 29.1 | 9.7 | -15.1 | -19.1 | -23.1 |
| | $T_1$, ms | 2.22(2) | 1.33(1) | 1.55(1) | 7.08(4) | 7.79(4) |
| | ν½, Hz | 987 | 270 | 244 | 61 | 67 |
| Sm-MC | δ , ppm | 27.8 | 10.6 | -16.5 | -20.2 | -24.0 |
| | $T_1$, ms | 3.3(5) | 1.5(2) | 1.53(1) | 6.83(2) | 7.50(2) |
| | ν½, Hz | 650 | 290 | 240 | 60 | 90 |
| Eu-MC | δ , ppm | 27.9 | 10.5 | -16.7 | -20.5 | -24.3 |
| | $T_1$, ms | 2.32(2) | 1.50(2) | 1.43(1) | 6.81(2) | 7.55(2) |
| | ν½, Hz | 680 | 380 | 310 | 100 | 120 |
| Gd-MC | δ , ppm | 27.8 | 10.1 | -16.5 | -20.5 | -24.2 |
| | $T_1$, ms | 0.14(1) | 0.66(2) | 0.93(4) | 3.06(5) | 3.35(5) |
| | ν½, Hz | 2090 | 793 | 450 | 170 | 170 |
| Dy-MC | δ , ppm | 20.2 | 22.9 | -7.8 | -14.4 | -18.9 |
| | $T_1$, ms | 0.70(2) | 0.93(5) | 1.8(4) | 5.1(3) | 5.5(3) |
| | ν½, Hz | 890 | 490 | 370 | 170 | 150 |
| Er-MC | δ , ppm | 33.1 | NA** | -21.2 | -23.8 | -27.1 |
| | $T_1$, ms | 1.17(1) | 1.20(2) | 1.42(1) | 6.23(1) | 7.02(1) |
| | ν½, Hz | 776 | NA | 310 | 91 | 86 |
| Tm-MC | δ , ppm | 47.8 | -5.3 | -27.4 | -27.9 | -30.7 |
| | $T_1$, ms | 2.1(4) | 1.3(2) | NA* | NA* | 7.0(1) |
| | ν½, Hz | 760 | 450 | 440 | 220 | 150 |
| Yb-MC | δ , ppm | 31.0 | 6.3 | -19.7 | -22.6 | -26.1 |
| | $T_1$, ms | 2.15(1) | 1.34(1) | 1.53(1) | 7.13(1) | 7.83(1) |
| | ν½, Hz | 540 | 391 | 259 | 71 | 67 |

*$T_1$ value was not calculated due to the significant coalescence of the peaks.

**$T_1$ values were determined by fitting the inversion recovery data of the intensity at the shoulder at 3.77 ppm.

From the observation of the bandwidths, it is noticeable how the signals of Shi undergo smaller changes in width, in comparison with the acetate signal, when going from Y-MC, where Y(III) is diamagnetic, to the end of the series. Hence, it seems that the Shi signals bandwidth may depend more heavily on the paramagnetic contribution of Mn(III) rather than on the nature of the Ln(III) ion. Contrarily, the acetate signal shows a dependence on the Ln(III) present, experiencing great increasing of width for lanthanides such as Gd(III), Pr(III) or Nd(III).

The stacked $^1$H NMR spectra of Y(III)-MC along with those of Pr(III), Nd(III), Sa(III), Eu(III), Gd(III) are reported in Fig. 6.11. The NMR spectra of the metallacrowns of Tb(III), Dy(III), Ho(III), Er(III), Tm(III) and Yb(III) are reported in Fig. 6.12, along with the reference spectrum of Y-MC. The difference in chemical shift values between the signals of each Ln-MC compared with those of Y-MC ($\Delta_{ps} = \delta_{Ln-MC} - \delta_{Y-MC}$), are reported in Tables 6.3 and 6.3. Both the stacked spectra in Fig. 6.11 and the data presented in Table 6.3 display that little differences in chemical shits ($\Delta_{ps}$) are experienced by MC species of earlier lanthanides, compared to the spectrum of Y-MC. On the contrary, the values of $\Delta_{ps}$ for heavier lanthanides (Fig. 6.12 and Table 6.4) are significant if compared with those of the earlier series. In particular Tb- and Tm-MCs experienced the largest $\Delta_{ps}$ shifts, which amount up to ca. 15 ppm, whilst the values of $\Delta_{ps}$ of the earlier lanthanides were all below 2.00 ppm, with the biggest shifts exhibited by Pr(III). By a qualitative recognition of the Shi peaks based on peak shape and integration, it was assumed that, for the Shi$^{3-}$ scaffold, the signals order remained unaltered, despite the differences in chemical shifts. In the spectra of Tb-MC and Dy-MC, the peak order between a signal of Shi and the acetate signal is inverted, but the two signals are easily discriminated from their integrals. Perhaps more interestingly, the presence of lanthanides with a large number of unpaired electrons such as Eu(III) or Gd(III) does not induce appreciable $\Delta_{ps}$ shifts if compared to the spectrum of the Y(III) MC. As for Gd(III), its properties reflect exclusively on the peaks bandwidth (see Table 6.3) but with almost no change in the observed chemical shifts.

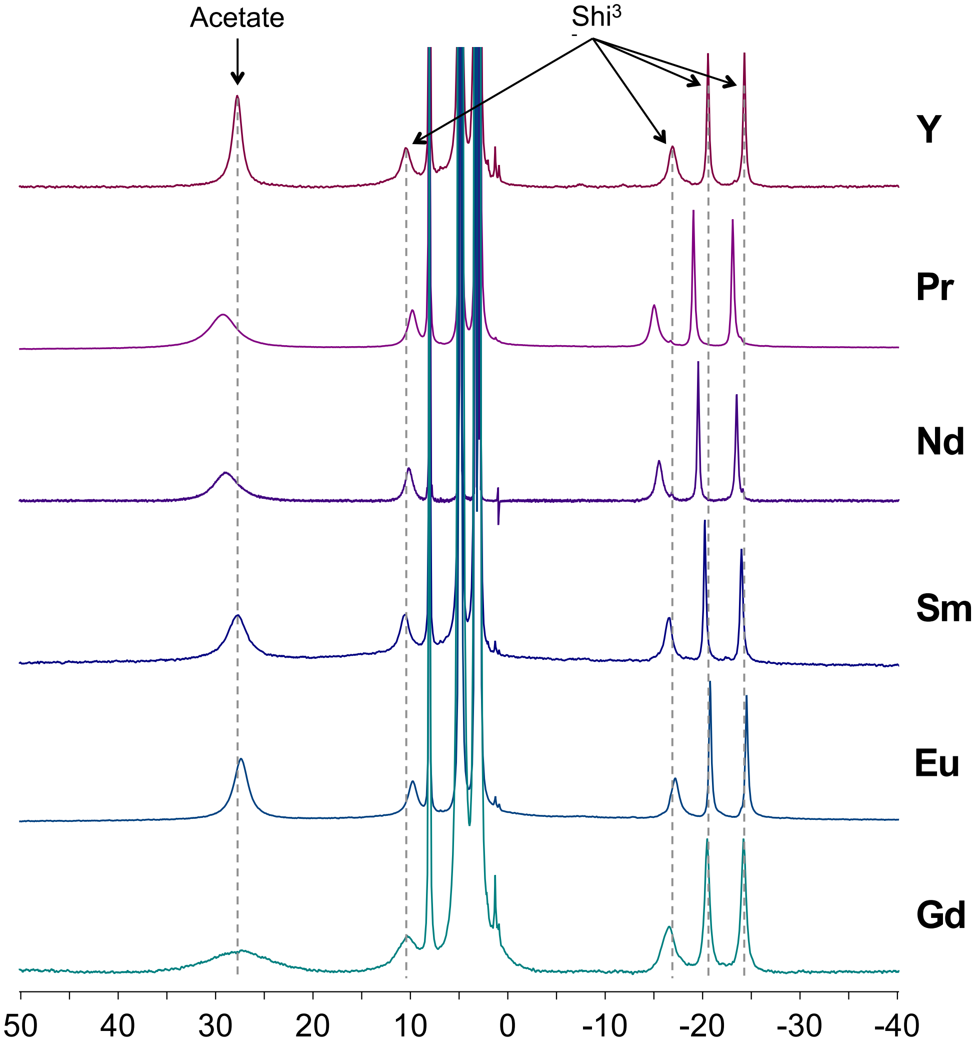

**Fig. 6.11**: Stacking of the $^1$H-NMR spectra of the species Y-MC, Pr-MC, Nd-MC, Sm-MC, Eu-MC, Gd-MC,

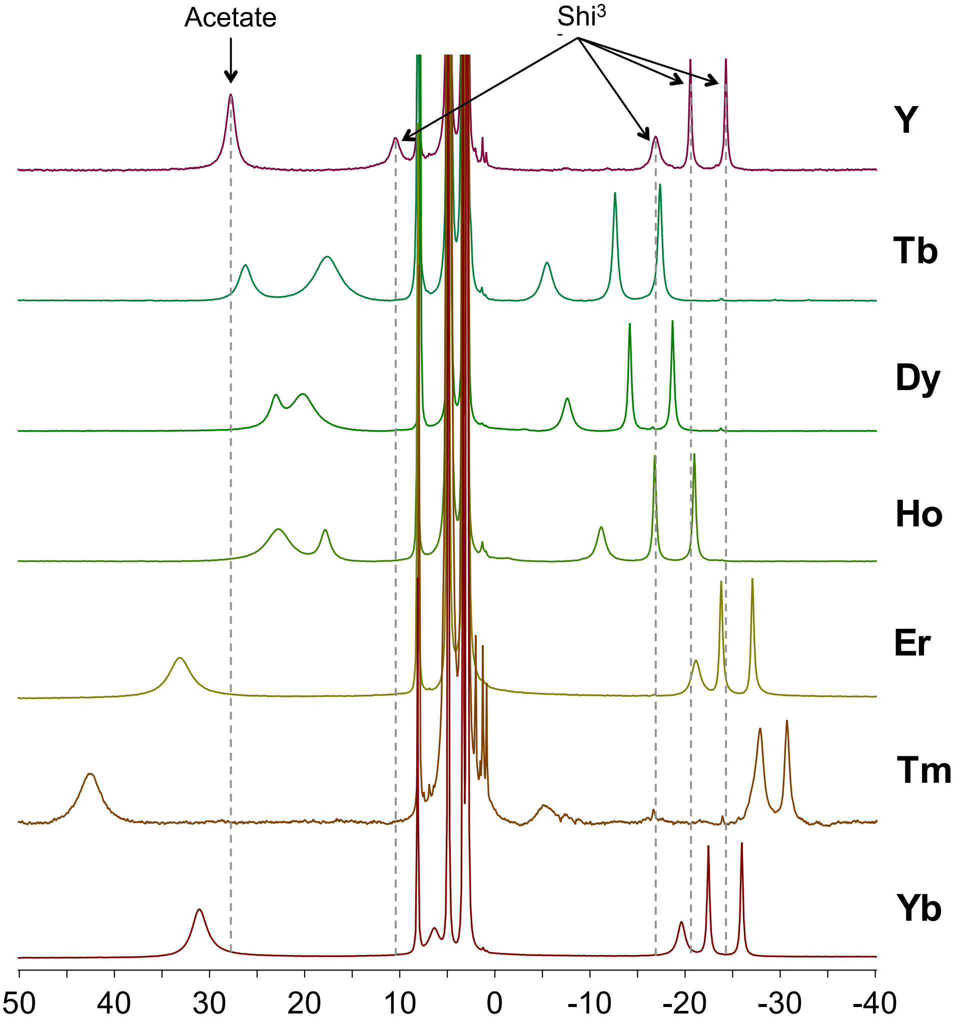

**Fig. 6.12**: Stacking of the $^1$H-NMR spectra of the species Tb-MC, Dy-MC, Ho-MC, Er-MC, Tm-MC, Yb-MC. The spectrum of Y-MC is reported as reference for the chemical shifts.

**Table 6.3**: Relative peak shifts ($\Delta_{ps}$) of the signals of $Shi^{3-}$ and of the acetate ions of the species Y-MC, Pr-MC, Nd-MC, Sm-MC, Eu-MC and Gd-MC, with respect to the signals of the reference spectrum of Y-MC. The signal of the acetate ion for Gd-MC is too broad to be measured accurately.

| **Relative Peak Shifts** ($\Delta_{ps}$, ppm) | | | | | |
|---|---|---|---|---|---|
| **$Ln^{3+}$** | $CH_3$ | $H_A$ | $H_B$ | $H_C$ | $H_D$ |
| Y-MC | 0.00 | 0.00 | 0.00 | 0.00 | 0.00 |
| Pr-MC | 1.50 | -0.60 | 1.92 | 1.52 | 1.22 |
| Nd-MC | 1.27 | -0.19 | 1.47 | 1.09 | 0.87 |
| Sm-MC | -0.12 | 0.13 | 0.36 | 0.32 | 0.29 |
| Eu-MC | -0.41 | -0.67 | -0.28 | -0.22 | -0.24 |
| Gd-MC | ≈ 0 | -0.09 | 0.28 | 0.04 | 0.01 |

**Table 6.4**: Relative peak shifts ($\Delta_{ps}$) of the signals of $Shi^{3-}$ and of the acetate ions of the species Y-MC, Pr-MC, Nd-MC, Sm-MC, Eu-MC and Gd-MC, with respect to the signals of the reference spectrum of Y-MC. The signal of the acetate ion for Gd-MC is too broad to be measured accurately.

| **Relative Peak Shifts** ($\Delta_{ps}$, ppm**)** | | | | | |
|---|---|---|---|---|---|
| **$Ln^{3+}$** | $CH_3$ | $H_A$ | $H_B$ | $H_C$ | $H_D$ |
| Y-MC | 0.00 | 0.00 | 0.00 | 0.00 | 0.00 |
| Tb-MC | -10.11 | 15.86 | 11.51 | 7.97 | 6.98 |
| Dy-MC | -7.42 | 12.68 | 9.40 | 6.48 | 5.71 |
| Ho-MC | -5.00 | 7.43 | 5.75 | 3.76 | 3.33 |
| Er-MC | 5.48 | N/A | -4.13 | -3.14 | -2.70 |
| Tm-MC | 14.99 | -15.50 | -10.98 | -7.34 | -6.44 |
| Yb-MC | 3.25 | -4.11 | -2.73 | -1.92 | -1.70 |

The total paramagnetic shift ($\delta_{para}$) experienced by protons in proximity of a paramagnetic centre is determined by the sum of two contributions, the "Contact" or Fermi Shift ($\delta_c$), the second "Pseudo-Contact" or Dipolar Shift ($\delta_{pc}$).

The contact shift ($\boldsymbol{\delta_c}$) is a through-bond paramagnetic induced shift operated by either the delocalization of the unpaired electron density in proximity of the resonating nucleus, or by phenomena of polarization of electron spins.[16] $\delta_c$ depends solely on the magnitude of the spin delocalization or polarization and

therefore it reflects the nature of the chemical bonds separating the paramagnetic centre and the resonating nucleus. Although this contribution decreases with distance, it does not reflect into a specific distance dependence between the two mentioned centres.

The pseudo-contact shift ($\boldsymbol{\delta_{pc}}$) is a through-space shift-inducing mechanism that rises from dipolar interactions between magnetic moments of the nuclei under investigation and the unpaired electrons of the paramagnetic ion. Such dipolar shifts arise when the metal centre exhibits significant magnetic anisotropy, as in the case of lanthanides. The sign and magnitude of these shifts is determined by the geometric distance and orientation between the nuclear and electronic moments with respect to the magnetic anisotropy tensor axes. Hence, $\delta_{pc}$ contains the geometric informations and may provide information on the extent of magnetic anisotropy of the paramagnetic centre.

In the Ln-MC presented here there are five paramagnetic centres, four Mn(III) and one lanthanide ion. Each centre provides its contribution to the final paramagnetic shift of the protons. This contributions sum up with the shift of the protons of the coordinated ligands operated by the charged ions present in the molecule ($\delta_{dia}$). The observed chemical shifts of the protons in the MC complexes result therefore

$$\delta = \delta_{dia} + \delta_{para}$$

The $\Delta_{ps}$ values presented in Table 6.4 may therefore be described as

$$\Delta_{ps} = (\delta_{dia} + \delta_{para})_{LnMC} - ((\delta_{dia} + \delta_{para})_{YMC}$$

In the hypothesis that the diamagnetic effects operated by a tripositive Y(III) or Ln(III) ions are not significantly different, the $\delta_{dia}$ contributions cancel out. Therefore:

$$\Delta_{ps} = (\delta_{para})_{LnMC} - (\delta_{para})_{YMC}$$

Due to the common presence of the Mn(III) coordination scaffold in all the isostructural compounds, and having set the spectrum of Y-MC as a reference, the second term in the previous equation contains solely the paramagnetic contribution of the Mn centres as a whole, obtaining:

$$\Delta_{ps} = \{ (\delta_{para})_{Ln} + (\delta_{para})_{Mn} \} - (\delta_{para})_{Mn} = (\delta_{para})_{Ln}$$

The relationship therefore reduces to the paramagnetic contribution of the Ln ions. Under these approximations the $\Delta_{ps}$ shift is the Lanthanide Induced Shift (LIS) and can be described as the sum of contact and dipolar contributions of the Ln centre to the chemical shifts:

$$\Delta_{ps} = (\delta_{para})_{Ln} = \delta_{c\text{-}Ln} + \delta_{pc\text{-}Ln}$$

We have already pointed out that lanthanides with a high S values (e.g. Eu(III) and Gd(III), S = 3 and 7/2, respectively) do not produce a significant shift on the protons compared to Y(III). We may reasonably deduce that the hyperfine coupling constant between the electrons at the paramagnetic centre and the protons is negligible. Under these circumstances, the $\Delta_{ps}$ values reduce to the $\delta_{pc\text{-}Ln}$ dipolar contribution, and therefore:

$$\Delta_{ps} = \delta_{pc\text{-}Ln} = \delta_{pc}$$

By analysing the $\Delta_{ps}$ shifts for the MCs presented here (Table 6.4, Figure 6.12), three features can be outlined: i) given a signal in the spectrum, for Tb-MC, Dy-MC and Ho-MC the shift is in the same direction with respect of the Y-MC reference spectrum, while the signals of Er-MC, Tm-MC and Yb-MC shift in the opposite direction; ii) the signals of the acetates shift always in the opposite direction compared to the peaks of Shi, with the exception of Pr(III), for which the acetate and three out of the four Shi protons experienced a downfield shift.

Given these spectral features, we attempted a qualitative interpretation of the data on the basis of the structure of the complexes and the theory of the NMR paramagnetic shift. For molecules that possess a 4-fold axial symmetry such as the MCs presented here, the pseudo contact shift ($\delta_{pc}$) is described by **Eq. (1)**:[18]

$$\delta_{pc} = \frac{C_J \mu_B^2}{60(kT)^2} \cdot \frac{B_0^2(3\cos^2\theta - 1)}{r^3}$$

where $C_j$, referred to as Bleaney constant, is specific of each Ln(III) ion, $r$ is the distance between the nucleus under investigation and the Ln(III) ion, $\theta$ is the angle between the nucleus and the principal magnetic axis of the lanthanide ion, $\mu_B$ is the Bohr magneton and $B_0^2$ is a crystal field coefficient.

The semi-quantitative relationship that describes the dipolar shift may therefore be described according to **Eq. (2)**:

$$\delta_{pc} \propto C_J \cdot \frac{B_0^2(3\cos^2\theta - 1)}{r^3}$$

The $B_0^2$ value has the dimension of an energy, and can be calculated form the ligand field on the lanthanide centre and its ionic radius. For a given isostructural series of lanthanide complexes, if the ligand field is the same, the $B_0^2$ values should decrease along the lanthanide series as an effect of the lanthanide contraction. However, the sign of $B_0^2$ is always positive and therefore the sign of the pseudocontact shift is determined by the $C_j$ and by the $\frac{(3\cos^2\theta - 1)}{r^3}$ term, referred to as the "**geometric term**".

The $C_j$ values have been computed and reported in the literature.[19] The extent and the sign of the $C_j$ values is determined by the distribution of the f-electron density around a paramagnetic ion or, from a different point of view, by the extent of anisotropy of the magnetic susceptibility tensor. For lanthanides, this distribution can be spherical (anisotropy $C_j = 0$), oblate ($C_j < 0$) or prolate ($C_j > 0$). The values of $C_j$ for the lanthanides can be found in the literature and are reported in Table S6.2 (Supporting Information).

The angular dependence of the pseudocontact shift, expressed by the geometric term, is represented in Fig. 6.13. Eq. (2) goes to zero when $\theta = 54.74°$, the value at which all dipolar couplings vanish, known as the *magic angle*. As a matter of fact, magic angle spin techniques are employed to maximize spectral resolution for solid samples, where dipolar couplings produce a loss in spectral quality.

The protons for which $\theta < 54.74°$ or $\theta > 125.26°$ will fall in the positive lobe and will acquire a positive sign in their geometric term. The protons that have $54.74° < \theta < 125.26°$ will fall within the negative lobe and will be characterized by a negative geometric term.

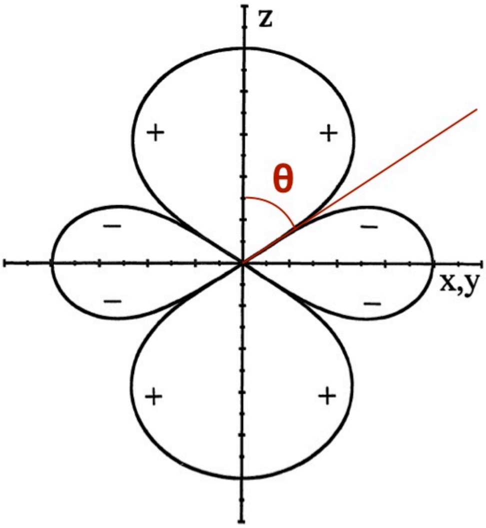

**Fig. 6.13**: Schematic representation of the angular dependence of pseudo contact shift $\delta_{pc}$.[16]

Fig. 6.14 displays the anisotropy of the magnetic susceptibility tensor, according to the quadrupolar approximation of the electron density for trivalent lanthanides, reported recently by Long and coworkers.[20] As it can be noticed, Eu(III) possesses $J = 0$, hence it does not exhibit any magnetic anisotropy as the $C_j$ constant equals to zero. Despite J is not zero, Gd(III) is the only lanthanide of the series analysed to be endowed with a spherical electron distribution. Therefore, both these lanthanides provide indeed non significant LIS compared to the species Y-MC. This justifies why Gd(III) compounds are in some cases taken as the reference compounds.

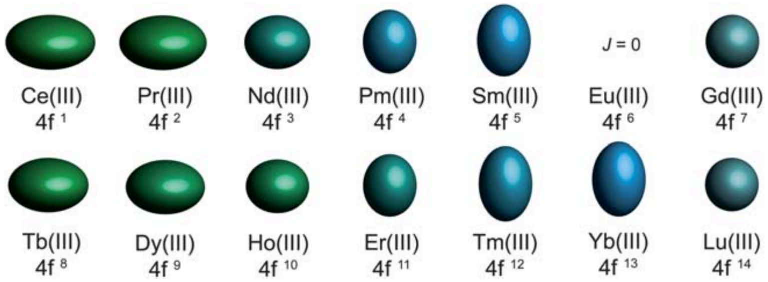

**Fig. 6.14**: Representation of the quadrupolar approximation of the 4f-shell electron density distribution for the series of Ln(III) ions.[20] Eu(III) is not displayed since it features a $J$ = 0 ground state.

The sign of $\Delta_{ps}$ for each proton in the MC compounds should depend exclusively on the sign of $C_j$ for the central Ln(III) ion and on the sign of the geometric term. More importantly, as the heterotrimetallic metallacrowns presented here are isostructural, a given signal should experience either a negative or a positive shift exclusively, in a first approximation, as a function of the $C_j$ value. This is determined by the fact that as each signal, in our approximations, is always in the same position in the structure and therefore should possess the same sign for the geometric term. Finally, the extent of lanthanide anisotropy (e.g. extent of the $C_j$ value) will give rise to more or less pronounced shifts of the peaks. More anisotropic lanthanides, with higher absolute values of $C_j$, will produce more significant $\Delta_{ps}$ and *vice versa*. It has to be mentioned, however, that a fully quantitative description of the $\Delta_{ps}$ values should take into account the $B_0^2$ value.

Among our series of compounds, the Ln(III) ions that showed larger $\Delta_{ps}$ were Tb(III), Dy(III), Ho(III), Er(III), Tm(III) and Yb(III). Fig. 6.15 shows the quadrupolar approximation of their magnetic susceptibility tensor anisotropy.

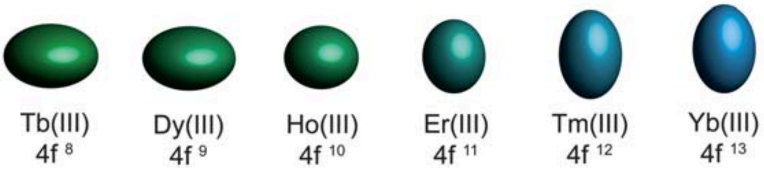

**Fig. 6.15**: Representation of the quadrupolar approximation of the anisotropy of the magnetic susceptibility tensor (described as the electron distribution in the 4f shell) for the Ln(III) ions of Tb(III), Dy(III), Ho(III), Er(III), Tm(III) and Yb(III).[20]

As can be seen from Fig. 6.16, Ln(III) ions with similar distribution (oblate or prolate) of the f-electron density behave in comparable ways in the spectra; hence, the sign of $C_j$ is indeed what causes peaks to shift either downfield (prolate ions) or upfield (oblate ions). Indeed, this description is in agreement with what expected from a theoretical description presented by Bertini and Luchinat in 1996 (Fig. 6.17).[16]

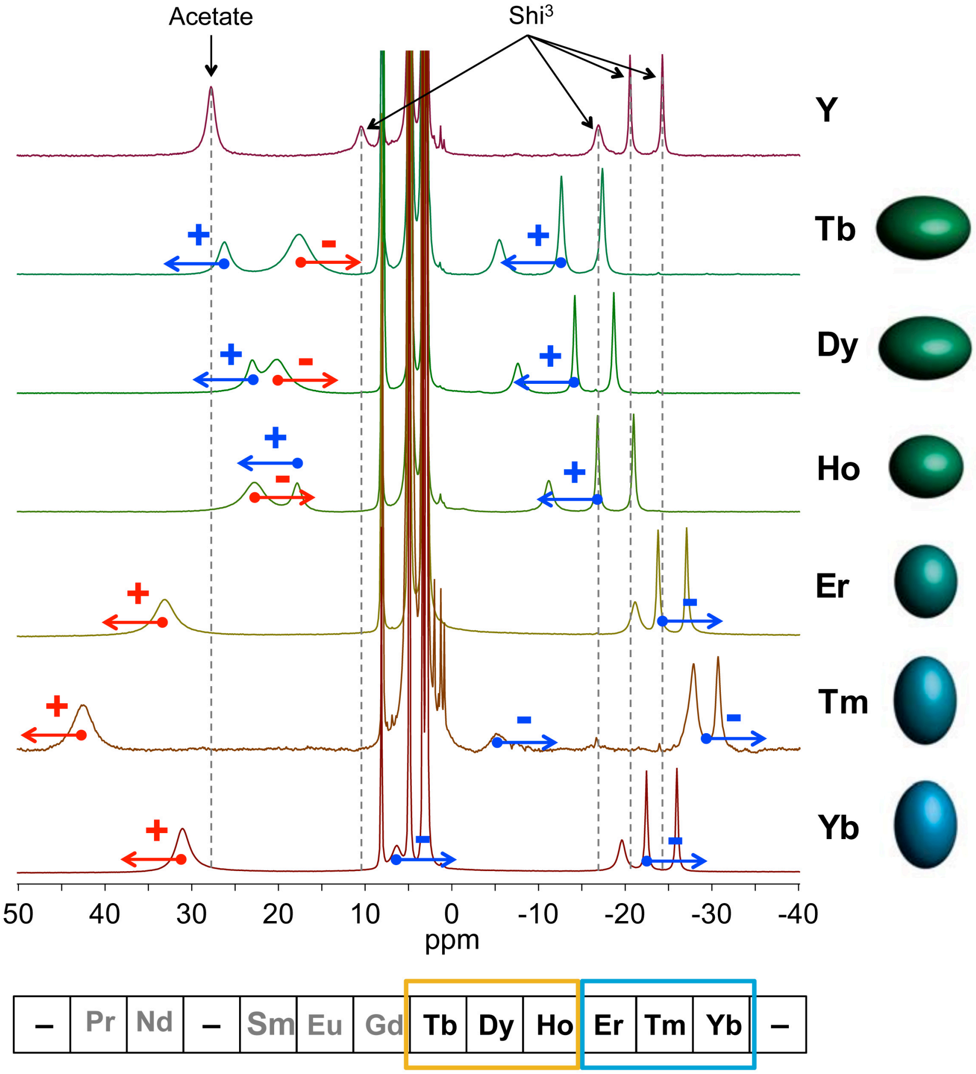

**Fig. 6.16**: Stacking of the spectra of the six MCs providing the largest shifts from the reference spectrum (Y-MC), which is reported on top. The relative shifts ($\Delta_{ps}$) for the signals of Shi are reported in blue, the relative shifts for the acetate protons in red. Aside, the oblate or prolate distribution of the 4f electron density for the Ln(III) ions.

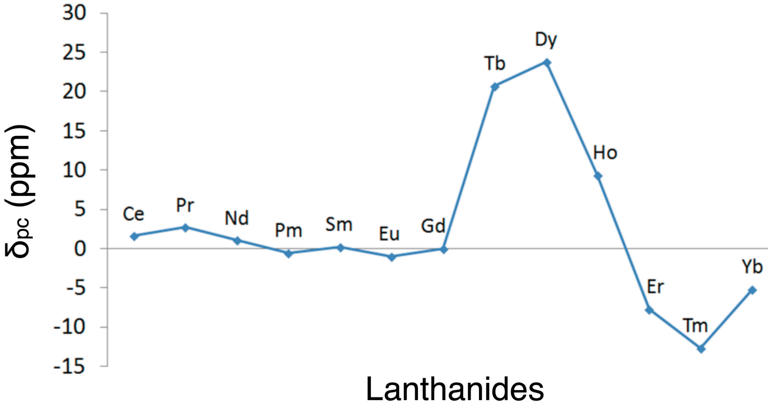

**Fig. 6.17**: Calculated pattern of pseudo contact shift induced by the Ln(III) ions, as reported by Bertini *et al.*[16]

It has been mentioned previously that an interesting feature of this set of spectra is that, for each compound, the Shi and the acetate protons shift towards opposite direction. Since the $C_j$ value is defined for each lanthanide, we expected that the reason of this behaviour lied in the geometric term. Also, Pr(III) does not behave as the other lanthanides, as three Shi protons experienced a downfield shift, in the same direction as the acetate protons.

To qualitatively rationalize the behaviour observed in the spectra, we evaluated the geometric term for the Shi and the acetate protons. All complexes are isostructural in the solid state but, since the metallacrown containing Dy(III) is one of those experiencing the largest $\Delta_{ps}$, we used its crystal data for structural evaluations. Fig. 6.18 displays the Ln(III)-$H_{Shi}$ distances ($r$) and the $H_{Shi}$-Ln(III)-$z$ angles ($\theta$), which are reported in Table 6.5 as their average values, along with the calculated value of the geometric term for each proton, for the species Dy-MC. Although the MC species presumably adopt a four-fold symmetric arrangement in solution, the solid state structures obtained for these complexes do not lie on a proper $C_4$ axes.

Thus, the ligands are disposed in slightly unsymmetrical ways around the central lanthanide and the average positions of their protons have to be considered. Table 6.5 shows that the geometric term is negative for all the Shi protons of compound Dy-MC, and so it results for the entire series of compounds, as evaluated by the crystal structures.

**Table 6.5**: Average *r*, *θ* and value of the geometric term for the Shi protons of the heterotrimetallic complex Dy-MC.

| | **Shi Protons** | | | |
|---|---|---|---|---|
| | $H_1$ | $H_2$ | $H_3$ | $H_4$ |
| ***r*** Dy – H (Å) | 6.962 | 8.914 | 9.294 | 7.918 |
| ***θ*** H–Dy–z (°) | 112.53 | 110.84 | 112.85 | 114.32 |
| $\frac{(3\cos^2\theta-1)}{r^3}$ | $- 1.65\mathrm{x}10^{-3}$ | $- 8.77\mathrm{x}10^{-4}$ | $- 6.82\mathrm{x}10^{-4}$ | $- 9.89\mathrm{x}10^{-4}$ |

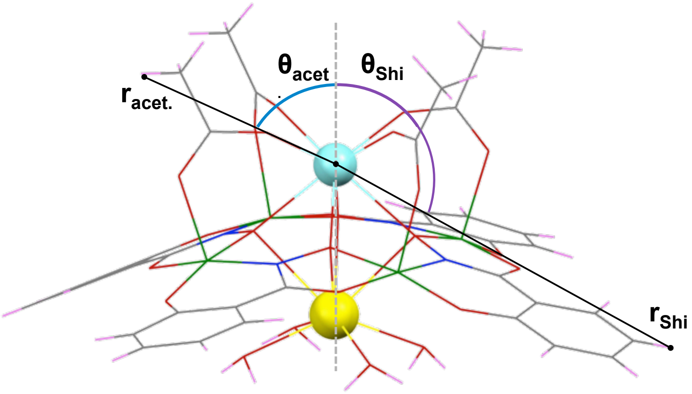

**Fig. 6.18**: Representation of the Dy - H distance *r* and of the H -Dy-z axis angle *θ* of a generic heterotrimetallic compound. Colour scheme: aqua - Ln(III), yellow - Na(I), green - Mn(III), red - oxygen, blue - nitrogen, gray - carbon, pink - hydrogen.

Recalling Table S6.2 and Fig. 6.16, it is evident that the three lanthanides with oblate electron density (*Cj* < 0), $Tb^{3+}$, $Dy^{3+}$ and $Ho^{3+}$, induce positive shifts on the Shi proton signals, while the other three lanthanides, $Er^{3+}$, $Tm^{3+}$ and $Yb^{3+}$, possessing a prolate electron density (*Cj* > 0), induce negative shifts on the Shi signals. In fact, being the geometric term of the Shi protons always negative, the sign of $\delta_{pc}$ depends exclusively on the sign of Bleaney's constant ($C_j$), as discusses earlier, and it always exhibits the opposite sign with respect to $C_j$. Therefore, $\Delta_{ps}$ (=

$\delta_{pc}$) assumes positive values for oblate lanthanides and negative values for prolate lanthanides.

As can be seen from Tables 6.3 and 6.4, this description is consistent with all $\Delta_{ps}$ , with the exception of two signals for the Pr(III) and for the Nd(III) metallacrowns (see below).

As previously discussed, the $\Delta_{ps}$ observed for the acetates always follows the opposite direction compared to the shifts of Shi protons (with the exception of Pr(III)). Therefore through our description we should expect the geometric term for the acetates to be positive in sign as it resulted negative for Shi protons, which means that the methyl group of the acetate should lie at $\theta_{Ac} < 54.74°$ (Figure 6.13).

In order to verify that our description is valid for the acetate protons, we considered as a first approximate description the centroid (**C**) of the three acetate protons (Fig. 6.19). The $\theta$ angle between the centroid **C**, the Ln(III) ion and the $z$ axis resulted greater than the magic angle for all metallacrowns (see Table 6.6 reporting representative data for Dy and Tm). Under these circumstances, the geometric term assumes a negative value, leading to $\Delta_{ps}$ values of the same sign as for Shi protons, which is the contray of what observed experimentally.

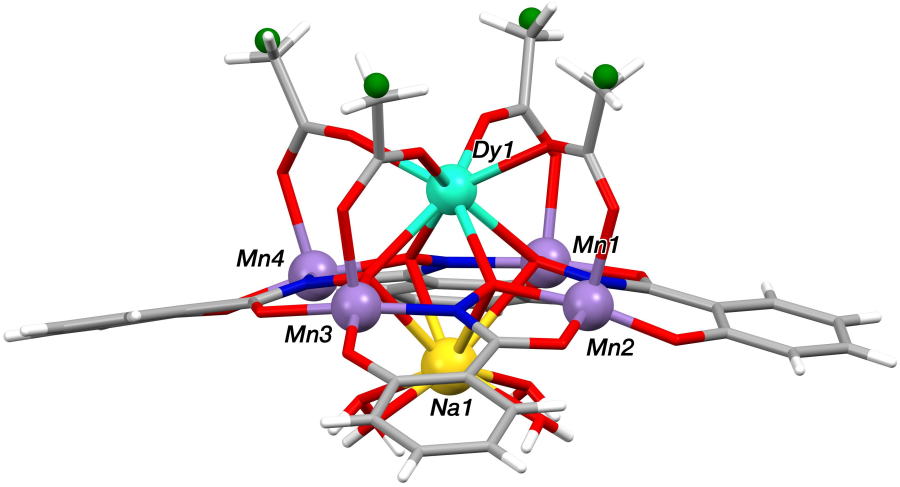

**Fig. 6.19**: Molecular structure of the compound Dy-MC displaying in green the centroids **C** between the acetate protons. Colour scheme: aqua - Dy(III), yellow - Na(I), purple - Mn(III), red - oxygen, blue - nitrogen, gray - carbon, white - hydrogen.

**Table 6.6**: Average *r*, *θ* and geometric term for the acetate protons of Dy-MC and Tm-MC, calculated by their centroid position.

| | **Acetate Protons** | |
|---|---|---|
| | Dy-MC | Tm-MC |
| ***r*** Ln – C (Å) | 4.835 | 4.819 |
| ***θ*** C–Ln–*z* (º) | 56.64 | 55.64 |
| $\frac{(3\cos^2\theta - 1)}{r^3}$ | - 8.21x$10^{-4}$ | - 3.97x$10^{-4}$ |

By comparing the calculated $\Delta_{ps}$ values, it is clear that the use of the centroid position is not a suitable description to explain the shift of the acetate signals. We have however observed that the *θ* value using the centroid approximation resulted very close to 54.74º, *i.e.* 56.64º for Dy-MC and 55.64º for Tm-MC (Fig. 6.6). Therefore, we put forward the hypothesis that structural modifications (even subtle ones) could induce the acetate groups to move inward, allowing the protons to pass into the positive lobe. This would cause a change of the geometric term sign, leading to the different behaviour of the acetate signals in the spectra, with respect to the signals of Shi.

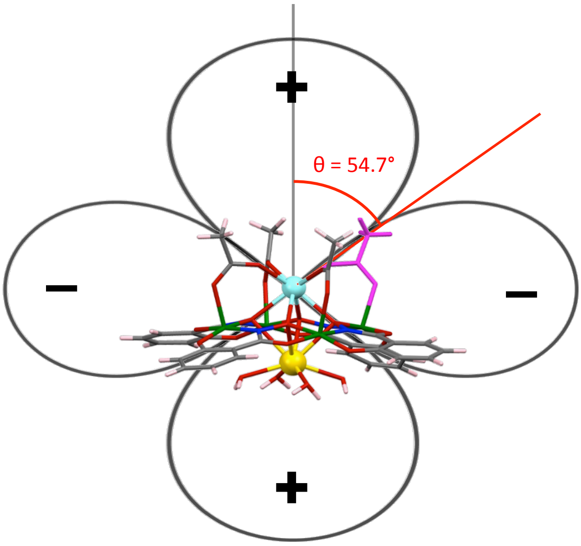

**Fig. 6.20**: Schematic representation of the angular dependence of the pseudo contact shift for the heterotrimetallic structures, overimposed to a structural representation of the MC complexes. Colour scheme: aqua - Ln(III), yellow - Na(I), green - Mn(III), red - oxygen, blue - nitrogen, gray - carbon, pink - hydrogen. An acetate ligand has been coloured in violet to highlight its position.

We have first considered that structural rearrangements can occur upon loss of the coordinated $Na^+$ ion. In particular the coordinated $Na^+$ might keep the Ln(III) ion away from the centre of the cavity by charge repulsion. Although the dimensions do not allow the lanthanides to perfectly encapsulate into the cavity, the loss of the alkali metal could allow the the lanthanide ion to penetrate more into the cavity. This rearrangement might would also drag the acetates into the positive lobe. Since an analogous crystal structure not bearing the alkali metal ion has never been obtained, we optimized the structure of Y-MC in absence of $Na^+$ by DFT calculations, using the software Gaussian. A generic double-z basis set was used, where the species C, H, N and O were modelled through *6-31G* functions, while the atoms of Mn(III) and Y(III) required the use of the set *lanl2dz* to describe the valence electrons and the pseudo-potential *lanl2dz* for the core electrons.

The optimized structure was analysed on Mercury, showing only marginal structural rearrangements when compared with the crystal structures. Table 6.7 reports the distances between Y(III) and the four acetate centroids **C** (*r*) and the angles *θ* between the centroids **C**, yttrium and the z-axis for the DFT-optimized structure. A slight increase in the $\theta$ angle and in the Y(III)-centroid distance was observed, as testified by an average calculated angle of $\theta = 58.36°$ and an average Y(III)-C distance of $r = 5.06$ Å. The limited conformational differences between the crystal structure of Y-MC and the calculated model in absence of Na(I) ion underlines that the structure adopts a similar energetically favourable conformation even when lacking Na(I); thus, the presence of Na(I) is not responsible for the structural arrangement adopted in the solid state, but the ion might only act as charge balancer. Therefore, the variations depicted by the computational study not only were not sufficient to motivate the crossing of the acetates within the positive lobe, but seem to be in disagreement with the initial hypothesis.

**Table 6.7**: Calculated distances r between Y(III) and the acetate centroids for the Gaussian-optimized structure in absence of $Na^+$ ion.

| DFT optimized structure | | | | | |
|---|---|---|---|---|---|
| **Y-MC** | ***AcO₁*** | ***AcO₂*** | ***AcO₃*** | ***AcO₄*** | **Mean** |
| $\theta$ (°) | 58.58 | 57.98 | 58.52 | 58.39 | **58.36** |
| $r$ (Å) | 5.06 | 5.05 | 5.07 | 5.06 | **5.06** |

To rationalize the behaviour of the acetate protons a deeper examination of the *geometric factor* $\frac{(3\cos^2\theta - 1)}{r^3}$ was required. Due to the $r^{-3}$ dependency of this term significantly short Ln-$H_{AcO}$ distance are accessible by the protons upon rotation of the $CH_3$ cone. These positions have a much higher weight on the final average geometric term and, more importantly, they are positions which lie in the positive lobe of the geometric term ($\theta < 54.74°$) These positions, being in the positive lobe, would motivate a $\Delta_{ps}$ opposite in sign with respect of those of the Shi protons. This behaviour is graphically represented in Fig. 6.21. In other words, those positions which give a greater contribution to the geometric term (in absolute value), are also those for which the term is positive (i.e. opposite to that of the Shi protons). As an example, the Tm-H distance $r$ for the three different protons of a single acetate ion are reported, and the relative $r^{-3}$ values are indicated. Besides the significant difference between the $r^{-3}$ values, it is important to notice that the shortest distances $r$ correspond to the smallest $\theta$ angles and vice versa.

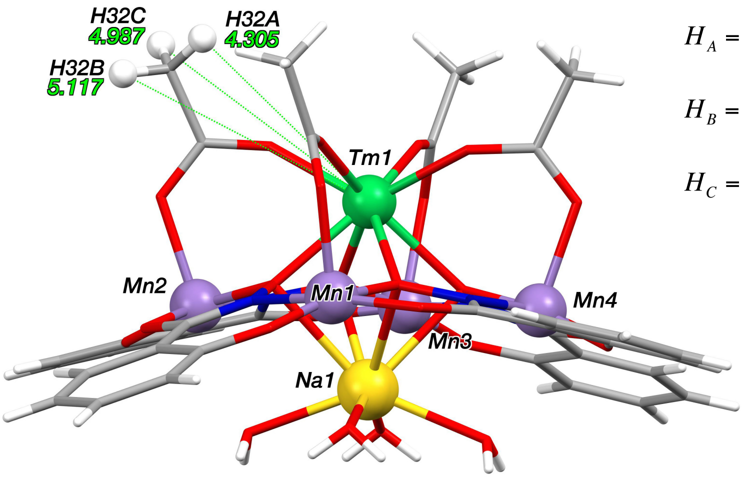

$$H_A = \frac{1}{r^3} = \frac{1}{4.30} = 0.013$$

$$H_B = \frac{1}{r^3} = \frac{1}{5.12} = 0.007$$

$$H_C = \frac{1}{r^3} = \frac{1}{4.99} = 0.008$$

**Fig. 6.21**: Crystal structure of the compound Tm-MC; next to the highlighted positions of the protons of an acetate ion are displayed the respective Tm-H distance. The factor $1/r^3$ is also reported for the three chosen protons.

This hypothesis has been verified by calculating the value of the geometric factor through a systematic rotation of the acetate cone by 10° using the crystal structures of each complex. This analysis was executed with the software HyperChem Professional: the torsion angle O-C-C-H (Fig. 6.22) was rotated over 360° and, for each of the 36 positions considered, $r$ and $\theta$ values were calculated; from the values of $r$ and $\theta$, the respective values of the geometric factor for each position were calculated and, finally, averaged. Since the scaffolds are not exactly four-fold symmetric, but they present two Shi ligand that are tilted downward and two tilted upward, the operation was repeated for the two different acetate ions of each molecule (Table 6.8).

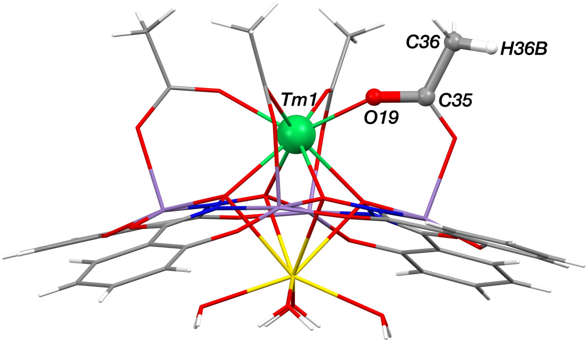

**Fig. 6.22**: Representation of the atoms constituting the torsion angle O-C-C-H that was studied through systematic rotation. Colour scheme: green - Tm(III), yellow - Na(I), purple - Mn(III), red - oxygen, blue - nitrogen, gray - carbon, white - hydrogen.

Table 6.8 shows the r and $\theta$ values for the closest proton positions to the Ln centre for the selected species Tm-MC, along with the average values obtained upon the 360º rotation. As can be seen, the shortest distances are obtained for a $\theta$ value well lower than the magic angle, which indeed reflects into an average ***positive*** value of the geometric term. Table S6.3 shows the different r and $\theta$ values obtained for each step of the rotation and their relative values of the ***C*** factor for the selected complex Tm-MC.

**Table 6.8**: Values of *r*, $\theta$ and *geometric term* obtained for two acetate molecules of Tm-MC, corresponding to the shortest distance *r* found. The corresponding value of geometric term has a positive sign; the average value of geometric term found with this method has also a positive sign.

| **Acetate Cone Rotation** | | |
|---|---|---|
| Tm-MC | $AcO_1$ | $AcO_2$ |
| ***r*** (Å)$_{min}$ | 4.518 | 4.298 |
| $\boldsymbol{\theta}$ (º)$_{min}$ | 45.366 | 45.211 |
| ***geom. term*** $_{min}$ | $+5.21\times10^{-3}$ | $+6.15\times10^{-3}$ |
| ***geom. term*** $_{aver}$ | $+3.27\times10^{-4}$ | $+8.00\times10^{-4}$ |

As a partial conclusion, the positive values of the geometric term was found for the acetate protons, as opposed to the negative values of the geometric term shown by Shi protons, qualitatively explains the $\Delta_{ps}$ values observed in the NMR spectra. Nevertheless, this model is not appropriate for the description of the $\Delta_{ps}$ observed for the Pr(III) and Nd(III). In fact, for these lanthanides the $\Delta_{ps}$ observed for the acetate protons follows the same sign of the Shi protons, shifting the signal to lower fields compared to Y-MC. The reason for this controversial behaviour might be related to the longer radii of Pr(III) and Nd(III) with respect to the following lanthanide ions.[7]

In fact, the bigger size of the two ions might cause the acetate ions to be tilted outwards from the z axis, increasing the value of the acetate θ angle for Pr-MC and Nd-MC and forcing the acetate protons into the negative lobe of the geometric term.

Although the cone rotation calculation on Pr-MC and Nd-MC has not been pursued yet, one prove of the just described mechanism lies in the z-Pr-H angles, which are wider than the ones of, for example, Tm-MC, testifying that the acetates are pushed outward from the z axis.

The signal referred to as $H_A$, which is the one to show a negative value of $\Delta_{ps}$, in disagreement with the rationalized behaviour, could not be rationalized using this description. Together with the evaluation of the quantitative extent of the shifts, a more detailed description is required.

### 6.3.3 - Carboxylate ligands substitution equilibria

We have performed $^1$H NMR titration experiments to investigate the solution equilibria related to the substitution of acetates with two carboxylates, namely benzoate and salicylate, in methanolic solution. A solution of Y-MC (which comprises four equivalents of acetate ligand) was titrated with a solution of sodium benzoate or of sodium salicylate and the evolution of the NMR spectra was monitored, registering a spectrum for each addition of titrant and comparing the integrals of the acetate proton signal (see Supporting Information).

Fig. S6.7 reports the spectrum of the species Y-MC before the first addition of titrant; the integral of the acetate signal integrates for 3.2, in accordance with the expected value of 3.0; this remarks that the acetates remain bound to the central lanthanide and do not partially dissociate in methanol.

The spectra of both titrations show the decrease of the acetate signal integral upon addition of the competing carboxylate, indicating the formation of exchange equilibria. When adding benzoate, the integral of the acetates decreases to *ca.* 5% of its original value (corrected by dilution) for 20 eq. of total added benzoate (Fig. 6.23). Upon addition of the same total amount of salicylate, the acetate integral decreases to only 32% of its initial value.

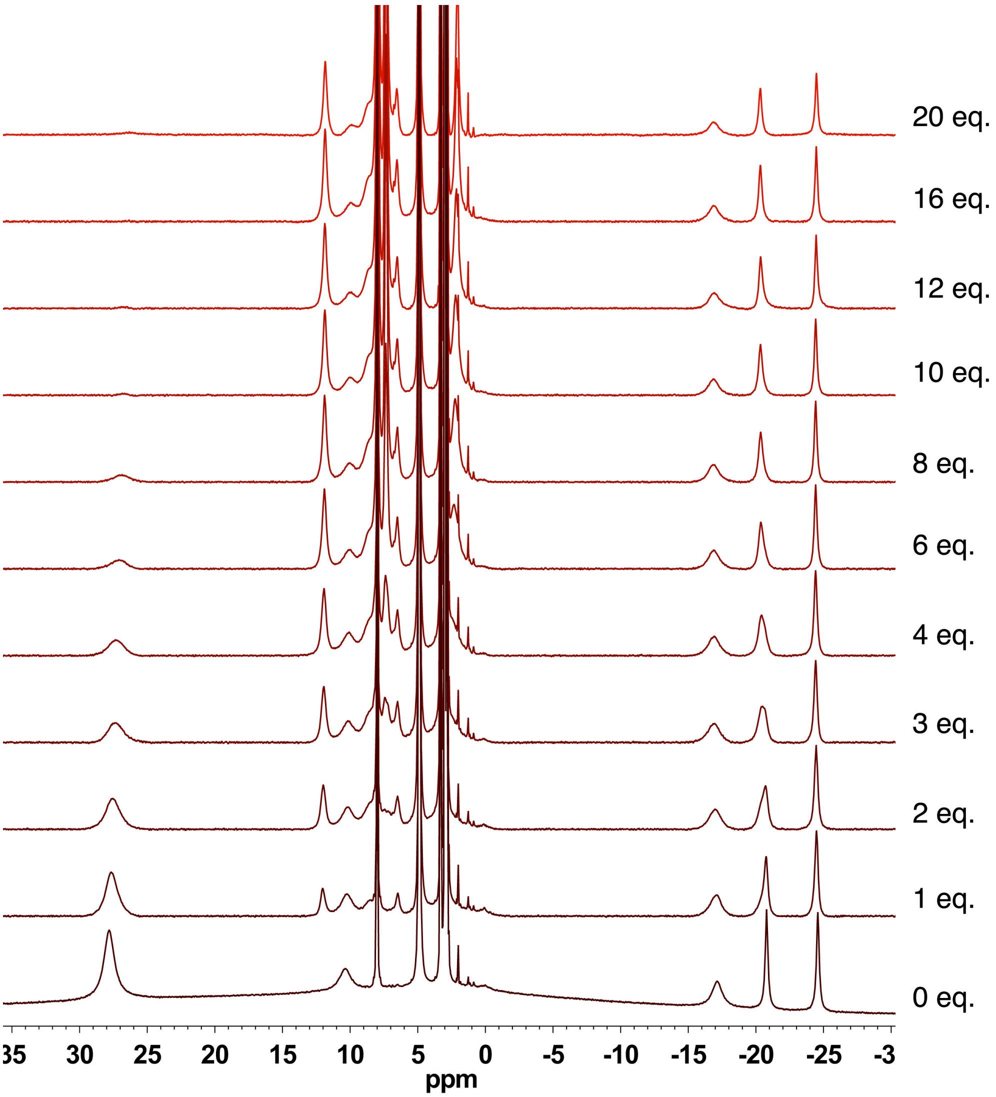

**Fig. 6.23**: Stacking of the spectra corresponding to the titration of sodium benzoate in a methanol-$d^6$ solution of Y-MC.

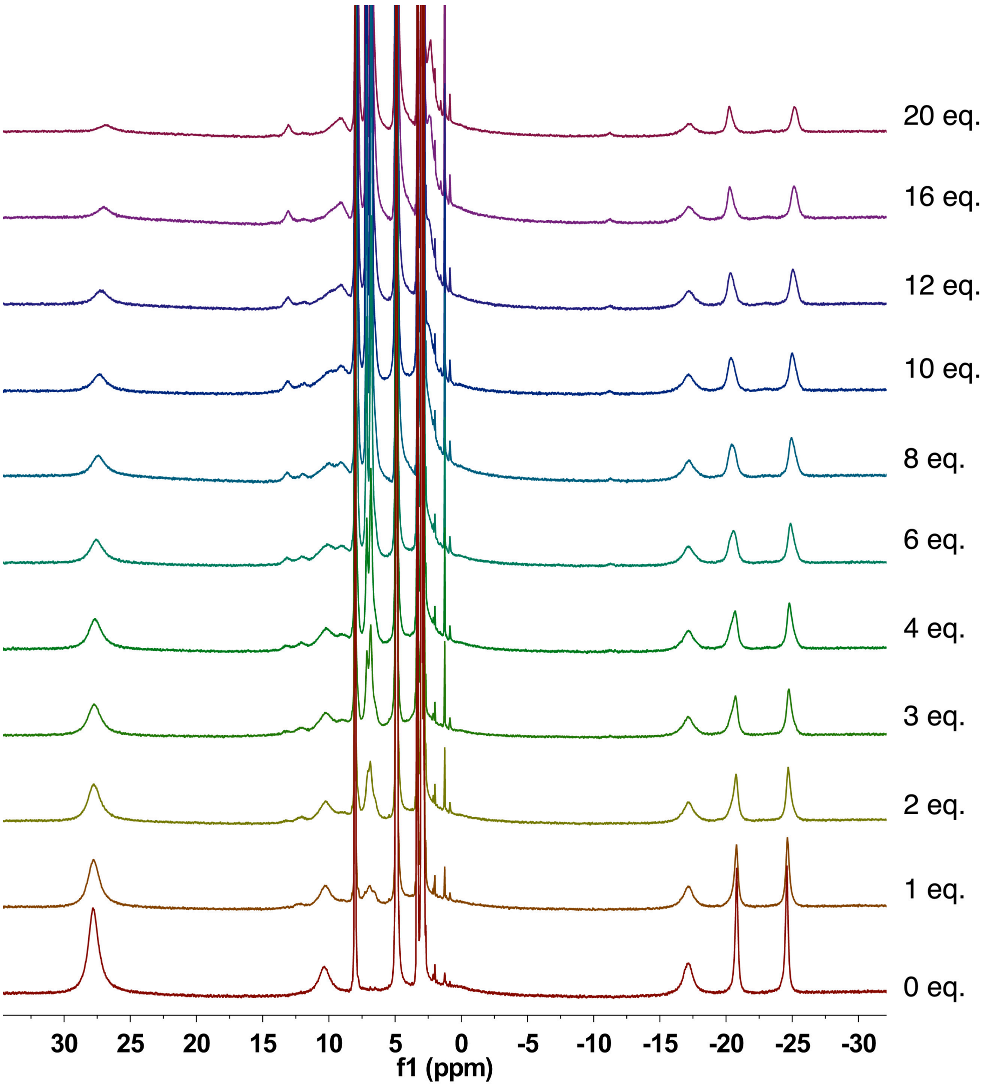

**Fig. 6.24**: Stacking of the spectra corresponding to the titration of sodium salicylate in a methanol-*d*$^6$ solution of Y-MC.

Furthermore, the data obtained from the titration experiments were treated using a model involving multiple equilibria. The following model allowed the fitting of the data for the titration with sodium benzoate (charges omitted):

$[MC(AcO)_4] + 3\ BzO = [MC(AcO)_1(BzO)_3] + 3\ AcO$ log K = 0.6(1)

$[MC(AcO)_1(BzO)_3] + BzO = [MC(BzO)_4] + AcO$ log K’ = -0.7(1)

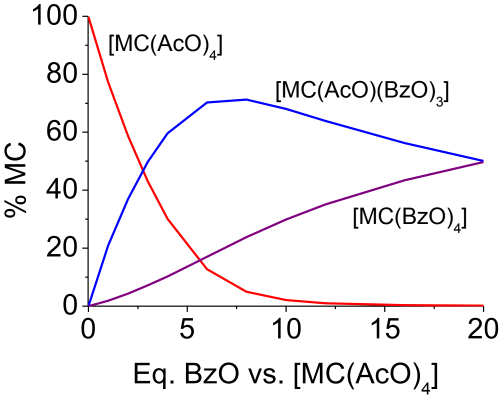

**Fig. 6.25**: Representative distribution diagram for the titration of a $[MC(AcO)_4]$ solution ($C_{MC}$ = 5.97 mM) with sodium benzoate in methanol-*d₄*.

The data for the titration with sodium salicylate could be fitted using a model consisting of only one equilibrium:

$[MC(AcO)_4] + 3\ HSalO = [MC(AcO)_1(HsalO)_3] + 3\ AcO$ log K = 0.7(2)

The log *K* values show that for both benzoate and salicylate the substitution of three out of the four bound acetates is a favoured process. It is interesting that the log *K* for the formation of the $[MC(AcO)_1(BzO)_3]$ and $[MC(AcO)_1(HsalO)_3]$ are not significantly different, irrespective of the different p$K_a$ values of the reacting carboxylates, while the latter suggest a greater complexation capacity of benzoate compared to salicylate (p$K_a$ 4.0 and 2.8 for the carboxylic functions in benzoic and salicylic acid, respectively).[21] The most interesting aspect is that the formation of the $[MC(BzO)_4]$ species is detected, while the same does not occur with salicylate. We tentatively attribute this behaviour to the greater steric hindrance of $HsalO^-$ compared to that of benzoate, which causes the complete substitution of acetates to become unfavourable.

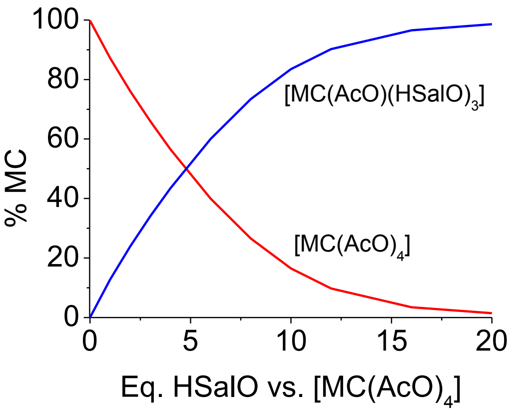

**Fig. 6.26**: Representative distribution diagram for the titration of a [MC(AcO)$_4$] solution ($C_{MC}$ = 5.97 mM) with sodium salicylate in methanol-d$_4$.

Unpublished data, previously collected by Zaleski *et al*., on the SMM behaviour of the analysed compounds suggests that the nature of the carboxylate ligand (i.e. its p$K_a$) influences the crystal field induced on the lanthanide, hence the magnetic coupling between the Ln(III) ion and the ring Mn(III) ions, changing the SMM behaviour of the complexes. Our titration data demonstrate that the presence of carboxylate ligands of different p$K_a$ do not impact significantly on the complex stability. Thus, this result suggests that several new compounds can be isolated even using carboxylates with moderate basicity.

### 6.3.4 - Core metal substitution equilibria

The possible existence of simple core lanthanide ion exchange was investigated by $^1$H-NMR titration. Yb-MC was titrated with a Y(III) nitrate solution in methanol. In a similar titration, Nd-MC was titrated with a Dy(III) nitrate solution in methanol. The inverse titrations were also pursued. The lanthanide ions to be used in the experiments were chosen in the attempt to provide an easier interpretation of NMR spectra, since they have different ionic radii and the related MCs are those which experience the largest chemical shift difference.

The addition of aliquots of free Ln(III) ion did not result in the neat change of the spectrum from that of one single lanthanide to that of the added one. Rather, evan after the first addition of 0.25 eq. of lanthanide, the spectra lost their normal patterns and the signals attributed to Shi and to the acetates were no longer easily attributable. Thus, we can assert that the addition of free Ln(III) ions to Ln(III)-MC species in solution does not result into a simple metal-exchange equilibrium, but it produces species possibly resulting from the coordination of free Ln(III) to peripheral oxygen atoms of the MC scaffold.

## 6.4 - Conclusions

In conclusion, a class of 12 heterometallic metallacrowns was studied by means of $^1$H-NMR. Relaxation rates, integrity in solution, and paramagnetic shifts were investigated, and rationalized on the basis of the structures determined in the solid state. A qualitative description of the Lanthanide Induced Shifts observed by $^1$H-NMR was developed on the basis of the magnetic anisotropies ($C_j$) of the different lanthanide ions assuming that the MCs are isostructural in solution. Also, we have demonstrated that these complexes, although self-assembled, retain their integrity in solution especially with respect of the bridging acetates.

In the future, we aim to carry out a quantitative treatment of the Lanthanide Induced Shifts, taking into account the calculated values of $B_0^2$. This study can allow a fast evaluation of some of the (para)magnetic properties of complexes and, possibly, a preliminary screening of compounds with promising SMM behaviour. In our opinion, even the rarely exploited paramagnetically shifted $^1$H-NMR technique can represent a valuable tool for conducing time- and resource-affordable studies on the solution behaviour and on the magnetic properties of extended classes of magnetic complexes.

## 6.5 - Supporting Information

### 6.5.1 - UV-Vis Spectrophotometry

Mother solutions of Y-MC and Eu-MC (ca. 1mM) were prepared by weight in DMF or acetonitrile (ca. 1.6-1.8 mg in 1 ml of solvent). A ca. 23 μM solution in acetonitrile was prepared by dilution of the mother solution. Titrant solutions of 18-C-6 (ca. 0.32 mM) were prepared by weight in acetonitrile. The hexamethylenetetramine (HEX) buffer solution (50 mM, pH 6) in methanol:water 9:1 (v/v) was prepared by suspending solid hexamethylenetetramine to the methanol:water mixture, and correcting the pH with conc. HCl to pH 6 where full dissolution of the base occurs. A mother solutions of xylenol orange (XO, ca. 0.52 mM) was prepared by weight in hexamethylene buffer solution. A mother solution of Y(NO3)3x6H2O (ca. 0.26 mM) was prepared by weight in methanol:water 9:1 mixture. Mother solutions of NaCl and KCl (ca. 53 mM) were prepared by weight in methanol:water 9:1 mixture.

For the titration of Y-MC and Eu-MC with 18-C-6, the titrand solution was prepared in a cuvette by adding a proper volume of the MC (ca. 1.5 ml of a 23 uM solution) to pure solvent. The final MC concentration was 13 μM. The solution was titrated with the 18-C-6 mother solution until MC:crown ratio of ca. 2.6 and the UV-vis spectrum collected for each addition.

The samples for the titration of xylenol orange with Y(III) nitrate were prepared as follows: 100 μL of XO mother solution were diluted in a cuvette with 2.5 ml of HEX buffer solution. The final XO solution (ca. 20 μM) was titrated with the mother solution of Y(III) nitrate up to Y:XO = 1.2:1. The samples for the titration of xylenol orange with NaCl or KCl were prepared as follows: 100 ul of XO mother solution were diluted in a cuvette with 2.5 ml of HEX buffer solution. The final XO solution (ca. 20 μM) was titrated with the mother solution of NaCl or KCl up to Na(K):XO ca. 500:1. The samples for the titration of the Y(III)/XO ensemble with NaCl or KCl were prepared as follows: 100 ul of XO mother solution and 200 μL of Y(III) nitrate mother solution were diluted in a cuvette with 2.5 ml of HEX buffer solution. The final solution ($C_Y$ ca. 19 μM, Y:XO = 1:1) was titrated with the mother solution of NaCl or KCl up to Na:Y ca. 600:1. The samples for the titration of the Y-MC/XO ensemble with NaCl or KCl were prepared as follows: 100 ul of XO mother solution and 200 µL of Y-MC mother solution were diluted in a cuvette with 2.5 ml of HEX buffer solution. The final solution ($C_{Y\text{-}MC}$ ca. 71 µM, Y-MC:XO = 3:1) was titrated with the mother solution of NaCl or KCl up to Na:Y ca. 600:1.

All spectra were collected in the 210-900 nm range using a quartz cuvette with 1 cm path length. All titrations were performed in triplicate.

*RESULTS:*

The Y(III) and Ln(III) complexes are all brown coloured and they present two overlapped bands at ca. 420 nm (ε ca. 4800 $M^{-1}$ $cm^{-1}$) and 330 nm (ε ca. 19000 $M^{-1}$ $cm^{-1}$). Two representative spectra (Y MC and Eu MC) are reported in Figure S6.1. Since we were interested in gaining information on the stability of the MC complexes in solution, we first studied the stability of the Y MC and Eu MC in the presence of 18-C-6 in acetonitrile.

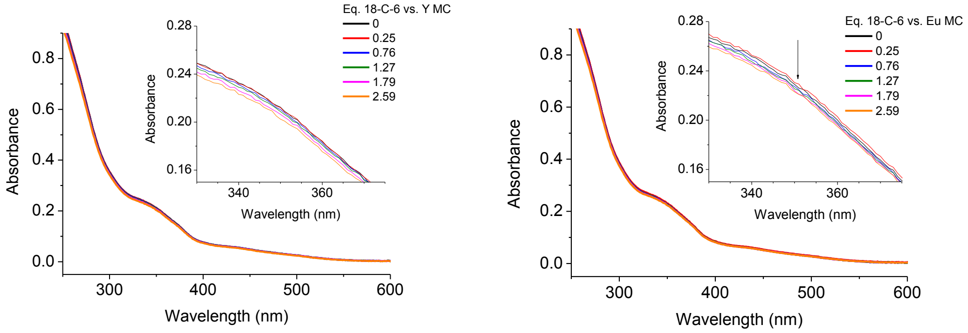

**Fig. S6.1**: UV-Vis spectra of the Y MC (left)and Eu MC (right) complexes in acetonitrile, for a successive addition of 18-C-6.

Fig. S6.1 shows that both Y(III) and Eu(III) MCs present the same UV-Vis spectra upon addition of up to ca. 2.6 eq. of 18-C-6. The slight decrease in absorbance are accounted by dilution effects. This behaviour is similar to that already observed in the literature for the copper(II)15-MC-5 encapsulating calcium and lanthanides, and suggests that the MC framework has better complexation capacities than the crown ether.[22]

Since the MC framework can form heterometallic species but also the disodium complex, we decided to perform a series of experiments aimed at elucidating if alkali metals such as Na(I) or K(I) interfere with the complexation of the trivalent metal as competing cations. We decided to use the metallochromic indicator Xylenol Orange (XO, Scheme S6.1), which is known to form coloured adducts with trivalent metals.

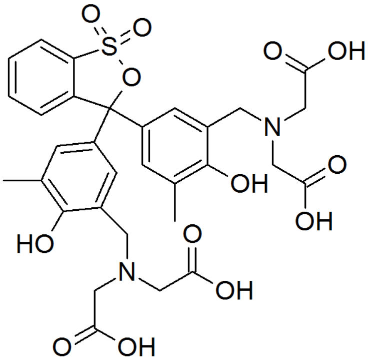

**Scheme S6.1:** Representation of xylenol orange in its fully protonated form ($H_6L$).

In the free form at pH 6, XO has a purple colour, which turns into yellow upon reaction with a trivalent metal such as a lanthanide or Y(III). Indeed, a solution of XO in methanol:water 9:1 (*v/v*) at pH 6 (hexamethylenetetramine buffer, 50 mM) reacts with Y(III) nitrate. Figure S6.2 shows that upon addition of Y(III) to XO the absorption band at 430 nm decreases with a concomitant increase of a band at ca. 580 nm. Up to 0.4 eq. of Y(III) there are no clear isosbestic points, while an isosbestic point appears at 492 nm for 0.5 eq. of Y(III) or more. This suggests that in large excess of XO a species different to 1:1 (XO:Y) is formed. For the addition of 1 eq. of Y(III), a band at 578 nm ($\varepsilon_{578\ nm}$ = 42512 $M^{-1}$ $cm^{-1}$) is obtained, which only slightly increases for further addition of Y(III) to 1.2 equivalents. Similar experiment carried out using NaCl or KCl in place of Y(III) nitrate showed no changes in the absorption profiles (Figure S6.3, decrease in absorbance is accounted by dilution effects). Also, the addition of sodium and potassium to a XO:Y(III) 1:1 solution did not show any changes in the absorbance (Figure S6.4, dilution accounts for the decrease in absorbance). These experiments overall showed that XO is a probe for the presence of Y(III), but that Na(I) and K(I) do not interfere with the XO-Y(III) binding equilibria.

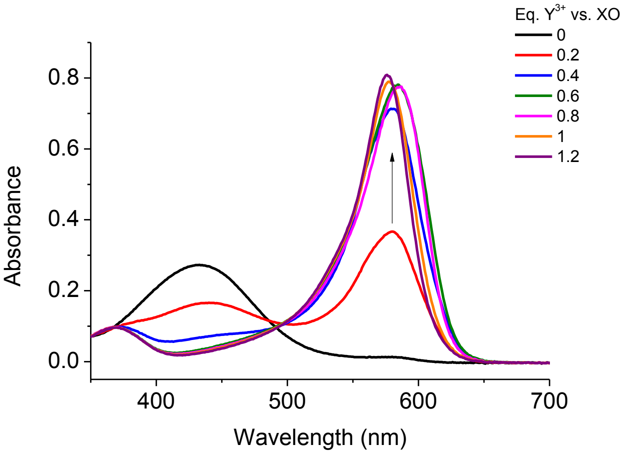

**Fig. S6.2**: UV-vis spectra for the addition of Y(III) nitrate to a solution of xylenol orange (0.52 mM) in methanol:water 9:1 (*v/v*) at pH 6 (hexamethylenetetramine buffer, 50 mM).

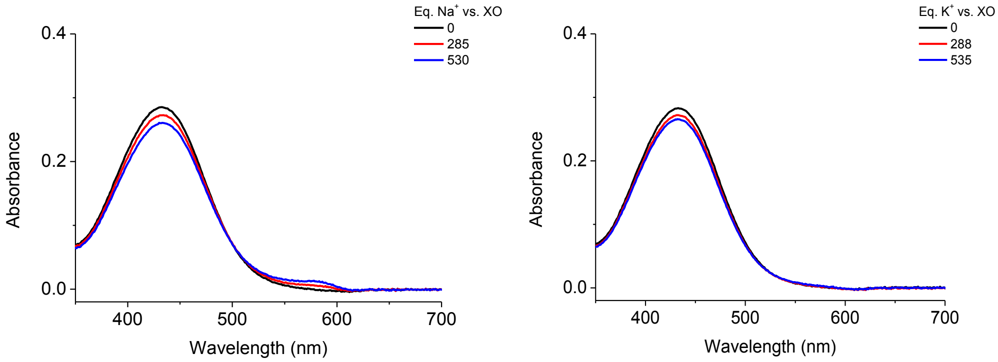

**Fig. S6.3**: UV-vis spectra for the addition of NaCl (left) or KCl (right) to a solution of xylenol orange (0.52 mM) in methanol:water 9:1 (v/v) at pH 6 (hexamethylenetetramine buffer, 50 mM).

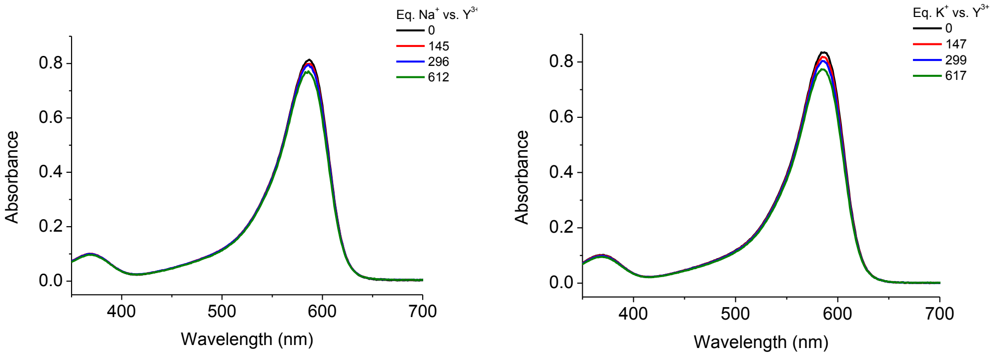

**Fig. S6.4**: UV-vis spectra for the addition of NaCl (left) or KCl (right) to a solution of xylenol orange:Y(III) 1:1 ($C_{XO}$ = 0.52 mM) in methanol:water 9:1 (v/v) at pH 6 (hexamethylenetetramine buffer, 50 mM).

When we prepared a sample by adding ca. 3 eq. of Y MC to a solution of XO, the absorbance at 578 nm of XO increases, suggesting that the indicator is capable to extract Y(III) from the MC framework (Figure S6.5). When either NaCl or KCl are added to this solution (up to 161 equivalents), an increase in absorbance of the band at 578 nm (and a decrease at ca. 450 nm) are observed, which are consistent with a partial occurrence of the $[Y \subset MC]^{3+} + Na^+ = [Na \subset MC]^+ + Y^{3+}$ displacement equilibrium. From these data it is not possible to assess with precision the stoichiometry of the two reactant and product metallacrowns (e.g. if one or two sodium ions are present in the product species). However, the data demonstrates that the alkali metals promote the partial displacement of Y(III) from MC. Also, the addition of 161 equivalents of alkali metals did not produce an increase of the band at 578 nm up to ca. 0.8 in absorbance expected  for the complete displacement of Y(III) from the cavity, and therefore the complete displacement of Y(III) is not complete even with a large excess of alkali metal.

Overall these data demonstrate that the Mn(III) 12-metallacrown-4 framework of Shi$^{3-}$ is a stronger complexing agent than 18-C-6 irrespective of its smaller cavity. As observed for the copper(II) 15-MC-5, this behaviour is accounted by the presence of negatively charged oxygen atoms in the cavity which make more favoured the interaction with MCs than with crown ethers. Also, they demonstrate that the 12-MC-4 framework forms stable complexes with Y(III), but also that alkali metals can be competing cations, although only at very high concentrations compared to the Y MC.

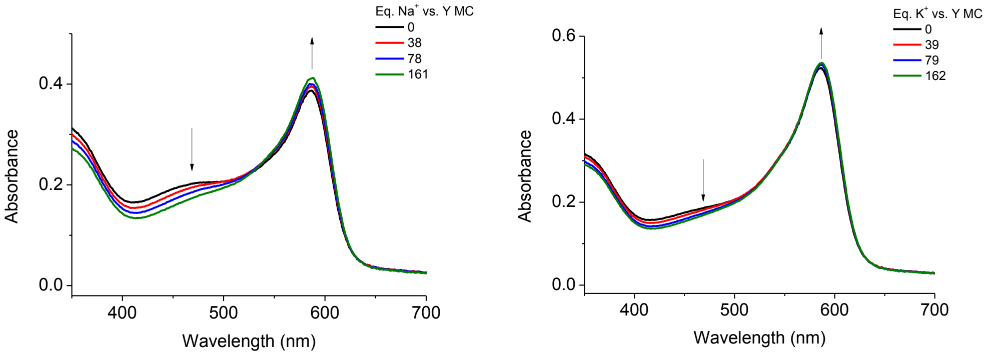

**Fig. S6.5**: UV-vis spectra for the addition of NaCl (left) or KCl (right) to a solution of xylenol orange:Y MC 1:3.8 (left) or 1:2.8 (right) ($C_{XO}$ = 0.52 mM) in methanol:water 9:1 (v/v) at pH 6 (hexamethylenetetramine buffer, 50 mM).

In the hypothesis that once extracted by XO, Y(III) leaves in solution a putative stable Mn(III) vacant 12-MC-4 species (perhaps stabilized by the presence of Na(I)), we can try to evaluate the thermodynamics of the displacement equilibrium (charges omitted):

$$[Y(MC)] + XO = [Y(XO)] + MC \qquad (1)$$

We indicate with XO and Y(XO) the free and complexed indicator forms, respectively, and with Y(MC) and MC the 12-MC-4 framework in the Y(III) complexed form and in the putative vacant species. The equilibrium constant of this process is:

$$K = \frac{[Y(XO)][MC]}{[XO][Y(MC)]} \qquad (2)$$

Taking into account that

$$[Y(XO)] = A_{578\ nm} / \varepsilon_{578\ nm} \qquad (3)$$

And the total concentrations of the species

$$C^T_Y = [Y(MC)] + [Y(XO)] \qquad (4)$$

$$C^T_{MC} = [MC] + [Y(MC)] \qquad (5)$$

$$C^T_{XO} = [XO] + [Y(XO)] \qquad (6)$$

We obtain, by substituting the eq. 4-6 into 2, that

$$K = \frac{[Y(XO)]\{C^T_{MC} - C^T_Y + [Y(XO)]\}}{\{C^T_{XO} - [Y(XO)]\} \cdot \{C^T_Y - [Y(XO)]\}} \qquad (7)$$

The [Y(XO)] value can be calculated from the first spectra of experiments in 6.5, taking into account an $\varepsilon_{578nm}$ for the [Y(XO)] species determined by experiment as in Figure S6.2 ($\varepsilon_{578\ nm}$ = 42512 $M^{-1}$ $cm^{-1}$, see above). By substituting the values in (7), we calculated a *K* value in the interval 0.12-0.17, which shows that MC is a better complexating agent than XO for Y(III), but that the difference is not extremely large.

It is also interesting to note that the [Y(XO)] stability constant has been reported in the literature (log β = 7.4).[23] The *K* value as in (2) can be written as the ratio between the *β* values of the following two equilibria (charges omitted):

$$Y + XO = Y(XO) \qquad \beta_{XO} = \frac{[Y(XO)]}{[Y][XO]} = 10^{7.4} = 2.5 \cdot 10^6 \qquad (8)$$

$$Y + MC = Y(MC) \qquad \beta_{MC} = \frac{[Y(MC)]}{[Y][MC]} \qquad (9)$$

The *K* value as in (2) results therefore

$$K = \frac{\beta_{XO}}{\beta_{MC}} \qquad (10)$$

And by substituting the value of K and that of $\beta_{XO}$ we obtained a $\beta_{MC}$ in the $1.5 \cdot 10^7$ – $2.1 \cdot 10^7$ range. As a comparison, nitrilotriacetate forms with Y(III) complexes with a conditional formation constant of ca. $10^9$ (pH 6, total Y(III):NTA 1:1, calculated using the Hyss 2006 program[24] and the stability constant reported in the literature[25]). Therefore, the small dimensions of the cavity the MC framework does not allow a complete encapsulation of the metal, which rather prefer to bind for instance to partially preorganized but sterically adaptable ligands such as, for instance, NTA.

### 6.5.2 - $^1$H-NMR

Parameters used in the $^1$H-NMR experiments:

- Time Domain (TD): 32768
- Number of Scans (NS): 16/512
- Dummy Scans (DS): 0
- Sweep Width (SW): 120 ppm
- Receiver Gain (RG): 512/1024
- Centre Frequency (O1P): 1.00 ppm
- Line Broadening (LB): 2.0
- Temperature (TE): 298.2 K

In inversion recovery experiments, the relaxation delay (*dl*) must be set according to the $T_1$'s of the specific signals. In this kind of experiment, the mixing time (τ, *d7* on Brüker instruments) between the inversion (π, 180° pulse) and the read pulse (π/2, 90° pulse) is incremented. The signals start out inverted (*d7* is very short, see Figure S6.6 below) and as the recovery time is increased, the signals recover their equilibrium magnetization and a typical 'positive' spectrum is obtained.

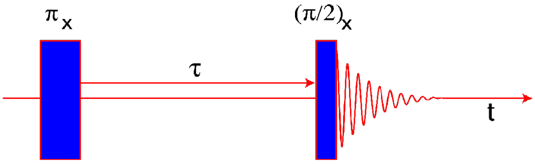

**Fig. S6.6**: Diagram depicting the Inversion Recovery pulse sequence.

$T_1$ Inversion recovery experiments were employed to measure $T_1$, the longitudinal relaxation time, or "spin-lattice" relaxation.

The analyses started by optimizing the pulse power (π pulse, P1) to be applied for the excitation of each signal set. Once the π pulse width was optimized, the *d7* recovery times (τ) were set in an increasing progression and the spectra were registered according to the increasing *d7* values for each set of peaks.

The following parameters were modified for the experiment execution:

- Pulse power (P1): optimized each time

- Number of Scans (NS): 16/32
- Delay time *d1*: 0.5 s
- Delay time *d7*: varied progressively from $10^{-4}$ to $5x10^{-2}$ s.

**Table S6.1**: List of $^1$H-NMR experiments conducted on the heterometallic compounds. Next to the complex composition ($Ln^{3+}$ is the central ion, $M^+$ the alkali metal and $RCO_2^-$ is the bridging carboxylate), the experiment performed is indicated (1D = standard 60 ppm at 298 K, IR = $T_1$ Inversion Recovery, VT = Variable Temperature, LX = Ligand Exchange Titration, MX = Metal Exchange Titration).

| **$Ln^{3+}M^+(RCOO^-)_4[12\text{-}MC_{Mn(III), Shi}\text{-}4](H_2O)_4 \cdot 6DMF$** | | | | |
|---|---|---|---|---|
| **$Ln^{3+}$, $M^+$, $RCOO^-$, (abbrev.)** | **1D** | **IR** | **VT** | **LX** |
| Y, Na, OAc, (Y-MC) | x | x | x | x |
| Pr, Na, OAc, (Pr-MC) | x | x | | |
| Nd, Na, OAc, (Nd-MC) | x | | | |
| Sm, Na, OAc, (Sm-MC) | x | x | | |
| Eu, Na, OAc, (Eu-MC) | x | x | | |
| Gd, Na, OAc, (Gd-MC) | x | x | | |
| Tb, Na, OAc, (Tb-MC) | x | | | |
| Dy, Na, OAc, (Dy-MC) | x | x | x | x |
| Ho, Na, OAc, (Ho-MC) | x | | | |
| Er, Na, OAc, (Er-MC) | x | x | | |
| Tm, Na, OAc, (Tm-MC) | x | x | | |
| Yb, Na, OAc, (Yb-MC) | x | x | | |
| Y, Na, Obz | x | | x | |
| Y, Na, Osal | x | | x | |
| Dy, K, Obz | x | | | |
| Dy, Na, Osal | x | | | |

**Table S6.2**: Bleaney's contant $C_j$ for Ln(III) ions at 300 K.[19]

| Configuration | $Ln^{3+}$ | $C_j$ |
|---|---|---|
| $4f^1$ | $Ce^{3+}$ | -11.8 |
| $4f^2$ | $Pr^{3+}$ | -20.7 |
| $4f^3$ | $Nd^{3+}$ | -8.08 |
| $4f^4$ | $Pm^{3+}$ | 4.28 |
| $4f^5$ | $Sm^{3+}$ | 0.943 |
| $4f^6$ | $Eu^{3+}$ | -- |
| $4f^7$ | $Gd^{3+}$ | -- |
| $4f^8$ | $Tb^{3+}$ | -157.5 |
| $4f^9$ | $Dy^{3+}$ | -181 |
| $4f^{10}$ | $Ho^{3+}$ | -71.2 |
| $4f^{11}$ | $Er^{3+}$ | 58.8 |
| $4f^{12}$ | $Tm^{3+}$ | 95.3 |
| $4f^{13}$ | $Yb^{3+}$ | 39.2 |

**Table S6.3**: Calculated values for *r*, *θ* and ***C*** obtained by simulating the rotation of the torsion angle O-C-C-H for two acetate ions (1 and 2) of the Tm-MC crystal structure.

| **Rotation of the dihedral O-C-C-H angle for Tm-MC** | | | | | | |
|---|---|---|---|---|---|---|
| Torsion angle | Acetate 1 | | | Acetate 2 | | |
| | *θ* | *r* | ***C*** | *θ* | *r* | ***C*** |
| 0 | 4.52052 | 46.031 | 4.828E-03 | 4.3676 | 44.196 | 6.506E-03 |
| 10 | 4.53766 | 47.053 | 4.202E-03 | 4.42029 | 44.688 | 5.978E-03 |
| 20 | 4.56841 | 48.37 | 3.398E-03 | 4.48479 | 45.538 | 5.231E-03 |
| 30 | 4.61157 | 49.907 | 2.491E-03 | 4.55869 | 46.679 | 4.350E-03 |
| 40 | 4.66551 | 51.585 | 1.558E-03 | 4.63934 | 48.04 | 3.416E-03 |
| 50 | 4.72826 | 53.328 | 6.628E-04 | 4.72402 | 49.548 | 2.493E-03 |
| 60 | 4.75759 | 55.068 | -1.521E-04 | 4.81001 | 51.139 | 1.627E-03 |
| 70 | 4.87118 | 56.749 | -8.485E-04 | 4.89469 | 52.758 | 8.420E-04 |
| 80 | 4.94665 | 58.323 | -1.427E-03 | 4.97563 | 54.357 | 1.521E-04 |
| 90 | 5.02167 | 59.754 | -1.886E-03 | 5.05061 | 55.899 | -4.425E-04 |
| 100 | 5.09403 | 61.014 | -2.235E-03 | 5.11764 | 57.352 | -9.468E-04 |

| | | | | | | |
|---|---|---|---|---|---|---|
| 110 | 5.16169 | 62.083 | -2.490E-03 | 5.17505 | 58.692 | -1.370E-03 |
| 120 | 5.2281 | 62.947 | -2.655E-03 | 5.22143 | 59.898 | -1.724E-03 |
| 130 | 5.27579 | 63.597 | -2.770E-03 | 5.25567 | 60.953 | -2.017E-03 |
| 140 | 5.3193 | 64.028 | -2.821E-03 | 5.27699 | 61.841 | -2.258E-03 |
| 150 | 5.35224 | 64.239 | -2.826E-03 | 5.28489 | 62.55 | -2.456E-03 |
| 160 | 5.37383 | 64.23 | -2.790E-03 | 5.27919 | 63.068 | -2.614E-03 |
| 170 | 5.38354 | 64.006 | -2.716E-03 | 5.26003 | 63.386 | -2.734E-03 |
| 180 | 5.38115 | 63.571 | -2.604E-03 | 5.22783 | 63.496 | -2.817E-03 |
| 190 | 5.3667 | 62.934 | -2.451E-03 | 5.18336 | 63.389 | -2.858E-03 |
| 200 | 5.34055 | 62.104 | -2.254E-03 | 5.12765 | 63.061 | -2.850E-03 |
| 210 | 5.30333 | 61.094 | -2.005E-03 | 5.06207 | 62.508 | -2.781E-03 |
| 220 | 5.25594 | 59.917 | -1.696E-03 | 4.98825 | 61.731 | -2.635E-03 |
| 230 | 5.19956 | 58.592 | -1.318E-03 | 4.90814 | 60.734 | -2.394E-03 |
| 240 | 5.13566 | 57.141 | -8.626E-04 | 4.8239 | 59.525 | -2.034E-03 |
| 250 | 5.06591 | 55.592 | -3.234E-04 | 4.73795 | 58.121 | -1.535E-03 |
| 260 | 4.99225 | 53.978 | 3.020E-04 | 4.65287 | 56.546 | -8.767E-04 |
| 270 | 4.91678 | 52.339 | 1.009E-03 | 4.57138 | 54.836 | -5.184E-05 |
| 280 | 4.84177 | 50.726 | 1.781E-03 | 4.49621 | 53.037 | 9.316E-04 |
| 290 | 4.76958 | 49.195 | 2.591E-03 | 4.33001 | 51.209 | 2.186E-03 |
| 300 | 4.70257 | 47.811 | 3.395E-03 | 4.37525 | 49.428 | 3.213E-03 |
| 310 | 4.60304 | 46.646 | 4.243E-03 | 4.33406 | 47.776 | 4.359E-03 |
| 320 | 4.59314 | 45.768 | 4.745E-03 | 4.30808 | 46.342 | 5.375E-03 |
| 330 | 4.55471 | 45.237 | 5.160E-03 | 4.29838 | 45.211 | 6.157E-03 |
| 340 | 4.52922 | 45.097 | 5.327E-03 | 4.30538 | 44.452 | 6.625E-03 |
| 350 | 4.51767 | 45.366 | 5.215E-03 | 4.32877 | 44.11 | 6.739E-03 |

## 6.5.2 - Ligand exchange - $^1$H NMR Titrations

*Experimental:*

The $^1$H NMR titration of Y-MC with sodium benzoate or sodium salicylate was carried out as follows. A ca. 6 mM solution of Y-MC in 500 µL of methanol-$d_4$ is prepared by weight and transferred quantitatively into an NMR tube (Fig.S6.7). The sample is titrated with a 0.149 M solution of sodium benzoate in methanol-$d_4$, using 20 µL aliquots (400 µL final titrant volume), or with a 0.30 M solution of sodium salicylate in methanol-$d_4$, using 10 µL aliquots (200 µL final titrant volume) For each titrant addition the $^1$H NMR spectrum was collected, and the integral of the acetate signal (ca. 28 ppm) was referenced to the residual DMF signal (2.9 ppm). The integral values were treated using the software HyperQuad2006.

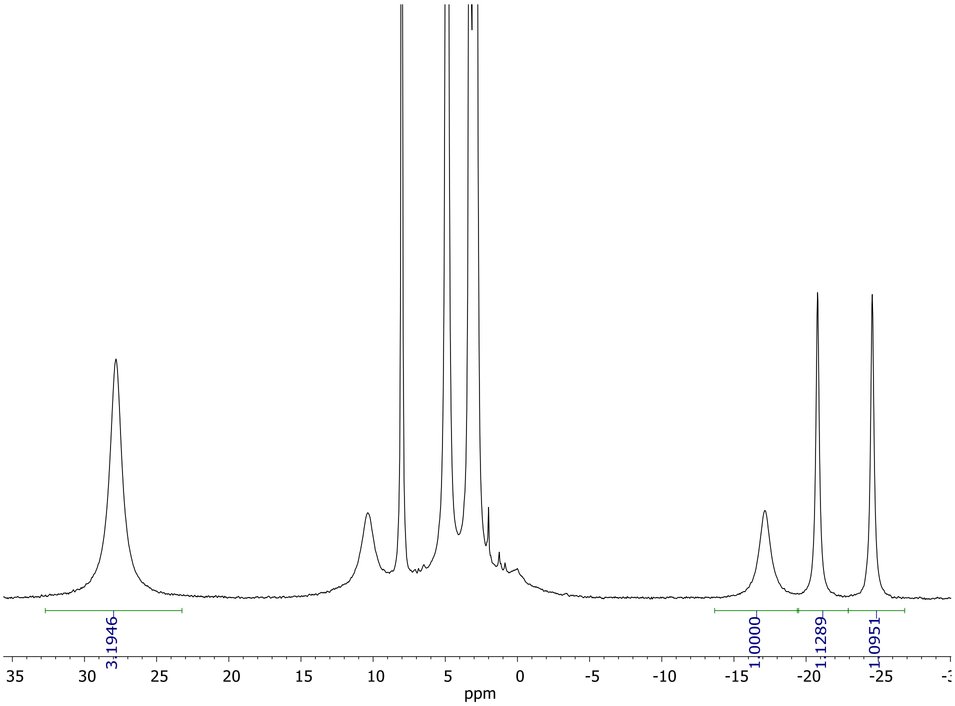

**Fig. S6.7**: $^1$H-NMR spectrum of a 6 mM solution of Y-MC before the first addition of titrant.

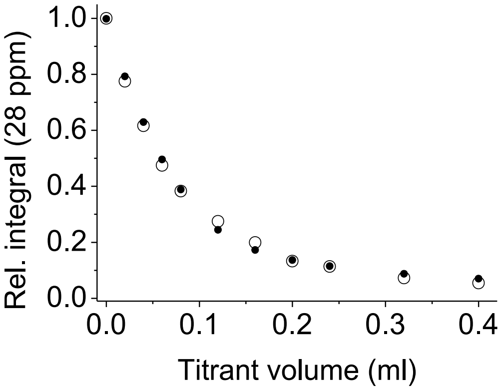

**Fig. S6.8**: Plot of the relative integral (uncorrected for dilution) of the $^1$H NMR signal of the acetate in [MC(AcO)$_4$] as a function of the titrant NaOBz solution added ($C^0_{MC}$ = 5.97 mM, $C_{titrant}$ = 0.149 M, $V_0$ = 0.5 ml, methanol-*d*$_4$).

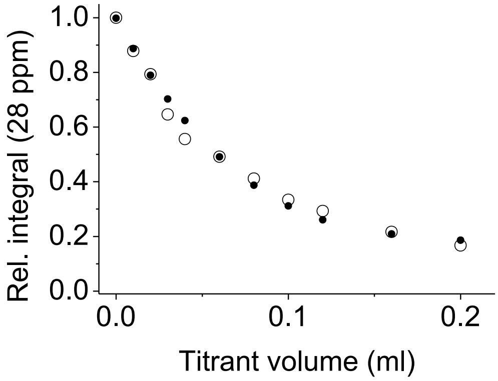

**Fig. S6.9**: Plot of the relative integral (uncorrected for dilution) of the $^1$H NMR signal of the acetate in [MC(AcO)$_4$] as a function of the titrant NaOSal solution added ($C^0_{MC}$ = 5.97 mM, $C_{titrant}$ = 0.30 M, $V_0$ = 0.5 ml, methanol-*d*$_4$).

## 6.6 - References

1 D. S. Nesterov, V. N. Kokozay, V. V. Dyakonenko, O. V. Shishkin, J. Jezierska, A. Ozarowski, A. M. Kirillov, M. N. Kopylovich and A. J. L. Pombeiro, *Chem. Commun.*, 2006, 4605.

2 D. S. Nesterov, V. N. Kokozay, J. Jezierska, O. V. Pavlyuk, R. Boča and A. J. L. Pombeiro, *Inorg. Chem.*, 2011, **50**, 4401–4411.

3 L. Ladner, T. Ngo, C. Crawford, Z. Assefa and R. E. Sykora, *Inorg. Chem.*, 2011, **50**, 2199–2206.

4 J.-P. Sutter, S. Dhers, R. Rajamani, S. Ramasesha, J.-P. Costes, C. Duhayon and L. Vendier, *Inorg. Chem.*, 2009, **48**, 5820–5828.

5 M. A. Palacios, A. J. Mota, J. Ruiz, M. M. Hänninen, R. Sillanpää and E. Colacio, *Inorg. Chem.*, 2012, **51**, 7010–7012.

6 J. Long, L.-M. Chamoreau and V. Marvaud, *Dalt. Trans.*, 2010, **39**, 2188.

7 M. R. Azar, T. T. Boron, J. C. Lutter, C. I. Daly, K. a. Zegalia, R. Nimthong, G. M. Ferrence, M. Zeller, J. W. Kampf, V. L. Pecoraro and C. M. Zaleski, *Inorg. Chem.*, 2014, **53**, 1729–1742.

8 J. Jankolovits, J. W. Kampf and V. L. Pecoraro, *Inorg. Chem.*, 2014, **53**, 7534–7546.

9 M. S. Lah and V. L. Pecoraro, *J. Am. Chem. Soc.*, 1989, **111**, 7258–7259.

10 C. M. Zaleski, S. Tricard, E. C. Depperman, W. Wernsdorfer, T. Mallah, M. L. Kirk and V. L. Pecoraro, *Inorg. Chem.*, 2011, **50**, 11348–52.

11 P. Happ, C. Plenk and E. Rentschler, *Coord. Chem. Rev.*, 2015, **289-290**, 238–260.

12 R. D. Shannon, *Acta Crystallogr.*, 1976, **A32**, 751–767.

13 E. S. Koumousi, S. Mukherjee, C. Beavers, S. J. Teat, G. Christou and T. C. Stamatatos, *Chem. Commun.*, 2011, **47**, 11128–11130.

14 C. Piguet, 2015, pp. 209–271.

15 Y. Y. Yakubovich and V. G. Alekseev, *Russ. J. Inorg. Chem.*, 2012, **57**, 911–915.

16 I. Bertini and C. Luchinat, *Coord. Chem. Rev.*, 1996, **150**, 29–75.

17 I. Bertini and C. Luchinat, *Coord. Chem. Rev.*, 1996, **150**, 77–110.

18 A. M. Funk, K.-L. N. A Finney, P. Harvey, A. M. Kenwright, E. R. Neil, N. J. Rogers, P. Kanthi Senanayake and D. Parker, *Chem. Sci.*, 2015, **6**, 1655–

1662.

19 B. Bleaney, *J. Magn. Reson.*, 1972, **8**, 91–100.

20 J. D. Rinehart and J. R. Long, *Chem. Sci.*, 2011, **2**, 2078–2085.

21 L. D. Pettit and H. K. J. Powell, *The IUPAC Stability Constants Database*, Royal Society of Chemistry, London, 2000.

22 M. . Tegoni, M. . Furlotti, M. . Tropiano, C. S. . Lim and V. L. Pecoraro, *Inorg. Chem.*, 2010, **49**, 5190–5201.

23 V. R. Sastri, J. R. Perumareddi, V. R. Rao, G. V. S. Rayudu and J.-C. G. Bünzli, *Modern Aspects of Rare Earths and their Complexes*, Elsevier, 2003.

24 L. . Alderighi, P. . Gans, A. . Ienco, D. . Peters, A. . Sabatini and A. Vacca, *Coord. Chem. Rev.*, 1999, **184**, 311–318.

25 R. M. Smith, A. E. Martell and R. J. Motekaitis, *NIST Critically Selected Stability Constants of Metal Complexes Database 46*, Gaithersburg, MD, USA.

# Acknowledgments

The research leading to these results received funding from the European Community's Seventh Framework Programme (FP7/2007-2013) under grant agreement n° 611488 (Marie Curie IRSES “Metallacrowns” project, for M.T.) and from the National Science Foundation, (CHE-1361779, for V.L.P.).

Speaking of science, my deepest gratitude goes to M.T. and L.M., for the help, support and motivation they have fed me during the last three years. I hope I have learnt a little bit from each one of you, for it would be the most important personal achievement.

For the wonderful and productive experience in Michigan, I would like to gratefully thank Prof. V.L.P., to whom goes all my admiration. Although I did not have the pleasure to stress him too many times, I wish to thank J.W.K. for his help and kindness.

For being the most amazing partners during my adventure overseas, my best thoughts go to J.P, C.V.S, J.D. and N.W.. I have rarely felt so blessed to have met someone in my entire life, all of you made Michigan so special. There are not many things as fulfilling as building friendships over the world.

Thank you to I.B., for the daily support, to F.B., A.B., D.M., for the amazing trip, one of the highlights of 2014.

To S.B., for the fun, amazing times and hope; also for making these months of writing less boring. Good luck!

To my friends S.P., O.D., P.F, F.C., M.M.; my years without you would have been so… pointless. Only our tight foolish friendship can make me miss Parma.

Finally, the biggest appreciation goes to my parents, who I love, admire and thank more than anyone else.

It is nice to think I have accomplished what I have because of my effort and qualities. The truth is, I have become what I am because I am both of you.